Tampereen teknillinen yliopisto. Julkaisu 1101
Tampere University of Technology. Publication 1101

Artem Migukin

Iterative Phase Retrieval from Multiple Noisy Observations: Variational and Sparse Object Approximation Techniques

Thesis for the degree of Doctor of Science in Technology to be presented with due permission for public examination and criticism in Tietotalo Building, Auditorium TB222, at Tampere University of Technology, on the 20th of December 2012, at 12 noon.

Tampereen teknillinen yliopisto - Tampere University of Technology
Tampere 2012

Suomen Yliopistopaino Oy
Juvenes Print TTY
2012 Tampere

ISBN 978-952-15-2974-0
ISSN 1459-2045

Abstract

A light field, considered with regard to the scalar diffraction theory, being monochromatic and linearly polarized, may be completely described by its amplitude/intensity and phase. The conventional digital imaging sensors detect only the light intensity. The phase of the radiation scattered from or transmitted through an object carries, however, a lot of important information about the object (e.g., its shape or thickness), which is of importance in many application areas such as microscopy, astronomy, material analysis, deformation detection, etc. The problem of recovering the phase from multiple (noisy) intensity observations of diffraction patterns recorded at different measurement planes is referred to as *phase retrieval*. This thesis is devoted to the development of novel iterative phase-retrieval methods and algorithms. The choice of the *iterative* phase-retrieval approach is due to its relatively simpler experimental arrangement and a lower sensitivity to noise and setting errors of the optical system comparing with interferomentic methods or deterministic phase-retrieval techniques.

In contrast to the conventional phase-retrieval methods focused mainly on wave fields at the sensor planes, the phase recovering discussed in this thesis is concentrated on the object wave field, which produces the diffraction patterns at the measurement planes. For the accurate discrete-to-discrete modeling of the free space diffraction propagation of the transverse object wave field to the sensor planes (dictated by the use of digital devices) a novel *discrete diffraction transform* is constructed and analysed. The backward wave field propagation and therefore the object estimation are represented by inverse imaging, via the regularized inverse of the forward propagation operator.

The complex-valued object wave field reconstruction is formulated in terms of the variational constrained maximum likelihood approach, targeting on the optimal object amplitude and phase reconstruction from noisy measurement data, and a good imaging. The developed *parallel* multi-plane phase-retrieval algorithms enable an efficient aggregation and processing a number of object estimates. Provided the given prior knowledge about the modulation type of the object (for the amplitude- or phase-only object to be reconstructed) a significant enhancement of phase retrieval is obtained by the corresponding modifications of the parallel algorithms. In addition, the incorporated object *sparse modeling* results in a very effective separate regularization (filtering) of noisy object amplitude and phase.

In this thesis we also consider the conventional 4f configuration with a phase modulating spatial light modulator as an optical mask to imitate the lensless multi-plane optical setup. Various disturbances arising in a real optical system

due to dirt/dust, misfocusing, aberrations, misalignment are suggested to be compensated by an introduced cumulative equivalent at the entrance of the optical system. Such a compensation of cumulative distortions is shown to essentially increase the reconstruction quality: a state-of-the-art filtering and a sharp imaging of the object are achieved from both synthetic and experimental data.

Preface

The research work presented in this thesis has been carried out at the Department of Signal Processing at Tampere University of Technology during the years 2008–2012. This thesis was financially supported by the Tampere Graduate School in Information Science and Engineering (TISE), and by the Academy of Finland funded projects 213462 (2006–2011) and 138207 (2011–2014).

I am deeply thankful to my supervisor Prof. Jaakko Astola for the possibility to work in a friendly international research environment and support during these years. I would like to express my sincere thanks and appreciation to my co-supervisor, Prof. Vladimir Katkovnik, for his excellent professional guidance, fruitful discussion, help and endless patience. My great gratitude goes to Prof. Karen Egiazarian for his valuable practical advices and support. I gratefully thank Prof. Galina Malykhina from the Department of Information and Measurement Technologies at St. Petersburg State Polytechnical University for introducing me to the world of science from the very basics to the accomplishment of my first scientific publishing.

I express my acknowledgements to Mostafa Agour from Bremer Institut für angewandte Strahltechnik (BIAS) for his help with experimental data.

I am indebted to the reviewers of my thesis, Prof. Jose Bioucas-Dias and Dr. Claas Falldorf, for their helpful and constructive comments.

I thank Virve Larmila, Marjo Elojoki, Pirkko Ruotsalainen, Ulla Siltaloppi and Elina Orava for their assistance and support in many practical matters.

Many thanks to all my colleges for creating a nice and friendly atmosphere. Especially, I would like to mention Sergey Smirnov, Mihail Georgiev, Alessandro Foi, Atanas Gotchev, Susanna Minasyan, Atanas Boev, Stanislav Stankovic, Robert Bregovic and many others. I wish to acknowledge Kostadin Dabov and Aram Danielyan for their skillful C/C++ implementation of the BM3D and BM3D-frame filters, which permitted the rapid development of the phase-retrieval algorithms.

Last but not least, my warmest appreciation to my family: my mother Olga, father Sergey, grandmother Zinaida, and my brother Maxim. I am grateful to them for their love, moral support and continuous belief in me.

Tampere, November 2012 *Artem Migukin*

Contents

Introduction to the thesis

A stationary monochromatic wave field, propagating in an isotropic, homogeneous, nondispersive and nonmagnetic medium, is commonly described at any point of space by its so-called complex amplitude, which contains the amplitude and phase. While the intensity of the scalar light wave field (amplitude is the square root of the intensity) is detected by eyes or measured using commodity digital cameras, the phase can not be directly recorded by an imaging sensor. However, the phase carries a lot of important information on the object, which the light wave is reflected from or passed through. It can be shown that the phase significantly determines imaging of objects. This phase information allows representing the volumetric object, i.e its shape, thickness, small surface distortions and so on. It is very essential for microscopy, material analysis, deformation detection, astronomy to name a few. In order to recover the complex amplitude of a light wave field one requires computational techniques recovering the phase.

The conventional approaches of the complex-valued wave field reconstruction can be divided into three groups according to the physical implementation:

- interferometric (holographic) techniques with an auxiliary reference beam;
- techniques based on the principle of the Shack–Hartmann sensor (microlenses array);
- phase-retrieval techniques with no reference beam.

The interferometric methods are based on the superposition of the coherent object and reference waves at the sensor plane. The phase information is extracted from a number of intensity measurements of the resulting interferometric patterns obtained by temporal or spatial phase shifting (see phase shifting holography and shearography). Despite a potentially high reconstruction accuracy and lateral resolution (high quality imaging), the requirement of an additional reference beam leads to a considerable efforts of adjustment, a more complex optical setup, and high demands regarding the temporal/spatial coherence of the light and mechanical stability of the optical system.

The Shack–Hartmann sensor based methods recover the phase (piecewise) from the measurement of the slops generated by a wavefront. An array of microlenses produces a number of spots on a sensor corresponding to portions of the incident wavefront. The phase is recalculated by measuring the displacement of the resulting spots with respect to the reference positions of the focal points of the used microlenses. No reference beam is required. However, the crucial disadvantage of

this method is the low spatial resolution related to the size of microlenses: evidently the smaller lenses are, the more accurate representation of the phase can be achieved. Thus, the arrangement of these sensors is relatively complex and expensive.

Phase retrieval is an approach of phase reconstruction using a number of intensity observations of diffraction patterns from different measurement planes. Experimental arrangements for phase-retrieval methods are often technically simpler and cheaper competing with the previous methods, because one detects only the result of the diffraction propagation with no reference waves. This latter approach has lower demands with respect to the coherence of the light and the mechanical stability of the setup, it is more reliable and robust to various disturbances such as vibration. Typically, these are two different phase-retrieval approaches: deterministic one based on the so-called transport-of-intensity and transport-of-phase equations, and iterative approach, which consists of periodic replacement of the estimated amplitude of the diffraction wave field at the observation planes by measured or a priori information. The deterministic methods are relatively fast but have high demands regarding to the setting accuracy of the optical system, and as the result they are very sensitive to noise, misfocusing, misalignment, etc. We consider iterative phase-retrieval techniques while we try to reduce these requirements to the accuracy of the experimental data.

In this thesis we propose iterative multi-plane phase-retrieval algorithms developed in terms of variational constrained optimization problem, and based on the maximum likelihood approach targeting on the optimal amplitude and phase reconstruction from noisy data. The phase recovering is focused on the object wave field: its good reconstruction quality and imaging. The developed parallel scheme of phase retrieval enables an efficient aggregation and processing a number of object estimates. Moreover, the use of a priori information on the object (in certain modifications of the phase-retrieval algorithms for the amplitude- and phase-only objects) significantly enhances the reconstruction accuracy. In addition, the incorporated object sparse modeling is employed for effective separate filtering of noisy object amplitudes and phases.

Outline of the thesis

This thesis can be roughly divided into three parts. The first part is devoted to preliminaries on the thesis topic. In Chapter 1 we firstly demonstrate the role of the phase information on object imaging: the phase significantly determines the resulting light wave field distribution. Section 1.1 provides a historical overview of philosophy of light and development of imaging devices. In Section 1.2 main used characteristics of light, its amplitude/intensity and phase, as well as light wave phenomena, namely: polarization, interference and diffraction, are discussed. In Section 1.3 we consider principles of the scalar diffraction theory and describe the link between two arbitrary points of the monochromatic linearly polarized light wave field in free space. In Section 1.4 the fundamental interferometric methods of the complex-valued light wave field reconstruction are described. Since the interferometric and phase-retrieval techniques process experimental data obtained

using real optical system, where spatial light modulators (SLMs) are exploited (e.g., in the 4f optical system as an optical mask to imitate the lensless optical setup for the free space diffraction propagation), then in Section 1.5 we briefly overview the optical diffractive elements used for the modulation of the optical wave field. In Chapter 2 we consider the basic principles of the phase-retrieval techniques. Firstly, in Section 2.1 we present the used plane-to-plane diffraction propagation model. Secondly, in Section 2.3 we formulate the inverse problem of phase retrieval. Then, in Section 2.4 two fundamental phase-retrieval techniques, deterministic and iterative ones are discussed. In addition, in Section 2.4.4 the concept of developed parallel iterative phase-retrieval algorithms is considered.

In the second part, in Chapter 3 we consider the novel discrete modeling of the wave field diffraction propagation. Due to the use of a digital devices such as an imaging sensor or a liquid crystal based phase modulating SLM it is straightforward to construct a precise discrete-to-discrete model linking the object and sensor plane discrete wave field distributions. In Section 3.2 the forward discrete diffraction transform is introduced: the values of the discrete wave field distributions both at the object and sensor planes are assumed to be averaged within their pixels. This idea enables an aliasing free forward propagation model given in the spatial and frequency domains. The so-called M–DDT and F–DDT models, constructed based on such an averaging, are presented in Section 3.2.1 and Section 3.2.3, respectively. In Section 3.3 we specify the sampling condition providing the perfect reconstruction in the considering discrete modeling of the diffraction propagation. The object reconstruction from the given (noisy) complex-valued measurement by inverse of the presented M–DDT is discussed in Chapter 3.5.

In the third part we propose the parallel iterative multi-plane phase-retrieval algorithms as they were developed and improved. In Section 4.1.2 we formulate the problem of phase retrieval in the used vector-matrix notation of the diffraction propagation. Then, in Section 4.2 the initial parallel multi-plane scenario of phase retrieval as a variation of the conventional Gerchberg–Saxton algorithm is presented. In Section 4.4 the augmented Lagrangian (AL) based parallel phase-retrieval algorithm and its modifications in case of known amplitude and phase modulations of the object are described. It is found that the parallel scenario enables much better results and imaging using the additive incorporate filtering of the object amplitude and phase. Chapter 5 is devoted to the object sparse regularization represented via the powerful block matching 3D (BM3D) filtering. In Section 5.2 we introduce the concept of the sparse approximation of the object amplitude and phase, reformulate the optimization problem and describe an advanced version of the AL phase-retrieval algorithm (denoted by D–AL) with a spatially adaptive separate filtering of the object amplitude and phase. Further, in Section 5.3 we take into account various disturbances arising in the real coherent imaging system, in particular in the used 4f configuration, due to misalignment, misfocusing, dust on optical elements, reflections, vibration, etc. The idea of the improvement of the reconstruction quality by the compensation the cumulative disturbances of the optical path[i] recalculated to the object plane by a

[i] Note that the optical path means the whole optical system with various optical elements (simple as lenses or quite sophisticated as SLMs) and the layer of free space which light passes through. The real optical path includes various distortions such as misalignment of optical

novel SPAR–BC algorithm is discussed in Section 5.3.2.

List of publications

Most of the material presented in this thesis appears in the following publications:

P1 [113]: V. Katkovnik, **A. Migukin**, and J. Astola, "Backward discrete wave field propagation modeling as an inverse problem: toward perfect reconstruction of wave field distributions, " *Appl. Opt.* **48**, 3407–3423 (2009).

P2 [116]: V. Katkovnik, **A. Migukin**, and J. Astola, "Computational inverse coherent wave field imaging, " ICIP 2009, Cairo, Egypt (2009), 3773–3776.

P3 [145]: **A. Migukin**, V. Katkovnik, and J. Astola, "Multiple plane phase retrieval based on inverse regularized imaging and discrete diffraction transform," *AIP Conf. Proc.* **1236**, 81–86 (2010).

P4 [148]: **A. Migukin**, V. Katkovnik, and J. Astola, "Wave field reconstruction from multiple plane intensity-only data: augmented Lagrangian algorithm," *J. Opt. Soc. Am. A* **28**, 993–1002 (2011).

P5 [150]: **A. Migukin**, V. Katkovnik, and J. Astola, "Optimal phase retrieval from multiple observations with Gaussian noise: augmented Lagrangian algorithm for phase objects,"in P. H. Lehmann, W. Osten, and K. Gastinger eds., *Optical measurement systems for instrumental inspection VII*, Proc. SPIE **8082**, 80820L, (2011).

P6 [151]: **A. Migukin**, V. Katkovnik, and J. Astola, "Advanced multi-plane phase retrieval using Graphic Processing Unit: augmented Lagrangian technique with sparse regularization,"in F. Wyrowski, J. T. Sheridan, J. Tervo, and Y. Meuret eds., *Optical Modelling and Design II*, Proc. SPIE **8429**, 84291N, (2012).

P7 [152]: **A. Migukin**, M. Agour, and V. Katkovnik, "Phase retrieval in 4f optical system: background compensation and sparse regularization of object with binary amplitude, "*Appl. Opt.* **52**, A269–A280 (2013).

In this monograph we highlight these papers by the following referring: **P1**, **P2**, ... **P7**.

The development of M–DDT is presented in **P1**–**P2** and [114, 115]. The most significant contributions of the author concerns the analysis of M–DDT. In the thesis we emphasize the following important aspects about the developed M–DDT model:

✓ The indication of the potential reconstruction accuracy by the numerical rank or conditioning number of individual transform matrices for processing

component, dirt, e.g., on the SLM or dust particles suspended in the air in front of a lens. In addition, dirt/dust may dramatically corrupt the results of the diffraction propagation even with no practical changes of the path of the rays, if it is, e.g., on the SLM in the Fourier domain.

of rows and columns of input 2D wave field distributions (images). In Section 3.5.2 we consider the general case of rectangular pixel and image sizes of the discrete wave field distributions at the object and sensor planes.

- ✓ Two alternatives for the backward wave field propagation introduced as the inverse imaging: in Section 3.5.3 we consider the regularization by truncation and compare it with the Tikhonov regularized inverse in the *approximate* and *accurate* (Kronecker product based) forms.
- ✓ In Section 3.7 we consider different parameter-choice methods for the Tikhonov regularization parameter.

The third part of this text, devoted to the developed phase-retrieval algorithms, is the core of this work. The publications **P3**–**P7** cited above and [149] represent the original work on parallel multi-plane phase retrieval, where the author of this thesis is the main contributor. Here we consider certain extensions of the published analysis and some aspects of the object reconstruction by these algorithms, namely:

- ✓ In Section 4.3 we consider the indication of the reconstructed accuracy for a sum of transform matrices what is essentially different from those that is described in Section 3.5.2.
- ✓ In Section 4.4.3 we present a modification of the AL phase-retrieval algorithm developed especially for the amplitude-only objects – the AL–A algorithm.
- ✓ In Section 4.4.5 we present the Gauss–Newton method for AL–Ph in case of the phase-only objects with a known and unknown scalar amplitude. This new approach is compared with the gradient descent AL–Ph phase-retrieval algorithm (originated in **P5**, see Sections 4.4.4).
- ✓ In Section 5.4.1 we introduce a novel concept of the enhancement of the reconstruction imaging using a synthetic background which accumulates different disturbances of the optical path. Such a background is generated by the object reconstruction using inpainting of its details to uniform smooth surface. It may be used for old unsuccessful object reconstructions, for which the optical setting can not be provided: e.g., the investigating specimen is destroyed or lost, the used optical system is not available, etc.

Notation and conventions

Here we declare some of the most significant notations and definitions used in the throughout text.

The symbols $\mathbb{C}$, $\mathbb{R}$, $\mathbb{R}^+$, $\mathbb{Z}$, and $\mathbb{N}$ indicate, respectively, the spaces of complex numbers, real numbers, positive real numbers, integers, and natural numbers. A complex number $z \in \mathbb{C}$ can be presented in the form $z = z_{re} + i \cdot z_{im}$, where $z_{re} = \mathrm{Re}\{z\} \in \mathbb{R}$ and $z_{im} = \mathrm{Im}\{z\} \in \mathbb{R}$ are the real and imaginary parts of z, respectively. i is called the imaginary unit, $i^2 = -1$. In the polar expression $z = r \cdot e^{i\,\mathrm{Arg}\{z\}}$, where $r = |z| = \sqrt{z_{re}^2 + z_{im}^2}$ is the absolute value of z (amplitude) or the length of the radius-vector joining the origin to the point with coordinates

(z_{re},z_{im}). The argument of z (the absolute phase) is denoted by $\mathrm{Arg}\{z\}$, $\mathrm{Arg}\{z\} \in (-\infty,\infty)$, and the so-called *principal value* of $\mathrm{Arg}\{z\}$, here *the phase*[ii], is denoted by $\phi = \arg\{z\}$, $\phi : \mathbb{C} \to [-\pi,\pi)$. The *phase wrapping operator* $\mathcal{W} : \mathbb{R} \to [-\pi,\pi)$ is introduced as

$$\mathcal{W}\{\mathrm{Arg}\{z\}\} = \mathrm{mod}(\mathrm{Arg}\{z\} + \pi, 2\pi) - \pi, \tag{1}$$

i.e. the phase is determined to be consistent with $\mathcal{W}$: $\phi = \mathcal{W}\{\phi\}$. The symbol $\circledast$ denotes the continuous convolution, e.g., the convolution of two functions of continuous variables

$$\{g \circledast h\}(x) = \int g(x-v) \cdot h(v)\, dv \;\forall x. \tag{2}$$

The continuous Fourier transform is denoted by $\mathcal{F}\{\cdot\}$ and the result of this Fourier transform is indicated by the corresponding upper case letters as in [79]

$$G(v) = \mathcal{F}\{g(x)\}(v) = \int g(x) \cdot \exp(-i2\pi vx)dx. \tag{3}$$

In particular, the Fourier transform of a (in general, complex-valued) function $g(x,y)$ of two independent continuous variables x and y is of the form

$$G(v_1,v_2) = \mathcal{F}\{g(x,y)\}(v_1,v_2) = \iint g(x,y) \cdot \exp(-i2\pi(xv_1 + yv_2))dxdy. \tag{4}$$

Similarly, we denote the inverse Fourier transform by $\mathcal{F}^{-1}\{\cdot\}$ as

$$g(x,y) = \mathcal{F}^{-1}\{G(v_1,v_2)\}(x,y) = \iint G(v_1,v_2) \cdot \exp(i2\pi(xv_1 + yv_2))dv_1dv_2. \tag{5}$$

The Dirac delta function can be loosely thought of as a function on the real line which is zero everywhere except at the origin, where it is infinite [79]

$$\delta(x) = \begin{cases} \infty, & x = 0 \\ 0 & \text{otherwise} \end{cases}. \tag{6}$$

In addition, $\int_{-\infty}^{\infty} \delta(x)\, dx = 1$, and $\delta(x,y)$ of two independent variables

$$\int_{-\infty}^{\infty}\int h(\xi,\eta)\delta(x-\xi,y-\eta)\, d\xi d\eta = \int_{-\infty}^{\infty}\int h(\xi,\eta)\delta(x-\xi)\delta(y-\eta)\, d\xi d\eta = h(x,y). \tag{7}$$

The Kronecker delta is a function of two (here integer) variables x and y given in the form

$$\delta_{x,y} = \begin{cases} 1, & x = y \\ 0 & x \neq y \end{cases}. \tag{8}$$

The rectangular function $\mathrm{rect}(\cdot)$ is defined in the following form [79, 80]

$$\mathrm{rect}\left(\frac{x}{\alpha}\right) = \begin{cases} 1, & |x| \leq \frac{\alpha}{2} \\ 0 & \text{otherwise} \end{cases}, \tag{9}$$

[ii] Despite the argument of $z = 0$ is, in general, indeterminate, we assume that $\arg\{0\} = 0$ as it is used in MATLAB, where our calculations are performed.

where the threshold $\alpha \in \mathbb{R}^+$.

Given a discrete set $\mathbf{d}$, the symbol # stands for the cardinality of $\mathbf{d}$, i.e. $\#\mathbf{d}$ is the number of elements in the set $\mathbf{d}$. The same notation is also used to indicate the number of component of either a vector or a matrix. We denote a vector by bold lower case (e.g., $\mathbf{x}$) and a matrix is denoted by bold upper case (e.g., $\mathbf{X}$) to distinguish matrices from vectors. $\mathbf{I}$ is denotes the identity matrix.

The modulus $|\mathbf{x}|$ and square of the modulus $|\mathbf{x}|^2$ are the elementwise operations applied to the elements of the corresponding vectors, thus $|\cdot|$ and $|\cdot|^2$ are vectors. The ℓ_p norms as denoted by $||\cdot||_p$. The ℓ_0-norm denoted by $||\mathbf{x}||_0$ is a number of non-zero components of the vector $\mathbf{x}$ [48, cf. Eq. (1.18)], and the ℓ_1 norm is a sum of absolute values of components of the vector (Manhattan distance), $||\mathbf{x}||_1 = \sum_s |\mathbf{x}[s]|$. The only norm for matrices used in this text is the quadratic Frobenius matrix norm defined by the formula $||\mathbf{A}||_F^2 = \sum_{l_1,l_2} |\mathbf{A}[l_1, l_2]|^2$.

The indicator function for a vector $\mathbf{x}$ of the length $\#\mathbf{x} = N$ is denoted as follows (con. Eq. (9))

$$\mathbf{1}(|\mathbf{x}| \geq \alpha) = \begin{cases} 1, \text{ if } |\mathbf{x}[s]| \geq \alpha \\ 0, \text{ otherwise} \end{cases}, \tag{10}$$

where $s = 1, ...N$. The input of $\mathbf{1}(\cdot)$ is a real-valued vector to be tested: the modulus of each component of the input vector to be compared with the threshold $\alpha \in \mathbb{R}^+$. The output is a binary vector of the same length as $\mathbf{x}$: if $|\mathbf{x}[s]|$ is smaller than the positive threshold, the s-th component of the output vector is equal to zero; otherwise – equal to one.

Let the matrix $\mathbf{X}$ be of the size $N_\xi \times N_\eta$. The operation $\mathbf{Y} = \mathrm{ZP}_{N_1 \times N_2}\{\mathbf{X}\}$ denotes zero-padding of the matrix $\mathbf{X}$ to the size $(N_\xi + N_1) \times (N_\eta + N_2)$ so that zero components of the resulting matrix $\mathbf{Y}[l_1, l_2]$=0 are for $l_1 = 1, ...\lfloor \frac{N_1}{2} \rfloor$, $l_2 = 1, ...\lfloor \frac{N_2}{2} \rfloor$ and $l_1 = N_\xi + 1, ...N_\xi + \lfloor \frac{N_1}{2} \rfloor$, $l_2 = N_\eta + 1, ...N_\eta + \lfloor \frac{N_2}{2} \rfloor$. $\lfloor \cdot \rfloor$ and $\lceil \cdot \rceil$ stand for the floor and ceiling operations, respectively.

The discretization of the Fourier transform (3) via the Riemann sum is of the form $\mathbf{q}[n] = \sum_l \mathbf{g}[l] \cdot \exp(-i2\pi n \Delta_1 l \Delta_\xi) \cdot \Delta_\xi$, where Δ_ξ and Δ_1 are the discretization step of the function $g(x)$ and its Fourier image $G(v)$, respectively. The discretization of Eq. (4) is

$$\begin{aligned} \mathbf{Q}[n_1, n_2] &= \sum_{l_2} \exp(-i2\pi l_2 \Delta_\eta n_2 \Delta_2) \cdot \Delta_\eta \times \\ &\times \sum_{l_1} \mathbf{G}[l_1, l_2] \exp(-i2\pi l_1 \Delta_\xi n_1 \Delta_1) \cdot \Delta_\xi, \text{ where } n_1,\ n_2,\ l_1,\ l_2 \in \mathbb{Z}, \end{aligned} \tag{11}$$

and $\Delta_\xi \times \Delta_\eta$ and $\Delta_1 \times \Delta_2$ are the discretization steps for the two-dimensional (2D) function $g(x, y)$ and its Fourier transform $G(v_1, v_2)$, respectively. If the matrix $\mathbf{G}$ in Eq. (11) is of the size $N_1 \times N_2$ and $l_1, n_1 = -N_1/2...N_1/2 - 1$, $l_2, n_2 = -N_2/2...N_2/2 - 1$, then 2D discrete Fourier transform for normalized frequencies can be expressed via the exponential Fourier series as follows [21, 76, 189]

$$\begin{aligned} &\mathbf{Q}[n_1, n_2] = F\{\mathbf{G}\}[n_1, n_2] = \\ &= \sum_{l_1=-N_1/2}^{N_1/2-1} \sum_{l_2=-N_2/2}^{N_2/2-1} \mathbf{G}[l_1, l_2] \cdot \exp\left(-i2\pi \left(\frac{l_1 n_1}{N_1} + \frac{l_2 n_2}{N_2}\right)\right), \end{aligned} \tag{12}$$

where conventionally $\Delta_\xi = \Delta_\eta = 1$. The discrete Fourier transform (DFT) in such a form is denoted by $F\{\cdot\}$. Similarly to Eq. (5), the inverse DFT for $\mathbf{Q}$ is denoted by $F^{-1}\{\cdot\}$ and defined by

$$\begin{aligned} &\mathbf{G}[l_1, l_2] = F^{-1}\{\mathbf{Q}\}[l_1, l_2] = \\ = \quad &\frac{1}{N_1 N_2} \sum_{n_1=-N_1/2}^{N_1/2-1} \sum_{n_2=-N_2/2}^{N_2/2-1} \mathbf{Q}[n_1, n_2] \cdot \exp\left(i2\pi\left(\frac{l_1 n_1}{N_1} + \frac{l_2 n_2}{N_2}\right)\right). \end{aligned} \tag{13}$$

To provide the one-to-one correspondence between the direct and inverse discrete Fourier transforms $\mathbf{G} = F^{-1}\{F\{\mathbf{G}\}\}$ the 2D spectrum $\mathbf{Q}$ is taken of the same size $N_1 \times N_2$ as the original $\mathbf{G}$, and $\Delta_1 = \frac{1}{N_1}$, $\Delta_2 = \frac{1}{N_2}$.

The symbol $\otimes$ denotes the Kronecker product. In order to express matrix operations via the standard vector-matrix notation, we use the vectorization operation $\mathrm{vec}\{\cdot\}$, which converts a matrix into a column vector. Then, the matrix multiplication can be represented as [99]:

$$\mathrm{vec}\{\mathbf{A} \cdot \mathbf{X} \cdot \mathbf{B}^T\} = (\mathbf{A} \otimes \mathbf{B}) \cdot \mathrm{vec}\{\mathbf{X}\}, \tag{14}$$

where the superscript ^{T} denotes the transpose operation.

The complex conjugation of a matrix or vector is denoted by the superscript * and the conjugate (Hermitian) transpose – by the superscript ^{H}: $\mathbf{x}^H = (\mathbf{x}^*)^T$. The hat decoration $\widehat{\ }$ denotes estimated values.

The leftwards arrow symbol $\leftarrow$ stands for the replacement operation: e.g., given the vectors $\mathbf{x}$ and $\mathbf{y}$ of the same length, $\mathbf{x} \leftarrow \mathbf{y}$ means that all components of $\mathbf{x}$ are replaced by the corresponding elements of $\mathbf{y}$.

The following standard criterion functions[iii] are used to represent the reconstruction accuracy of an estimate of the vector $\mathbf{x}$:

$$\begin{aligned} \text{(peak signal-to-noise ratio)} \quad \mathrm{PSNR} &= 20\log_{10}\left(\frac{\max(\mathbf{x}) \cdot \sqrt{\#\mathbf{x}}}{\|\mathbf{x} - \widehat{\mathbf{x}}\|_2}\right), \\ \text{(root-mean-square error)} \quad \mathrm{RMSE} &= \frac{\|\mathbf{x} - \widehat{\mathbf{x}}\|_2}{\sqrt{\#\mathbf{x}}}. \end{aligned}$$

For convenience we list the abbreviations, symbols and acronyms most frequently used in the thesis.

[iii] The reconstruction quality is represented via PSNR and RMSE as the conventional metrics for imaging. Moreover, they are experimentally found to be more valuable for comparison of object wave field reconstructions than, e.g., the structure similarity (SSIM, [225]) or correlation coefficient.

List of abbreviations

2D, 3D = Two-, Three-Dimensional

AL = Augmented Lagrangian

AM = Amplitude modulation of the object wave field

ASD = Angular Spectrum Decomposition

BM3D = Block Matching 3D[iv]

CCD = Charge-Coupled Device

DDT = Discrete Diffraction Transform

DFT = Discrete Fourier Transform

F–DDT = Frequency domain Discrete Diffraction Transform

FFT = Fast Fourier Transform

GS = Gerchberg-Saxton iterative phase-retrieval algorithm

LS = Least Squares

M–DDT = Matrix Discrete Diffraction Transform

M-DFrT = Matrix Discrete Fresnel Transform

M-IDFrT = Matrix Inverse Discrete Fresnel Transform

ML = Maximum Likelihood

PM = Phase modulation of the object wave field

PSNR = Peak Signal-to-Noise Ratio

RI = Regularized Inverse

RMSE = Root-Mean-Square Error

RS = Rayleigh–Sommerfeld[v]

SLM = Spatial Light Modulator[vi]

SVD = Singular Value Decomposition

[iv] Sparse modeling based filtering procedure developed in [34, 35, 37, 38, 117].
[v] Typically it means the Rayleigh–Sommerfeld diffraction kernel or its integral.
[vi] Here it is basically a liquid crystal (LC) based phase modulating SLM.

List of symbols

$\Delta_.$ = Pixel size [m]

Δ_z = Fixed distance between the sensor planes [m]

$\boldsymbol{\varepsilon}_r$ = Additive noise at the r-th sensor plane

$\vec{\mathcal{E}}$ = Electric field [V/m]

λ = Wavelength [m]

μ = Regularization parameter in the Tikhonov regularized inverse

σ = Standard deviation of the additive Gaussian noise

τ_ε = Tolerance used for calculation of the numerical rank of the M–DDT transform matrices

ϕ = Phase

$i = \sqrt{-1}$

f = Focal length [m]

k = Wave number [m^{-1}]

u = Complex amplitude of a scalar wave field

$\mathcal{F}$ / $\mathcal{F}^{-1}$ = Continuous direct / inverse Fourier transform

F / F^{-1} = Discrete direct / inverse Fourier transform

$\vec{\mathcal{H}}$ = Magnetic field [A/m]

∂ = Partial differential

$\circledast$ = Convolution operator

$\otimes$ = Kronecker product

$\circ$ = Hadamard (element-wise) product

$\arg\{\cdot\}$ = Principal value of the argument $\mathrm{Arg}\{\cdot\}$

$\mathrm{diag}(\mathbf{x})$ = Square diagonal matrix with the components of the vector $\mathbf{x}$ in the main diagonal

$\mathrm{Im}\{\cdot\}$ = Imaginary part

$\mathrm{Re}\{\cdot\}$ = Real part

$\mathrm{vec}\{\cdot\}$ = Vectorization procedure of a matrix to a column vector

Chapter 1

Preliminaries

Imaging is an interdisciplinary research area with profound applications in many areas of science, engineering, technology, and medicine. The most natural form of imaging is visual inspection, which has dominated before the technical and computer revolution era. Optical technologies and the study of light go way back in human culture, reflecting in the development of optical artifacts such as mirrors, lenses, imaging devices and knowledge about sight and ocular diseases.

Nowadays digital (computer) imaging covers various aspects of image acquisition, processing, compression, storage, printing/visualization. Traditionally, light is considered via its *intensity* only. Captured (observed) images may be corrupted by various distortions due to, e.g., dust, aberrations in optical systems, digital noise of a camera and some other more sophisticated causes (say, atmospheric turbulence in astronomy). In this case various filtering procedures such as denoising and/or deblurring are required in order to improve the intensity imaging quality. Note that the *phase* of the light field plays an important role (perhaps, more important than intensity) in imaging. In general, the visualization quality of small objects can be significantly improved using the wave properties of light.

A scalar monochromatic linearly polarized light wave field can be completely described at any point of space by a complex function called "complex amplitude" which contains the amplitude and phase of the light field. The conventional sensors detect only the light intensity. The phase of radiation diffracted by an object carries however important information about the object surface and structure. The issue of imaging the phase of an object has been of considerable interest for many years. Starting from landmark works by Frits Zernike (e.g., [239], Nobel prize in 1953) a variety of phase visualization techniques have been developed that are now in routine use by optical microscopists. At the same time, none of the phase contrast microscopy based techniques is able to yield quantitative phase data [171].

The *phase problem* is the name given to the problem of loss of phase information in physical measurements. Since conventionally the phase cannot be measured directly, computational phase recovering techniques are required for imaging and data processing. Moreover, it can be shown that the phase significantly determines the resulting object image, hence the accuracy of the phase estimation is a

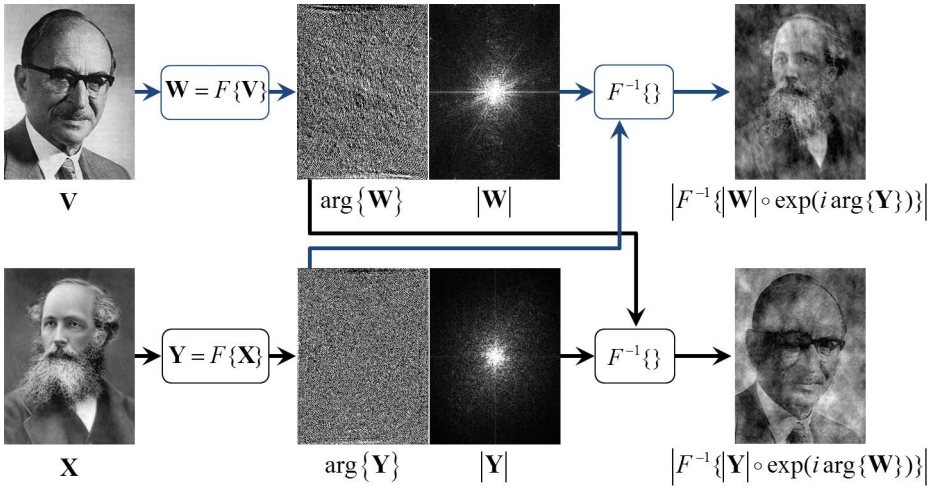

Figure 1.1: Phase carries more information than amplitude (intensity) [64, cf. slide 8]. The phase swapping ($\arg\{\mathbf{W}\} \leftarrow \arg\{F\{\mathbf{X}\}\}$ and $\arg\{\mathbf{Y}\} \leftarrow \arg\{F\{\mathbf{V}\}\}$) in the Fourier domain leads to almost complete swapping of the amplitude content of two original images in the spatial domain.

crucial point. This key idea can be illustrated by the classical experiment with the replacement of the phase information in the Fourier domain (see Fig. 1.1). It is known that the diffraction wave field propagation to the so-called far-field zone[1] can be described by the Fourier transform. Let the complex-valued Fourier transforms of two images $\mathbf{W} = F\{\mathbf{V}\}$ and $\mathbf{Y} = F\{\mathbf{X}\}$ considered as observations be obtained. Swapping the phases of these Fourier transforms $\arg\{\mathbf{W}\}$ and $\arg\{\mathbf{Y}\}$ we almost completely swap the amplitude content of these images in the spatial domain $|F^{-1}\{|\mathbf{W}| \circ \exp(i \arg\{\mathbf{Y}\})\}|$ and $|F^{-1}\{|\mathbf{Y}| \circ \exp(i \arg\{\mathbf{W}\})\}|$. That is very different from the conventional light representation via the intensity only.

This thesis deals with one of the computational approaches for the reconstruction of the complex-valued light field, called phase retrieval. Also we consider the filtering of the reconstructed object amplitude and phase for imaging enhancement.

In this Chapter we present important introductory principles required for understanding the problems of reconstruction of a complex-valued wave field, which this thesis is dedicated to. In Section 1.1 we present brief historical overview of understanding the nature of light and the invention of imaging devices. An introduction to certain basic fundamentals of the phenomenon of light wave field and used terminology is given in Section 1.2. The mathematical description of the diffraction propagation of the light wave field in free space is presented in Section 1.3. The conventional interferometric methods used to reconstruct the complex-valued object wave field are described in Section 1.4. The diffractive optical elements, which are used in optical systems for the light modulation, are discussed in Section 1.5.

[1] It means the Fraunhofer distance, see Section 1.3.7.

1.1 Historical overview

The history of direct imaging began in the ancient times [179, 220]. For instance, the oldest lens artifact, *Nimrud lens*, unearthed by Austen Henry Layard, is dating back over three thousands years to ancient Assyria. Another artifact, a well-preserved flat-convex lens of rock crystal in a frame made 2500 years BC, was discovered by Heinrich Schliemann during his famous excavations of Troy. A small lens of crystal made around 1600 BC is found in the ruins of the palace of Knossos on Crete. Ancient Egyptian statues were decorated with rock crystals, semi-precious stones and glass to imitate eyes. The Babylonians manufactured convex lenses from polished crystals, often quartz. Lenses made of the artificial material – glass – dating 600–400 BC were found in Sargon (Mesopotamia). However, since these lenses had poor magnifying qualities, they were most likely used in ornamentation or as curiosities.

The first documented works on the nature of light and vision occurred toward the middle of the first millennium BC in oriental and Greek schools of philosophy. Chinese Mohism dealt with the ray propagation, reflection and refraction of light: in particular, Chinese philosopher Mozi (ca. 470 – ca. 391 BC) wrote on the use of concave mirrors to focus the sun's rays [179]. In India, the Samkhva, Nyaya, and Vaisheshika approximately from the sixth to fifth century BC constructed a theory of light and made light or fire (tejas) one of the five elements of the world; the two latter schools distinguished between the fire from luminaries and the fire from the eye, and conceived both as diverging streams of atoms [39].

In the sixth century BC, a few bold Greek thinkers rejected the traditional appeal to supernatural forces in the explanation of natural phenomena and replaced these forces with causes to be found in nature itself. The ancient Greeks held diverse (emission/extramission and reception/intromission [173, 188]) theories of visual perception that differed from modern optics in essential manner: their speculations about light were hindered by the lack of knowledge about how the eye works. Plato combined the analysis of visual perception by Pythagoras, Empedocles and Democritus in his dialogue *Timaeus* (ca. 360 BC): sight is possible upon the notion that eyes are composed of some "internal fire" which goes out from eyes to investigate objects and is interacted with the "external fire"of visible light ("day light"reflected or emitted from luminous sources) [65]. Some early ideas of the Greeks, however, were correct. Aristophanes in his play (*The clouds*, 423 BC) describes the light focus effect of a lens. The philosopher and statesman Empedocles of Agrigentum (ca. 490 – 430 BC) believed that the light travels with finite speed, and the philosopher and scientist Aristotle (384 – 322 BC) rightly explained the rainbow as a kind of reflection from raindrops.

The ancient Greek philosophers (Plato, Aristotle and the Stoics) did not provide any precise understanding of visual appearances and deceptions, they relied more on philosophical debate and pure thought rather than on experimentations to prove ideas, and their theories were essentially qualitative. There was, however, the Greek geometrical optics according to which the perception of image depended on the incidence of visual rays on the various points of the objects [39]. In about 300 BC, Euclid wrote *Optica*, in which he studied the light propagation and postulated that light travelled in straight lines. Where Euclid had limited his

analysis to simple direct vision, Hero of Alexandria (ca. 10 – 70 AD) extended the principles of geometrical optics to consider problems of reflection (catoptrics). In his *Catoptrica*, Hero demonstrated the equality of the incident and reflected angles on the grounds that this is the shortest path between the source and point of observation (*Hero's principle*, e.g., [190, Chapter 1.1]). The use of optical devices can be illustrated by, e.g., "Archimedes heat ray": Archimedes may have used mirrors acting collectively as parabolic reflectors to burn ships during the Siege of Syracuse (ca. 214 – 212 BC).

The renowned Roman emperor Nero was said to watch the gladiatorial games using an emerald (presumably concave to correct for myopia [182]). Both Pliny the Elder (23 – 79 AD) and Seneca the Younger (3 BC – 65 AD) described the magnifying effect of a glass globe filled with water. Claudius Ptolemy (ca. 90 – ca. 168 AD[2]) extended the study of vision beyond direct and reflected vision: he also studied the nature of refraction. His works and records of experimental data on optics was further used by the Islamic scholar and scientist Alhazen (Abu Ali al-Hasan ibn al-Haitham, 965 – ca. 1040). This Egyptian scientist made significant contributions to the principles of optics, as well as to physics, astronomy, mathematics, ophthalmology, philosophy and visual perception, what strongly influenced the further study of light. He investigated the magnification produced by lenses, reflection and refraction. Following the ancient Greek physician and philosopher Galen of Pergamon (ca. 129 – ca. 200), Alhazen described the process of sight, the structure of the eye, image formation in the eye, and the visual system. In his *Kitāb al-Manāẓir* he extended the work of Ptolemy on binocular vision; gave a full account of the principle of *camera obscura*. Using Alhazen's work, the English philosopher and Franciscan, Roger Backon (ca. 1214 – 1294), studied in his *Opus Majus* the magnification by convex lenses and suggested the application of lenses in the correction of defective eyesight. Around 1284[3] spectacles were invented.

The inventor of optical microscope is unknown. Dutch spectacle-makers Hans Janssen and his son Zacharias are often said to have invented the first *compound microscope* around 1595. While experimenting with several lenses in a tube, they discovered a great magnification of objects what was a forerunner of the compound microscope and telescope. Hans Lippershey, a German-Dutch lensmaker, is generally credited with the earliest recorded design for an optical telescope (a refracting telescope) in 1608. A description of Lippershey's instrument quickly reached Galileo Galilei, who created his own improved version in 1609, "*perspicillum,*"with which he made the observations of the Moon, the stars, and the moons of Jupiter found in his *Sidereus Nuncius* of 1610. The refraction law was named after the Dutch mathematician Willebrord Snellius: he discovered the law empirically in 1621. However, the French philosopher Rene Descartes was the first how published (in his *La Dioptrique*, 1637) the now familiar formulation of the law of refraction in terms of sines.

The effects of diffraction of light were first carefully observed and characterized by Francesco Maria Grimaldi, who also coined the term diffraction, from the Latin

[2] Note, that we hereafter consider the historical overview and dates for the Current Era only and the year label AD is therefore omitted.

[3] Salvino D'Armato degli Armati of Florence is credited with inventing the first wearable eye glasses, but the modern evidence suggests that this was a hoax.

diffringere, "to break into pieces", referring to light breaking up into different directions. The results of Grimaldi's observations were published posthumously in 1665 [85]. The interference generated by thin films was observed and described by Robert Hooke (1635–1703). James Gregory (1638–1675) observed the diffraction patterns caused by a bird feather, which was effectively the first *diffraction grating*. In 1704 Isaac Newton described in his *Opticks* multiple-prism dispersion in terms of the corpuscular theory of light. Christiaan Huygens constructed the mathematical basis for the wave theory of light and published it in his *Traité de la lumière* in 1690. He proposed that light was transmitted through an all pervading *luminiferous aether* that is made up of small elastic particles each of which can act as a secondary source of wavelets. The interference principle introduced by English polymath Thomas Young (1773–1829) and the Huygens principle were used by Augustin-Jean Fresnel (1788–1827) to calculate the diffraction patterns of different objects [125]. The polarization of light was described by Young, Fresnel and Francois Arago (1786–1853) as a vibration in the aether transverse to the direction of propagation [198]. In 1811 Fresnel and Arago discovered that two beams of light, polarized in perpendicular directions, did not interfere. Such physical experiments on polarization, interference and diffraction were convincing arguments in favour of the wave theory and helped to overturn Newton's corpuscular theory (about 1840 [198]). The relations between light, electricity and magnetism were recognized by Michael Faraday (1791–1867). These phenomena were summarized by James Clerk Maxwell in *A treatise on electricity and magnetism* (1873) in this well known equations. The further works of Heinrich Hertz (1857 – 1894), Max Planck (1858 – 1947), Albert Einstein (1879 – 1955), Louis de Broglie (1892 – 1987), Arthur Compton (1892 – 1962), Niels Bohr (1885 – 1962) and many others, and the construction of quantum mechanics were convincing evidence that there is no aether, and all particles exhibit both wave and particle properties (*wave–particle duality*). Nowadays light is interpreted as a stream of massless particles, *photons*, which in many physical effects exhibit the properties of *electromagnetic waves*.

In the nineteenth century there was a revolutionary step in imaging – *a photographic camera*: the first permanent photograph was made in 1826 by Joseph Niépce and the daguerreotype (introduced in 1839) was the first commercially successful photographic process. Photographic plates/films combine three functions: image recording, image storage and image display. X-ray imaging is originated from the works by Wilhelm Conrad Röntgen (1895, the first Nobel Price in 1901) [236]. In 1907, Russian scientist Boris Rosing used a cathode ray tube (CRT) in the receiving end of an experimental video signal to form a picture: he managed to display simple geometric shapes onto the screen. The CRT technology was used as a display device (in particular, for television). Further, in 1931, the *electron microscope* was constructed by German physicist Ernst Ruska (Nobel Prize in Physics, 1986) and electrical engineer Max Knoll. The works of Otto Lehmann and Viktor Nikolaevich Zvetkov on liquid crystals (LCs), and the invention of the charge-coupled device (CCD) by Willard Boyle and George Smith (Bell Labs, 1969; Nobel Prize in Physics, 2009) gave a powerful tool for modern sophisticated techniques of image acquisition, processing and imaging. With the invention of the laser (around 1960, [82, 141]) and the computer the process of interpenetration of

optics and electronics has begun. One of the consequences of that process was the appearance of new optical elements recalculated or reprogramming by computer (spatial light modulators, SLMs [47, 159, 207]) in the late 1960s. The development of computer technologies and new materials gave the real possibility of numerical calculation of complex characteristics of a light field.

1.2 Foundations for description of light field

Let us describe the physical properties of light waves and the primary used phenomena – interference and diffraction, which take place because of the wave nature of light.

1.2.1 Light intensity

The only parameter of light which is directly amenable to sensor – eye, photodiode, CCD-target, etc. – is the *intensity* (and in a rough scale the frequency as color) [125]. Here we consider a monochromatic light field in a nonmagnetic and nondispersive medium. Intensity is defined by the energy flux (optical power) through an area per time. Let $\mathcal{E}(x, y, z)$ be the complex amplitude of the electric field. From the Maxwell equations for an electromagnetic wave propagation in an isotropic medium the light intensity I is [56, 190]

$$I(x, y, z) = \frac{c\epsilon_0 n}{2} \cdot |\mathcal{E}(x, y, z)|^2, \tag{1.1}$$

where n is the refractive index of the optical medium, ϵ_0 is the vacuum permittivity[4] and c_0 is the vacuum velocity of light. Thus, the intensity of a monochromatic wave is simply proportional to the absolute square of its complex amplitude, and the amplitude of the light wave is defined as

$$a(x, y, z) = \sqrt{I(x, y, z)}. \tag{1.2}$$

Taking into account that there is no sensor which can follow the frequency of light[5], the momentary intensity is not measurable, and we have to integrate over a measuring time[6] T

$$I(x, y, z) = \frac{1}{T} \int_{-T/2}^{T/2} \mathcal{E}(x, y, z, t)\mathcal{E}^*(x, y, z, t)dt, \tag{1.3}$$

where the proportionality constant $\frac{c_0\epsilon_0 n}{2}$ is hereafter omitted for simplicity, and $T \gg 0$ is much longer than the time of an optical cycle but much shorter than any other time of interest [125, 190].

[4] The electric permittivity of vacuum $\epsilon_0 \approx (1/36\pi) \cdot 10^{-9}$ [F/m].

[5] For instance, the visible light frequency range extends from about 384 up to 769 THz.

[6] Note that in general the flow of electromagnetic power is governed by the time average of the Poynting vector $\vec{\mathcal{E}}(x, y, z, t) \times \vec{\mathcal{H}}(x, y, z, t) = \mathrm{Re}\{\vec{\mathcal{E}}(x, y, z) \cdot e^{i2\pi vt}\} \times \mathrm{Re}\{\vec{\mathcal{H}}(x, y, z) \cdot e^{i2\pi vt}\}$, where $\vec{\mathcal{E}}(x, y, z, t)$ and $\vec{\mathcal{H}}(x, y, z, t)$ are the electric- and magnetic-field vectors, v is an optical frequency. The optical intensity is the magnitude of the vector $\mathrm{Re}\{\vec{\mathcal{S}}(x, y, z)\}$, where $\vec{\mathcal{S}}(x, y, z) = \frac{1}{2}\vec{\mathcal{E}}(x, y, z) \times \vec{\mathcal{H}}^*(x, y, z)$ may be regarded as a complex Poynting vector [190, cf. §5.3].

1.2.2 Phase of light wave field

In addition to the intensity, there is also the *phase* of the light field. In general, the phase of a wave field is a function of the position in 3D space and time, because it describes the part of a complete wave oscillation. In this work we consider a harmonic wave function of the monochromatic light in the form [79, 80]

$$\mathcal{U}(x,y,z,t) = \mathrm{Re}\{a(x,y,z)\cdot e^{i(\phi(x,y,z)-2\pi vt)}\} = \mathrm{Re}\{u(x,y,z)\cdot e^{-i2\pi vt}\}, \quad (1.4)$$

where v is the optical frequency, $\mathcal{U}(x,y,z,t)$ represents any of the scalar components of the electric (or magnet) field. The time dependent term $2\pi vt$ in Eq. (1.4) is known a priori: it is spatial-independent, but constantly changes in time. Thus, this time-dependent term is equal for all light wave field having the same wavelength λ (frequency v) and propagating in exactly the same medium with refraction index n. $\phi(x,y,z)$ describes the spatial distribution of the phase. Practically it may also be of importance the wavefront – the surface of equal phase $\phi(x,y,z) = const$ (even rather $\phi(x,y,z) - 2\pi vt = const$), which represents the structure and behavior of light waves (see Fig. 1.2).

The phase is defined here in the interval $[-\pi,\pi)$. In order to correct jumps modulo 2π and overcome the discontinuity, where two adjacent phase values have extreme values of either $-\pi$ or π (or close to them), one produces so-called *phase unwrapping*, depending on the sign of the jump underlying phase change. For instance, if the phase difference between two neighboring pixels is less than $-\pi$ (larger then π), one adds (subtracts) multipliers of 2π to the following pixels onward, what result in a (piecewise) continuous phase distribution [194, Chapter 2.7.6]. For 2D phase distributions the problem becomes more complicated because a proper path of processing is required. Such a path is typically found in accordance with the structure of the phase distribution[7].

Note that the phase unwrapping can only be performed in the areas with no phase singularities[8], i.e. zeros of the light wave field (points of zero intensity) [51]. Phase unwrapping and phase singularities are out of scope of this thesis.

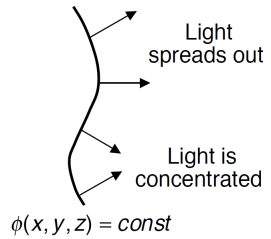

Figure 1.2: "Redistribution" of the optical intensity by the phase [64, cf. slide 9]. Light travels in direction perpendicular to the wave front $\phi(x,y,z) = const$. In addition, we obtain dimmer spot where light wave spreads out, and brighter one – where light is concentrated.

[7] See, e.g., [72] for basic principles of 2D phase unwrapping, and powerful algorithms of 2D phase unwrapping from noisy data like [44, 45, 222].

[8] In these points the phase gradient becomes infinite, and the phase variation along a closed loop around such points is always an integer multiple of 2π [70, 163].

1.2.3 Polarization of light

Since the light is an electromagnetic vector wave field, we need to mention about the *polarization*. The polarization of light at a fixed position is traditionally determined by the time course of the electric-field vector $\vec{\mathcal{E}}(x, y, z, t)$. In a simple (isotropic) medium, this vector lies in a plane tangential to the wavefront at that position. For monochromatic light, any two orthogonal components of the complex-amplitude vector $\vec{\mathcal{E}}(x, y, z)$ in that plane vary sinusoidally with time, with amplitudes and phases that are generally different, so that the endpoint of the vector $\vec{\mathcal{E}}(x, y, z)$ traces an ellipse. Since the wavefront generally has different directions at different positions, the plane, the orientation, and the shape of the ellipse also vary with the position [190, cf. Fig. 6.0-1]. We consider a monochromatic light wave traveling in the z direction, and assume that the light wave is vibrating in a single plane. Thus, we consider a plane polarized wave in the xy plane. Let us write the polarization vector of the light for this case as [81, cf. Eq. (4.3-1)], [190, cf. Eqs. (6.1-3), (6.1-4)]

$$\vec{\mathcal{E}}(z,t) = \begin{bmatrix} \mathcal{E}_x(z,t) \\ \mathcal{E}_y(z,t) \end{bmatrix} = \begin{bmatrix} a_x e^{i\phi_x} \cos(i2\pi(\frac{z}{\lambda} - vt)) \\ a_y e^{i\phi_y} \cos(i2\pi(\frac{z}{\lambda} - vt)) \end{bmatrix}, \tag{1.5}$$

what describes the state of polarization in that plane. For a plane wave the wavefronts are parallel to transverse planes and the polarization ellipses are the same everywhere (see [190, Fig. 6.0-1]). The orientation and ellipticity of the polarization ellipse determine the state of polarization of the plane wave, whereas the size of the ellipse is determined by the optical intensity. When the ellipse degenerates into a straight line or becomes a circle, the wave is said to be linearly polarized or circularly polarized, respectively. The polarized light can be described via the so-called Jones vector [79, 125]

$$\mathrm{q} = \begin{bmatrix} a_x e^{i\phi_x} \\ a_y e^{i\phi_y} \end{bmatrix}. \tag{1.6}$$

The linearly polarized light with polarization direction at an angle θ is defined by $\mathrm{q} = \begin{bmatrix} \cos\theta \\ \sin\theta \end{bmatrix}$ and represented via its time course and the trajectory of the endpoint of the vector $\vec{\mathcal{E}}(z, t)$ (Eq. (1.5)) at a fixed time t as it is illustrated in Fig. 1.3.

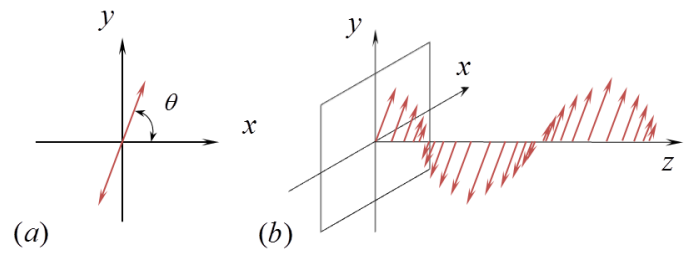

Figure 1.3: Linearly (plane) polarized light: (a) time course at a fixed position z, (b) a snapshot of the trajectory of the endpoint of the vector $\vec{\mathcal{E}}(z, t)$ at a fixed time t [190, cf. Fig. 6.1-3].

In this thesis a monochromatic linearly polarized light wave is considered. Firstly, such a light wave is completely characterized at every point of space by its intensity/amplitude and phase only [190], what significantly simplify the mathematical apparatus used to describe the free space wave field propagation. Secondly, our choice is based on the conventional approach in laser optics. Nevertheless, it can be used different wavelengths λ (frequencies v), and our work can be applied in a hyperspectral imaging system (see, e.g., [105, 184]).

1.2.4 Diffraction and interference of light waves

Diffraction refers to various phenomena which occur when a wave encounters an obstacle. Following Grimaldi's experiments, when a light wave is transmitted through a small aperture in an opaque screen and travels some distance in free space, one may observe a quite specific intensity distribution called the diffraction pattern. If light were treated as rays, the diffraction pattern would be a shadow of the aperture. Because of the wave nature of light, however, the diffraction pattern may deviate slightly or substantially from the aperture shadow (see [85, pg. 9]), depending on the distance between the aperture and observation plane, the wavelength, and the dimensions of the aperture [190]. The term *diffraction* can be defined as any deviation of light rays from rectilinear paths which cannot be interpreted as reflection, refraction or bending of light rays in a medium with a continuously varying refractive index [79, 204].

The initial step in the evolution of the wave theory that would explain diffraction effects was made by Huygens in 1678. He expressed the intuitive conviction that if each point on the wavefront of a disturbance were considered to be a new source of a "secondary" spherical disturbance, then the wavefront at a later instant could be found by constructing the "envelope" of the secondary wavelets[9], as illustrated in Fig. 1.4 [79, 194].

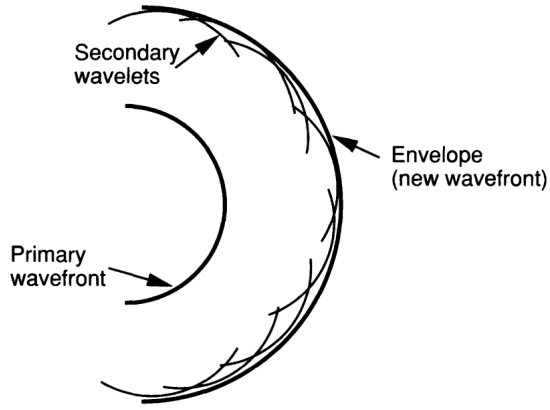

Figure 1.4: Huygens' envelope construction [79, cf. Fig. 3.4].

[9] *"Each element of a wavefront may be regarded as the centre of a secondary disturbance which gives rise to spherical wavelets "*; and moreover *"the position of the wavefront at any later time is the envelope of all such wavelets "* [20, Chapter 3.3.3].

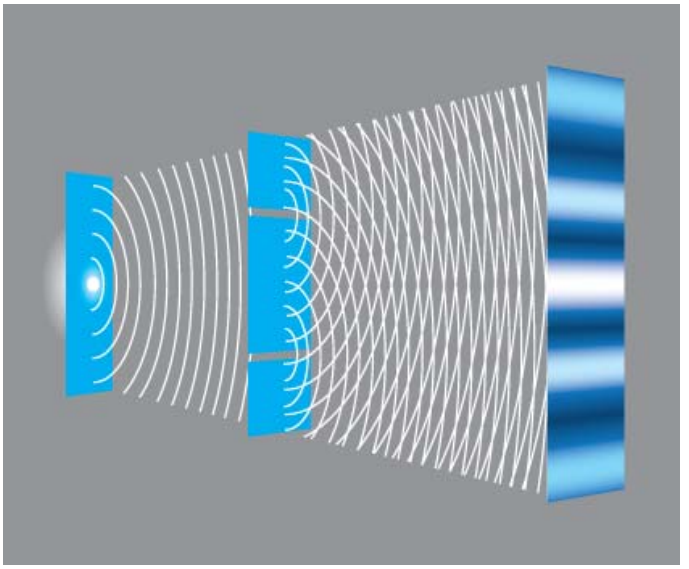

Figure 1.5: Young's double-slit interferometer: a point source of light illuminates two narrow adjacent slits in a screen, and the image of the light that passes through the slits is observed on a second screen. The dark and light regions are called *interference fringes*, the constructive (greater amplitude than either one) and destructive (lesser amplitude) interference of light waves [190].

In 1803 further significant progress occurred: Thomas Young strengthened the wave theory of light by introducing the critical concept of *interference*, according to which two coherent waves superimpose to form a resultant wave of greater or lower amplitude (intensity). The idea was a radical one at those time, because light could be added to light and produce darkness (see Young's double-slit interferometer in Fig. 1.5, [204, cf. Fig. 114, Eq. (26.14)]). Generally, it is difficult to determine the exact difference between interference and diffraction. We rather refer to the following quotation from the known Feynman lectures [55, Chapter 30-1]: *"No one has ever been able to define the difference between interference and diffraction satisfactorily. It is just a question of usage, and there is no specific, important physical difference between them. The best we can do, roughly speaking, is to say that when there are only a few sources, say two, interfering, then the result is usually called interference, but if there is a large number of them, it seems that the word diffraction is more often used".*

The ideas of Huygens and Young were brought together in 1818 in the famous memoir of Fresnel (*the Huygens–Fresnel principle* [20, 190]), and further put on a firmer mathematical foundation by Gustav Kirchhoff, who showed in 1882 that the amplitudes and phases ascribed to the secondary sources by Fresnel were indeed logical consequences of the wave nature of light. The Kirchhoff theory was also modified by Arnold Sommerfeld (1896), who gave the first truly rigorous solution of a diffraction problem using the theory of Green's functions [79, 80]. In this thesis the used mathematical apparatus of the diffraction propagation is based on

the Kirchhoff and Rayleigh–Sommerfeld theories treated as a scalar phenomenon, neglecting the fundamentally vectorial nature of the electromagnetic fields.

1.2.5 Coherence of light waves

Note that with the sunlight or lamplight we rarely observe interference. Only light of sufficient coherence will exhibit this effect. Roughly speaking, *coherence* means the ability of light waves to interfere. Precisely, coherence describes the correlation between individual light waves[10] [125]. Let we consider the concept of interference. Since the time-dependent part in Eq. (1.4) is known a priori, we consider the complex amplitude of a monochromatic light wave which is purely spatially dependent. When two or more light waves are simultaneously present in the same region of space and time, the total wave function is the sum of the individual wave functions. This basic *principle of superposition* follows from the linearity of the wave equation, in particular for monochromatic waves of the same frequency (wavelength), the superposition principle carries over to the complex amplitudes, which follows from the linearity of the Helmholtz equation [190, Chapter 2.2]. If two monochromatic waves with complex amplitudes $u_1(x,y,z) = \sqrt{I_1}e^{i\phi_1}$ and $u_2(x,y,z) = \sqrt{I_2}e^{i\phi_2}$ are superposed, the result is a monochromatic wave of the same frequency that has a complex amplitude [190, 194]

$$u(x,y,z) = u_1(x,y,z) + u_2(x,y,z). \tag{1.7}$$

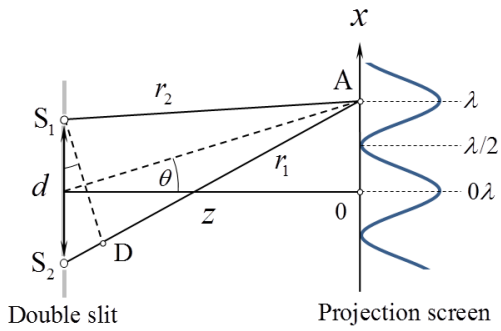

Figure 1.6: Young's double-slit experiment showing the source of the phase shift geometrically (one-dimensional case). Two slits are idealized as two closely located point sources S_1 and S_2 of a monochromatic light with the wavelength λ. The point A is the observation point with the abscissa x. A projection screen is parallel to the plane of the sources S_1 and S_2. The distance between these planes z is much larger than the size of the sources, distance between the light sources $d \ll z$ and linear dimensions of the observations area $x \ll z$. The path difference of the interfering waves is $r_1 - r_2 = S_2D = d\sin\theta \approx \frac{xd}{z}$ [190, 204, 205].

[10] *Temporal* coherence describes the correlation with itself as it behaves at different time instants and *spatial* coherence describes the mutual correlation of different parts of the same wavefront (see [125]).

Taking into account that the intensity of a monochromatic wave function is the absolute square of its complex amplitude, the intensity of the total wave is

$$\begin{aligned} I &= |u|^2 = |u_1 + u_2|^2 = |u_1|^2 + |u_2|^2 + u_1 u_2^* + u_1^* u_2 = \\ &= I_1 + I_2 + 2\sqrt{I_1 I_2} \cdot \cos(\phi_2 - \phi_1). \end{aligned} \tag{1.8}$$

This relation, called the *interference equation* (*interferogram* [194]), demonstrates that the amplitude of u is sensitive not only to the magnitudes of the constituent waves u_1 and u_2, but also to the phase difference $\phi_2 - \phi_1 = \frac{2\pi}{\lambda}(r_2 - r_1)$. In contrast to that, the sum of two incoherent waves is simply[11] $I = I_1 + I_2$.

Interference is accompanied by a spatial redistribution of the optical intensity without a violation of power conservation [190, cf. Fig. 2.5-1]. Furthermore, I in Eq. (1.8) has its maximum and minimum value for $\phi_2 - \phi_1 = 2\pi m$ and $\phi_2 - \phi_1 = 2\pi(m + \frac{1}{2})$, respectively ($m \in \mathbb{Z}$), what is called *constructive* and *destructive* interference (see Fig. 1.5). The interpretation via an object shape can be given by the path difference $r_1 - r_2$ of interfering waves (by replacing $2\pi \leftarrow \lambda$, Fig. 1.6): the maximum and minimum of I can be defined as $r_1 - r_2 = \lambda m$ and $r_1 - r_2 = \lambda(m + \frac{1}{2})$, respectively [204].

1.2.6 Holography and holograms

Holography got its name from the Greek words ὅλος (hólos) meaning "whole/entire" and γράφή (graphē) meaning "to write". It is a means for recording and reconstructing the whole information contained in an optical wavefront, namely amplitude and phase, and not just intensity as ordinary photography does. Holography essentially is a clever combination of interference and diffraction. In 1948 Dennis Gabor (1900 – 1979) presented holography as a lensless process for image formation by reconstructed wavefronts [68]. Invention of holography was motivated by the desire to improve resolution power of electron microscopes that was limited by the fundamental limitations of the electron optics and avoid the previous aberrations. But the interest in holography declined after a few years, mainly because of the poor quality of the holographic images obtained in those days [125]. Moreover, powerful sources of coherent light were also not available at that date, and holography remained an "optical paradox" until the invention of lasers. The very first implementation of holography was demonstrated in the early 1960s by Emmett Leith and Juris Upatnieks [133] and by Yuri Nikolaevich Denisyuk [41].

In holography, one records the interference patterns between two optical waves: an object u_{obj} (reflected from or transmitted through the object) and a special "reference" u_{ref} ones. Since recording media respond typically to the light intensity only[12], one detects the intensity of the coherent superposition of these waves:

[11] The complex degree of coherence is hereafter assumed to be equal to 1, what corresponds to the full coherence of waves [125, 190]. In case of incoherent waves this factor is equal to 0, hence there will be no additional (latter) term in Eq. (1.8).

[12] Optical media for recording holograms may be classified into three categories: amplitude/intensity-only (e.g., CCD), phase-only (kinoform [134, 135]) and combined amplitude-phase media [207, 236].

$$\mathcal{I}(x,y) = |u_{obj}(x,y) + u_{ref}(x,y)|^2 = \tag{1.9}$$
$$= \underbrace{|u_{obj}(x,y)|^2 + |u_{ref}(x,y)|^2}_{\text{DC term}} + u^*_{obj}(x,y)u_{ref}(x,y) + u_{obj}(x,y)u^*_{ref}(x,y),$$

where the last term in the sum is proportional to the complex amplitude of the wave field which travels from the object. That is what we call the *hologram* [236]. It is denoted here by $\mathcal{I}(x,y)$ in order to distinguish it from the simple sum of intensities of two waves, $\mathcal{I}(x,y) \neq I_1(x,y) + I_2(x,y)$.

The optical reconstruction is achieved by illuminating a recording medium with the reference beam [125, 194, 232, 234, 236]. Since the wave field u_{obj} on a detector is formed by the forward diffraction propagation from the object to the sensor plane, the numerical reconstruction is to compute this complex-valued u_{obj} (e.g., by phase shifting) and to perform the backward wave field propagation.

1.3 Principles of scalar diffraction theory

An electromagnetic field is described by two related *vector* fields that are functions of the position in the Cartesian coordinate system and time: the electric field $\vec{\mathcal{E}}(x,y,z,t)$ and the magnetic field $\vec{\mathcal{H}}(x,y,z,t)$. Since in this thesis the linearly polarized light is used, a monochromatic light field may be completely characterized within the scope of the scalar wave theory at every point in space by means of its amplitude and phase [120]. Therefore, in order to define light in free space one uses six *scalar* functions of position and time, which must satisfy the celebrated set of coupled partial differential equations known as *Maxwell's equations* [190].

1.3.1 Maxwell's wave equation

For a medium with no currents and charges, these equations for the electric- and magnetic-field vectors can be written as follows [79, cf. Eq. (3-2)]

$$\nabla \cdot \vec{\mathcal{E}}(x,y,z,t) = 0, \tag{1.10}$$
$$\nabla \cdot \vec{\mathcal{H}}(x,y,z,t) = 0, \tag{1.11}$$
$$\nabla \times \vec{\mathcal{E}}(x,y,z,t) = -\mu_m \frac{\partial \vec{\mathcal{H}}(x,y,z,t)}{\partial t}, \tag{1.12}$$
$$\nabla \times \vec{\mathcal{H}}(x,y,z,t) = \epsilon_m \frac{\partial \vec{\mathcal{E}}(x,y,z,t)}{\partial t}, \tag{1.13}$$

where μ_m and ϵ_m are the magnetic permeability and electric permittivity, respectively, of the medium within which the light wave is propagating. The vector operators $\nabla\cdot$ and $\nabla\times$ represent the divergence and curl (rotor), respectively.

In this thesis the propagation of light is considered in free space (vacuum or air). In a linear, isotropic, homogeneous ($\epsilon_m = const$), nonmagnetic and nondispersive medium both μ_m and ϵ_m are always equal to the constants of free space [4,13]

[13] Magnetic permeability of vacuum $\mu_0 = 4\pi \cdot 10^{-7}$ [H/m] .

$$\mu_m = \mu_0,\ \epsilon_m = \epsilon_0. \tag{1.14}$$

Let $\mathcal{U} = \mathcal{U}(x, y, z, t)$ represents any of the scalar field components of the electric or magnetic field. The light field at any point of free space (with the refractive index $n \cong 1$) can be found from the scalar wave equation [79]

$$\nabla^2\mathcal{U} - \frac{1}{c^2} \cdot \frac{\partial^2\mathcal{U}}{\partial t^2} = 0, \tag{1.15}$$

derived from Maxwell's equations[14], where the Laplace operator $\nabla^2 = \partial^2/\partial x^2 + \partial^2/\partial y^2 + \partial^2/\partial z^2$ and $c = \frac{1}{\sqrt{\mu_0\epsilon_0}}$ is the speed of light in vacuum.

Indeed, applying the curl operation to the left and right sides of Eq. (1.12) and using the vector equation

$$\nabla \times (\nabla \times \vec{\mathcal{E}}(x, y, z, t)) = \nabla(\nabla \cdot \vec{\mathcal{E}}(x, y, z, t)) - \nabla^2\vec{\mathcal{E}}(x, y, z, t), \tag{1.16}$$

we arrive at

$$\nabla^2\vec{\mathcal{E}}(x, y, z, t) - \frac{1}{c^2} \cdot \frac{\partial^2\vec{\mathcal{E}}(x, y, z, t)}{\partial t^2} = 0. \tag{1.17}$$

The magnetic field satisfies an identical equation

$$\nabla^2\vec{\mathcal{H}}(x, y, z, t) - \frac{1}{c^2} \cdot \frac{\partial^2\vec{\mathcal{H}}(x, y, z, t)}{\partial t^2} = 0. \tag{1.18}$$

Since both $\vec{\mathcal{E}}(x, y, z, t)$ and $\vec{\mathcal{H}}(x, y, z, t)$ satisfy the identical vector wave equation, an identical scalar wave equation is obeyed by all components of those vectors [56, 79], and two vector wave equations (1.17) and (1.18) are divided into six scalar wave equations similar to Eq. (1.15), but with respect to the individual components $\mathcal{E}_x, \mathcal{E}_y, \mathcal{E}_z, \mathcal{H}_x, \mathcal{H}_y, \mathcal{H}_z$. The behavior of all components of the electric and magnetic field is fully described by the single scalar wave Eq. (1.15).

1.3.2 Helmholtz wave equations

As it is mentioned above (see Section 1.2.3), the consideration of this thesis is limited (for simplicity) to the propagation of monochromatic light waves (hereafter wave field propagation). In such a case, a light field at the position (x,y,z) and time t can be accurately described by a scalar wave function of the form [20, Eq. (25)]

$$\mathcal{U}(x, y, z, t) = \mathrm{Re}\{u(x, y, z) \cdot e^{-i2\pi vt}\}, \tag{1.19}$$

where v is the optical frequency as in Eq. (1.4). The complex function [20, 79, 190]

$$u(x, y, z) = a(x, y, z) \cdot \exp(i\phi(x, y, z)) \tag{1.20}$$

[14] Note that, following [56], the general solution of the one-dimensional wave equation is the sum of two arbitrary functions of the form of d'Alambert formula $\mathcal{U} = \mathcal{U}(x, t) = h(x-ct)+g(x+ct)$ [56, cf. Eq. (20.24)], [125, cf. Eq. (2.6)], representing two waves travelling with the speed c: the wave h travels toward positive x, and g – toward negative x. This is the superposition of the waves existing at the same time.

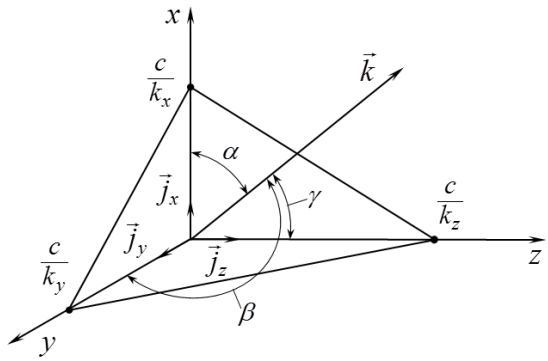

Figure 1.7: The wave vector $\vec{k}$ and the plane cutting off segments $\frac{c}{k_x}$, $\frac{c}{k_y}$ and $\frac{c}{k_z}$ on the Cartesian coordinate axes. The angles between $\vec{k}$ and the x, y and z axes are denoted by α, β and γ, respectively.

works as an adequate description of a light wave, because the time dependence $e^{-i2\pi\nu t}$ is deterministic. Here a and ϕ are the amplitude and phase of the light wave, respectively. The complex amplitude of the light wave (1.20) depends only on the spatial position and is often called a phasor. Substituting Eq. (1.19) in Eq. (1.15) it follows that $u(x, y, z)$ must obey the time-independent equation

$$(\nabla^2 + k^2) \cdot u(x, y, z) = 0, \tag{1.21}$$

where k denotes the wave number given by $k = 2\pi/\lambda$, and $\lambda = v/c$ is the wavelength of the monochromatic light wave in the dielectric medium. This equation is known as the *Helmholz equation*. The most straightforward solutions of Eq. (1.21) are those which describe uniform plane and symmetric spherical waves.

For a plane wave [138, Eq. (III.3)]

$$u(x, y, z) = a \cdot e^{\pm i\vec{k}\vec{r}} = a \cdot e^{\pm i(k_x x + k_y y + k_z z)}, \; a = const, \tag{1.22}$$

where k_x, k_y, k_z and x, y, z are the projections of the wave vector $\vec{k}$ and the radius-vector $\vec{r}$ onto the Cartesian coordinate axes, respectively. Substituting Eq. (1.22) in Eq. (1.21) we arrive at

$$k_x^2 + k_y^2 + k_z^2 = k^2 = \left(\frac{2\pi}{\lambda}\right)^2. \tag{1.23}$$

The equal-phase surfaces is defined from the relation

$$k_x x + k_y y + k_z z = c = const, \tag{1.24}$$

which represents an equation of the plane which cuts off the segments $\frac{c}{k_x}$, $\frac{c}{k_y}$ and $\frac{c}{k_z}$ on the coordinate axes (see Fig. 1.7).

In this thesis the waves generated by a source are assumed to be propagating

outward[15] from this source [56]. Thus, the full expression for the plane wave is of the form

$$\mathcal{U}(x,y,z,t) = a \cdot e^{i(k_x x + k_y y + k_z z - 2\pi\nu t)}, \tag{1.25}$$

i.e. Eq. (1.22) is given for $t = 0$. If $t = t_1 > 0$ the wave surface is described by the expression $k_x x + k_y y + k_z z = c + 2\pi\nu t_1$ representing the equation of the plane which cuts off segments $\frac{c+2\pi\nu t_1}{k_x}$, $\frac{c+2\pi\nu t_1}{k_y}$ and $\frac{c+2\pi\nu t_1}{k_z}$ on the coordinate axes. It follows that the plane wave propagates parallel to itself. If $c = c(x,y,z) = k_x x + k_y y + k_z z - 2\pi\nu t_1$ as we have seen before, then

$$\begin{aligned} \nabla c &= \frac{\partial c}{\partial x}\cdot\vec{j_x} + \frac{\partial c}{\partial y}\cdot\vec{j_y} + \frac{\partial c}{\partial z}\cdot\vec{j_z} = \\ &= k_x\cdot\vec{j_x} + k_y\cdot\vec{j_y} + k_z\cdot\vec{j_z} = \vec{k}_x + \vec{k}_y + \vec{k}_z = \vec{k}, \end{aligned} \tag{1.26}$$

i.e. the propagation direction of the plane wave coincides with the direction of the wave vector. $\vec{j_x}$, $\vec{j_y}$ and $\vec{j_z}$ are hereafter the unit vectors in Cartesian coordinates.

The Helmholtz wave equation (1.21) in spherical coordinates is of the form

$$\frac{1}{r}\cdot\frac{\partial^2}{\partial r^2}(ru) + \frac{1}{r^2\sin\theta}\cdot\frac{\partial}{\partial\theta}(\sin\theta\frac{\partial u}{\partial\theta}) + \frac{1}{r^2\sin^2\theta}\frac{\partial^2 u}{\partial\varphi^2} + k^2 u = 0, \tag{1.27}$$

where variables r, θ and φ are defined from equations $x = r\sin\theta\cos\varphi$, $y = r\sin\theta\sin\varphi$ and $z = r\cos\theta$. For the symmetric spherical waves $\frac{\partial u(r,\theta,\varphi)}{\partial\theta} = 0$ and $\frac{\partial u(r,\theta,\varphi)}{\partial\varphi} = 0$ due to the circular symmetry, therefore Eq. (1.27) can be simplified as [56, cf. Eq. (20.34)]

$$\left(\frac{\partial^2}{\partial r^2} + k^2\right)\cdot ru(r,\theta,\varphi) = 0. \tag{1.28}$$

Then, for a diverging (expanding [79], outgoing [56]) spherical wave we arrive at

$$u(r,\theta,\varphi) = a\frac{e^{ikr}}{r}, \quad a = const, \tag{1.29}$$

and the equal-phase surfaces is determined from the identity $kr = const$, hence $r = const$. Taking into account that $r = \sqrt{x^2+y^2+z^2}$ the wave propagation direction is defined by

$$\nabla kr = k\nabla r = k\cdot\left(\frac{x}{r}\cdot\vec{j_x} + \frac{y}{r}\cdot\vec{j_y} + \frac{z}{r}\cdot\vec{j_z}\right) = \frac{k}{r}\vec{r}, \tag{1.30}$$

i.e. the spherical wave propagates along the radius-vector $\vec{r}$. Eq. (1.29) can be rewritten as

$$u(x,y,z) = a\frac{e^{ik\sqrt{x^2+y^2+z^2}}}{\sqrt{x^2+y^2+z^2}}. \tag{1.31}$$

Note that the wave source is assumed to be at the origin and r is only real positive ($z > 0$ [56]). One observes that the amplitude $\frac{a}{r}$ decreases proportionally to $\frac{1}{r}$, and at a long distance from the origin the spherical wave locally approximates a plane wave [125].

[15] Although Maxwell's equations would allow either possibilities, we will put an additional fact, that only the outgoing wave solution makes "physical sense" [56]. Thus, in contrast to the general solution by d'Alembert's formula [20, § 1.3, Eq. (8)], [56, Eq. (20.24)], here we consider the wave field propagation in the positive c direction only.

1.3.3 Paraxial approximation and angular spectrum

It can be shown [79, 138] that the complex amplitude and spatial Fourier components of the monochromatic wave field distribution can be decomposed by plane waves travelling in different directions.

Let us consider the plane wave given by Eq. (1.22). Denote the angles between the wave vector $\vec{k}$ and the Cartesian coordinate axes x, y and z by α, β and γ, respectively (see Fig. 1.7). Then, $\cos\alpha = \frac{k_x}{k}$, $\cos\beta = \frac{k_y}{k}$, $\cos\gamma = \frac{k_z}{k}$ and $\vec{k} = k \cdot (\cos\alpha \cdot \vec{j_x} + \cos\beta \cdot \vec{j_y} + \cos\gamma \cdot \vec{j_z})$. Taking into account Eq. (1.23),

$$\cos^2\alpha + \cos^2\beta + \cos^2\gamma = 1. \tag{1.32}$$

It is of interest to describe paraxial waves whose propagation direction *almost* coincides with the direction of the optical axis z (propagates in the positive z direction), i.e. the angle γ is small, α and β are close to $\frac{\pi}{2}$. Then, $\cos\gamma \approx 1$ and

$$\cos\alpha \approx \frac{\pi}{2} - \alpha \triangleq \alpha_1, \;\; \cos\beta \approx \frac{\pi}{2} - \beta \triangleq \beta_1. \tag{1.33}$$

According to Eq. (1.32) the propagation direction is fully determined by only two angles. The projections of the wave vector $\vec{k}$ onto the xz and yz planes are equal to $k_{xz} = \sqrt{k_x^2 + k_z^2}$ and $k_{yz} = \sqrt{k_y^2 + k_z^2}$, respectively (see Fig. 1.8). The angles between these projections and the z axis α_{xz} and β_{yz} can be found from

$$\sin\alpha_{xz} = \frac{k_x}{\sqrt{k_x^2 + k_z^2}}, \;\; \sin\beta_{yz} = \frac{k_y}{\sqrt{k_y^2 + k_z^2}}. \tag{1.34}$$

Since for the paraxial approximation $k_z \gg k_x$, $k_z \gg k_y$ and $k_z \approx k$

$$\begin{aligned} \sin\alpha_{xz} &\approx \frac{k_x}{k} = \cos\alpha = \sin\alpha_1, \\ \sin\beta_{yz} &\approx \frac{k_y}{k} = \cos\beta = \sin\beta_1, \end{aligned} \tag{1.35}$$

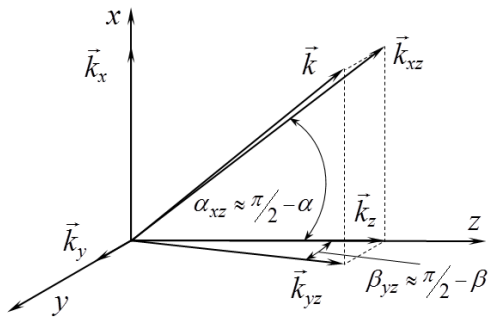

Figure 1.8: The wave vector $\vec{k}$ and its projections onto the coordinate axes and coordinate planes. In case of the paraxial approximation, the angles between the projections of $\vec{k}$ onto the (x,z) and (y,z) planes and the z axis are close to $\frac{\pi}{2} - \alpha$ and $\frac{\pi}{2} - \beta$ (see Fig. 1.7).

what results in $\alpha_{xz} \approx \alpha_1$, $\beta_{yz} \approx \beta_1$. Therefore the plane wave can be describe as a two-dimensional harmonic oscillation with the frequencies ($k\alpha_1$,$k\beta_1$) [138]

$$u(x,y,z) = a \cdot e^{ikz} e^{ik(\alpha_1 x + \beta_1 y)}, \quad a = const. \tag{1.36}$$

In the Fourier decomposition of u the complex amplitude of the plane-wave component with the angular frequencies $(\frac{\alpha_1}{\lambda}, \frac{\beta_1}{\lambda})$ is $U\left(\frac{\alpha_1}{\lambda}, \frac{\beta_1}{\lambda}, z\right) d\frac{\alpha_1}{\lambda} d\frac{\beta_1}{\lambda}$. The two-dimensional Fourier transform of the function u across the xy plane

$$U\left(\frac{\alpha_1}{\lambda}, \frac{\beta_1}{\lambda}, z\right) = \iint_{-\infty}^{\infty} u(x,y,z) \cdot e^{-i2\pi(\frac{\alpha_1}{\lambda}x + \frac{\beta_1}{\lambda}y)} dxdy \tag{1.37}$$

is called the *angular spectrum* of the wave $u(x,y,z)$.

1.3.4 Plane wave decomposition

Suppose that the complex amplitude of the wave field across the xy plane at the distance $z_0 > 0$ is given by $u(x,y,z_0)$, where its angular spectrum is of the form

$$U(k_x, k_y, z_0) = \iint_{-\infty}^{\infty} u(x,y,z_0) \cdot e^{-i(k_x x + k_y y)} dxdy. \tag{1.38}$$

Here $\gamma = 0$. Note that the angular frequencies are chosen as $k_x = k\cos\alpha$, $k_y = k\cos\beta$ (cf. Eq. (1.37)). Let us calculate $u(x,y,z_0+z)\Big|_{z=const}$, the wave field distribution at a parallel plane, which appears at the distances z from (to the right of) the first plane. It is known that $u(x,y,z_0)$ must satisfy the Helmholtz Eq. (1.21) at all source-free points [79]. Therefore, direct multiplication of Eq. (1.21) by $e^{-i(k_x x + k_y y)}$ and its integration with respect to x and y shows that the angular spectrum must satisfy the homogeneous second order differential equation (see [138, Chapter III, §2] for the derivation)

$$\frac{d^2}{dz^2} U(k_x, k_y, z) + (k^2 - k_x^2 - k_y^2) \cdot U(k_x, k_y, z) = 0, \tag{1.39}$$

yielding

$$U(k_x, k_y, z) = c_1(k_x, k_y) \cdot e^{iz\sqrt{k^2 - k_x^2 - k_y^2}} + c_2(k_x, k_y) \cdot e^{-iz\sqrt{k^2 - k_x^2 - k_y^2}}, \tag{1.40}$$

where $c_1(k_x, k_y)$ and $c_2(k_x, k_y)$ are integration constants determined from the boundary conditions. The first term in Eq. (1.40) corresponds to the direct, outgoing wave, and the second term – to the incoming wave. Since the wave field propagation is assumed to be taken in a homogeneous medium from the source in the positive direction of z, the second term is equal to zero due to lack of sources for the incoming wave, $c_2 = 0$. Then

$$U(k_x, k_y, z_0 + z)\Big|_{z=const} = c_1(k_x, k_y) \cdot e^{i(z_0+z)\sqrt{k^2 - k_x^2 - k_y^2}}, \tag{1.41}$$

where $c_1(k_x, k_y)$ can be found from the initial condition at the plane $z = z_0$

$$U(k_x, k_y, z)\Big|_{z=z_0} = U(k_x, k_y, z_0) = c_1(k_x, k_y) \cdot e^{iz_0\sqrt{k^2-k_x^2-k_y^2}}. \tag{1.42}$$

Thus, we arrive at

$$U(k_x, k_y, z_0 + z)\Big|_{z=const} = U(k_x, k_y, z_0) \cdot e^{iz\sqrt{k^2-k_x^2-k_y^2}}, \tag{1.43}$$

i.e. a layer of free space works as a filter, where the transfer function is of the form

$$H_z(k_x, k_y) = e^{iz\sqrt{k^2-k_x^2-k_y^2}}. \tag{1.44}$$

Note that $|H(k_x, k_y)| = 1$, $\phi(k_x, k_y) = z\sqrt{k^2 - k_x^2 - k_y^2}$ for $k_x^2 + k_y^2 \le k^2$. For $\sqrt{k_x^2 + k_y^2} > k$ the module of the transfer function decreases according to $e^{-z\sqrt{k_x^2+k_y^2-k^2}}$, $\phi(k_x, k_y) = 0$. Hence, a layer of free space behaves as a low-pass filter with a finite bandwidth equal to $k = \frac{2\pi}{\lambda}$. The wave components with wavelengths less than λ are rapidly attenuated by the propagation phenomenon with increasing of the distance z. Since the distances z and z_0 are taken much larger than a few wavelengths, we can completely drop the evanescent components of the spectrum, i.e. exclude from our consideration the case of $k_x^2 + k_y^2 > k^2$ [79]. The subindex "z" in Eq. (1.44) just emphasizes that H_z is a 2D transfer function calculated for the space layer of the width z.

The inverse Fourier transform of Eq. (1.43) yields the *plane wave decomposition* integral

$$\begin{aligned} & u(x, y, z_0 + z)\Big|_{z=const} = \\ = \; & \frac{1}{4\pi^2}\int_{-\infty}^{\infty}\int \underbrace{U(k_x, k_y, z_0) \cdot (e^{iz\sqrt{k^2-k_x^2-k_y^2}}}_{U(k_x,k_y,z_0+z)\Big|_{z=const}} e^{i(k_x x + k_y y)})dk_x dk_y = \\ = \; & \mathcal{F}^{-1}\{\mathcal{F}\{u(x, y, z_0)\}(k_x, k_y) \cdot H_z(k_x, k_y)\}(x, y), \end{aligned} \tag{1.45}$$

which represents the wave field in free space $u(x, y, z_0 + z)$ as a superposition of plane waves $e^{i(k_x x + k_y y + z\sqrt{k^2-k_x^2-k_y^2})}$ (cf. Eq.(1.36)) weighted by the complex amplitude $U(k_x, k_y, z_0)$, where z_0, $z \gg 0$.

The 3D Fourier transform of a scalar function $u(x, y, z)$ can be defined as

$$U(k_x, k_y, k_z) = \int_{-\infty}^{\infty}\int\int u(x, y, z) \cdot e^{-i(k_x x + k_y y + k_z z)}dxdydz. \tag{1.46}$$

Similar to Eq. (1.39), we apply the Helmholtz Eq. (1.21), but this time consider the integration with respect to x, y and z. It results in

$$(k^2 - k_x^2 - k_y^2 - k_z^2) \cdot U(k_x, k_y, k_z) = 0, \tag{1.47}$$

i.e. the Fourier transform $U(k_x, k_y, k_z)$ must by equal to zero for the spatial frequencies k_x, k_y and k_z outside the sphere (1.23) known as Ewald's sphere.

It should be noticed that the plane wave decomposition (1.45) is valid under certain conditions related mainly to the existence and invertibility of the Fourier transform of the wave field distributions at the mentioned transverse planes, namely: the pairs $u(x, y, z_0)$, $U(k_x, k_y, z_0)$ and $u(x, y, z_0 + z)$, $U(k_x, k_y, z_0 + z)$. We refer to, e.g., [79, Section 2.1.1], [130] for discussion on the existence and sufficient conditions of the Fourier transform to be obeyed.

1.3.5 Rayleigh–Sommerfeld diffraction integral

In Section 1.3.4 we demonstrate that the wave field propagation phenomenon acts as a linear space-invariant system described by a relatively simple transfer function H_z. In many situations it is more convenient to define a layer of free spacenot by the 2D transfer function using Eq. (1.44) or (in case of spatial frequencies $v_1 = \frac{k_x}{\lambda k}$, $v_2 = \frac{k_y}{\lambda k}$) using [79, cf. Eq. (3-74)]

$$H_z(v_1, v_2) = \begin{cases} \exp(i\frac{2\pi}{\lambda} z\sqrt{1-\lambda^2(v_1^2+v_2^2)}), & \sqrt{v_1^2+v_2^2} < \frac{1}{\lambda} \\ 0, & \text{otherwise} \end{cases}, \tag{1.48}$$

but with an impulse response, calculated as the inverse Fourier transform of H_z

$$\begin{aligned} h_z(x,y) &= \frac{1}{4\pi^2}\iint_{-\infty}^{\infty} e^{iz\sqrt{k^2-k_x^2-k_y^2}} \cdot e^{i(k_x x + k_y y)} dk_x dk_y = \\ &= \iint_{-\infty}^{\infty} e^{i2\pi\frac{z}{\lambda}\sqrt{1-(\lambda v_x)^2+(\lambda v_y)^2}} \cdot e^{i2\pi(v_1 x + v_2 y)} dv_1 dv_2. \end{aligned} \tag{1.49}$$

The expression describing the wave field in an arbitrary point $(x,y,z_0+z)\Big|_{z=const}$ by the wave field at the transverse xy plane $z = z_0$ is defined in the form

$$u(x, y, z_0 + z)\Big|_{z=const} = \iint_{-\infty}^{\infty} u(\xi, \eta, z_0) \cdot h_z(x - \xi, y - \eta) d\xi d\eta, \tag{1.50}$$

where the impulse response of free space propagation

$$\begin{aligned} h_z(x-\xi, y-\eta) &= \frac{1}{i\lambda}\cos\theta \cdot \frac{e^{ikr}}{r}\left(1 - \frac{1}{ikr}\right), \\ r &= \sqrt{(x-\xi)^2 + (y-\eta)^2 + z^2} \end{aligned} \tag{1.51}$$

and $\cos\theta = \frac{z}{r}$ describes the direction of radiation. $\theta = 0$ corresponds to the maximum of radiation and if $\theta = \frac{\pi}{2}$ these is no radiation (see Fig. 1.9).

Note that the physical interpretation of the impulse response is a wave field generated by a 2D point source. A common derivation of the impulse response starts from the Green's theorem [79, Eq. (3-14)] and a prudent choice of an

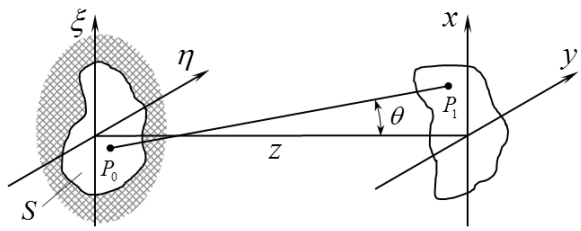

Figure 1.9: Geometrical scheme of the diffraction problem. The wave field at the $\xi\eta$ plane is localized only in the finite area denoted by S.

auxiliary function: a spherical wave as the Green's function [20, 79] with the Sommerfeld radiation condition (see, e.g., [79, Eq. (3-22)]).

Eq. (1.50) shows that the field $u(x, y, z_0 + z)\Big|_{z=const}$ is calculated as a two-dimensional convolution between the initial (given) field $u(\xi, \eta, z_0)$ and the diffraction kernel (1.51). Therefore, the free space wave field propagation to the distance z is represented as a linear shift-invariant system with the impulse response h_z [167, 168].

Note that the diffraction kernel h_z has a circular symmetry with respect to the z axis. The field of a 2D point source consists of two terms: the first term describes the radiation field decaying as $\frac{1}{r}$, and the second one – the induction field decaying according to $\frac{1}{r^2}$.

We are interesting in the radiation field. The expression for it can be found assuming that $1 - \frac{1}{ikr} = \sqrt{1 + \frac{1}{k^2 r^2}} e^{i \arctan \frac{1}{kr}} \approx 1$ for $\frac{1}{kr} \ll 1$. It follows that even for $r \approx \lambda$ the radiation field of a point source is $h_z \approx \frac{z}{i\lambda} \frac{e^{ikr}}{r^2}$ ($h_z \approx \frac{e^{ikr}}{i\lambda r}$ for the paraxial approximation $\theta \approx 0$). Thus, the Rayleigh–Sommerfeld diffraction kernel can be represented in the form

$$h_z(x - \xi, y - \eta) = \frac{z}{i\lambda} \cdot \frac{e^{ikr}}{r^2}, \tag{1.52}$$

i.e. omitting the second term in brackets in Eq. (1.51), Eq. (1.50) can be rewritten as follows

$$u(x, y, z_0 + z)\Big|_{z=const} = \frac{z}{i\lambda} \iint_{-\infty}^{\infty} u(\xi, \eta, z_0) \frac{e^{ikr}}{r^2} d\xi d\eta, \tag{1.53}$$

what is known as the *Rayleigh–Sommerfeld diffraction integral*.

Despite the apparent differences of the angular spectrum decomposition (ASD) method (Eqs. (1.43) and (1.45)) and the first Rayleigh–Sommerfeld (RS) solution (Eq. (1.53)), these two approaches yield identical predictions of diffracted wave fields [79]. The proof can be found, e.g., in [138, Chapter III.3] or [197].

1.3.6 Fresnel approximation

The Rayleigh–Sommerfeld diffraction integral (1.53) is quite complex, and it can be essentially simplified using additional restrictions imposed on the interesting

region of space. First of all, we note that the wave field at the plane $z = z_0$ is, in practice, localized in a finite region S[16](see Fig. 1.9), so we can use finite limits of integration

$$u(x, y, z_0 + z)\Big|_{z=const} = \tag{1.54}$$
$$= \frac{z}{i\lambda}\iint\limits_S u(\xi, \eta, z_0)\frac{e^{ik\sqrt{(x-\xi)^2+(y-\eta)^2+z^2}}}{(x-\xi)^2+(y-\eta)^2+z^2}d\xi d\eta.$$

We are considering the wave field at the xy observation plane parallel to the $\xi\eta$ plane at the normal distance z to it. The size of the space layer is characterized by the following important parameters: the size S of the initial wave field (source), the distance between these planes and the lateral distances x, y from the longitudinal axis z.

Let us assume that the wave field at the observation plane is many wavelengths from the source (diffracting aperture), i.e. the distance between the points P_0 and P_1 in Fig. 1.9 $r = \sqrt{(x-\xi)^2+(y-\eta)^2+z^2} \gg \lambda$ [79]. Moreover, the distance $z > 0$ is taken much larger than the maximum lateral dimension of the aperture S [80]. Then, taking into account these assumptions, we can say that $\cos\theta \approx 1$[17], and r^2 in the denominator of Eq. (1.54) is only slightly different from z^2.

The component r in the exponent cannot be replaced by z, because the occurring error is multiplied by the very large k . Then, the phase changes are much larger than 2π, but these phase changes even by a fraction of a radian can result in significant difference of the value of the exponent. Let us rewrite

$$r = \sqrt{(x-\xi)^2+(y-\eta)^2+z^2} = z\cdot\sqrt{1+\frac{(x-\xi)^2+(y-\eta)^2}{z^2}}, \tag{1.55}$$

where $b = \frac{(x-\xi)^2+(y-\eta)^2}{z^2} < 1$ is assumed to be small. In order to represent Eq. (1.54) in a simpler and more usable manner, we use the approximation based on the binomial expansion of the square root

$$\sqrt{1+b} = 1 + \frac{b}{2} - \frac{b^2}{8} + ... \tag{1.56}$$

Retaining only the first two terms of the expansion Eq. (1.56), we arrive at the so-called *Fresnel approximation*

$$r \approx z + \frac{(x-\xi)^2+(y-\eta)^2}{2z}, \tag{1.57}$$

and the approximation error does not exceed $\frac{[(x-\xi)^2+(y-\eta)^2]^2}{8z^3}$, because the Taylor series in the brackets in Eq. (1.56) is alternating. Taking into account that

[16] Following [79] we have an infinite opaque screen with a hole of finite size, diffracting aperture S at the $\xi\eta$ plane which is illuminated in the positive z direction.

[17] with an accuracy better than 5% , if the angle θ is less than 18 degrees [80].

$u(\xi,\eta,z_0)=0$ outside the region S, the resulting expression for the field at the observation xy plane therefore becomes

$$\begin{aligned} & u(x,y,z_0+z)\Big|_{z=const} = \\ = \; & \frac{e^{ikz}}{i\lambda z}\int\limits_{-\infty}^{\infty}\!\!\int u(\xi,\eta,z_0)e^{\frac{ik}{2z}((x-\xi)^2+(y-\eta)^2)}d\xi d\eta = \\ = \; & \{u(\xi,\eta,z_0)\circledast g_z(\xi,\eta)\}(x,y,z_0+z)\Big|_{z=const}, \end{aligned} \tag{1.58}$$

what can be considered as the convolution of the function $u(\xi,\eta,z_0)$ with the kernel

$$g_z(\xi,\eta)=\frac{e^{ikz}}{i\lambda z}e^{\frac{ik}{2z}(\xi^2+\eta^2)}. \tag{1.59}$$

Another form of the result (1.58) is found if the term $e^{\frac{ik}{2z}(x^2+y^2)}$ is factored outside the integral signs, yielding [79, cf. Eq. (4-17)]

$$\begin{aligned} & u\left(\frac{x}{\lambda z},\frac{y}{\lambda z},z_0+z\right)\Big|_{z=const} = \\ = \; & \frac{e^{ikz}}{i\lambda z}e^{\frac{ik}{2z}(x^2+y^2)}\int\limits_{-\infty}^{\infty}\!\!\int [u(\xi,\eta,z_0)e^{\frac{ik}{2z}(\xi^2+\eta^2)}]e^{-i2\pi(\xi\frac{x}{\lambda z}+\eta\frac{y}{\lambda z})}d\xi d\eta = \\ = \; & \frac{e^{ikz}}{i\lambda z}e^{i\pi\lambda z((\frac{x}{\lambda z})^2+(\frac{y}{\lambda z})^2)}\mathcal{F}\{u(\xi,\eta,z_0)e^{\frac{ik}{2z}(\xi^2+\eta^2)}\}\left(\frac{x}{\lambda z},\frac{y}{\lambda z}\right), \end{aligned} \tag{1.60}$$

which we recognize (aside from multiplicative factors) to be the 2D Fourier transform of the product of the complex field just to the right of the diffracting aperture by a quadratic phase exponential.

The results in the form of Eq. (1.58) and Eq. (1.60) are known as the *Fresnel diffraction integral*.

Considering the approximation in the exponent (1.57), which is the most critical approximation, it can be seen that the spherical secondary wavelets of the Huygens–Fresnel principle have been replaced by wavelets with parabolic wavefronts. Such an approximation imposes certain restrictions on the relative sizes of S, the observation field at the xy plane and the distance z. A sufficient condition for accuracy would be that the maximum phase change, induced by dropping the $b^2/8$ term, be much less than 1 radian, what is met if

$$z^3 \gg \frac{\pi}{4\lambda}[(x-\xi)^2+(y-\eta)^2]^2_{\max}. \tag{1.61}$$

However, for the Fresnel approximation to yield accurate results, it is only necessary that the higher-order terms of the expansion not change the value of the Fresnel diffraction integral significantly [79]. If the distance z is small and the condition (1.61) is not fulfilled, $k/2z$ generally becomes large and oscillations of the quadratic phase factor in Eq. (1.59) so fast that the major contribution to the integral will come only from the points (ξ,η) close to (x,y) where the phase changes are minimal [80]. To investigate the approximation error more completely,

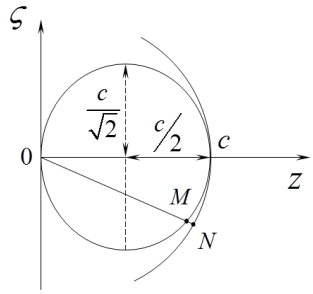

Figure 1.10: A circle of the radius $c/2$ and an ellipse with semi-axes $c/\sqrt{2}$ and $c/2$ which is close to the circle.

let us consider the equal-phase surfaces of the functions $e^{ik\sqrt{(x-\xi)^2+(y-\eta)^2+z^2}}$ and $e^{ikz}e^{\frac{ik}{2z}((x-\xi)^2+(y-\eta)^2)}$ determining by the identities $(x-\xi)^2+(y-\eta)^2+z^2=c_1^2$ and $z+\frac{(x-\xi)^2+(y-\eta)^2}{2z}=c^2$, respectively. The first identity represents a sphere of radius c_1 centred at the point (ξ,η). Let us rewrite

$$z+\frac{\varsigma^2}{2z}=c \Leftrightarrow \frac{\varsigma^2}{\frac{c^2}{2}}+\frac{\left(z-\frac{c}{2}\right)^2}{\left(\frac{c}{2}\right)^2}=1, \tag{1.62}$$

what gives an ellipse with semi-axes $\frac{c}{\sqrt{2}}$ and $\frac{c}{2}$ and centred at the point $(0,\frac{c}{2})$. In Eq. (1.62) and further in this Section $\varsigma^2=(x-\xi)^2+(y-\eta)^2$, then the spherical surface can be of the form

$$\varsigma^2+z^2=c_1^2. \tag{1.63}$$

In order to estimate the approximation error, we are considering the difference of the surface given by (1.62) from the spherical surface (1.63). If these two surfaces intersect with each other for $x=\xi$ and $y=\eta$, then $c=c_1$. In Fig. 1.10 the ellipse (1.62) and the circle $\varsigma^2+z^2=c^2$ are depicted. We use a spheroid as an approximation for the spherical surface. Let us draw a line $0N$ through the center of the sphere. $0N$ intersects the spherical and elliptical surfaces at the points N and M, respectively. These surfaces are close to each other, when MN is small. Taking into account that $0N=c$, the coordinates of the point M is (ς,z) and using Eqs. (1.56), (1.62) and (1.63) we arrive at

$$\begin{aligned} MN &= 0N-0M=c-\sqrt{\varsigma^2+z^2}= \\ &= c-z\cdot\left(1+\frac{\varsigma^2}{2z^2}-\frac{\varsigma^4}{8z^4}+\ldots\right)=\frac{\varsigma^4}{8z^4}+\ldots. \end{aligned} \tag{1.64}$$

According to the Rayleigh criterion, a spherical surface can be approximated by an elliptical one if MN does not exceed one-tenth of the wavelength, i.e. in our case $\frac{\varsigma^4}{8z^3}\le\frac{\lambda}{10}$ or

$$((x-\xi)^2+(y-\eta)^2)^2\le 0.8z^3\lambda\le z^3\lambda. \tag{1.65}$$

Let us consider the worst case when the inequality in Eq. (1.65) is satisfied. Suppose that the region S is a rectangular of the size $2a\times 2b$, then for $x>0$, $y>0$

we take $\xi = -a$ and $\eta = -b$. Let $R = \sqrt{a^2 + b^2}$ be a parameter characterized the size of the radiation source and $\varrho = \sqrt{x^2 + y^2}$ determines the position of the point P_1 at the xy plane. Let we replace ς by the larger value $R + \varrho \geq \varsigma$. Thus, the Fresnel diffraction integral in Eqs. (1.58) or (1.60) is valid when [138, Table III.1]

$$z \geq \sqrt[3]{\frac{(R+\varrho)^4}{\lambda}},$$

what defines the lower limit for z. Taking into account that [83]

$$\int_{-\infty}^{\infty} e^{-i\alpha x^2 \pm i\beta x} dx = \sqrt{\frac{\pi}{i\alpha}} \cdot e^{\frac{-\beta^2}{4i\alpha}}, \tag{1.66}$$

we can say that the transfer function G_z, corresponding to the Fresnel diffraction kernel g_z in Eq. (1.59), is of the form

$$\begin{aligned} G_z(v_1, v_2) &= \int\int_{-\infty}^{\infty} \frac{e^{ikz}}{i\lambda z} e^{\frac{ik}{2z}(x^2+y^2)} \cdot e^{-i2\pi(v_1 x + v_2 y)} dx dy = \\ &= \frac{e^{ikz}}{i\lambda z} \int_{-\infty}^{\infty} e^{\frac{ik}{2z}x^2 - i2\pi v_1 x} dx \int_{-\infty}^{\infty} e^{\frac{ik}{2z}y^2 - i2\pi v_2 y} dy = \\ &= \exp\left(i\frac{2\pi}{\lambda} z\right) \cdot \exp(-i\pi\lambda z(v_1^2 + v_2^2)) \end{aligned} \tag{1.67}$$

or

$$G_z(k_x, k_y) = \exp(ikz) \cdot \exp\left(-iz\frac{k_x^2 + k_y^2}{2k}\right). \tag{1.68}$$

Then, similar to Eq. (1.45),

$$\begin{aligned} & u(x, y, z_0 + z)\Big|_{z=const} = \\ &= \frac{e^{ikz}}{4\pi^2} \int\int_{-\infty}^{\infty} \breve{u}(k_x, k_y, z_0) e^{-\frac{iz}{2k}(k_x^2+k_y^2)} e^{i(k_x x + k_y y)} dk_x dk_y = \\ &= e^{ikz} \int\int_{-\infty}^{\infty} \breve{u}(v_1, v_2, z_0) e^{-\pi i\lambda z(v_1^2+v_2^2)} e^{2\pi i(v_1 x + v_2 y)} dv_1 dv_2 = \\ &= \mathcal{F}^{-1}\{\mathcal{F}\{u(x, y, z_0)\}(v_1, v_2) \cdot G_z(v_1, v_2)\}(x, y), \end{aligned} \tag{1.69}$$

what is met again for $\sqrt{v_1^2 + v_2^2} \ll \frac{1}{\lambda}$. Then the approximation error is negligible. It implies that the angles of the plane wave decomposition α, β and γ are small $\cos^2\alpha = \frac{k_x^2}{k^2} \ll 1$, $\cos^2\beta = \frac{k_y^2}{k^2} \ll 1$, $\cos^2\gamma = \frac{k_z^2}{k^2} \ll 1$. Hence only a small portion of the field bandwidth is required to be covered, but the high-frequency details of the wave field at the observation plane are lost (see Eq. (1.68)). It is recognized that the Fresnel approximation for the transfer function is valid for [138]

$$\frac{(v_x^2 + v_y^2)^2_{\max}}{8k^3} \cdot z \leq 0.1 \cdot 2\pi, \tag{1.70}$$

what defines the upper limit for z.

1.3.7 Fraunhofer approximation

If the size of the radiation source S is small, and the distance z is significantly large, then the terms of the second order with respect to variables ξ and η in $\frac{(x-\xi)^2+(y-\eta)^2}{2z}$ can be neglected as

$$\frac{(x-\xi)^2+(y-\eta)^2}{2z} \approx \frac{x^2+y^2}{2z} - \frac{x\xi+y\eta}{z}, \tag{1.71}$$

and the expression for the wave field at an arbitrary point in free space can be given as (cf. Eq. (1.60))

$$\begin{aligned} & u\left(\frac{kx}{z}, \frac{ky}{z}, z_0+z\right)\Big|_{z=const} = \qquad (1.72)\\ = \; & \frac{e^{ikz}}{i\lambda z} e^{\frac{ik}{2z}(x^2+y^2)} \iint_{-\infty}^{\infty} u(\xi,\eta,z_0) e^{-i(\xi\frac{kx}{z}+\eta\frac{ky}{z})} d\xi d\eta = \\ = \; & \frac{e^{ikz}}{i\lambda z} e^{i\frac{z}{2k}((\frac{kx}{z})^2+(\frac{ky}{z})^2)} \mathcal{F}\{u(\xi,\eta,z_0)\}\left(\frac{kx}{z}, \frac{ky}{z}\right), \end{aligned}$$

what is known as the *Fraunhofer approximation*. Thus, the wave field at an arbitrary point in the Fraunhofer approximation is proportionally to the Fourier transform of the wave field at the plane z_0:

$$\left|u(x,y,z_0+z)\Big|_{z=const}\right| = \frac{1}{\lambda z}\left|U\left(\frac{kx}{z}, \frac{ky}{z}, z_0\right)\right|. \tag{1.73}$$

Neglecting the term $\frac{\xi^2+\eta^2}{2z}$, one assumes the maximum error (for a rectangular region S) in phase equal to $k\frac{a^2+b^2}{2z}$. Using the Rayleigh criterion, we obtain

$$k\frac{a^2+b^2}{2z} \le 0.1 \cdot 2\pi, \text{ i.e. } z \ge 5\frac{R^2}{\lambda}, \tag{1.74}$$

where $R=\sqrt{a^2+b^2}$ is (again) a parameter characterized the size of the radiation source [138], what defines the (far-field) region for the Fraunhofer approximation.

1.4 Interferometric methods of light field reconstruction

There are many methods to recover the complex amplitude of the wave field, often quite sophisticated. For instance, the conventional setup of the Shack–Hartmann wavefront sensor [97, 181, 195] is a 2D array of microleses (often called lenslets), and the wavefront of the incident wave is determined via displacements of focused spots, generated by an illuminated array of microlenses, from their reference positions as it is illustrated in Fig. 1.11. Since only tilts are measured, discontinuous

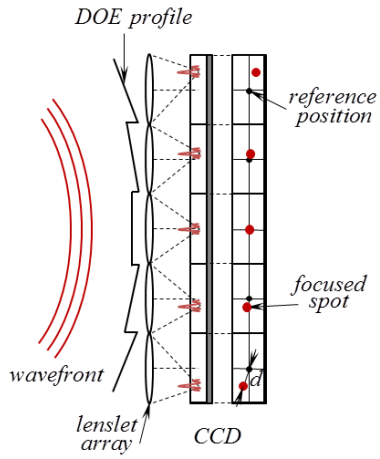

Figure 1.11: Principle of the Shack–Hartmann wavefront sensor as a 2D array of microlenses (lenslets). Lenslet (typically) with the same focal distance correspond to the reference positions of their focal points on a detector (CCD sensor). They focus light onto different areas of detector pixels (focused spots) depending on the shape of the incident local wavefront. The localized wavefront slope, and therefore the whole wavefront (object phase), is calculated by measuring the displacements d of the focused spots from the reference positions. The static lenslets may be replaced by diffractive optical elements (DOE), e.g., a programmable spatial light modulator (SLM) [200].

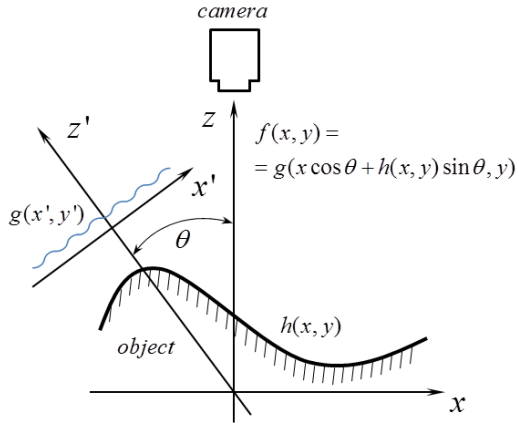

Figure 1.12: Structured illumination method: an optical scheme of the observation model [122]. An object is illuminated (at an angle θ) by parallel light stripes with sinusoidal amplitude distribution $g(x', y') = A(1 + \cos vx')$ and the resulting light amplitude distribution on the object $f(x, y) = A(1+\cos[v(x\cos\theta+h(x, y)\sin\theta)])$ is detected by a camera. Here $h(x, y)$ is the function describing the object profile, $A = x_{\max} - x_{\min}$ and v is the spatial frequency of the stripes. In [121] it is shown that the problem of recovering the object profile based on its structured illumination coincides with the problem of phase reconstruction via interferograms.

steps in the wavefront can not be detected by the Shack-Hartmann sensor. However, the sensor can work using partially coherent light sources, which are generally cheaper than lasers [3]. The Shack–Hartmann sensor based approach seems to be close to shearography by means of recalculation of the phase by spatial displacement of the incident wavefront from the reference one. One uses a simple adjustment method, and the typical arrangement contains no moveable parts, what leads to low demands regarding the mechanical stability and environment noise. Moreover, an array of static lenslets may be replaced by a diffractive optical element (see Section 1.5 and Appendix B.2), e.g., by a digital micromirror device or a liquid crystal based spatial light modulator (LC-SLM).

A volumetric representation of an object, 3D shapes can be achieved by the 2D structured images of objects ([122], see Fig. 1.12): one distinguishes moiré topography [213], the shear moiré topography [14], Fourier transform profilometry [215], the phase profilometry [209]. These methods are very similar to the conventional interferometry based methods: the Fourier transform method [214] and the method of allocation of the centres of bands [237]. In this case there is no strict restriction imposed on the light coherence. Despite the apparent (at first glance) simplicity and low cost of the structured illumination based methods, they have essential disadvantages: the sensitivity to background illumination, the result significantly depends on the structure of the object and lighting conditions, complexity of mathematical methods and computational algorithms [87].

In this thesis we consider two fundamental light coherence based approaches used to determine the phase of light wave fields and reconstruct the complex object amplitude: interferometric and phase-retrieval methods. They accumulate both the relative simplicity of the optical system and the numerical methods. In this Section we consider the established interferometric techniques, namely: phase shift holography and shearography, linked by the common mathematical apparatus. In Section 1.4.4 certain limitations of the interferometric methods are presented. In the next Chapter 2 the phase-retrieval approaches are discussed.

1.4.1 Phase shifting method

The coherent superposition of two waves is the basic principle of all interference based methods. Here we present the extraction of the phase information from a set of observed interferograms obtained using the *Michelson interferometer*[18] with the phase shifting method (see [194]).

Let $u_1(x,y)$ and $u_2(x,y)$ be complex amplitudes of transverse wave fields, which are linearly polarized in the same direction. Let $u_1 = \sqrt{I_1}e^{i\phi_1}$ and $u_2 = \sqrt{I_2}e^{i\phi_2}$ propagate in different directions as it is illustrated in Fig. 1.13. The resulting interference pattern at the sensor plane can be found similarly to Eq. (1.8) $I = I_1 + I_2 + 2\sqrt{I_1 I_2}\cos(\Delta\phi)$, where $\Delta\phi = \phi_2 - \phi_1$ is the phase difference between these two waves. Due to the ambiguity of the arguments of the cosine, the phase difference cannot be directly determined from the measurement. However, the

[18] An interferometer is an optical instrument that splits a wave into two waves using a beam splitter: delays them by (in general) unequal distances, redirects them using mirrors, recombines them using another (or the same) beam splitter, and detects the intensity of their superposition. Three classical interferomenters, the *Mach-Zehnder, Michelson and Sagnac interferometers*, are described, e.g., in [190, Chapter 2.5].

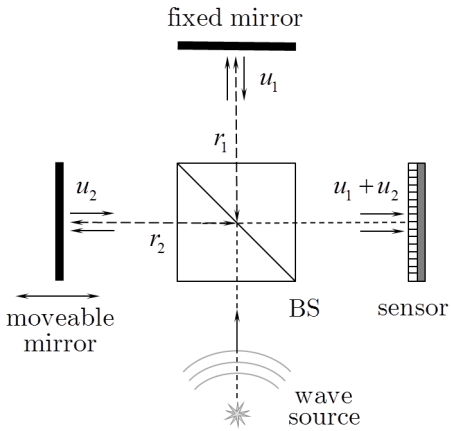

Figure 1.13: A scheme of the Michelson interferometer, where BS denotes a beam splitter. Two complex amplitude u_1 and u_2 are propagated at different distances r_1 and r_2, respectively, and superposed at the observation (sensor) plane.

complex amplitude u_1 can be found from a number of recorded interferograms by shifting the phase of u_2 [67, 228]. The phase shift is often realized by translating a mirror of the optical setup in Fig. 1.13 via piezoelectric transducers. Thus, the intensities of interference pattern is defined as

$$\begin{aligned}\mathcal{I}_r(x,y) &= |u_1(x,y) + u_2(x,y)\exp(i\theta_r)|^2 = I_1 + I_2 + \\ &+ u_1^*(x,y)u_2(x,y)\exp(i\theta_r) + u_1(x,y)u_2^*(x,y)\exp(-i\theta_r),\ r = 1,...K,\end{aligned} \tag{1.75}$$

where $\{\theta_r\}$ are phase shifts of u_2. In order to reconstruct the term $u_1(x,y)$, which can represent the object wavefront, K holograms are summed up with the same phase shifts used during their recording [236]

$$\begin{aligned}\bar{\mathcal{I}}(x,y) &= \frac{1}{K}\sum_{r=1}^{K}\mathcal{I}_r(x,y)\exp(i\theta_r) = u_1(x,y)\cdot u_2^*(x,y) + \\ &+(|u_1(x,y)|^2 + |u_2(x,y)|^2)\cdot\frac{1}{K}\sum_{r=1}^{K}\exp(i\theta_r) + \\ &+(u_1^*(x,y)\cdot u_2(x,y))\cdot\frac{1}{K}\sum_{r=1}^{K}\exp(i2\theta_r).\end{aligned} \tag{1.76}$$

It can be shown that at least three exposures $\{\mathcal{I}_r\}_{r=1}^3$ (e.g., with phase shifts $\theta_r = \{0, 2\pi/3, 4\pi/3\}$) are required in this method. Assume that $\theta_r = r\theta_0\ \forall\ r$. For a perfect reconstruction of the first term $u_1(x,y)\cdot u_2^*(x,y)$ phases $\{\theta_r\}$ should be found from the following expressions [83]

$$\sum_{r=1}^{K}\exp(ir\theta_0) = \frac{\exp(iK\theta_0) - 1}{\exp(i\theta_0) - 1}\exp(i\theta_0) = 0, \tag{1.77}$$

$$\sum_{r=1}^{K} \exp(i2r\theta_0) = \frac{\exp(iK\theta_0)-1}{\exp(i\theta_0)-1}\frac{\exp(iK\theta_0)+1}{\exp(i\theta_0)+1}\exp(i\theta_0) = 0. \tag{1.78}$$

The solution for Eq. (1.77) is $\theta_r = 2\pi\frac{r}{K}$ for any integer $K \geq 3$. For $K = 2$ the solution $\theta_0 = \pi$ does not satisfy Eq. (1.78) as [83]

$$\frac{\exp(i2\theta_0)-1}{\exp(i\theta_0)-1}\frac{\exp(i2\theta_0)+1}{\exp(i\theta_0)+1}\exp(i\theta_0) = 2. \tag{1.79}$$

Thus, the complex-valued wave field u_1 can be therefore found by, e.g., three or four holograms exposures. Let $\{\mathcal{I}_r\}$ be the interferograms with the corresponding phase shifts $\theta_r = \{0, \frac{\pi}{2}, \pi, \frac{3\pi}{2}\}$ for $r = \{0, 1, 2, 3\}$, respectively. Then

$$u_1(x,y) = \frac{\mathcal{I}_0(x,y) - \mathcal{I}_2(x,y) + i[2\mathcal{I}_1(x,y) - \mathcal{I}_0(x,y) - \mathcal{I}_2(x,y)]}{4u_2^*(x,y)}, \tag{1.80}$$

$$u_1(x,y) = \frac{\mathcal{I}_0(x,y) - \mathcal{I}_2(x,y) + i[\mathcal{I}_1(x,y) - \mathcal{I}_3(x,y)]}{4u_2^*(x,y)}. \tag{1.81}$$

Note that the intensity distribution of the interferograms can be also represented in the form (cf. Eq. (1.75))

$$\mathcal{I}_r(x,y) = \underbrace{I_1(x,y) + I_2(x,y)}_{I_{DC}(x,y)} + 2\sqrt{I_1(x,y)I_2(x,y)}\cos(\Delta\phi(x,y) + \theta_r), \tag{1.82}$$

thus, the (wrapped) phase difference can be found, e.g., using four shifts as

$$\mathcal{W}\{\Delta\phi(x,y)\} = \arg\{\mathcal{I}_0(x,y) - \mathcal{I}_2(x,y) + i(\mathcal{I}_3(x,y) - \mathcal{I}_1(x,y))\}. \tag{1.83}$$

1.4.2 Digital holography

First experiments in numerical reconstruction of optical holograms date back to the late 1960s – early 1970s [78, 127]. The widespread use of computers and replacement of photographic plates by a CCD sensor is considered to be an origin of digital holography: numerical wave field reconstruction in digital holography became properly available only since its practical confirmation (starting from 1994, [192]). A quick and effective method for both the wave field reconstruction and registration was necessary, and CCD based systems showed its efficiency and usability: all data could be sent direct to a computer without any additional operations.

A typical scheme of recording a digital hologram is illustrated in Fig. 1.14. A plane laser beam is divided by a beam splitter[19] (BS) into two beams: a reference beam, which falls directly onto a digital sensor (u_{ref}), and an object beam, which illuminates an object and after being scattered from the investigating object, also travels to the sensor (u_{obj}).

The numerical reconstruction of the hologram consists of applying to the recorded hologram (1.9) a transform that implements the backward wave field

[19] It is assumed that a beam splitter reflects 50% of the incident light and transmits the other 50% [125].

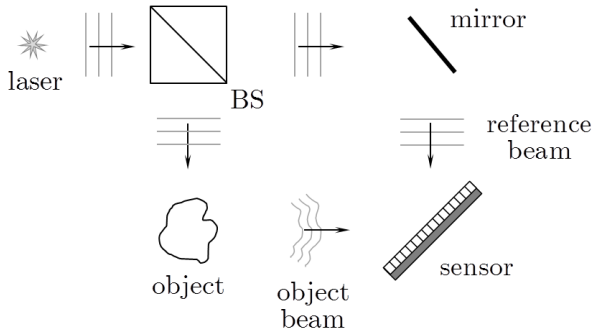

Figure 1.14: Schematic diagram of a digital holographic setup with the Mach–Zender interferometer. The intensity of the interference patterns, generated by superposed object (diffracted by an object) and (unchanged) reference beams, is detected on a sensor.

propagation from the sensor plane to the object plane. Recall that the hologram exposure $\mathcal{I}$ contains a zero order DC term of diffraction and two conjugated (twin virtual and real) images. In order to obtain the complex-valued object wave field, one has either to eliminate other three terms before the reconstruction or apply the reconstruction transform to the entire hologram and only than extract the interesting term. The latter solution is known as the so-called *off-axis* recording hologram (the classical Leith-Upatnieks's method, see, e.g., [79, 80, 125, 190, 194, 232, 234, 236]). Typically it can be found using the first Rayleigh–Sommerfeld diffraction integral[20] as [192, cf. Eq. (1)], [194, cf. Eq. (3.1)]

$$\Gamma(\xi,\eta) = \frac{iz}{\lambda}\iint \mathcal{I}(x,y)u_{ref}(x,y)\frac{\exp(-ikr)}{r^2}dxdy, \tag{1.84}$$

where $r = \sqrt{(\xi-x)^2+(\eta-y)^2+z^2}$ is the distance between a point in the hologram plane and a point in the reconstruction plane, z is the distance between the object and sensor planes. In off-axis holography [132, 133], a spatial offset angle between the reference and object beams is introduced. When this angle exceeds a minimum allowable angle (discussed in, e.g., [79, § 9.4.3]), the twin images are not contaminated by each other nor by other, say DC, wave components. Thus, the object wave field is extracted.

The method of eliminating interfering terms in recorded holograms before the reconstruction is called *on-axis* or *in-line* holography[21]. In the on-axis method of recording holograms the object and reference beams are collinear, and several exposures of holograms $\{\mathcal{I}_r\}_{r=1}^K$ of the object are recorded with phase shifting $\{\theta_r\}_{r=1}^K$ of the reference beam as it is discussed before. This method can be realized via the mentioned phase shifting method using a moveable mirror or a spatial light modulator (digital phase shifting holography [228, 230]). In this case the recorded holograms are of the form:

[20] see Section 1.3.5

[21] Note while Gabor had no sources giving light with sufficient coherence, he had to produce *in-line* holograms where object and reference waves were travelling in the same direction orthogonally to the hologram. Leith and Upatniks were the first who took advantage of the coherence of laser light and who gave the object and the reference beams different directions [125].

$$\begin{aligned}\mathcal{I}_r(x,y) &= |u_{obj}(x,y)+u_{ref}(x,y)\exp(i\theta_r)|^2 = \\ &= |u_{obj}(x,y)|^2+|u_{ref}(x,y)|^2+u^*_{obj}(x,y)u_{ref}(x,y)\exp(i\theta_r)+ \\ &\quad +u_{obj}(x,y)u^*_{ref}(x,y)\exp(-i\theta_r),\ r=1,...K.\end{aligned} \tag{1.85}$$

Note that the wave u_1 in Eq. (1.75) can be interpreted in terms of in-line holography as the object beam, u_2 – as the reference beam, and the fixed mirror in Fig. 1.13 represents (could be replaced by) the investigating object. Therefore, the complex amplitude of the wave field u_{obj} at the observation plane can be found according to, e.g., Eqs. (1.80)–(1.81), and the phase difference is calculated similar to Eq. (1.83). If the complex-valued u_{obj} at the sensor plane is extracted the wave field at the object plane is obtained by applying the backward diffraction propagation, e.g., as $h_z \circledast u_{obj}$, where h_z is the RS diffraction kernel (1.52).

1.4.3 Shearography

Digital phase shifting holography has a very widespread application, especially for nondestructive deformation detection and remote testing [16, 169], measurement of surface shapes [157, 229], study of material properties [199] and vibrational processes [177]. The conventional and digital holographic interferometry are very high sensitive to optical path changes. This high sensitivity is a drawback for applications in a rough environment, where no vibration isolation is available. Unwanted optical path length variations due to vibrations disturb the recording process [194].

Shearography is an interferometric method, where holograms (interferograms) are generated by superposing of the investigating wave field with its copy, but now slightly spatially shifted (see landmark works by Hung [102, 103] and also [52, 54, 125, 194]). Since only the spatial variations of the displacement in a predetermined direction are measured, the methods are rather insensitive to rigid body motions. In general shearography may be employed to completely recover the complex amplitude of an arbitrary wave field [54]. This method is often used for nondestructive deformation detection.

The shifting of the wave fields is performed by a shearing elements, e.g., a glass wedge in front of one half of the imaging lens, two tilted glass plates, a double refractive (Wollaston) prism [103, 125], or a Michelson interferometer-like arrangement [52, 102] with one mirror slightly tilted (see Fig. 1.15). Depending on the used recording medium one distinguishes photographic (photographic emulsions) or digital shearography (computerized process with the use of CCDs). The developed phase shifting technique allows the determination of phase distributions in digital shearography to be automated (phase shift shearography).

Let we consider the basic principle of shearography in terms of phase shifting shearography with a Michelson interferometer-like arrangement. In Fig 1.15 two wave fields (again), the object u_1 and reference u_2 are superposed at the sensor plane. The role of this reference wave u_2 is taken by one of the two mutually tilted (at the xz plane) object wave fields, called *self-reference*. In this case, according to the principle of superposition, at the sensor plane we have the following complex

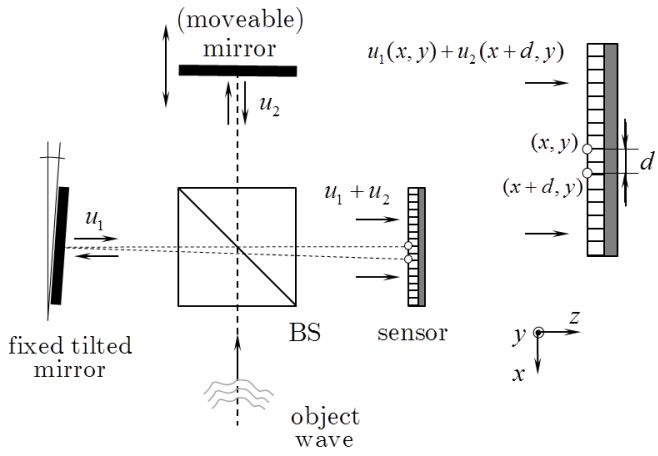

Figure 1.15: Arrangement for digital shear interferometer. The input object wave is divided by a beam splitter (BS), so two wave, the object u_1 and so-called *self-reference* wave u_2, travel along different ways and superpose at the sensor plane. Since the fixed mirror is here tilted in the xz plane, u_1 is shifted on a sensor by d.

amplitude:

$$\begin{aligned} u(x,y) &= u_1(x,y) + u_2(x+d,y) = \\ &= \sqrt{I_1(x,y)}e^{i\phi(x,y)} + \sqrt{I_2(x+d,y)}e^{i\phi(x+d,y)}, \end{aligned} \tag{1.86}$$

where the spacing between the two correlated areas of the object surface d is called the *share*. The shearographic image (interference pattern of u) may be mathematically represented [52, 102, 103, 125] as follows [54, cf. Eq. (3)]

$$\mathcal{I}(x,y) = \underbrace{I_1(x,y) + I_2(x+d,y)}_{I_{DC}(x,y)} + \underbrace{2\sqrt{I_1(x,y)I_2(x+d,y)}}_{I_m(x,y)} \cdot \cos(\varphi(x,y)), \tag{1.87}$$

where $\varphi(x,y) = \phi(x,y) - \phi(x+d,y)$ is the phase difference due to shearing, $I_{DC}(x,y)$ is again the DC term as in Eq. (1.82) and $I_m(x,y)$ is a modulation of the interference. Deformation of the object results in the wave fields $\sqrt{I_1(x,y)}e^{i(\phi(x,y)+\Delta\phi(x,y))}$ and $\sqrt{I_2(x,y)}e^{i(\phi(x+d,y)+\Delta\phi(x+d,y))}$ and their superposition yields [103, cf. Eq. (2)]

$$\mathcal{I}'(x,y) = I_{DC}(x,y) + I_m(x,y)\cos(\varphi(x,y) + \Delta\varphi(x,y)), \tag{1.88}$$

where $\Delta\varphi(x,y)$ denotes a phase change due to the object surface deformation. According to the described phase shifting method with four phase shifts $\theta_r = \{0, \frac{\pi}{2}, \pi, \frac{3\pi}{2}\}$ one records four exposures $\mathcal{I}_r(x,y) = I_{DC}(x,y) + I_m(x,y)\cos(\varphi(x,y) + \theta_r)$ and $\mathcal{I}'_r(x,y) = I_{DC}(x,y) + I_m(x,y)\cos(\varphi(x,y) + \Delta\varphi(x,y) + \theta_r)$ for these phase shifts, $r = \{1,2,3,4\}$. Then, the phase differences can be found similar to Eq. (1.83) as [54, cf. Eq. (5)]

$$\mathcal{W}\{\varphi(x,y)\} = \arg\{\mathcal{I}_0(x,y) - \mathcal{I}_2(x,y) + i(\mathcal{I}_3(x,y) - \mathcal{I}_1(x,y))\}, \tag{1.89}$$

and the process is repeated for the deformed patterns, yielding [54, cf. Eq. (5)]

$$\mathcal{W}\{\varphi(x,y)+\Delta\varphi(x,y)\}=\arg\{\mathcal{I}_0'(x,y)-\mathcal{I}_2'(x,y)+i(\mathcal{I}_3'(x,y)-\mathcal{I}_1'(x,y))\}. \quad (1.90)$$

Therefore, the phase change due to the deformation $\Delta\varphi(x,y)$ is subsequently determined by subtracting of the unwrapped phase $\varphi(x,y)+\Delta\varphi(x,y)$ from the unwrapped $\varphi(x,y)$ [102, 103].

1.4.4 Limitation of interferometric techniques

Let us summarize certain limitations of the interferometric (holographic) methods:

- Since these methods are based on the superposition principle, they have an essential demand regarding the temporal/spatial coherence. The insufficient coherence leads to poor imaging of interference patterns (the additional interference component of Eq. (1.8) is small).
- The superposition of two waves requires considerable efforts to align optical components on an optical system, and the proper alignment is very time consuming and troublesome. In some cases it is very difficult to realize fitting and fine overlapping of the investigating object wave $u_{obj}\equiv u_1$ with the reference wave $u_{ref}\equiv u_2$ [3].
- Since these two waves travel along their separate paths, the result of measurements is high sensitive to various environmental disturbances as vibrations or thermal fluctuations. Thus, the experimental configuration must be isolated from vibration to a large extent. In particular, it is of importance for temporal phase shifting, because the mechanical stability over the entire period of measurement must be ensured [3].
- Experimental arrangements for interferometric methods are technically quite complex and therefore expensive due to the use of many optical components such as beam splitters, lenses, etc. Moreover, the more complex optical system, the more sources of various distortions to be compensated.

1.5 Diffractive optical elements (DOEs)

The phase change can be easily realized using not a moveable mirror but diffractive optical elements, e.g., with LC-SLMs, by the modulation of a light wave field. Let us consider the modulating optical elements which help realizing the linear operations to obtain a desired wave field distribution for various applications.

The modulating optical systems may contain both classical optical elements, such as lenses, prisms or beam splitters, and quite sophisticated ones with a fixed profile/relief or reconfigurable (electronically controlled) structure. The light modulation in such an optical system is primarily based on diffractive media which transform either the amplitude or phase of the incident beam.

One of the straightforward applications of such modulating optical elements is the *wave field synthesis/design*, i.e. generating of a desired volumetric light wave field distribution within a region of interest in 3D space.

1.5.1 DOEs with fixed profiles

The first modulating optical element, called *diffractive optical element* (DOE), is a *diffraction grating* constructed more than two hundreds years ago [207]. It had binary amplitude or phase transmittance and looked like a transmissive or reflective plate with a thin microrelief, calculated according to the diffraction theory. For instance, the simplest amplitude one-dimensional diffraction grating is a flat optical transparency[22] with alternate light and dark stripes of the same width d. After one-dimensional binary amplitude and phase diffraction gratings one constructed two-dimensional radially-symmetric gratings (zone plates). The essential development of diffraction optics was held back by the absence of suitable materials and technologies of their processing which would have allowed accurate constructing of diffraction patterns with a complex surface/profile. The use of computers made a revolution in the creation of DOEs: in the late 1960s computers were used for the synthesis of holograms of mathematically determined objects. First computer generated holograms were again binary, invented by Lohmann [23, 24, 139]. They were printed on a computer line printer, then optically reduced and reconstructed in optical setups using coherent laser illumination [233]. The recording medium was represented in the form of square cells. A full transparent opening inside each cell modulates both the amplitude (by the size of the opening) and phase (by a shift of the opening within cells) of the desired object [221], [236, Lecture 5]. Then, the use of more sophisticated devices capable of recording grey scale images was suggested for recording computer generated holograms [128]. In addition, the key problem of coding – recording on a physical medium complex-valued functions and construction of corresponding amplitude-phase transparencies – has been resolved. Progress in microelectronics and laser technology gave in the 1980s the photoplotter and electron-beam lithography, what made the problem of creation of DOEs with a complex profile practically realizable, e.g., creation of DOEs with unique characteristics, unattainable in the traditional optics, such as focusators of laser beam.

1.5.2 Reconfigurable DOEs: spatial light modulators (SLMs)

Generally, DOEs can be specified by the numeric value (binary and with a complex profile), amplitude-phase characteristics of the transmission function (amplitude, phase, or complex-valued) and by the specifics of their microrelief: the linear or circular gratings, zone plate/kinoform lens, computer generated hologram and spatial light modulator (see, e.g., [207, 236] for more details).

Spatial light modulators (SLMs) are reconfigurable DOEs, which give a significant flexibility of the optical system to modulate the light wave field and find very widely application of light wave field synthesis. SLMs are based on liquid crystals, microelectromechanical systems or magneto- and acusto-optic modula-

[22] If such a grating is illuminated by the monochromatic light beam with the wavelength λ, which is incident normal to the plane of the grating, a number of light beams will be formed as the result of diffraction on a periodic structure of stripes. These beams will travel at different angles θ^p corresponding to various diffraction orders. The angle θ^p depends on the grating period d, and assuming that the angles are small $\theta^p = p\frac{\lambda}{d}$, where $p = 0, \pm 1, \pm 2...$ The light intensity changes in the inverse proportion to p as $I(\theta^p) \sim (\frac{2\lambda}{\pi d \theta^p} \sin(\frac{\pi d}{2\lambda}\theta^p))^2 \approx \frac{1}{(2p+1)^2}$ [207].

tors (see [47, 101, 159] for mode details). *Digital micromirror devices* (DMDs) are a type of such a reconfigurable devices which modulate an incident wave by reflection [221]. These devices consist of a large 2D array of electronically controlled micromirrors taking one of a few present angles [43]. In [124] one of pioneering works, where DMDs are used to reconstruct a binary hologram, is presented. A holographic 3D image projection by DMD is presented in [100]. At present time, one uses typically the electronically reconfigurable SLMs[23], and commodity SLMs are primarily based on liquid crystals. The main principle of LCs, and therefore liquid crystal based SLMs (LC-SLMs), is based on *birefringence*, i.e. the refractive index of liquid crystals depends on the orientation of molecules of LCs, which, in turn, can be controlled by apply an electrical charge. In general one distinguishes optically and electrically addressed LC-SLMs depending on the way the electrical charge is applied to a LC. The *optically addressed* SLMs use incoherent light to control the orientation of the liquid crystal molecules. The intensity of the incoming incoherent light is sensed by a photo-sensor, which transforms the light intensity into an electrical charge directly over the liquid crystal. In *electrically addressed* SLMs the voltage to the liquid crystals is applied via an electrodes connected with a silicon chip of pixel cells.

The structure of DOEs or data which is required to be programmed on SLMs are commonly calculated by iterative projection methods (see, e.g., [121, 122, 207, 238]) derived based on the mentioned Gerchberg–Saxton algorithm [71]. This algorithm can be used to specify the desired volumetric wave field [203]. In [11] the amplitude and phase are tried to be separately controlled by two phase-only SLMs (double-phase hologram for the complex modulation). SLMs (and more generally DOEs) may be used extensively in holographic data storage [90, 210], optical computing and imaging [12, 15, 86] and as a component of a holographic display technology [25, 126, 172]. They also often find application in phase-contrast microscopy and holographic optical tweezers [131, 161, 176, 187]. For instance, the Shack–Hartmann wavefront sensor illustrated in Fig. 1.11 can be realized using a DMD or an LC-SLM. Typically there are LC-SLMs for the amplitude- and phase-only modulations.

The structure of an LC-SLM in the used 4f optical system and the resulting transfer function of a phase modulating SLM is presented in Appendix B.2.

[23] Note, however, that DMDs are still very attractive as they provide higher contrast ratio, brightness and optical efficiency comparing to SLMs [221].

Chapter 2

Introduction to phase retrieval

Previously, in Section 1.4, the recovering quantitative phase information from interference patterns by interferometric (holographic) techniques is considered. In this Chapter we deal with the diffraction propagation of a light wave field, where each point of the illuminated object is a source of interfering secondary wavelets. The so-called *phase retrieval* is an alternative approach used to estimate the phase of a complex-valued light wave field from a number of the spatial intensity measurements of diffraction patterns at different observation planes. The main advantage in comparison with the conventional interference based methods is that no distinct reference wave is required. Thus, phase retrieval has relatively low demands regarding both the coherence of light and the mechanical stability of the experimental arrangement [3]. Moreover, the optical system for phase-retrieval methods are often simpler, more robust with respect to disturbances such as vibration and, what is also important, cheaper comparing with interferometric methods with a reference beam. In other hand, the complex-valued wave field and, in particular, the phase can not be computed so straightforward as before: see Eqs. (1.80)–(1.81) and (1.83). Let us overview the used diffraction propagation model and the conventional phase recovering techniques more in detail, and consider the author's contribution in the development of parallel iterative phase-retrieval algorithms.

2.1 Plane-to-plane propagation modeling

A typical setup of the diffraction wave field propagation is illustrated in Fig. 2.1. Let a plane laser beam illuminates an object, and being scattered by it (or passed through a transparent object) travels in the direction to a sensor along the optical axis z. The light wave field which appears immediately after the object is typically called the *object wave field* [79, 80] denoted hereafter by $u_0(\xi, \eta)$. The corresponding $\xi\eta$ plane, where the transverse u_0 is defined, is called the *object plane*. This object wave field, propagated to a sensor according to the Huygens–Fresnel principle, results in the diffracted wave field $u_z(x, y)$ at the *observation plane*. The link

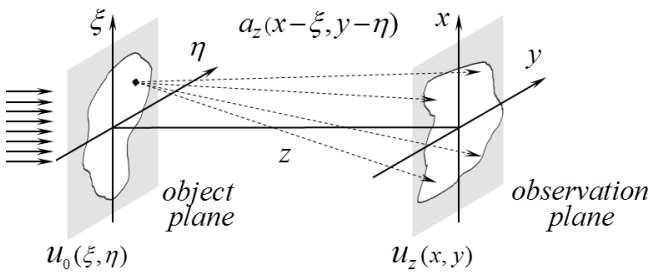

Figure 2.1: Propagation model of the diffracted wave field. The transverse $\xi\eta$ object plane is parallel to the observation xy plane at the distance z from it. The link between the object $u_0(\xi,\eta)$ and sensor $u_z(x,y)$ wave fields is defined in the convolutional form by $u_z(x,y) = \{u_0 \circledast a_z\}(x,y)$, where a_z denotes a shift-invariant diffraction kernel of the forward wave field propagation from the object to the observation/sensor plane.

between these two transverse wave fields in terms of the scalar diffraction theory is formulated with the used plane-to-plane propagation model as follows

$$u_z(x,y) = \{u_0 \circledast a_z\}(x,y) = \iint_{-\infty}^{\infty} u_0(\xi,\eta) \cdot a_z(x-\xi, y-\eta) d\xi d\eta, \tag{2.1}$$

where a_z is a shift-invariant diffraction kernel[1] of the wave field propagation from the object to the sensor plane and the subindex z emphasizes the propagation distance between these planes.

If the complex amplitude $u_z(x,y)$ at the sensor plane is given (e.g., from a number of hologram exposures $\{\mathcal{I}_r\}$), the object wave field is calculated by the backward wave field propagation from the sensor to the object plane. If the diffraction kernel a_z is invertible, the estimate of the complex-valued transverse wave field at the object plane $\widehat{u}_0$ is calculated as

$$\widehat{u}_0(\xi,\eta) = \iint_{-\infty}^{\infty} u_z(x,y) \cdot a_{-z}(x-\xi, y-\eta) dx dy, \tag{2.2}$$

Eq. (2.1) can be represented via a linear diffraction operator $u_z(x,y) = \mathcal{D}_z\{u_0\}(x,y) = \{u_0 \circledast a_z\}(x,y)$, and the object reconstruction according to Eq. (2.2) – via the inverse operator $\widehat{u}_0(\xi,\eta) = \mathcal{D}_z^{-1}\{u_z\}(\xi,\eta) = \{u_z \circledast a_{-z}\}(\xi,\eta)$. Note that the size of the detector (photographic plate, CCD sensor) is finite. The estimate $\widehat{u}_0(\xi,\eta)$ is perfect (precise for any u_0, $\widehat{u}_0 = u_0$) only if $u_z(x,y)$ is given for the whole transverse xy plane, i.e. the detector is of infinite size [125]. The finite size of the sensor (given measurements) may lead to the ill-posedness of the inverse problem of the object wave field u_0 reconstruction and, as the result, to corrupted (e.g., blurred) wave field reconstructions. Note also, that the observations (e.g., $\{\mathcal{I}_r\}$) are generally noisy due to various disturbances of the optical path such as

[1] The diffraction propagation for the near-field zone is typically defined by the Rayleigh–Sommerfeld solution of the Maxwell–Helmholtz equation or its Fresnel approximation, see Section 1.3.5 and 1.3.6.

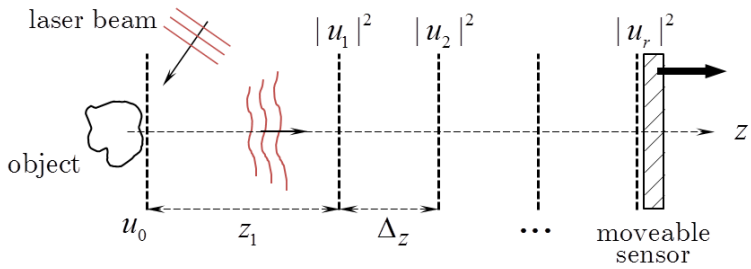

Figure 2.2: An experimental configuration for multi-plane phase retrieval. The intensity of the light wave field scattered by an object is recorded across a sequence of different observation planes using a sensor which moves along the optical axis z. Here the object wave field is denoted by u_0 and the intensity observations $\{|u_r|^2\}$, $r = 1, ...K$ are obtained at the distances $z_r = z_1 + (r-1) \cdot \Delta_z$, where z_1 is the distance between the object and the first measurement plane and Δ_z is the fixed distance between following transverse observation planes.

vibration, dust and so on. In addition, the problem of the object wave field reconstruction is complicated due to nonlinearity of the computation (unwrapping) of the object phase (see Eq. (1.83)).

2.2 Free space diffraction propagation models

The straightforward experimental setup for recording the result of the free space diffraction propagation to different distances $\{z_r\}$ can be realized by a moveable sensor as it is illustrated in Fig. 2.2 or [7, Fig. 1]: a CCD camera is sequentially moved between K measurement planes (separated by a distance Δ_z) using a motorized precision stage. Here the wave field propagation through the space layer of the width z_r can be described via the (say, ASD, Eq. (1.48)) transfer functions or (e.g., RS (1.52) or Fresnel (1.59)) diffraction kernels. If the diffraction operator $\mathcal{D}_{z_r}$ corresponding to the forward wave field propagation to the distance z_r is invertible (in particular, in [197] it is shown that the RS diffraction operator $\mathcal{D}_{z_r}$ is invertible) and the complex-valued wave field $u_r(x, y)$ at the r-th sensor plane is given, one can reconstruct the wave field at the object plane with the inverse diffraction operator $\mathcal{D}_{z_r}^{-1}$, namely $\widehat{u}_0(\xi, \eta) = \mathcal{D}_{z_r}^{-1}\{u_r\}(\xi, \eta)$ by various methods. One distinguishes the following conventional continuous methods of the complex-valued wave field reconstruction [125]

- reconstruction via the Rayleigh–Sommerfeld diffraction integral ($z_r \gg \lambda$, con. Eq. (1.52))

$$\begin{aligned} u_r(x,y) &= \mathcal{F}^{-1}\{\mathcal{F}\{u_0\}(v_1,v_2) \cdot \mathcal{F}\{h_r\}(v_1,v_2)\}(x,y), \\ \widehat{u}_0(\xi,\eta) &= \mathcal{F}^{-1}\{\mathcal{F}\{u_r\}(v_1,v_2) \cdot (\mathcal{F}\{h_r\}(v_1,v_2))^*\}(\xi,\eta); \end{aligned} \tag{2.3}$$

- reconstruction via the angular spectrum decomposition (con. Eq. (1.45))

$$\widehat{u}_0(\xi,\eta) = \mathcal{F}^{-1}\{\mathcal{F}\{u_r\}(v_1,v_2) \cdot H_r^*(v_1,v_2)\}(x,y); \tag{2.4}$$

- reconstruction with the Fresnel approximation of the diffraction kernel ($z_r \gg \sqrt{\xi^2+\eta^2}$, con. Eq. (1.59))

$$\begin{aligned} u_r(x,y) &= \mathcal{F}^{-1}\{\mathcal{F}\{u_0\}(v_1,v_2)\cdot\mathcal{F}\{g_r\}(v_1,v_2)\}(x,y), \\ \widehat{u}_0(\xi,\eta) &= \mathcal{F}^{-1}\{\mathcal{F}\{u_r\}(v_1,v_2)\cdot(\mathcal{F}\{g_r\}(v_1,v_2))^*\}(x,y); \end{aligned} \tag{2.5}$$

- reconstruction via the Fresnel approximation in terms of chirp functions[2](con. Eq. (1.60))

$$\widehat{u}_0(\xi,\eta) = \frac{e^{-ikz_r}}{-i\lambda z_r} e^{\frac{-ik}{2z_r}(\xi^2+\eta^2)} \mathcal{F}^{-1}\{u_r\left(\frac{x}{\lambda z_r},\frac{y}{\lambda z_r}\right) e^{\frac{-ik}{2z_r}(x^2+y^2)}\}(\xi,\eta); \tag{2.6}$$

- reconstruction using the Fresnel transfer function (con. Eq. (1.69))

$$\widehat{u}_0(\xi,\eta) = \mathcal{F}^{-1}\{\mathcal{F}\{u_r\}(v_1,v_2)\cdot G_r^*(v_1,v_2)\}(x,y). \tag{2.7}$$

The subindex r emphasizes the calculation of the transfer functions (H_r, G_r) and diffraction kernels (h_r, g_r) of the diffraction wave field propagation to various distances $\{z_r\}_{r=1}^K$, $r = 1,...K$. Note that, the free space wave field propagation can be also imitated by the 4f configuration using a phase modulating LC-SLM [4, 53] (see Section 5.1).

2.3 Inverse problem of phase retrieval

Phase retrieval is exploited in many engineering and scientific areas as astronomy [36, 63], crystallography [73, 96, 153], microscopy [71, 155] aberrations estimation/correction [62, 174], diffraction and 3D imaging, tomography, remote sensing, nondestructive testing, material analysis to name just a few. We refer to the books [104, 211] and review articles (e.g., [59, 107, 119, 140]) for descriptions of various instances of the phase-retrieval problem and further references.

From the mathematical point of view, recovering the phase information can be stated as an *inverse problem* [91, 109], where the measured intensities of diffraction patterns represent the observed effect caused by (aside from the amplitude) a unknown object phase. Since the wave fields at the sensor planes are assumed to be generated by radiation from the object plane, in this thesis the reconstruction of the phases, missed in measurements, is produced through the object plane distribution considered as the only unknown variable. Following Eq. (2.1), the problem of multi-plane phase retrieval can be formulated as [91]

$$\underbrace{\left|u_r(x,y)\right|^2}_{output} = \left|\iint_{-\infty}^{\infty} \underbrace{u_0(\xi,\eta)}_{input}\cdot\underbrace{a_r(x-\xi,y-\eta)}_{system}d\xi d\eta\right|^2, \quad r=1,...K, \tag{2.8}$$

[2] A chirp is a signal in which the frequency of oscillations linearly increases/decreases depending on the spatial coordinates [125, Chapter A.13]. The exponential one-dimensional *chirp function* of infinite support can be presented as $c(t) = \exp(i\alpha\pi t^2)$ with its Fourier transform as again a scaled chirp function with a constant amplitude $\mathcal{F}\{c(t)\}(v) = \frac{i}{\sqrt{\alpha}}\exp(-\pi\frac{v^2}{\alpha})$. This function got its name from applications in testing transmission systems for acoustic signals, and is of the extensively usage in diffraction theory.

where the investigating complex-valued object u_0 is the input of the optical system and the diffraction kernels $\{a_r\}_{r=1}^K$ give the mathematical description of the used coherent imaging system of the wave field propagation at different distances from the object plane $\{z_r\}_r$. In contrast to Eq. (2.1), we use here the subindex r to emphasize various distances of the diffraction propagation. In this formulation, the direct problem is to compute the output – a number of intensity observations $\{|u_r|^2\}$ as the result of the forward wave field propagation of the object wave field u_0 to distances $\{z_r\}_r$ (see Section 2.2), the output of the optical system for various settings. The goal of the inverse problem is to determine the input of the system that gives rise to the (noisy) measurements of the output [91]. Note that since the phase ϕ_r of the wave field at the r-th sensor plane $u_r = |u_r|e^{i\phi_r}$ is absent, the integral in Eq. (2.8) can not be directly inverted (similar to Eq. (2.2)).

2.4 Overview of phase-retrieval techniques and our contribution

In the past decades, the inverse problem of phase retrieval is treated in two fundamentally different ways: by *deterministic* or *iterative* approaches.

2.4.1 Deterministic phase retrieval

The *deterministic* approaches are based on the so-called transport-of-phase [217, cf. Eq. (5)] and transport-of-intensity (TIE, [217, cf. Eq. (4)]) equations originated by Teague [216, 217, 218]. The main idea is to derive formulas which describe a one-to-one relation between the measured intensity and the undetected phase. These formulas are calculated via physical properties of the light waves, mainly directly from the Maxwell–Helmholtz wave equations (see, e.g., [120]), typically provided the light wave propagation in only one direction, say along the z axis. In addition, TIE based methods are widely used to define the phase of a monochromatic light field [120, 218]. The phase of a wave field is shown to be retrieved by computing the axial intensity derivative $\frac{\partial}{\partial z} I(x, y, z)$, and the direct solution can be found from two [217] or multiple defocusing images [6, 206]. Note that since the intensity derivative can not recorded directly, it is obtained by the central, forward and backward finite differences [206, cf. Eqs. (1)]:

$$\frac{\partial}{\partial z} I(x, y, z = 0) = \frac{I(x, y, \Delta_z) - I(x, y, -\Delta z)}{2\Delta_z}, \tag{2.9}$$

$$\frac{\partial}{\partial z} I(x, y, z = 0) = \frac{I(x, y, \Delta_z) - I(x, y, 0)}{\Delta_z}, \tag{2.10}$$

$$\frac{\partial}{\partial z} I(x, y, z = 0) = \frac{I(x, y, -\Delta_z) - I(x, y, 0)}{-\Delta_z}. \tag{2.11}$$

The conventional image is denoted by $I(x, y, z = 0)$ and (also measured) diversity images are $\{...I(x, y, -\Delta_z), I(x, y, \Delta_z), ...\}$. In Fig. 2.3 the recording process of the phase-diversity images is illustrated.

The phase diversity incorporates the additional information on the wave field propagation and allows improving the phase imaging by multiple measurements

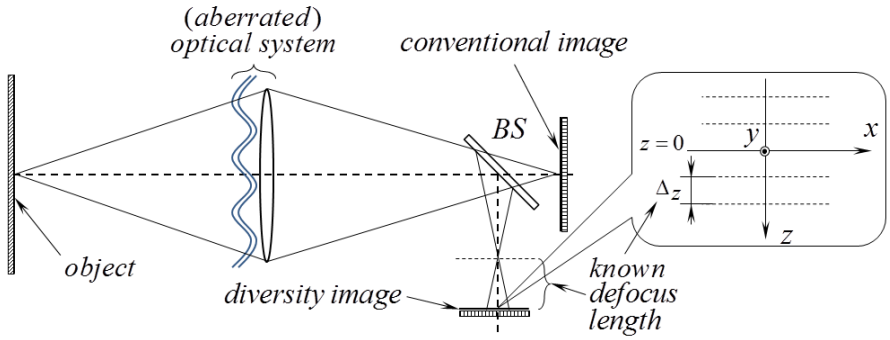

Figure 2.3: Optical layout of a phase-diversity system. If the conventional image is degraded by aberrations in the optical system, the phase-diversity images will be therefore degraded by the combination of the same aberrations and a known amount of defocus. The reconstruction is performed by a number of diversity images recorded at different distances z by various defocusing $\pm\Delta_z, \pm 2\Delta_z, \ldots$. Dashed lines in the right image represent the positions of a sensor to measure the diversity images [6, 171, 174, 202].

with various defocusing Δ_z [206]. We refer to [120] for the phase gradient based method and to the mentioned works by Teague and [3, 6, 171, 174, 202] for the additional details.

TIE based techniques are relatively fast, computationally efficient and can be implemented in many existing systems. Nevertheless, their are very sensitive to inaccuracy of the optical setup such as misalignment at the xy plane, misfocusing (with respect to z) and noise. In general, *TIE based techniques are recognized to fail in the case of a significant large amount of noise* [171, 224].

2.4.2 Iterative phase retrieval

Perhaps the first efficient *iterative* algorithm for phase retrieval is originated by Gerchberg and Saxton [71], initially for a single measurement plane. It is shown in Section 1.3.7 that the wave field propagation to the far field, the Fraunhofer region, is proportional to the Fourier transform (see Eqs. (1.72)–(1.73)). Originally, the Gerchberg–Saxton (GS) algorithm was applied in the specific case, where the intensity of the wave field is known across a spatial and the corresponding Fourier domain, e.g., at the far-field zone or at the focal plane of a lens [138, 238]. In Fig. 2.4 a two lenses scheme of the conventional iterative Gerchberg–Saxton phase-retrieval algorithm is presented. The common idea consists of the iterative replacement of the estimated amplitude at the object $|u_0(\xi,\eta)|$ and Fourier (observation) planes $|u_F(\frac{k\xi}{f}, \frac{k\eta}{f})|$ by measured or *a priori* information keeping the computed phase.

The work on the GS algorithms was continued and improved by many authors (see, e.g., [57, 231]). It is shown that such iterative phase recovering can be realized not only with respect to the object plane [57], but also to measurement planes, using defocus images only (e.g., Misell's variation of the GS algorithm [155]). In 1982 Fienup systematized the earlier works and introduced some, for now classi-

Algorithm: Gerchberg–Saxton error-reduction phase retrieval (GS)
Initialization: $\phi_0^0(\xi,\eta) = \phi_0^{init}(\xi,\eta)$ for $t = 0$
Repeat for $t = 0, 1, 2, ...$
1. Object update by *a priori* $a_0(\xi,\eta)$, say $a_0(\xi,\eta) = 1$:
$u_0^t(\xi,\eta) = a_0(\xi,\eta) \cdot \exp(i\phi_0^t(\xi,\eta))$
2. Forward propagation and calculation of the phase ϕ_F^t
$\phi_F^t(\frac{k\xi}{f}, \frac{k\eta}{f}) = \arg\{\frac{e^{ikf}}{i\lambda f} e^{i\frac{f}{2k}((\frac{k\xi}{f})^2+(\frac{k\eta}{f})^2)} \mathcal{F}\{a_0 \circ \exp(i\phi_0^t)\}(\frac{k\xi}{f}, \frac{k\eta}{f})\}$
3. Update of the Fourier image by the measured $a_F(\frac{k\xi}{f}, \frac{k\eta}{f}) = \sqrt{I_F(\frac{k\xi}{f}, \frac{k\eta}{f})}$:
$u_F^t(\frac{k\xi}{f}, \frac{k\eta}{f}) = a_F(\frac{k\xi}{f}, \frac{k\eta}{f}) \cdot \exp(i\phi_F^t(\frac{k\xi}{f}, \frac{k\eta}{f}))$
4. Backward propagation and calculation of the object phase $\phi_0^{t+1}(\xi,\eta)$
$\phi_0^{t+1}(\xi,\eta) = \arg\{i\frac{e^{-ikf}}{\lambda f} e^{\frac{-ik}{2f}(\xi^2+\eta^2)} \mathcal{F}^{-1}\{a_F \circ \exp(i\phi_F^t)\}$
End on t

cal, types of phase-retrieval algorithms[3][59]: error-reduction (GS), gradient search (steepest-descent) methods and input-output algorithm (further developed to the hybrid input-output algorithm, see, e.g., [212]). Similar methods are proposed for fractional Fourier and Fresnel transforms [238] instead of Fourier transforms as the transfer functions of the wave field propagation for both the wave field reconstruction [238] and optical design [58, 111].

In [31, 59, 201] it is shown that the prior knowledge about the wave field and its support is employed (as constraints) for successful phase retrieval, to make the solution unique. However, in practice, when the intensity information contains measurement noise, the iterative scheme is accompanied with problems of convergence (the convergence rate depends on the investigating object and in some cases is quite slow [60, 61]), stagnation [61, 201] and uncertainty [212] (more than one solution consistent with the noisy measurements). It makes phase retrieval a difficult ill-posed inverse problem. In general, the problem of the uniqueness of phase retrieval is open[4]: even if in practical situations the phase-retrieval problems do have unique solutions and reasonably reliable reconstruction algorithms have been developed [154] in the presence of noise, it has not yielded any quantitative results on the probability of uniqueness for any given level of noise [201].

Despite the fact that solutions are in general not unique [31, 201], the ambiguity of the reconstructed phase can be substantially reduced using a number of observations [6] either at the sensor plane [7, 178] or diffraction patterns with spatial phase/amplitude modulations at the object plane [22, 241], what can be applied for both the reconstruction [106, 240] and synthesis [203]. It is recognized that a

[3] The common idea is always the same: replace the calculated amplitude at the observation plane by the measured one and modify the calculated object wave field.

[4] We refer to, e.g., [31, cf. Fig. 7] for more details. Note also than whether the objects are discrete or continuous, it is easy to make up cases that they are ambiguous. If, for instance, $c(x,y)$ and $d(x,y)$ are two functions of finite support with Fourier transforms $C(v_1,v_2)$ and $D(v_1,v_2)$, respectively, then the convolutions $q_1 = c(x,y) \circledast d(x,y)$ and $q_2 = c(x,y) \circledast d^*(-x,-y)$ are different objects as long as neither c nor d is conjugate centrosymmetric. They have Fourier transforms $Q_1(v_1,v_2) = C(v_1,v_2) \cdot D(v_1,v_2)$ and $Q_2(v_1,v_2) = C(v_1,v_2) \cdot D^*(v_1,v_2)$ that have the same modulus $|Q_1(v_1,v_2)| = |Q_2(v_1,v_2)| = |C(v_1,v_2)| \cdot |D(v_1,v_2)|$ and the objects q_1 and q_2 are therefore ambiguous.

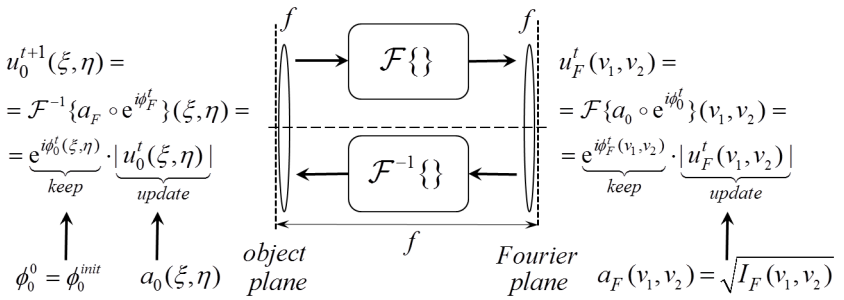

Figure 2.4: The scheme of the iterative error-reduction GS phase-retrieval algorithm [59, 238] and the optical setup for its implementation [138, 238]. Two lenses with the same focal distances f are arranged to provide accurate mapping of the object wave field u_0 into the Fourier plane giving the wave field $u_F(v_1,v_2) = \mathcal{F}\{u_0\}(v_1,v_2)$, $v_1 = \frac{k\xi}{f}$, $v_2 = \frac{k\eta}{f}$. The backward propagation is numerically calculated via the inverse Fourier transform. At each iteration ($t = 0, 1, ..$) the amplitude of the wave field at the object $a_0^t(\xi,\eta) = |u_0^t(\xi,\eta)|$ and the observation (Fourier) plane $a_F^{t+1}(v_1,v_2) = |u_F^{t+1}(v_1,v_2)|$ are updated by the prior information (e.g., $a_0(\xi,\eta) = 1$) or given measurements (typically $a_F = \sqrt{I_F}$, where I_F is the (noisy) intensity observation). The initial guess for the object phase ϕ_0^{init} is typically taken randomly. The multiplicative components connected with the Fourier transform in GS are omitted for simplicity.

proper choice of the initial guess and/or applying additional constraints/penalties can also be employed to improve the uniqueness of the solution, helps to overcome the convergence uncertainty, decrease the influence of the noise and, as the result, leads to better reconstruction quality. Here we wish also to mentioned that the problem with misalignments, say with the displacement of a sensor can be solved by, e.g., the recent work by M. Agour [3, 4].

It is recognized that the iterative multi-plane ($K > 2$ in Eq. (2.8)) phase-retrieval techniques are more flexible, effective (e.g., iteratively the misfocusing error may be compensated by aggregating of a number of estimates) and robust to a significantly large amount of noise in measurements with respect to deterministic approaches. Thus, *iterative phase retrieval is considered to be more productive for treating the phase problem**.

It is found [3, §4.1],[120] that the the complex-valued 3D wave field can be obtained by *four* intensity measurements of diffraction patterns, $K = 4$. It is, however, not sufficient in case of noise and possible (mechanical) distortions of the optical system. In contrast to the deterministic TIE based methods with a significantly large number of observation from $K = 3$ [217] up to $K = 80$ [223], the iterative phase-retrieval algorithms usually operate with 5–10 (including in our papers **P4**–**P7**), up to 20 [7, 8] intensity measurements.

Note also, that the distance between the sensor plane Δ_z in both the referred [7, 8] and our works [**P4**, cf. Fig. 3] is found experimentally. Rather we present our recommendations how to choose Δ_z depending on K and object size. Note that this distance does not necessarily have to be equal for all sensor planes. By using the concept of spatial correlation for wave fields at the sensor planes, for both their complex amplitude and the measured intensity of these fields, we can

infer, which planes are suitable to retrieve the phase and which are not [69, cf. Fig. 1] to choose proper distances between the sensor planes. The accurate choice of Δ_z is our further work.

2.4.3 Successive iterative multi-plane phase retrieval

Traditionally, the iterative phase-retrieval methods are used to reconstruct the volumetric wave field represented at a number of sensor planes. Let us describe the procedure of the whole wave field reconstruction, namely: the sequence of phase distributions $\{\phi_r\}_{r=1}^K$ associated with the individual propagation states through the captured volume. Let $u_r(x,y) = \sqrt{I_r(x,y)}\exp(i\phi_r(x,y))$, $r = 1,...K$, denote 2D transverse complex-valued wave field distributions at the observation planes with given (noisy) intensities $\{I_r(x,y)\}_{r=1}^K$. The index $_r$ corresponds to a distance $z_r = z_1 + (r-1)\cdot\Delta_z$ between the parallel object and the $r-th$ observation planes, Δ_z is a fixed distance between the observation planes. The optical setup of data acquisition is presented in Fig. 2.2. Then, the circular algorithm, where the volumetric wave field is reconstructed by wave field propagation from one measurement plane to another one (ignoring the object plane), can be written as follows

$$\hat{u}_{\chi(t+1)} = \mathcal{D}_{z_{\chi(t+1)}-z_{\chi(t)}}\left\{\sqrt{I_{\chi(t)}}\cdot\hat{u}_{\chi(t)}\cdot|\hat{u}_{\chi(t)}|^{-1}\right\},\ t = 1,2... \tag{2.12}$$

Let $\hat{u}_{\chi(1)} = \sqrt{I_{\chi(1)}}e^{\phi_{\chi(1)}}$ be the initial guess of the wave field distribution at the $\chi(1)$-th observation plane, which consists of the measured amplitude $I_{\chi(1)}$ and (for example) random phase $\phi_{\chi(1)}$. The subindex $\chi(t)$, $t = 1,2...$ shows the serial number of the observation plane, where the estimates of the wave field $\hat{u}_\chi(t)$ are calculated. Here $\mathcal{D}_{z_{\chi(t+1)}-z_{\chi(t)}}\{\cdot\}$ denotes an invertible operator of the wave field propagation from the $\chi(t)$-th to the $\chi(t+1)$-th observation plane, which may be represented via, e.g., ASD [7, 8, 178]. This operator represents[5] the forward wave field propagation to the distance $\Delta_z = |z_{\chi(t+1)} - z_{\chi(t)}|$ if $z_{\chi(t+1)} > z_{\chi(t)}$ or the backward propagation to the same distance if $z_{\chi(t+1)} < z_{\chi(t)}$, $z_{\chi(t+1)} \neq z_{\chi(t)}$. The operation in the curly brackets means a replacement of the amplitude of the calculated estimate at the $\chi(t)$-th sensor plane by the amplitude from the intensity observations, keeping the phase of the estimate $\hat{u}_{\chi(t)}$. The formula (2.12) defines the modern iterative circular algorithm known as the *single-beam multiple-intensity phase reconstruction* (SBMIR, [7, 8, 178]) algorithm used in our works **P3**–**P5**, **P7** as a reference method.

There is no specific rule determining the sequence of the sensor planes in a set. For instance, the index of the sensor plane in a sequence for the so-called forward-forward (FF, from the K-th to the first sensor plane) and forward-backward (FB, from the K-th to the $(K-1)$-th sensor plane) algorithms (see [8, cf. Fig. 2]) can be found as follows:

$$\chi(t) = \begin{cases} \alpha_K(t), & \text{for FF} \\ \alpha_{2K-2}(t) - 2\alpha_K(\alpha_{2K-2}(t))\beta_K(\alpha_{2K-2}(t)), & \text{for FB,} \end{cases} \tag{2.13}$$

[5] Evidently $\mathcal{D}_{z_1\pm z_2}\{\cdot\} = \mathcal{D}_{z_1}\{\mathcal{D}_{\pm z_2}\{\cdot\}\} = \mathcal{D}_{\pm z_2}\{\mathcal{D}_{z_1}\{\cdot\}\}$, thus $\mathcal{D}_{z_1-z_2}\{\cdot\}$ can be considered as the backward propagation to the distance z_2 and then forward propagation to z_1.

where $\alpha_K(t) = \mathrm{mod}(t-1, K) + 1$ and $\beta_K(t) = \lfloor (t-1)/K \rfloor$, where $\mathrm{mod}(t, K)$ means t modulo K. Recall $\lfloor \cdot \rfloor$ denotes the floor operation.

2.4.4 Parallel iterative multi-plane phase retrieval

Despite the widespread use of the phase-retrieval algorithms by Gerchberg, Saxton, Misell and Fienup, current mathematical theory cannot satisfactorily explain their remarkable success: in this case we deal with a nonconvex nonsmooth optimization problem [26, 140, 164]. It is shown that these algorithms can be identified as an alternating projections [17, 18, 49, 136, 144, 164] both to the image and object planes. This interpretation gives an opportunity to design novel phase-retrieval algorithms with flexible use of extra prior information on measurements and reconstructed distributions. In particular, there are a variety of papers, where the variational formulation of the phase-retrieval problem is used, e.g., the wave field reconstruction is framed as a nonlinear optimization with minimizing of a relative entropy [28, 40, 164].

Assuming that the measurement noise at the sensor plane observations is zero-mean Gaussian we formulate the phase-retrieval problem as the variational (constrained) optimization problem in terms of the maximum log-likelihood approach. In our works **P3**–**P7** we introduce novel parallel phase-retrieval procedures focused on the object plane what is different comparing with the successive SBMIR algorithm. If the wave field operator $\mathcal{D}_{z_r}\{\cdot\}$ is defined, e.g., by the invertible ASD, the parallel algorithm originated in **P3** is of the form

$$u_r^t = \mathcal{D}_{z_r}\{u_0^t\}, \quad \text{for } r = 1, \ldots K, \ t = 1, 2, \ldots \tag{2.14}$$
$$u_0^t = \frac{1}{K} \sum_{r=1}^{K} \mathcal{D}_{z_r}^{-1} \left\{ \sqrt{I_r} \cdot u_r^t \cdot |u_r^t|^{-1} \right\},$$

where, similar to Eq. (2.12), the operation in the curly brackets stands (again) for the replacement of the calculated amplitude of the sensor plane wave fields u_r^t by the measured $\sqrt{I_r}$ keeping the phase unchanged. This scheme allows aggregating a number of object estimates and filtering out the noise, as well as incorporating a priori information on the object. The significant point of **P3** is the use of the novel discrete diffraction transform for the forward/backward wave field propagation modeling and additional filtering of the object estimate [34]. Following [40] in the further papers we use the intensity (squared amplitude), instead of the amplitude, in the optimization criteria to avoid the mathematical difficulties inherent with the amplitude function. In **P4** we care about both the accuracy of the calculation of the complex-valued estimates at the sensor plane and fitting of the computed $|u_r^t|^2$ to the measured intensities I_r. It is realized using the optimization of the augmented Lagrangian criterion. The use of a priori information on the object is presented in **P5** by the developed modifications of the phase-retrieval algorithms constructed especially for the amplitude- and phase-only objects to be reconstructed. Since the quality of the object reconstructions from experimental data are generally poor, we apply sparse object regularization to enhance the imaging quality: **P6** and [149] are devoted to an improvement of imaging with an incorporated filtering separately both the object amplitude and phase.

The conventional phase-retrieval techniques are mainly based on an ideal wave field propagation modeling. In practice, wave fields in real coherent imaging systems and their observations are different from those predicted by theory due to non-idealities of optical system (misalignment, misfocusing, aberrations), dust on optical elements, reflections, vibration and so on. Hence, the propagation operators $\mathcal{D}_{z_r}\{\cdot\}$ can not fully describe the propagation through the real optical path, and the wave field reconstructions obtained by numerical simulations (i.e. theoretical results) and using real experimental data can be dramatically different. There are many various numerical approaches, which are used for calibration [227], filtering parasitic reflections [33], compensating for curvature introduced by microscope objective [175], for aberrations [242] or astigmatism [84]. However, the sources of different distortions in the optical path are hard to localize and specify. In **P7** we do not even try to identify these particular sources but estimate and compensate their accumulated effects. In other words, we assumed that there is a *generalized pupil function* [79, §6.4.1] at the object plane which describes distortions in the coherent imaging system manifested at the sensor plane, and this cumulative disturbance of the light wave field in the optical path can be recalculated to the entrance pupil of the optical system (in particular, of the 4f configuration). We refer to the cumulative distortions as "background" disturbances. Thus, in our work this background is estimated and compensated in order to achieve sharp imaging of the investigating object. Moreover, we also incorporate some prior information on the true object wave field to enhance the reconstruction quality: in **P7** the reconstruction of a binary object with unknown lower and upper levels using such a background compensation and object sparse modeling is presented.

Chapter 3

Discrete diffraction transform (DDT)

The Rayleigh–Sommerfeld diffraction integral can not be solved analytically, except for very few situations, and in most practical applications the integral can be calculated only numerically. In general, the RS diffraction formula is not widely used – usually one computes the result of the light diffraction by its Fresnel approximation [158]. In this Chapter we consider the discrete diffraction propagation model based on the Fresnel approximation and describe its modifications with averaging within pixels of the discrete object and sensor wave field distributions resulting in an accurate pixel-to-pixel modeling of the diffraction propagation.

Following the notations in Sections 2.1, $u_0(\xi,\eta)$ and $u_z(x,y) = \mathcal{D}_z\{u_0\}(x,y)$ denote transverse complex amplitudes at the object and measurement (sensor) planes, respectively, as it is illustrated in Fig. 2.1. Numerical computations require discrete data of finite size, hence the integrals are discretized over the finite support of integration [221], within the region where $u_0(\xi,\eta) \neq 0$ (region S in Eq. (1.54) and Fig. 1.9): in particular, the object $u_0(\xi,\eta)$ is assumed to be localized in a rectangular of the size $N_\xi\Delta_\xi \times N_\eta\Delta_\eta$. For discrete modeling, the continuous arguments are replaced by the digital ones with a corresponding replacement of the continuous functions by their discrete counterparts: $u_0(\xi,\eta) \to u_0[l] = u_0(l_1\Delta_\xi, l_2\Delta_\eta)$, $u_z(x,y) \to u_z[l'] = u_z(l'_1\Delta_x, l'_2\Delta_y)$, $u_F(\frac{v_1}{\lambda f}, \frac{v_2}{\lambda f}) \to u_F[n] = u_F(\frac{\Delta_1}{\lambda f}n_1, \frac{\Delta_2}{\lambda f}n_2)$ with 2D integer arguments. Different variables $l = (l_1, l_2)$, $n = (n_1, n_2)$ and $l' = (l'_1, l'_2) \in \mathbb{Z}^2$ are chosen for the object, Fourier and sensor domains, respectively. This discretization is dictated by the use of digital devices such as a CCD sensor or a pixelated SLM as a 2D array of liquid crystal cells. Thus, we hereafter consider the discrete wave fields at the object $u_0[l]$, Fourier $u_F[n]$ and sensor planes $u_z[l']$ with pixel (pitch) sizes $\Delta_\xi \times \Delta_\eta$, $\Delta_1 \times \Delta_2$ and $\Delta_x \times \Delta_y$, respectively, and the corresponding supports $N_\xi \times N_\eta$, $N_1 \times N_2$ and $N_x \times N_y$, respectively. In general, u_0, u_F and u_z are of different image and pixel size.

It should be mentioned that in this thesis and in all our publications (in **P1**–**P7** and [112, 114, 115, 149]) we consider the discrete object wave field distribution in the form (cf. Eq. (1.20))

$$\mathbf{u}_0 = \mathbf{a}_0 \circ \exp(i\boldsymbol{\phi}_0), \tag{3.1}$$

where $\mathbf{a}_0 = |\mathbf{u}_0|$ is the vector of the object amplitude and $\boldsymbol{\phi}_0$ is the vector of the object phase, $\boldsymbol{\phi}_0 = \arg\{\mathbf{u}_0\}$. The amplitude modulation (AM) of the object means that the phase $\boldsymbol{\phi}_0[l] = 0\ \forall l$ and the amplitude is defined by the vectorized test-image $0 < \mathbf{c}[l] \leq 1$, i.e. $\mathbf{u}_0 = \mathbf{c}$. In our experiments we use *chessboard*, *logo*, *Lena* or *Baboon* test-images as $\mathbf{c}$. Analogically the phase modulation (PM) of the object is represented by the phase only: the amplitude is constant, in particular $\mathbf{a}_0[l] = 1\ \forall l$, and the object phase vector is defined by the vectorized test-image as $\mathbf{u}_0 = \exp(i\pi(\mathbf{c} - \frac{1}{2}))$.

Since the phase estimate $\widehat{\boldsymbol{\phi}}_0$ from the intensity measurements can be obtained up to an arbitrary constant only, the RMSE or PSNR values for the object phase are calculated for $\widetilde{\boldsymbol{\phi}}_0 = (\widehat{\boldsymbol{\phi}}_0 - \mathrm{mean}(\widehat{\boldsymbol{\phi}}_0 - \boldsymbol{\phi}_0)) - \boldsymbol{\phi}_0$ in order to eliminate this phase ambiguity. Here $\mathrm{mean}(\widehat{\boldsymbol{\phi}}_0 - \boldsymbol{\phi}_0)$ stands for the mean value of the estimation error calculated over the test-image $\boldsymbol{\phi}_0$.

Evidently, we have no absolute phase and $\arg\{\widehat{\mathbf{u}}_0\}$ gives the wrapped object phase estimate. However, in this text the estimate of the object phase is considered to be localized in the interval $[-\pi, \pi)$ and not exceeding π by its absolute value. The issues related to phase unwrapping and phase singularities are beyond the scope of this thesis.

3.1 Discrete modeling of diffraction propagation

It is straightforward to obtain digital models for the forward/backward wave field propagations by taking the Riemann sums instead of the integrals in the diffraction transforms mentioned in Section 2.2. Following the well-known Whittaker–Nyquist–Kotelnikov–Shannon theorem the transformation of Eqs. (2.1)–(2.2) into a discrete convolution is correct, if at least one of the integrands in the continuous convolution is bandlimited [168]. According to Eq. (1.23) the Fourier spectrum of $u(x, y, z)$ is supported on a sphere of radius $2\pi/\lambda$ and hence $u_0(\xi, \eta)$ is bandlimited to $k = 2\pi/\lambda$. The principal difficulty of discretization in the space domain follows from the fact that the diffraction kernel is modulated by a high-frequency harmonic component. The required sampling rate, governed by the Nyquist sampling rate is unacceptably too high for practical purposes: in our case λ is significantly small, say $\lambda = 532nm$. Fortunately, we have an attractive alternative in the frequency domain. Firstly, it follows from Eqs. (1.48), (1.67) that for $|v_1| \ll 1/\lambda$ and $|v_2| \ll 1/\lambda$ the phase $\phi = \frac{2\pi z}{\lambda}\sqrt{1 - \lambda^2(v_1^2 + v_2^2)} \approx \frac{2\pi z}{\lambda} - \pi z\lambda(v_1^2 + v_2^2)$ is slowly varying in v_1 and v_2 [111]. Secondly, for the object and sensor planes of finite support, the convolution in Eqs. (2.1)–(2.2) involves only a sub-range of the full support of a_z whose size equals to the sum of the supports of these planes [167, 221]. Since no components of a_z for large radial distances are required[1], thus the impulse response can be sampled with respect to the involved bandwidth, and the convolutions – discretized [221].

The discrete convolutional models as sampled versions of the formulas (2.1)–(2.2) are of the following form:

[1] In case of the Fresnel approximation, it is also mentioned that the high-frequency details of the sensor wave field are lost.

$$u_z(l'_1\Delta_x, l'_2\Delta_y) = \sum_{l_1,l_2} u_0(l_1\Delta_\xi, l_2\Delta_\eta)\cdot a_z(l'_1\Delta_x - l_1\Delta_\xi, l'_2\Delta_y - l_2\Delta_\eta)\cdot \Delta_\xi\Delta_\eta, \quad (3.2)$$

$$\widehat{u}_0(l_1\Delta_\xi, l_2\Delta_\eta) = \sum_{l'_1,l'_2} u_z(l'_1\Delta_x, l'_2\Delta_y)\cdot a_{-z}(l_1\Delta_\xi - l'_1\Delta_x, l_2\Delta_\eta - l'_2\Delta_y)\cdot \Delta_x\Delta_y, \quad (3.3)$$

where the hat in $\hat{u}_0$ means an estimate of u_0. These formulas are valid for arbitrary parameter values, i.e. for any size of the object and diffraction planes and the pixels at these planes. In particular, the discrete Fresnel transform ($a_z = g_z$) for the forward and backward wave field propagation can be represented using the discrete convolution in the follows matrix form [**P1**, cf. Eqs. (15)–(16)]

$$\mathbf{U}_z = \Delta_\eta\Delta_\xi \cdot \mathbf{C}_x \cdot \mathbf{U}_0 \cdot \mathbf{C}_y^T, \quad (3.4)$$

$$\widehat{\mathbf{U}}_0 = \Delta_x\Delta_y \cdot \mathbf{C}_x^H \cdot \mathbf{U}_z \cdot \mathbf{C}_y^*, \quad (3.5)$$

where $\mathbf{C}_y = (\mathbf{C}_y[l'_2, l_2])_{N_y\times N_\eta}$, $\mathbf{C}_x = (\mathbf{C}_x[l'_1, l_1])_{N_x\times N_\xi}$ are the Fresnel transform matrices calculated according to

$$\mathbf{C}_x[l'_1, l_1] = \frac{e^{\frac{i\pi z}{\lambda}}}{\sqrt{i\lambda z}} \exp\left(\frac{i\pi}{\lambda z}(l'_1\Delta_x - l_1\Delta_\xi)^2\right), \quad (3.6)$$

$$\mathbf{C}_y[l'_2, l_2] = \frac{e^{\frac{i\pi z}{\lambda}}}{\sqrt{i\lambda z}} \exp\left(\frac{i\pi}{\lambda z}(l'_2\Delta_y - l_2\Delta_\eta)^2\right). \quad (3.7)$$

Following **P1**, we call the transforms defined by Eq. (3.4) and Eq. (3.5) *Matrix Discrete Fresnel Transform* (M–DFrT) and *Matrix Inverse Discrete Fresnel Transform* (M–IDFrT), respectively.

3.2 Forward DDT with averaging

Let us assume that the input of our model is defined by a pixelwise constant distribution what may be determined, e.g., by an SLM with 100% fill factor of pixels; and the output is also discrete defined by the outputs of the (CCD) sensor pixels. Here we introduce the forward discrete diffraction transform (DDT) for such pixelwise invariant distributions which enables an accurate *discrete-to-discrete* modeling due to the precise integration in Eq. (2.1).

Let the 2D discrete wave field distributions at the object u_0 and observation/sensor u_z planes of the size $N_\xi \times N_\eta$ and $N_x \times N_y$ be pixelwise constant within the rectangular pixels $\Delta_\xi \times \Delta_\eta$ and $\Delta_x \times \Delta_y$, respectively. Then, taking into account Eq. (3.2), the integral (2.1) can be represented in the form

$$u_z(x,y) = \quad (3.8)$$

$$= \sum_{l_1=-N_\xi/2}^{N_\xi/2-1} \sum_{l_2=-N_\eta/2}^{N_\eta/2-1} u_0[l_1,l_2] \int_{-\Delta_\xi/2}^{\Delta_\xi/2} \int_{-\Delta_\eta/2}^{\Delta_\eta/2} a_z(x - l_1\Delta_\xi + \xi, y - l_2\Delta_\eta + \eta)d\xi d\eta,$$

$$u_0[l_1,l_2] = u_0(l_1\Delta_\xi + \xi, l_2\Delta_\eta + \eta), \quad |\eta| \le \Delta_\eta/2,\ |\xi| \le \Delta_\xi/2,$$

i.e. the integration is performed within each pixel of the object wave field assumed to be pixelwise constant, and the sum is calculated over $N_\xi \times N_\eta$ pixels of the input rectangular array. Let the output of a sensor pixel be the mean value of the distribution impinging on this pixel (averaging within sensor pixels)

$$u_z[l'_1, l'_2] = \frac{1}{\Delta_x \Delta_y} \int\limits_{-\Delta_x/2}^{\Delta_x/2} \int\limits_{-\Delta_y/2}^{\Delta_y/2} u_z(l'_1 \Delta_x + \xi', l'_2 \Delta_y + \eta') d\xi' d\eta'. \tag{3.9}$$

Inserting Eq. (3.8) into Eq. (3.9) we arrive at the following spatial domain DDT

$$u_z[l'_1, l'_2] = \sum\nolimits_{l_1=-N_\xi/2}^{N_\xi/2-1} \sum\nolimits_{l_2=-N_\eta/2}^{N_\eta/2-1} d_z[l'_1, l_1; l'_2, l_2] \cdot u_0[l_1, l_2], \tag{3.10}$$
$$l'_1 = -N_x/2, ..., N_x/2 - 1,\ l'_2 = -N_y/2, ..., N_y/2 - 1$$

with the diffraction kernel $d_z[l'_1, l_1; l'_2, l_2]$ calculated as

$$d_z[l'_1, l_1; l'_2, l_2] = \frac{1}{\Delta_x \Delta_y} \int\limits_{-\Delta_x/2}^{\Delta_x/2} \int\limits_{-\Delta_\xi/2}^{\Delta_\xi/2} d\xi d\xi' \times \tag{3.11}$$
$$\int\limits_{-\Delta_y/2}^{\Delta_y/2} \int\limits_{-\Delta_\eta/2}^{\Delta_\eta/2} a_z(l'_1 \Delta_x - l_1 \Delta_\xi + \xi' + \xi, l'_2 \Delta_y - l_2 \Delta_\eta + \eta' + \eta) d\eta d\eta',$$
$$l'_1 = -N_x/2, ..., N_x/2 - 1,\ l_1 = -N_\xi/2, ..., N_\xi/2 - 1,$$
$$l'_2 = -N_y/2, ..., N_y/2 - 1,\ l_2 = -N_\eta/2, ..., N_\eta/2 - 1.$$

The kernel d_z in Eq. (3.11) is an averaged (pixelwise double-averaged) version of the original kernel a_z in Eq. (2.1): the smoothing in Eq. (3.11) takes into consideration discretization for both the object and sensor arrays. For the Fresnel diffraction kernel $a_z = g_z$ the kernel d_z allows the following factorization

$$d_z[l'_1, l_1; l'_2, l_2] = \mathbf{A}_x[l'_1, l_1] \cdot \mathbf{A}_y[l'_2, l_2], \tag{3.12}$$

where

$$\mathbf{A}_x[l'_1, l_1] = \tag{3.13}$$
$$\frac{e^{\frac{i\pi z}{\lambda}}}{\Delta_x \sqrt{i\lambda z}} \int\limits_{-\Delta_x/2}^{\Delta_x/2} \int\limits_{-\Delta_\xi/2}^{\Delta_\xi/2} \exp\left(\frac{i\pi}{\lambda z}(l'_1 \Delta_x - l_1 \Delta_\xi + \xi' + \xi)^2\right) d\xi d\xi',$$
$$\mathbf{A}_y[l'_2, l_2] = \tag{3.14}$$
$$\frac{e^{\frac{i\pi z}{\lambda}}}{\Delta_y \sqrt{i\lambda z}} \int\limits_{-\Delta_y/2}^{\Delta_y/2} \int\limits_{-\Delta_\eta/2}^{\Delta_\eta/2} \exp\left(\frac{i\pi}{\lambda z}(l'_2 \Delta_y - l_2 \Delta_\eta + \eta' + \eta)^2\right) d\eta d\eta'$$

represent the transform matrices with respect to rows and columns, respectively.

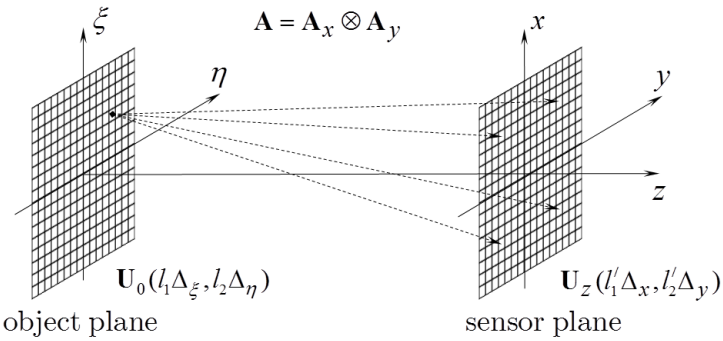

Figure 3.1: Principal setup of a discrete-to-discrete wave field propagation model. Here $\mathbf{U}_0$ and $\mathbf{U}_z$ denotes the discrete object and sensor plane 2D wave field distributions. The accurate link between them is given by $\mathrm{vec}\{\mathbf{U}_z\} = (\mathbf{A}_x \otimes \mathbf{A}_y) \cdot \mathrm{vec}\{\mathbf{U}_0\}$, where transform matrices $\mathbf{A}_x$ and $\mathbf{A}_y$ manipulate rows and columns of the input matrix $\mathbf{U}_0$, respectively.

3.2.1 Two-matrix DDT (M–DDT)

Inserting (3.12) into (3.10) we arrive at

$$\mathbf{U}_z[l'_1, l'_2] = \sum_{l_1=-N_\xi/2}^{N_\xi/2-1} \sum_{l_2=-N_\eta/2}^{N_\eta/2-1} \mathbf{A}_x[l'_1, l_1] \cdot \mathbf{U}_0[l_1, l_2] \cdot \mathbf{A}_y[l_2, l'_2], \tag{3.15}$$

what defines the matrix form of the discrete input–output forward propagation model

$$\mathbf{U}_z = \mathbf{A}_x \cdot \mathbf{U}_0 \cdot \mathbf{A}_y^T. \tag{3.16}$$

Let $\mathbf{u}_0 = \mathrm{vec}\{\mathbf{U}_0\}$ and $\mathbf{u}_z = \mathrm{vec}\{\mathbf{U}_z\}$ denote the column vectors constructed by vectorization of the discrete wave field distributions at the object and sensor planes [99]. Then, Eq. (3.16) can be rewritten in even more compact form

$$\mathbf{u}_z = \mathbf{A} \cdot \mathbf{u}_0, \quad \mathbf{A} = \mathbf{A}_x \otimes \mathbf{A}_y, \tag{3.17}$$

where the vectors $\mathbf{u}_z$ and $\mathbf{u}_0$ have the lengths $\#\mathbf{u}_z = N_x \cdot N_y$ and $\#\mathbf{u}_0 = N_\xi \cdot N_\eta$, respectively, and the transform matrix $\mathbf{A} \in \mathbb{C}^{N_x N_y \times N_\xi N_\eta}$.

The formulas (3.16)–(3.17) define what we call the *Matrix Discrete Diffraction Transform* ($\mathcal{M} - \mathcal{DDT}$) with so-called *averaged* matrices $\mathbf{A}_x$ (Eq. (3.13)) and $\mathbf{A}_y$ (Eq. (3.14)). In Fig. 3.1 a discrete-to-discrete wave field propagation model described in terms of M–DDT is illustrated.

3.2.2 Simplification of M–DDT

Let the pixels' sizes be so small that the averaging in the forward propagation integrals (3.11) is not essential. Then the diffraction transform kernel can be calculated significantly simpler. The corresponding matrices with no averaging are denoted by $\mathbf{B}_y$ and $\mathbf{B}_x$, respectively, and defined as follows

$$\mathbf{B}_x[l'_1, l_1] = \lim_{\Delta_\xi, \Delta_x \to 0} \mathbf{A}_x[l'_1, l_1] = \tag{3.18}$$

$$= \frac{\Delta_\xi e^{\frac{i\pi z}{\lambda}}}{\sqrt{i\lambda z}} \exp\left(\frac{i\pi}{\lambda z}(l'_1\Delta_x - l_1\Delta_\xi)^2\right) = \Delta_\xi \cdot \mathbf{C}_y[l'_1, l_1],$$

$$l'_1 = -N_x/2, ..., N_x/2 - 1, \quad l_1 = -N_\xi/2, ..., N_\xi/2 - 1,$$

$$\mathbf{B}_y[l'_2, l_2] = \lim_{\Delta_\eta, \Delta_y \to 0} \mathbf{A}_y[l'_2, l_2] = \tag{3.19}$$

$$= \frac{\Delta_\eta e^{\frac{i\pi z}{\lambda}}}{\sqrt{i\lambda z}} \exp\left(\frac{i\pi}{\lambda z}(l'_2\Delta_y - l_2\Delta_\eta)^2\right) = \Delta_\eta \cdot \mathbf{C}_y[l'_2, l_2],$$

$$l'_2 = -N_y/2, ..., N_y/2 - 1, \quad l_2 = -N_\eta/2, ..., N_\eta/2 - 1,$$

where $\mathbf{C}_x$ and $\mathbf{C}_y$ are calculated according to Eqs. (3.6)–(3.7). The relations

$$\mathbf{B}_x = \Delta_\xi \cdot \mathbf{C}_x, \quad \mathbf{B}_y = \Delta_\eta \cdot \mathbf{C}_y \tag{3.20}$$

mean that within the scalar factors Δ_ξ and Δ_η the matrices $\mathbf{B}_x$ and $\mathbf{B}_y$ are identical to the matrices of M–DFrT $\mathbf{C}_x$ and $\mathbf{C}_y$. $\mathbf{B}_x$ and $\mathbf{B}_y$ are called the *non-averaged* matrices in order to emphasize that the averaging effect is omitted.

The kernel $d_z[l'_1, l_1; l'_2, l_2]$ in Eq. (3.11) becomes shift-invariant and depends on the differences of the arguments $l'_1 - l_1$ and $l'_2 - l_2$ as soon as the pixels at the object and sensor planes take equal sizes, $\Delta_\xi = \Delta_x$ and $\Delta_\eta = \Delta_y$. In this particular case M–DDT is essentially simpler to calculate because the transform matrices in Eqs. (3.14)–(3.13) are symmetrical with respect to the differences of indices: $\mathbf{A}_y[l'_2, l_2] = \mathbf{A}_y[l'_2 - l_2] = \mathbf{A}_y[l_2 - l'_2]$, $\mathbf{A}_x[l'_1, l_1] = \mathbf{A}_x[l'_1 - l_1] = \mathbf{A}_x[l_1 - l'_1]$. If $\Delta_\eta = \Delta_y = \Delta_x = \Delta_\xi$ and $N_x = N_\xi = N_y = N_y$, then $\mathbf{A}_x = \mathbf{A}_y$ and only one transform matrix in Eq. (3.16) is required.

If the pixel and image at the object and sensor planes are, in general, rectangular of the same size, i.e. $\Delta_\eta = \Delta_y = \Delta_a$, $\Delta_x = \Delta_\xi = \Delta_b$ and $N_x = N_\xi$, $N_y = N_y$, then Eqs. (3.10) and (3.11) can be simplified as follows

$$u_z[l'_1, l'_2] = \sum_{l_1=-N_\xi/2}^{N_\xi/2-1} \sum_{l_2=-N_\eta/2}^{N_\eta/2-1} d_z[l'_1 - l_1, l'_2 - l_2] \cdot u_0[l_1, l_2], \tag{3.21}$$

$$l'_1 = -N_x/2, ..., N_x/2 - 1, \; l'_2 = -N_y/2, ..., N_y/2 - 1,$$

where d_z here is a large diffraction transform matrix defined as follows

$$d_z[l_1, l_2] = \frac{1}{\Delta_a \Delta_b} \iint_{-\Delta_a/2}^{\Delta_a/2} \iint_{-\Delta_b/2}^{\Delta_b/2} a_z(l_1\Delta_a + \xi' + \xi, l_2\Delta_b + \eta' + \eta) d\xi d\xi' d\eta d\eta', \tag{3.22}$$

$$l_1 = -\frac{N_\xi + N_x}{2} + 1, ..., \frac{N_\xi + N_x}{2} - 1, \quad l_2 = -\frac{N_\eta + N_y}{2} + 1, ..., \frac{N_\eta + N_y}{2} - 1.$$

Note that the support of d_z in Eq. (3.22) is larger comparing with what we have in Eq. (3.11). Moreover, for the Fresnel diffraction kernel $a_z = g_z$ of such an enlarger size, d_z allows the following factorization [111, cf. Eqs. (23), (24)]

$$d_z[l_1, l_2] = \rho_z[l_1] \cdot \rho_z[l_2], \quad \text{where}$$

$$\rho_z[l_1] = \frac{e^{\frac{i\pi z}{\lambda}}}{\Delta_a\sqrt{i\lambda z}} \iint\limits_{-\Delta_a/2}^{\Delta_a/2} \exp\left(\frac{i\pi}{\lambda z}(l_1\Delta_a + \xi' + \xi)^2\right) d\xi d\xi' = \tag{3.23}$$

$$= \frac{\Delta_a e^{\frac{i\pi z}{\lambda}}}{\sqrt{i\lambda z}} \int\limits_{-1}^{1} (1-|\alpha|) \exp\left(\frac{i\pi}{\lambda z}(l_1\Delta_a + \alpha\Delta_a)^2\right) d\alpha,$$

$$\rho_z[l_2] = \frac{e^{\frac{i\pi z}{\lambda}}}{\Delta_b\sqrt{i\lambda z}} \iint\limits_{-\Delta_b/2}^{\Delta_b/2} \exp\left(\frac{i\pi}{\lambda z}(l_2\Delta_b + \eta' + \eta)^2\right) d\eta d\eta' = \tag{3.24}$$

$$= \frac{\Delta_b e^{\frac{i\pi z}{\lambda}}}{\sqrt{i\lambda z}} \int\limits_{-1}^{1} (1-|\beta|) \exp\left(\frac{i\pi}{\lambda z}(l_2\Delta_b + \beta\Delta_b)^2\right) d\beta.$$

The proof that the double integral in Eqs. (3.23)–(3.24) can be calculated as a single integral is given in [111, Appendix B] and [**P1**, Appendix A].

3.2.3 Double size frequency domain DDT (F–DDT)

It can be shown [111, Appendix 1], that the convolution (3.21) can be solved in the frequency domain via the fast Fourier transform (FFT), but in this case the support of the kernel d_z is equal to $(N_\xi + N_x - 1) \times (N_\eta + N_y - 1)$. To make FFT applicable, zero-padding of $\mathbf{U}_0$ and $\mathbf{U}_z$ is required (see, e.g., [196]) to extend their size and cover the support of the kernel.

The DDT model with averaged matrices and the above mentioned simplification (Eqs. (3.23)–(3.24)) realized using DFT/FFT is called *Frequency domain Discrete Diffraction Transform* ($\mathcal{F}-\mathcal{DDT}$). It is originated in [111] and computed according to the following algorithm:

- calculate the Fourier transform of $\mathbf{U}_0$ zero-padded to the size $N_a \times N_b$, where $N_a = N_\xi + N_x - 1$, $N_b = N_\eta + N_y - 1$ as

$$\mathbf{\Pi}_0[n_1, n_2] = F\{\mathrm{ZP}_{(N_x-1)\times(N_y-1)}\{\mathbf{U}_0\}\}[n_1, n_2]; \tag{3.25}$$

- calculate the extended Fourier image of the discrete wave field at the sensor plane

$$\mathbf{\Pi}_z[n_1, n_2] = \mathbf{M}_z[n_1, n_2] \cdot \mathbf{\Pi}_0[n_1, n_2], \tag{3.26}$$

  where $n_1 = -N_a/2, \ldots N_a/2 - 1$, $n_2 = -N_b/2, \ldots N_b/2 - 1$ and

$$\mathbf{M}_z[n_1, n_2] = F\{d_z\}[n_1, n_2], \tag{3.27}$$

  is the "averaged" DDT transfer function (a discrete optical mask in the Fourier domain) of the extended size calculated by 2D FFT of Eq. (3.22);

- calculate the sensor plane $\mathbf{U}_z$ of the original size $N_x \times N_y$ as

$$\mathbf{U}_z[l_1', l_2'] = F^{-1}\{\mathbf{\Pi}_z\}[l_1', l_2'], \tag{3.28}$$
$$l_1' = -N_x/2, \ldots, N_x/2 - 1, \quad l_2' = -N_y/2, \ldots, N_y/2 - 1.$$

Note that for small pixels' sizes the kernel smoothing effect in Eq. (3.23)–(3.24) becomes negligible and instead of Eq. (3.22) we arrive at the simple formula [111, cf. Eq. (14)]

$$d_z[l_1,l_2] \underset{\Delta_a,\Delta_b\to 0}{\longrightarrow} \Delta_a\Delta_b \cdot g_z(l_1\Delta_a, l_2\Delta_b). \tag{3.29}$$

If the diffraction kernel d_z used in Eq. (3.27) is defined according to the simplification (3.29), then the resulting $\mathbf{M}_z$ in Eq. (3.26) is called the non-averaged F–DDT transfer function.

It is found that for the same pixel and image sizes at the object and sensor planes F–DDT (3.25)–(3.28) and M–DDT (3.16) give the same result of the forward diffraction propagation $\mathbf{U}_z$. F–DDT is computationally faster, but the M–DDT model is more flexible because it is valid for arbitrary settings of the optical setup. Moreover, in contrast to F–DDT, M–DDT does not require zero-padding for the accurate calculation.

3.3 Sampling conditions

Traditionally the discrete models of the free space diffraction propagation are considered as *approximation* for underlying continuous ones given in continuous variables and in integral forms (see Section 2.2). In particular, the discrete model of Eq. (1.60) and Eq. (2.6) for the Fresnel approximation $a_z = g_z$ can be represented as follows

$$u_z\left(l_1'\frac{\Delta_x}{\lambda z}, l_2'\frac{\Delta_y}{\lambda z}\right) = \frac{e^{ikz}}{i\lambda z} e^{\frac{i\pi}{\lambda z}((l_1'\Delta_x)^2+(l_2'\Delta_y)^2)}\Delta_\xi\Delta_\eta \times \tag{3.30}$$
$$\times \sum_{l_1,l_2} u_0(l_1\Delta_\xi, l_2\Delta_\eta)\cdot e^{\frac{i\pi}{\lambda z}((l_1\Delta_\xi)^2+(l_2\Delta_\eta)^2)} e^{-i2\pi(l_1l_1'\frac{\Delta_\xi\Delta_x}{\lambda z}+l_2l_2'\frac{\Delta_\eta\Delta_y}{\lambda z})},$$

$$\widehat{u}_0(l_1\Delta_\xi, l_2\Delta_\eta) = \frac{e^{-ikz}}{-i\lambda z} e^{\frac{-i\pi}{\lambda z}((l_1\Delta_\xi)^2+(l_2\Delta_\eta)^2)}\Delta_x\Delta_y \times \tag{3.31}$$
$$\times \sum_{l_1',l_2'} u_z\left(l_1'\frac{\Delta_x}{\lambda z}, l_2'\frac{\Delta_y}{\lambda z}\right)\cdot e^{\frac{-i\pi}{\lambda z}((l_1'\Delta_x)^2+(l_2'\Delta_y)^2)} e^{i2\pi(l_1l_1'\frac{\Delta_\xi\Delta_x}{\lambda z}+l_2l_2'\frac{\Delta_\eta\Delta_y}{\lambda z})}.$$

The sampling and aliasing issues are of importance for these approximations as they define preconditions for reconstruction of continuous signals from sampled ones [111]. The motivation for the above mentioned DDT models is different: for the pixelwise constant wave field distributions at the object and sensor plane the constructed discrete-to-discrete model is precise as the accurate integration of diffraction propagation (2.1) is assumed. In this development the standard assumptions concerning the sampling and bandlimitedness can be omitted as they are replaced by the hypothesis that the object plane distribution is piecewise constant or well approximated by this sort of distribution.

Note that Eqs. (3.2)–(3.3) (or, in particular, Eqs. (3.30)–(3.31)) are valid for arbitrary parameter values, but even if the diffraction kernel a_z is invertible, the perfect reconstruction in Eq. (3.3) is not guaranteed, i.e., in general, $\widehat{u}_0 \neq u_0$. We

are looking for such a condition, which results in the inversion

$$\widehat{u}_0[l_1'', l_2''] = \sum_{l_1, l_2} u_0[l_1, l_2] \times \tag{3.32}$$
$$\times \underbrace{\sum_{l_1', l_2'} a_{-z}[l_1'' - l_1', l_2'' - l_2'] \cdot a_z[l_1' - l_1, l_2' - l_2] \cdot \Delta_x \Delta_\xi \Delta_y \Delta_\eta}_{\delta_{l_1'', l_1} \cdot \delta_{l_2'', l_2}}$$

providing the perfect reconstruction $\widehat{u}_0[l_1'', l_2''] = u_0[l_1'', l_2'']$. Here δ_{l_1'', l_1}or δ_{l_2'', l_2} denotes the Kronecker delta (8).

Suppose the discrete wave field distributions at the object and sensor planes are of the same size $N_x \times N_y$. It can be seen [125, 236] that provided the *sampling condition* [**P1**, cf. Eqs. (11)]

$$\Delta_x \Delta_\xi N_x = \lambda \cdot z, \qquad \Delta_\eta \Delta_y N_y = \lambda \cdot z, \tag{3.33}$$

Eqs. (3.30)–(3.31) can be rewritten via DFTs as follows

$$u_z\left(l_1' \frac{\Delta_x}{\lambda z}, l_2' \frac{\Delta_y}{\lambda z}\right) = e^{i(kz - \frac{\pi}{2})} \cdot e^{\frac{i\pi}{\lambda z}((l_1' \Delta_x)^2 + (l_2' \Delta_y)^2)} \times \tag{3.34}$$
$$\times F\{u_0(l_1 \Delta_\xi, l_2 \Delta_\eta) \cdot e^{\frac{i\pi}{\lambda z}((l_1 \Delta_\xi)^2 + (l_2 \Delta_\eta)^2)}\} \frac{\Delta_\xi \Delta_\eta}{\lambda z},$$
$$\widehat{u}_0(l_1 \Delta_\xi, l_2 \Delta_\eta) = e^{-i(kz - \frac{\pi}{2})} e^{\frac{-i\pi}{\lambda z}((l_1 \Delta_\xi)^2 + (l_2 \Delta_\eta)^2)} \times \tag{3.35}$$
$$\times F^{-1}\{u_z\left(l_1' \frac{\Delta_x}{\lambda z}, l_2' \frac{\Delta_y}{\lambda z}\right) \cdot e^{\frac{-i\pi}{\lambda z}((l_1' \Delta_x)^2 + (l_2' \Delta_y)^2)}\} N_x N_y \frac{\Delta_x \Delta_y}{\lambda z};$$

and, substituting Eq. (3.34) into Eq. (3.35), we arrive at the perfect reconstruction $\widehat{u}_0 = u_0$. Eq. (3.33) is used in our works to calculate the condition for the perfect object wave field reconstruction.

More generally, if the image and pixel sizes at the object and sensor planes are equal ($N_x = N_\xi$, $\Delta_x = \Delta_\xi$ and $N_y = N_\eta$, $\Delta_y = \Delta_\eta$), then, provided the sampling condition (3.33), we can treat Eqs. (3.2)–(3.3) as a discrete shift-invariant convolution and apply DFT (12) to both parts of these equations [125] yielding [**P1**, cf. Eqs. (6)–(7)]

$$u_z[l_1', l_2'] = F^{-1}\{F\{u_0\}[n_1, n_2] \cdot F\{a_z\}[n_1, n_2]\}[l_1', l_2'], \tag{3.36}$$
$$\widehat{u}_0[l_1, l_2] = F^{-1}\{F\{u_z\}[n_1, n_2] \cdot (F\{a_z\}[n_1, n_2])^*\}[l_1, l_2], \tag{3.37}$$

where for the invertible diffraction kernel $\widehat{u}_0 = u_0$.

3.4 Numerical implementation

These formulas (3.30)–(3.31) and (3.36)–(3.36) represent the conventional discrete wave field propagation models. F–DDT from Section 3.2.3 gives an accurate forward wave field propagation via the frequency domain. Note that the numerical calculation via DFT is time-consuming: $\mathcal{O}(N^2)$ complexity for 1D DFT.

The computation of the discrete wave field propagation is typically based on the fast Fourier transform (1D FFT has $\mathcal{O}(N \log N)$ complexity): it is the commonly used, traditional approach [13, 235], because the computation time of algorithms can be reduced by order of magnitude. Shen and Wang [196] enhance the FFT based approach by introducing weights in the discrete convolution, whose values are found by Simpson's rule for numerical integration. Naskov and Logofătu [158] use different sampling intervals (unequal sampling step) for the object and sensor planes in order to widen the spatial range of accuracy of the discrete convolution. As a result, they obtain a scaled convolution which is still computed fast in $\mathcal{O}(N \log N)$ calculations by the use of the discrete fractional Fourier transform.In [9] the RS impulse response is approximated by polynomial and parabolic phasors. We also wish to mention that the discrete space domain modeling for holography is discussed in details in [125], the accuracy of the frequency domain approach can be found in [166], and interesting developments concern continuous and discrete Fresnel transforms and their multiresolution versions can be found in, e.g., [5, 165, 235]. We also usually realize the wave field propagation with FFT.

Note, while the parameters $\lambda, z, \Delta_\xi, \Delta_\eta, \Delta_x, \Delta_y \in \mathbb{R}^+$ are generally real positive numbers, the image size is defined in pixels, i.e. $N_y, N_x, N_\xi, N_y \in \mathbb{N}$. We wish to say that using the conventional FFT routines (say, Fortran or C/C++ libraries) the accurate choice of parameters is out of our control. For instance, we choose the image sizes as integer multiples of 2 (the conventional size of an image for FFT should be a power of 2). Thus, the accurate diffraction propagation can be computed only for a certain sequence of propagation distances with respect to positive integer image sizes

$$N'_x = 2\lceil \frac{\lambda \cdot z}{2\Delta_x \Delta_\xi} \rceil, \qquad N'_y = 2\lceil \frac{\lambda \cdot z}{2\Delta_\eta \Delta_y} \rceil, \tag{3.38}$$

where $\lceil \cdot \rceil$ denotes the ceiling operation.

Indeed, let z be an arbitrary distance, $\Delta_x = \Delta_y$, $\Delta_\xi = \Delta_\eta$ and λ are given and fixed. $\frac{\lambda \cdot z}{\Delta_x \Delta_\xi}$ and $\frac{\lambda \cdot z}{2\Delta_\eta \Delta_y}$ are equal, but most likely not integer. Then, the propagation distance corresponding to the sampling condition and valid for the implementation via FFT (Eq. (3.38)) is $z' = \frac{\Delta_x \Delta_\xi}{\lambda} N'_x = \frac{\Delta_x \Delta_\xi}{\lambda} \cdot 2\lceil \frac{\lambda \cdot z}{2\Delta_x \Delta_\xi} \rceil$. Therefore, in this thesis and in our publications the so-called *in-focus* distance [125] with respect to x or y directions, corresponding to the perfect object reconstruction, is defined by

$$z_{f,x} = \frac{\Delta_x \Delta_\xi}{\lambda} N'_x, \qquad z_{f,y} = \frac{\Delta_\eta \Delta_y}{\lambda} N'_y. \tag{3.39}$$

If $z_{f,y} = z_{f,x}$ the in-focus distance is simply denoted by z_f. The influence of the sampling condition on the reconstruction quality is well presented in [**P1**, Fig. 2].

Evidently the propagation distance should be taken with the step $\frac{2\Delta_x \Delta_\xi}{\lambda}$ or $\frac{2\Delta_\eta \Delta_y}{\lambda}$ for the x and y directions[2], namely: $z = z_{f,x} \pm m \cdot \frac{2\Delta_x \Delta_\xi}{\lambda}$ or $z = z_{f,x} \pm m \cdot \frac{2\Delta_\eta \Delta_y}{\lambda}$, $m \in \mathbb{N}$. Otherwise FFT automatically (and unpredictable) modifies parameters of the optical setup, including the propagation distance, to satisfy $\frac{1}{N_x} = \frac{\Delta_x \Delta_\xi}{\lambda z}$ and $\frac{1}{N_y} = \frac{\Delta_y \Delta_\eta}{\lambda z}$.

[2] This step is found from the minimal distance between two positive integer even numbers $N_2 > N_1$: e.g., $z_2 - z_1 = \frac{\Delta_x \Delta_\xi}{\lambda}(N_2 - N_1)$.

3.5 Inverse of M–DDT

The conventional wave field reconstruction models [125, 236] are based on digital approximations of the inverse operator $\mathcal{D}_z^{-1}\{\cdot\}$ and, the discrete algorithms (see, e.g., Eq. (3.5)) inherit the principal limitation of the integral inverse operator just because of the finite size of the sensor plane. In contrast to it, we follows to another approach, the so-called *inverse imaging*: the object reconstruction is performed by the numerical inverse of the forward propagation operator $\mathcal{D}_z$. For example, the reconstruction of $\widehat{\mathbf{U}}_0$ from $\mathbf{U}_z$ in case of M–DFrT can be also obtained as a solution of the equation (3.4). For the nonsingular $\mathbf{C}_{y,z}$ and $\mathbf{C}_{x,z}$ we arrive at the following backward propagation modeling

$$\widehat{\mathbf{U}}_0 = \frac{1}{\Delta_\eta \Delta_\xi} \cdot \mathbf{C}_x^{-1} \cdot \mathbf{U}_z \cdot \mathbf{C}_y^{-T}, \tag{3.40}$$

and it is different from Eq. (3.5) because in general $\mathbf{C}_x^{-1} \neq \mathbf{C}_x^H$ and $\mathbf{C}_y^{-T} \neq \mathbf{C}_y^*$, and the inverse of M–DFrT has a place if and only if $\mathbf{C}_y^H \mathbf{C}_y = \mathbf{I}$ and $\mathbf{C}_x^H \mathbf{C}_x = \mathbf{I}$ are the identity matrices. This condition can be guaranteed under the conditions (3.33) and has no place in the general case.

Following Eq. (3.17), the linear observation model of a holographic scenario is defined as follows

$$\mathbf{u}_z = \mathbf{A} \cdot \mathbf{u}_0 + \boldsymbol{\varepsilon}, \tag{3.41}$$

where $\mathbf{u}_0 \in \mathbb{C}^{N_\xi N_\eta}$ is the object vector, $\mathbf{A} \in \mathbb{C}^{N_x N_y \times N_\xi N_\eta}$ is the M–DDT transform matrix and the vector $\mathbf{u}_z \in \mathbb{C}^{N_x N_y}$ describes the result of the forward diffraction propagation to the distance z. Here and in our works **P1**–**P2** and [114, 115] the complex-valued $\mathbf{u}_z$ is assumed to be corrupted by the additive circular symmetric complex zero-mean Gaussian noise [77]. It means that the real and imaginary components of the random noise vector $\boldsymbol{\varepsilon}[l']$ are not correlated (the expectation $E\langle \mathrm{Re}\{\boldsymbol{\varepsilon}[l']\} \cdot \mathrm{Im}\{\boldsymbol{\varepsilon}[l']\}\rangle = 0$), independent and identically distributed (i.i.d.) according to the normal distribution, $\mathrm{Re}\{\boldsymbol{\varepsilon}[l']\} \sim \mathcal{N}\left(0, \sigma^2\right)$ and $\mathrm{Im}\{\boldsymbol{\varepsilon}[l']\} \sim \mathcal{N}\left(0, \sigma^2\right)$ with the same standard deviation $\sigma \geqslant 0$ [3].

The simplest way to recover the estimate of the object wave field distribution $\hat{\mathbf{u}}_0$ is applying the inverse of the transform matrix to the given (noisy) complex-valued data according to the naive reconstruction: $\hat{\mathbf{u}}_0 = \mathbf{A}^{-1} \cdot \mathbf{u}_z$ [109]. This inverse of M–DDT gives an acceptable reconstruction of the pixelwise object distribution (depending on the noise level σ in $\boldsymbol{\varepsilon}$), if the M–DDT operator is non-singular. In general case such a straightforward approach of the wave field reconstruction will typically fail due to the ill conditioning of the transform matrix (see [**P1**, Fig. 9]).

The concept of well-posed and ill-posed inverse problems goes back to Jacques Hadamard (1865–1963) at the beginning of the 20th century (e.g., [88]). According to Hadamard's definition for mathematical models of physical phenomena a *well-posed* problem must have a solution (existence), at most one solution (uniqueness), and this solution must depend continuously on the input data (stability).

[3] Recall that values of the used test-image vary from 0 to 1, and in case of AM for the wave field at the object plane σ=0.01 represents a small amount of noise (1%). However, we deal with noisy (complex-valued) diffraction patterns at the sensor plane, and for a large distance of the wave field propagation, say $z > 2 \cdot z_f$, even such a small noise may cause significant degradations of the object reconstruction due to ill-posedness of the propagation operator.

A problem is defined as *ill-posed*, if the solution is not unique or if it is not a continuous function of the data, i.e. if an arbitrary small perturbation of the data can cause an arbitrarily large perturbation of the solution [91]. Further we focus on the problem of the backward wave field propagation computed using the inverse of M–DDT, the object reconstruction accuracy and imaging obtained in our numerical simulations from synthetic data. In this thesis and in **P1**–**P2** and [114, 115] the problem related to the ambiguity of the object phase is out of scope.

3.5.1 Ill-posedness in M–DDT

Traditionally any discussion about the properties of the transform matrices requires knowledge of its singular value decomposition (SVD). The conventional numerical "tools" that allows explicit analysis of the diffraction transform and possible difficulties related to Hadamard's conditions, are the numerical rank and conditioning number calculated by SVD of the DDT matrices.

It is well-known that the matrix $\mathbf{A} = (\mathbf{A}_y \otimes \mathbf{A}_x)$ can be rewritten using the SVD decomposition [99]

$$\mathbf{A} = (\mathbf{\Lambda}_y \mathbf{D}_y \mathbf{V}_y^H) \otimes (\mathbf{\Lambda}_x \mathbf{D}_x \mathbf{V}_x^H) = (\mathbf{\Lambda}_y \otimes \mathbf{\Lambda}_x)(\mathbf{D}_y \otimes \mathbf{D}_x)(\mathbf{V}_y \otimes \mathbf{V}_x)^H, \tag{3.42}$$

where $\mathbf{\Lambda}_y, \mathbf{\Lambda}_x$ and $\mathbf{V}_y, \mathbf{V}_x$ are square orthogonal matrices of eigenvectors, and $\mathbf{D}_y, \mathbf{D}_x$ are the diagonal matrices with the real-valued nonnegative singular values $\boldsymbol{\chi}_y[j]$ $(j = 1, \dots \min(N_\eta, N_y))$ and $\boldsymbol{\chi}_x[s]$ $(s = \min(N_\xi, N_x))$, respectively, appearing in nonincreasing order.

Let us assume for a moment that there is no noise in the complex-valued observation data: $\boldsymbol{\varepsilon}$ in Eq. (3.41) is a zero vector. The least square (LS) estimate $\widehat{\mathbf{u}}_0$ is a solution of the normal equation

$$\mathbf{A}^H \mathbf{u}_z = \mathbf{A}^H \mathbf{A} \cdot \mathbf{u}_0, \tag{3.43}$$

where [160, 99]

$$\mathbf{A}^H \mathbf{A} = \mathbf{A}_x^H \mathbf{A}_x \otimes \mathbf{A}_y^H \mathbf{A}_y = (\mathbf{V}_y \otimes \mathbf{V}_x)(\mathbf{D}_y^T \mathbf{D}_y \otimes \mathbf{D}_x^T \mathbf{D}_x)(\mathbf{V}_y \otimes \mathbf{V}_x)^H. \tag{3.44}$$

The rank of the Hermitian matrices $\mathbf{A}_y^H \mathbf{A}_y$ or $\mathbf{A}_x^H \mathbf{A}_x$ is, from a mathematical point of view, the number of linearly independent rows (columns) or these matrices. The rank is equal to the number of strictly positive singular values $(\boldsymbol{\chi}_y[j])^2$ or $(\boldsymbol{\chi}_x[s])^2$, respectively, and the maximum value of $(\boldsymbol{\chi}_y[j])^2$ or $(\boldsymbol{\chi}_x[s])^2$ is equal to $\min(N_\eta, N_y)$ or $\min(N_\xi, N_x)$, respectively. In the presence of errors (in practice, the measurement data always has some noise, particularly by approximation and discretization errors, and even computer simulated data are corrupted with round-off errors) this definition is not useful. Thus, we use, from a practical point of view, the *numerical rank* as the number of rows (columns) of $\mathbf{A}_y^H \mathbf{A}_y$ or $\mathbf{A}_x^H \mathbf{A}_x$, which are *almost* linearly independent with respect to some error level [91, cf. Chapter 3]. Hence, the numerical rank of the square matrices $\mathbf{A}_y^H \mathbf{A}_y$ and $\mathbf{A}_x^H \mathbf{A}_x$ is defined regarding to a tolerance τ_ε by [91, cf. Eq. (3.3)]

$$\begin{aligned} rank(\mathbf{A}_y^H \mathbf{A}_y) &= \max_j (j : (\boldsymbol{\chi}_y[j])^2 > \tau_\varepsilon), \\ rank(\mathbf{A}_x^H \mathbf{A}_x) &= \max_s (s : (\boldsymbol{\chi}_x[s])^2 > \tau_\varepsilon), \end{aligned} \tag{3.45}$$

where the tolerance $\tau_\varepsilon = 10^{-12}$ is taken experimentally (as in **P1**) and it is the same for both $\mathbf{A}_y^H\mathbf{A}_y$ and $\mathbf{A}_x^H\mathbf{A}_x$.

The *conditioning number* of $\mathbf{A}_y^H\mathbf{A}_y$ and $\mathbf{A}_x^H\mathbf{A}_x$ is defined as the ratio between the largest and the smallest singular values of these matrices

$$cond(\mathbf{A}_y^H\mathbf{A}_y) = \frac{(\boldsymbol{\chi}_y[1])^2}{(\boldsymbol{\chi}_y[\min(N_\eta, N_y)])^2}, \quad cond(\mathbf{A}_x^H\mathbf{A}_x) = \frac{(\boldsymbol{\chi}_x[1])^2}{(\boldsymbol{\chi}_x[\min(N_\xi, N_x)])^2}. \tag{3.46}$$

For simplicity, we typically consider the case, when $N_x = N_\xi$ and $N_y = N_\eta$.

It is known that the conditioning number (the rank) of the matrix $\mathbf{A}^H\mathbf{A}$ is the product of the conditioning numbers (ranks) calculated separately for the matrices $\mathbf{A}_x^H\mathbf{A}_x$ and $\mathbf{A}_y^H\mathbf{A}_y$ [99]. In general, this statement is not true for the numerical rank: *rank* is computed depending on the chosen tolerance[4]. It is, however, much simpler to work with the individual transform matrices $\mathbf{A}_y^H\mathbf{A}_y$ and $\mathbf{A}_x^H\mathbf{A}_x$ due to their much smaller dimensions comparing with $\mathbf{A}^H\mathbf{A}$. For the same reason, it is simpler to characterize the conditioning of M–DDT using *cond* or *rank* of the matrices $\mathbf{A}_y^H\mathbf{A}_y$ and $\mathbf{A}_x^H\mathbf{A}_x$ separately. Therefore, the numerical rank $rank(\mathbf{A}^H\mathbf{A})$ is hereafter defined by the product of the numerical ranks of $\mathbf{A}_x^H\mathbf{A}_x$ and $\mathbf{A}_y^H\mathbf{A}_y$ as a more rigorous, even though rough, evaluation, i.e.

$$\begin{aligned} cond(\mathbf{A}^H\mathbf{A}) &= cond(\mathbf{A}_x^H\mathbf{A}_x) \cdot cond(\mathbf{A}_y^H\mathbf{A}_y), \\ rank(\mathbf{A}^H\mathbf{A}) &\tilde{=} rank(\mathbf{A}_x^H\mathbf{A}_x) \cdot rank(\mathbf{A}_y^H\mathbf{A}_y). \end{aligned} \tag{3.47}$$

In addition, such *cond* and *rank* of $\mathbf{A}^H\mathbf{A}$ serve as a conventional indicator of the reconstruction quality.

For rectangular object and sensor planes the perfect reconstruction $\widehat{\mathbf{U}}_0 = \mathbf{U}_0$ is achieved provided the following assumptions:

1. The support of the sensor plane distribution is equal to or larger than the support of the object plane distribution $N_x \geq N_\xi$ and $N_y \geq N_\eta$, otherwise it is already referred to super resolution methods. In addition, we introduce here the size ratio of these image $q_x = N_x/N_\xi \geq 1$, $q_y = N_y/N_\eta \geq 1$;

2. $\mathbf{A}_y^H\mathbf{A}_y$ and $\mathbf{A}_x^H\mathbf{A}_x$ are full rank matrices, i.e.

$$rank(\mathbf{A}_x^H\mathbf{A}_x) = N_\xi, \; rank(\mathbf{A}_y^H\mathbf{A}_y) = N_\eta.$$

To address the second statement, we use the numerical rank calculated by Eq. (3.45), and the perfect reconstruction is replaced by the *numerical perfect* reconstruction, i.e. those which provides practically high reconstruction accuracy

[4] For instance, in the experiment with rectangular pixels of the size $\Delta_\eta = \Delta_y = 5\mu m$, $\Delta_x = \Delta_\xi = 8\mu m$ and square images $N_x = N_\xi = N_y = N_y = 64$ for $z = 2 \cdot z_y$ provided Eqs. (3.39), the numerical ranks $rank(\mathbf{A}_x^H\mathbf{A}_x) = 61$, $rank(\mathbf{A}_y^H\mathbf{A}_y) = 43$ for the tolerance $\tau_\varepsilon = 10^{-12}$ and $\max_{j,s}(j, s : (\boldsymbol{\chi}_y[j])^2 \cdot (\boldsymbol{\chi}_x[s])^2 > \tau_\varepsilon^2) = 3152$, where $rank(\mathbf{A}_x^H\mathbf{A}_x) \cdot rank(\mathbf{A}_y^H\mathbf{A}_y) = 2623$. Note that the strict relation between the numerical ranks of $\mathbf{A}^H\mathbf{A}$ and the individual matrices $\mathbf{A}_x^H\mathbf{A}_x$ and $\mathbf{A}_y^H\mathbf{A}_y$ is out of scope of this thesis.

in RMSE or PSNR. If the conditions 1 and 2 are held, then the numerical perfect reconstruction is given by the formula

$$\widehat{\mathbf{U}}_0 = (\mathbf{A}_x^H \mathbf{A}_x)^{-1} \mathbf{A}_x^H \cdot \mathbf{U}_z \cdot \mathbf{A}_y^* (\mathbf{A}_y^T \mathbf{A}_y^*)^{-1}, \tag{3.48}$$

or, in other words,

$$\widehat{\mathbf{u}}_0 = (\mathbf{A}^H \mathbf{A})^{-1} \mathbf{A}^H \cdot \mathbf{u}_z \tag{3.49}$$

In addition, the transform matrices $\mathbf{A}_y^H \mathbf{A}_y$ and $\mathbf{A}_x^T \mathbf{A}_x^*$ in Eq. (3.48) become well conditioned and invertible. Thus, in case of the same pixels' size $\Delta_x = \Delta_\xi$ and $\Delta_y = \Delta_\eta$ the object estimate is defined by $\widehat{\mathbf{u}}_0 = \mathbf{A}^H \cdot \mathbf{u}_z$ or

$$\widehat{\mathbf{U}}_0 = \mathbf{A}_x^H \cdot \mathbf{U}_z \cdot \mathbf{A}_y^*, \tag{3.50}$$

what represents M–IDFrT model with averaged matrices. Here and in **P2** we additionally consider the reconstruction quality obtained by this scheme.

Let the size ratios $q_x = q_y = 1$ and the conditions (3.33) be fulfilled. Then, taking into account Eqs. (3.20) and

$$\frac{\lambda z}{\Delta_\xi^2 N_x} \mathbf{B}_x^H \mathbf{B}_x = \frac{\lambda z}{N_x} \mathbf{C}_x^H \mathbf{C}_x = \mathbf{I}, \quad \frac{\lambda z}{\Delta_\eta^2 N_y} \mathbf{B}_y^T \mathbf{B}_y^* = \frac{\lambda z}{N_y} \mathbf{C}_y^T \mathbf{C}_y^* = \mathbf{I}, \tag{3.51}$$

we can express the object reconstruction via the non-averaged matrices as

$$\widehat{\mathbf{U}}_0 = (\mathbf{B}_x^H \mathbf{B}_x)^{-1} \mathbf{B}_x^H \cdot \mathbf{U}_z \cdot \mathbf{B}_y^* (\mathbf{B}_y^T \mathbf{B}_y^*)^{-1} = \tag{3.52}$$
$$\frac{(\lambda z)^2}{\Delta_\xi^2 N_x \Delta_\eta^2 N_y} \mathbf{B}_x^H \cdot \mathbf{U}_z \cdot \mathbf{B}_y^* = \frac{(\lambda z)^2}{\Delta_\xi N_x \Delta_\eta N_y} \mathbf{C}_x^H \cdot \mathbf{U}_z \cdot \mathbf{C}_y^*$$

or, provided the same pixels, as $\widehat{\mathbf{U}}_0 = \mathbf{B}_x^H \cdot \mathbf{U}_z \cdot \mathbf{B}_y^*$.

The numerical study in **P1**–**P2** and [114, 115] shows that, depending on the parameters of the propagation system (the propagation distance z, the pixel and images sizes), the matrices $\mathbf{A}_y$ and $\mathbf{A}_x$ are *correctly* ill conditioned [91], i.e. this ill-posedness is a part of the formulation of the diffraction propagation model using M–DDT. Providing the accurate forward wave field propagation the transform matrices for z larger than the in-focus distances become numerically singular and Eqs. (3.48)–(3.50) – practically useless: they give either unstable results highly sensitive regarding to the parameter variations and observation noise or just fail.

3.5.2 Conditioning of M–DDT and inverse reconstruction accuracy

It can be shown that the numerical rank and the conditioning number of the transform matrices $\mathbf{A}_y^H \mathbf{A}_y$ and $\mathbf{A}_x^H \mathbf{A}_x$ (in general, $\mathbf{A}^H \mathbf{A}$) can be used as a good indicator of the accuracy of the object distribution reconstruction. *rank* and *cond* in Eqs. (3.45)–(3.47) are seriously dependent on the sensor size, pixel size, propagation distance z and on the the parameters q_x and q_y, which define a redundancy of the sensor with respect to the object distribution[5].

[5] The larger sensor image is, the better accuracy of reconstruction for the object plane.

Firstly, let us consider the conditioning number in case of square images and pixels of the same size at the object and sensor plane, $N_x = N_y$, $q_x = q_y = 1$ and $\Delta_\xi = \Delta_\eta = \Delta_x = \Delta_y$. It can be seen that the minimum value of *cond* corresponds exactly to the in-focus distance $z = z_f$ (Eqs. (3.33) and (3.39), see [**P2**, Fig. 5], [114, Fig. 4(a)]), what results in the best reconstruction quality in RMSE (cf. [**P2**, Fig. 4], [114, Fig. 4(b)]). This distance $z = z_f$ also corresponds to the peak of the curve of the numerical rank computed for the averaged matrices (see [**P1**, Fig. 3], [115, Fig. 1(top image)]). However, even for slightly smaller $z = 0.95 \cdot z_f$ (larger $z = 1.05 \cdot z_f$) distances the conditioning number grows rapidly increasing by orders of magnitude, and the reconstruction of the object distribution becomes more and more questionable for distances different from z_f.

For large propagation distances $z > z_f$, precisely $z > z_{f,x}$, $z > z_{f,y}$ there is a problem related to the support of the discrete diffraction kernel. In [125, Chapter A.13] it is mentioned that the continuous diffraction kernels are chirp-like functions of infinite extent, where the frequency of the oscillations increases together with the radial distances from the origin and decreases for larger propagation distances. But things dramatically change, if we investigate the finite chirp function, which represents only a section of the infinite one in a finite interval. Let us consider the used Fresnel diffraction kernel (1.59). It is easy to see that, provided the sampling conditions Eqs. (3.33) and (3.39), the support of the discrete kernel is $\frac{\Delta_\xi}{\Delta_x} N'_x \times \frac{\Delta_\eta}{\Delta_y} N'_y$, and in case of the same pixel size at the object and sensor plane regarding to the x and y direction the support is $N'_x \times N'_y$ because

$$\exp\left(\frac{i\pi\Delta_\xi^2}{\lambda z_x}(l_1 + N'_x)^2\right) = \tag{3.53}$$

$$= \underbrace{\exp\left(i2\pi\frac{\Delta_\xi}{\Delta_x} l_1\right)}_{=1,\ \text{if } \Delta_\xi = \Delta_x} \cdot \exp\left(\frac{i\pi\Delta_\xi^2}{\lambda z_x} l_1^2\right) \cdot \exp\left(i\pi\frac{\Delta_\xi}{\Delta_x} N'_x\right),$$

$$\exp\left(i\pi\frac{\Delta_\xi}{\Delta_x} N'_x\right) = \begin{cases} -1, & \text{odd } N'_x,\ \Delta_\xi = \Delta_x \\ 1, & \text{even } N'_x,\ \Delta_\xi = \Delta_x \end{cases}$$

analogically

$$\exp\left(\frac{i\pi\Delta_y^2}{\lambda z_y}(l_2 + N'_y)^2\right) = \exp\left(\frac{i\pi\Delta_y^2}{\lambda z_y} l_2^2\right), \tag{3.54}$$

if N'_y is even[6] and $\Delta_\eta = \Delta_y$. For $z < z_{f,x}$, $z < z_{f,y}$ the mentioned support size becomes larger than the available 2D measurement array (e.g., for $z = \frac{1}{2} \cdot z_f$ the kernel support is exactly two times smaller than the image size), what is indicated by the numerical rank close to its maximum value.

In case of $z > z_{f,x}$, $z > z_{f,y}$ we lose the high-frequency components of the kernel. Hence, the reconstruction quality will be (much) worse, what is indicated by the conditioning number which immediately becomes very large and numerical ranks of the M–DDT transform matrices which start to decrease monotonically. In Fig. 3.2 we demonstrate the Fresnel diffraction kernel calculated on square $\frac{3}{2}N'_x \times \frac{3}{2}N'_y$ grid, $N'_x = N'_y = 256$ for square pixels $\Delta_\eta = \Delta_y = \Delta_x = \Delta_\xi = 3.45\mu m$

[6] It could be another reason to choose the image sizes as integer multiples of 2.

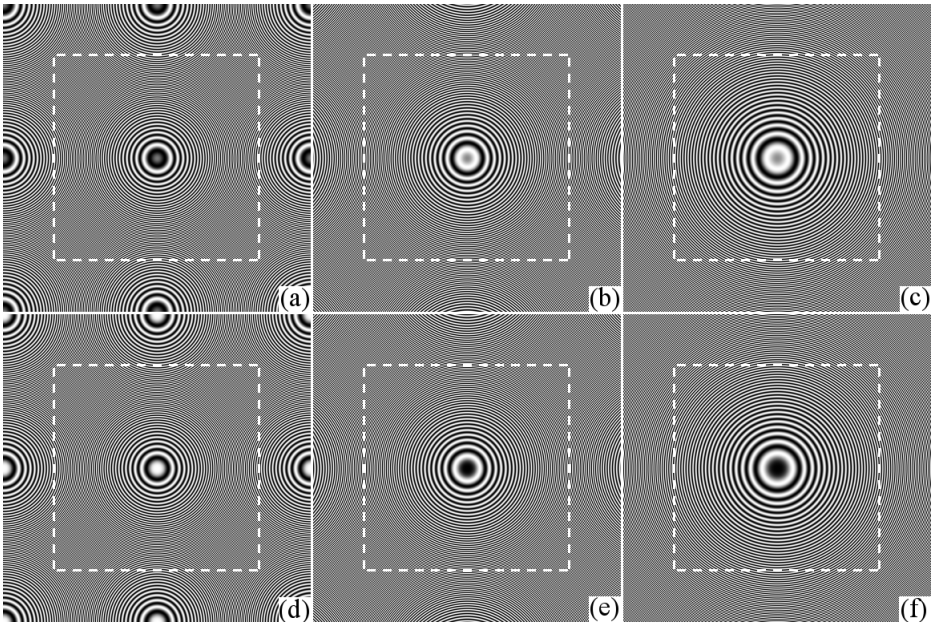

Figure 3.2: The Fresnel diffraction kernel $g_z(l_1\Delta_\xi l_2\Delta_\eta) = \frac{e^{ikz}}{i\lambda z} e^{\frac{ik}{2z}((l_1\Delta_\xi)^2+(l_2\Delta_\eta)^2)}$ calculated on the grid $\frac{3}{2}N'_\xi \times \frac{3}{2}N'_\eta$ samples, $N'_\xi = N'_\eta = 256$, with square pixels $\Delta_\eta = \Delta_y = \Delta_x = \Delta_\xi = 3.45\ \mu m$ for the propagation distances (from left to right column-wise) $z = \{\frac{3}{4}\cdot z_f\ , z_f$ and $\frac{3}{2}\cdot z_f\}$, $z_f = \frac{\Delta_x\Delta_\xi N'_x}{\lambda} = \frac{\Delta_x\Delta_\xi N'_y}{\lambda}$. The support of the kernel $N'_x \times N'_y$ is marked by a dashed square. The real part $\mathrm{Re}\{g_z\}$ is presented in the top row, and the imaginary part $\mathrm{Im}\{g_z\}$ – in the bottom row, respectively.

for different propagation distances: $z = \frac{3}{4}\cdot z_f$, $z = z_f$ and $z = \frac{3}{2}\cdot z_f$. The real part of this kernel is presented for the corresponding distances in the top row: $\mathrm{Re}\{g_{3/4\cdot z_f}[l_1, l_2]\}$ in Fig. 3.2(a); $\mathrm{Re}\{g_{z_f}\}$ in Fig. 3.2(b) and $\mathrm{Re}\{g_{3/2\cdot z_f}\}$ in Fig. 3.2(c), respectively. The imaginary part is shown in the bottom row: $\mathrm{Im}\{g_{3/4\cdot z_f}\}$ in Fig. 3.2(d); $\mathrm{Re}\{g_{z_f}\}$ and $\mathrm{Im}\{g_{z_f}\}$ in Fig. 3.2(e) and $\mathrm{Im}\{g_{3/2\cdot z_f}\}$ in Fig. 3.2(f), respectively. The support of the kernel of the size $N'_x \times N'_y$ corresponding to the in-focus distance $z_f = \frac{\Delta_x\Delta_\xi N'_x}{\lambda} = \frac{\Delta_y\Delta_\eta N'_y}{\lambda}$ is marked by a dashed square. It can be seen that for larger distances we operate with smaller and smaller portion of the kernel support with low frequencies only.

It is well known that the Kronecker delta can be expressed as a summation of complex exponents $\delta_{l',l''} = \frac{1}{N}\sum_{l=-N/2}^{N/2-1} \exp(\pm i2\pi\frac{l}{N}[l' - l''])$. The decay of the matrix conditioning [**P2**, Fig. 5] and, as the result, decreasing of the object reconstruction accuracy [**P1**, Fig. 4] for $z < z_f$ can be explained by the failure of the assumption (3.32): for $\frac{1}{2}\cdot z_f < z < z_f$ the numerical size (in pixels) of the used diffract kernel is larger than its support, but the number of components is not a multiple of N. For $z = \frac{1}{2}\cdot z$ we have a multiple redundancy, i.e. the used size is precisely two times larger than the diffraction kernel support. In this case the averaging of the M–DDT matrices practically provides a very good imaging: see Fig. 3.3, [**P1**, Fig. 8] and [**P2**, Fig. 3] for AM. While the reconstructions by M–

Figure 3.3: Amplitude reconstruction for the close distance $z = \frac{1}{2} \cdot z_f$, AM, Lena test-image. The results are obtained (a) by the inverse M–DDT as $|\widehat{\mathbf{U}}_0| = |\mathbf{A}_x^{-1}\mathbf{A}_x \cdot \mathbf{U}_0 \cdot \mathbf{A}_y^T\mathbf{A}_y^{-T}|$; (b) by M–IDFrT with the averaged matrices as $|\widehat{\mathbf{U}}_0| = |\mathbf{A}_x^H\mathbf{A}_x \cdot \mathbf{U}_0 \cdot \mathbf{A}_y^T\mathbf{A}_y^*|$. M–IDFrT with the non-averaged matrices calculated by (c) $|\widehat{\mathbf{U}}_0| = c_0 \cdot |\mathbf{C}_x^H\mathbf{C}_x \cdot \mathbf{U}_0 \cdot \mathbf{C}_y^T\mathbf{C}_y^*|$ or (d) $|\widehat{\mathbf{U}}_0| = \frac{c_0}{\Delta_\xi \Delta_\eta} \cdot |\mathbf{C}_x^H\mathbf{A}_x \cdot \mathbf{U}_0 \cdot \mathbf{A}_y^T\mathbf{C}_y^*|$ fails due to aliasing. Here $c_0 = \frac{(\lambda z)^2}{N_x N_y}$.

IDFrT with non-averaged matrices are completely destroyed by the aliasing effects (see Fig. 3.3(c) and Fig. 3.3(d[7])), the reconstruction imaging by the averaged matrices is good: the inverse of M–DDT (cf. Eq. (3.48)) results in a numerically perfect imaging, Fig. 3.3(a); M–IDFrT with the averaged matrices gives a good reconstruction quality corrupted however by certain "waves" on the borders, Fig. 3.3(b). For even smaller $z < \frac{1}{2} \cdot z$ we have larger redundancy: the conditioning number [**P2**, Fig. 5], numerical rank [**P1**, Fig. 3] as well as the RMSE curve [**P2**, Fig. 4] become erratic, but the inverse of M–DDT result in a good imaging.

For the redundant sensor size with, say $q_x = q_y = \{2, 4\}$, the numerical ranks are also decreasing functions for $z > \frac{q_x \cdot \Delta_x \Delta_\xi N'_x}{\lambda}$ and/or $z > \frac{q_y \cdot \Delta_y \Delta_\eta N'_x}{\lambda}$, but *rank* of the averaged matrices for $z \le z_f$ take the maximum value up to the very small distances z (in **P1**–**P2**, [114, 115] more details are presented). It means that M–DDT with the averaged matrices is able to give object reconstructions of the very high accuracy for the whole interval $\lambda \ll z \le \min(\frac{q_x \cdot \Delta_x \Delta_\xi N'_x}{\lambda}, \frac{q_y \cdot \Delta_y \Delta_\eta N'_x}{\lambda})$.

[7] We additionally present the object reconstruction from the accurate M–DDT measurement data by M–IDFrT with the non-averaged matrices.

3.5.3 Regularization of inverse M–DDT

Since we always deal with noisy data at least due to discretization and computational rounding errors, it is necessary to incorporate some additional information about the used transformation or the desired solution in order to modify the problem and to single out a useful and stable solution. This is the purpose of *regularization*. We use the regularization for the numerical treatment of Eqs. (3.48) and (3.50) with ill conditioned transform matrices.

Traditionally, ill conditioning problems belong to one of these two classes: rank-deficient and discrete ill-posed problems. No regularization method is superior to the other methods. Rather, each method has its advantages, depending on the properties of the transform matrices and application in which it is used. In our case both methods, described below, can be used to obtain a regularized inverse solution, however in **P1**–**P2** we use the classical Tikhonov regularization because it is found to be more stable for large amount of noise, simpler and enables better imaging in case of large propagation distances.

Regularization by truncation

Rank-deficient problems are characterized by the transform matrix, having a cluster of small singular values, and there is a well-determined gap between large and small singular values. This implies that one or more rows (columns) of transform matrices are nearly linear combinations of some or all of the remaining rows (columns). Therefore, the matrices $\mathbf{A}_y$ and $\mathbf{A}_x$ contain almost redundant information, and the key to the numerical treatment of such problems is to extract the linearly independent information in these matrices, to arrive at another problem with a well conditioned matrices [91].

This problem can be dealt using the *truncated SVD*

$$\widehat{\mathbf{U}}_0 = \mathbf{V}_x \mathbf{D}^+_{\tau_x} \mathbf{D}^T_x \mathbf{\Lambda}^H_x \cdot \mathbf{U}_z \cdot \mathbf{\Lambda}^*_y \mathbf{D}_y \mathbf{D}^+_{\tau_y} \mathbf{V}^T_y. \tag{3.55}$$

Here the components of the diagonal matrix $\mathbf{D}^+_{\tau_x} = \mathrm{diag}(\{\boldsymbol{\chi}^+_x[s]\}) \in \mathbb{R}^{N_\xi \times N_\xi}$ is expressed via the truncated vector of the singular values [91, cf. Eq. (2.3)]

$$\boldsymbol{\chi}^+_x[s] = \begin{cases} 1/(\boldsymbol{\chi}_x[s])^2, & s = 1, \ldots \tau_x \\ 0 & s > \tau_x \end{cases} \tag{3.56}$$

where $\tau_x \leq rank(\mathbf{A}^H_x \mathbf{A}_x)$ is the threshold, which characterizes the number of non-zero singular values. Similarly, the non-zero components of $\mathbf{D}^+_{\tau_y} = \mathrm{diag}(\{\boldsymbol{\chi}^+_y[j]\})$ are $\boldsymbol{\chi}^+_y[j] = 1/\boldsymbol{\chi}^2_y[j]$ for $j = 1, \ldots \tau_y$, $\tau_y \leq rank(\mathbf{A}^H_y \mathbf{A}_y)$. That technique is called *regularization by truncation* [109]. In addition, the sensitivity of the LS solutions $\widehat{\mathbf{U}}_0$ to perturbations of the transform matrices and measurements $\mathbf{U}_z$ can be measured by

$$cond(\mathbf{A}^H_y \mathbf{A}_y) = \frac{(\boldsymbol{\chi}_y[1])^2}{(\boldsymbol{\chi}_y[rank(\mathbf{A}^H_y \mathbf{A}_y)])^2}, \tag{3.57}$$

$$cond(\mathbf{A}^H_x \mathbf{A}_x) = \frac{(\boldsymbol{\chi}_x[1])^2}{(\boldsymbol{\chi}_x[rank(\mathbf{A}^H_x \mathbf{A}_x)])^2}.$$

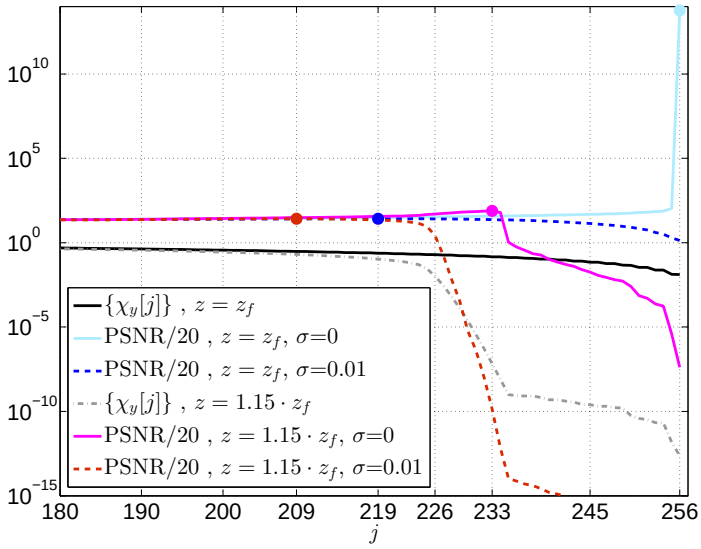

Figure 3.4: Influence of the used amount of singular values $\{\boldsymbol{\chi}_y[j]\}$, j=180,...256 of the transform matrix $\mathbf{A}_y^H\mathbf{A}_y$ of the size 256×256 on the reconstruction accuracy (in PSNR) by the truncated SVD. The maximum values of PSNR in case of noiseless and noisy ($\sigma = 0.01$) measurement data are emphasized by large dots of the corresponding color. The amplitude reconstruction are made for $z = z_f$ and $z = 1.15 \cdot z_f$.

In case of noise data (see Eq. (3.41)) we can write [109]

$$\mathbf{A}^{-1}\mathbf{u}_z = \mathbf{A}^{-1}(\mathbf{A}\mathbf{u}_0 + \boldsymbol{\varepsilon}) = \widehat{\mathbf{u}}_0 + \mathbf{A}^{-1}\boldsymbol{\varepsilon}, \tag{3.58}$$

where the error $\mathbf{A}^{-1}\boldsymbol{\varepsilon}$ can be bounded by

$$||\mathbf{A}^{-1}\boldsymbol{\varepsilon}||_2^2 \le ||\mathbf{A}^{-1}||_2^2 \cdot ||\boldsymbol{\varepsilon}||_2^2 \tag{3.59}$$

Even if $||\boldsymbol{\varepsilon}||_2^2$ is small the error $\mathbf{A}^{-1}\boldsymbol{\varepsilon}$ will be quite large, because $||\mathbf{A}^{-1}||_F^2$ is large due to the Kronecker product based structure of the transform matrix. This is a kind of amplification of noise. Taking into account the truncated SVD, Eq. (3.55), we arrive at

$$\widehat{\mathbf{U}}_0 = \mathbf{V}_x\mathbf{D}_{\tau_x}^{+}\mathbf{D}_x^T\boldsymbol{\Lambda}_x^H \cdot (\mathbf{A}_x \cdot \mathbf{U}_0 \cdot \mathbf{A}_y^T + \mathbf{E}) \cdot \boldsymbol{\Lambda}_y^*\mathbf{D}_y\mathbf{D}_{\tau_y}^{+}\mathbf{V}_y^T, \tag{3.60}$$

where $\mathbf{E}$ is the matrix, constructed from the vector of noise $\boldsymbol{\varepsilon} = \text{vec}\{\mathbf{E}\}$. The error term can be estimated as follows

$$||\mathbf{V}_x\mathbf{D}_{\tau_x}^{+}\mathbf{D}_x^T\boldsymbol{\Lambda}_x^H \cdot \mathbf{E} \cdot \boldsymbol{\Lambda}_y^*\mathbf{D}_y\mathbf{D}_{\tau_y}^{+}\mathbf{V}_y^T||^2 \le ||\mathbf{D}_{\tau_x}^{+}\mathbf{D}_x^T||^2 \cdot ||\mathbf{E}||^2 \cdot ||\mathbf{D}_{\tau_y}^{+}\mathbf{D}_y^T||. \tag{3.61}$$

It means that the noise gets amplified less and less if we choose smaller number of components of $\mathbf{D}_{\tau_x}^{+}$ and $\mathbf{D}_{\tau_y}^{+}$.

Let the images and pixels at the object and sensor planes are square and of the same size, i.e. $\mathbf{A}_x = \mathbf{A}_y$, where $N_\xi = N_\eta = 256$ and $\Delta_\xi = \Delta_\eta = 7.4\mu m$. In Fig. 3.4 we compare the behavior of singular values $\{\boldsymbol{\chi}_y[j]\}$ for (solid curve) $z = z_f$ and

Figure 3.5: Amplitude reconstruction using the regularization by truncation, Eq. (3.55), for noiseless data σ=0 and $z = 1.15 \cdot z_f$. The reconstruction is performed for different number of singular values $\tau_x = \tau_y$: (a) τ_x=210, RMSE=0.0294; (b) τ_x=233, RMSE=0.0118 (c) τ_x=235, the reconstruction fails.

(dashed-dotted curve) for $z = 1.15 \cdot z_f$, and consider the reconstruction quality of an amplitude-only object (AM) in PSNR from noiseless and noisy data depending on the number of involved $\{\boldsymbol{\chi}_y[j]\}$ (sorted in descending order). Note that the gap between large and small singular values becomes more and more evident with

Figure 3.6: Amplitude reconstruction (AM, Lena test-image) obtained using the regularization by truncation, Eq. (3.55), $\tau_x = \tau_y$, for different distances, noisy and noiseless data: (a) $z = z_f$, τ_x=256, σ=0, RMSE=$1.6{\cdot}10^{-14}$; (b) $z = z_f$, τ_x=219, σ=0.01, RMSE=0.0344; (c) $z = 1.15 \cdot z_f$, τ_x=233, σ=0, RMSE=0.0118; (d) $z = 1.15 \cdot z_f$, τ_x=209, σ=0.01, RMSE=0.039.

increasing the propagation distance. While the singular values $\{\boldsymbol{\chi}_y[j]\}$ decrease monotonically for $z = z_f$, in case of $z = 1.15 \cdot z_f$ their values decreases rapidly (by approximately eight orders of magnitude): see $\{\boldsymbol{\chi}_y[j]\}$ in the interval from $j \in [226, 235]$.

In case of noiseless data ($\sigma = 0$, solid curves) the peaks of PSNR can be easily seen in $\tau_y = 256$ and $\tau_y = 233$ for $z = z_f$ and $z = 1.15 \cdot z_f$, respectively. Nevertheless, in Fig. 3.5 it is illustrated the choice of the proper number of singular values is not trivial: the reconstruction with too small singular values fails, but too small number of used singular values leads to a significant degradation of the object reconstruction. For noisy data, $\sigma = 0.01$, we have a gently sloping curve of PSNR: a slow, monotonic increase and then a fairly rapid decrease (more rapid decay for larger distances z). In Fig. 3.4 it is shown that the best results for noisy data are for $\tau_x = 219$ if $z = z_f$ and for $\tau_x = 209$ if $z = 1.15 \cdot z_f$, respectively. Here $\tau_x = \tau_y$. In Fig. 3.6 the object amplitude reconstructions for these optimal number of singular values τ_x with respect to PSNR are illustrated: Fig. 3.6(a) demonstrates the practically perfect reconstruction; in Fig. 3.6(c) we have slightly worse reconstruction accuracy and imaging, respectively. The amplitude reconstructions from noisy data in Fig. 3.6(b) and Fig. 3.6(d) look equally poor due to strong degradation by "wave" artifacts.

Tikhonov's regularization

Discrete ill-posed problems arise technically from the discretization of ill-posed problems when all singular values of transform matrices decay gradually (on the average) to zero and there is no precise notion of a proper numerical rank for these matrices (cf. Fig. 3.5(b) and 3.5(c)). Then, such an ill-posed problem needs to be reformulated for numerical treatment. Typically this involves additional assumptions, such as smoothness of solution or a priori information on the object distribution. This is a classical regularization process, and *Tikhonov's regularization* [91, 109, 219] is a common and well-known form of regularization of linear ill-posed problems.

Although many types of additional information about $\widehat{\mathbf{u}}_0$ is possible in principle, the dominating approach to regularize the discrete ill-posed problems is the requirement that the ℓ_2 norm of the solution must be small. An initial estimate $\mathbf{u}_0^{\dagger}$ of the solution may be also included in the side constraint. Thus, instead of the solving the conventional LS problem $\min_{\mathbf{u}_0} ||\mathbf{u}_z - \mathbf{A} \cdot \mathbf{u}_0||$ one is looking for a regularized estimate of $\mathbf{u}_0$ that defined by minimization of the quadratic criterion

$$\widehat{\mathbf{u}}_0 = \arg\min_{\mathbf{u}_0} ||\mathbf{u}_z - \mathbf{A} \cdot \mathbf{u}_0||_2^2 + \mu^2 \cdot ||\mathbf{L}(\mathbf{u}_0 - \mathbf{u}_0^{\dagger})||_2^2, \tag{3.62}$$

where $\mathbf{L}$ could be, for instance, a differentiation matrix (discretized differential operator [91, 95, 109]). For discrete ill-posed problems, the goal is to find a balance between the residual norm $||\mathbf{u}_z - \mathbf{A} \cdot \mathbf{u}_0||_2^2$ and the penalty $||\mathbf{L}(\mathbf{u}_0 - \mathbf{u}_0^{\dagger})||_2^2$ (the size of the solution) that matches the errors in the data as well as one's expectations to the computed solution [91]. The regularization parameter μ^2 serves for this purpose. In our work (as in **P1**–**P2** and [114, 115]) we have no initial estimate (i.e. $\mathbf{u}_0^{\dagger}[l] = 0 \ \forall l$) and the matrix $\mathbf{L}$ in Eq. (3.62) is, for simplicity, the identity

matrix $\mathbf{L} = \mathbf{I}$. Thus, we are looking for the regularized estimate of the object as the solution of the following optimization problem

$$\widehat{\mathbf{U}}_0 = \arg\min_{\mathbf{U}_0} ||\mathbf{U}_z - \mathbf{A}_x \cdot \mathbf{U}_0 \cdot \mathbf{A}_y^T||_F^2 + \mu^2 \cdot ||\mathbf{U}_0||_F^2 \quad \text{or} \tag{3.63}$$

$$\widehat{\mathbf{u}}_0 = \arg\min_{\mathbf{u}_0} ||\mathbf{u}_z - \mathbf{A} \cdot \mathbf{u}_0||_2^2 + \mu^2 \cdot ||\mathbf{u}_0||_2^2 \tag{3.64}$$

$||\cdot||_F^2$ in Eq. (3.63) denotes the quadratic Frobenius matrix norm. The regularization penalty $||\mathbf{U}_0||_F^2$ or $||\mathbf{u}_0||_2^2$ enables to obtain a bounded and smooth object estimate and the regularization parameter μ^2 controls the level of the smoothness of this estimate. The regularized inverse $\widehat{\mathbf{u}}_0$ defined as a minimizer of $\mathcal{J} = ||\mathbf{u}_z - \mathbf{A} \cdot \mathbf{u}_0||^2 + \mu^2||\mathbf{u}_0||^2$ is calculated by [**P1**, Appendix B]

$$\frac{\partial}{\partial \mathbf{u}_0^H}\mathbf{u}_z^H\mathbf{u}_z - \mathbf{u}_z^H\mathbf{A}\mathbf{u}_0 - \mathbf{u}_0^H\mathbf{A}^H\mathbf{u}_z - \mathbf{u}_0^H\mathbf{A}^H\mathbf{A}\mathbf{u}_0 + \mu^2\mathbf{u}_0^H\mathbf{u}_0 = 0$$

Using SVD (3.44), the *accurate solution* can be given in the form of the Tikhonov regularized inverse (RI)

$$\widehat{\mathbf{u}}_0 = \underbrace{(\mathbf{A}^H\mathbf{A}+\mu^2\mathbf{I})^{-1}}_{\mathbf{A}_\mu^{-1}}\mathbf{A}^H \cdot \mathbf{u}_z = \tag{3.65}$$

$$= (\mathbf{V}_y \otimes \mathbf{V}_x)((\mathbf{D}_y^T\mathbf{D}_y \otimes \mathbf{D}_x^T\mathbf{D}_x) + \mu^2\mathbf{I})^{-1}(\mathbf{D}_y^T \otimes \mathbf{D}_x^T)(\mathbf{\Lambda}_y^H \otimes \mathbf{\Lambda}_x^H) \cdot \mathbf{u}_z.$$

Note, however, that the *approximate* Tikhonov RI originated in **P1** and given by

$$\widehat{\mathbf{U}}_0 \approx (\mathbf{A}_x^H\mathbf{A}_x + \mu\mathbf{I})^{-1}\mathbf{A}_x^H \cdot \mathbf{U}_z \cdot \mathbf{A}_y^*(\mathbf{A}_y^T\mathbf{A}_y^* + \mu\mathbf{I})^{-1} = \tag{3.66}$$

$$= \mathbf{V}_x(\mathbf{D}_x^T\mathbf{D}_x + \mu\mathbf{I})^{-1}\mathbf{\Lambda}_x^H \cdot \mathbf{U}_z \cdot \mathbf{\Lambda}_y^*(\mathbf{D}_y^T\mathbf{D}_y + \mu\mathbf{I})^{-1}\mathbf{V}_x^H$$

is, in general, computationally simpler because of the significantly smaller dimension of transform matrices. Comparing the latter equation with Eq. (3.48), note that the inverse of $\mathbf{A}_x^H\mathbf{A}_x$ and $\mathbf{A}_y^T\mathbf{A}_y^*$ is just replaced by the inverse of their regularized versions $\mathbf{A}_y^H\mathbf{A}_y + \mu\mathbf{I}$ and $\mathbf{A}_x^T\mathbf{A}_x^* + \mu\mathbf{I}$. Using Eqs. (3.51) and (3.52) we may rewrite the approximate regularized inverse solution for non-averaged matrices [**P1**, cf. Eq. (44)] as follows

$$\widehat{\mathbf{U}}_0 \approx \frac{(\lambda z)^2}{\Delta_\xi^2 N_x \Delta_\eta^2 N_y}(\mathbf{B}_x' + \frac{\mu\lambda z}{\Delta_\xi^2 N_x}\mathbf{I})^{-1}\mathbf{B}_x^H \cdot \mathbf{U}_z \cdot \mathbf{B}_y^*(\mathbf{B}_y' + \frac{\mu\lambda z}{\Delta_\eta^2 N_y}\mathbf{I})^{-1}, \tag{3.67}$$

$$\mathbf{B}_x' = \frac{\lambda z}{\Delta_\xi^2 N_x}\mathbf{B}_x^H\mathbf{B}_x, \qquad \mathbf{B}_y' = \frac{\lambda z}{\Delta_\eta^2 N_y}\mathbf{B}_x^T\mathbf{B}_x^*.$$

3.6 Actual results and accuracy prediction

The comparison of the reconstruction accuracy obtained by the approximate Tikhonov RI and by M–IDFrT (with no regularization, $\mu = 0$) using the averaged or non-averaged matrices can be found in [**P2**, Fig. 2]. Following this text these results are obtained by Eq. (3.66) or Eq. (3.67) for the regularized inverse and by

Eqs. (3.48)–(3.50) or Eq. (3.52) for M–IDFrT. It can be seen that M–IDFrT is systematically worse than M–DDT for $z > 1.5 \cdot z_f$. However, as it is also shown in Fig. 3.3, that *averaging* allows significantly improving the reconstruction quality comparing with the conventional Fresnel diffraction transform.

In [114, Fig. 3] and [115, Fig. 2] it is illustrated the comparison of the amplitude reconstruction accuracy by different methods: M–DDT with the approximate

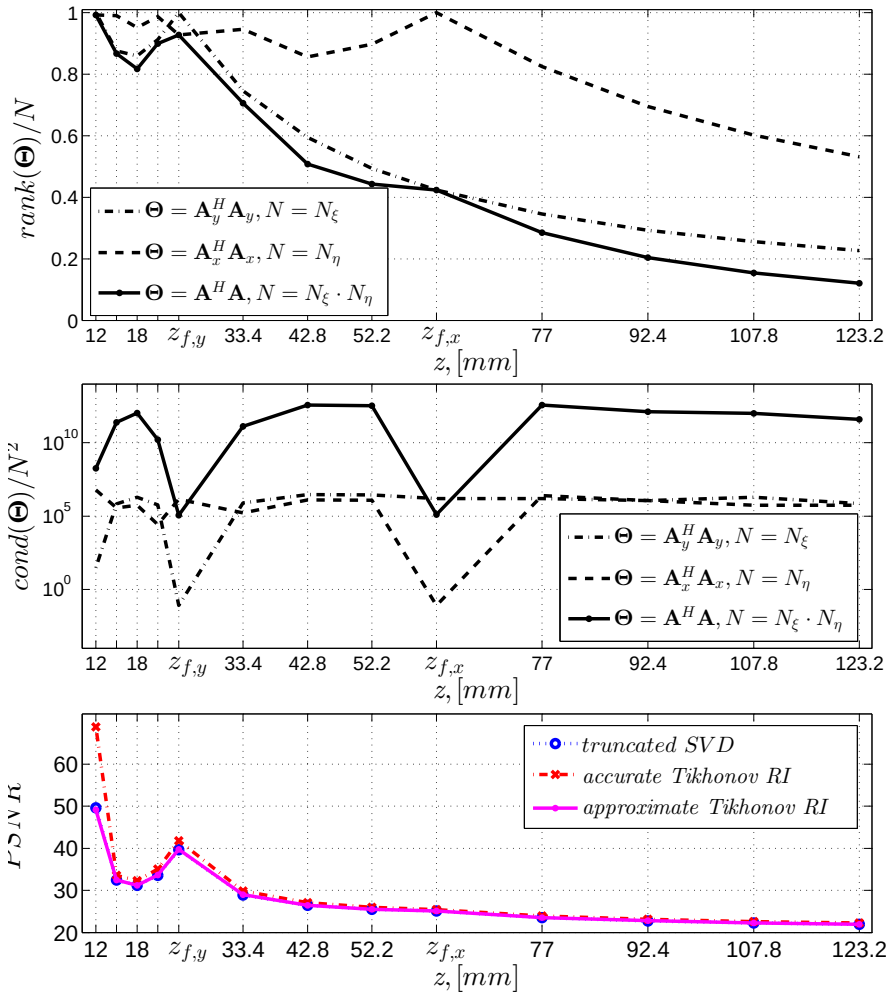

Figure 3.7: The amplitude reconstruction quality (in PSNR [dB], bottom image) versus conditioning number (*cond*, middle image) and the numerical rank (*rank* for $\tau_\varepsilon = 10^{-12}$, top image) of the transform matrices $\mathbf{A}_y^H\mathbf{A}_y$, $\mathbf{A}_x^H\mathbf{A}_x$ and $\mathbf{A}^H\mathbf{A}$ for rectangular pixels of the same size at the object and sensor plane 8×5 (μm). The results are obtained by the *truncated SVD*, Eq. (3.55); Tikhonov *accurate* (Eq. (3.65), μ^2=10^{-24}) and *approximate* regularized inverse (Eq. (3.66), μ=10^{-12}) for $z \in [\frac{z_{f,y}}{2}, 2 \cdot z_{f,x}]$. $z_{f,y}$ =24.1mm, $z_{f,x}$ =61.6mm, AM, Baboon test-image (512×512 pixels), σ=0.

solution (3.66), F–DDT (Eqs. (3.25)–(3.28)), M–IDFrT with no averaging, and conventional convolutional methods of the single (*conv1*, Eq. (3.29)) and double size (*conv2*, zero-padding as in F–DDT or [196]). It is found that the best result is almost always in favor of M–DDT.

In Fig. 3.7 and [**P1**, Fig. 10] the comparison of the amplitude reconstruction accuracy with respect to the numerical *rank* and conditioning number *cond* for noiseless data is presented. The results are given for square images of the size 512×512 and rectangular pixels at the object and sensor planes of the size $\Delta_\xi = \Delta_x = 8\mu m$, $\Delta_\eta = \Delta_y = 5\mu m$. The conditioning number $cond(\mathbf{A}^H\mathbf{A})$ has two local minima corresponding to $z_{f,x} = 61.6mm$ and $z_{f,y} = 24.1mm$ (see Fig. 3.7(middle image)), thus the single in-focus distance for the M–DDT algorithm is recommended to be chosen with respect to the numerical rank as an alternative.

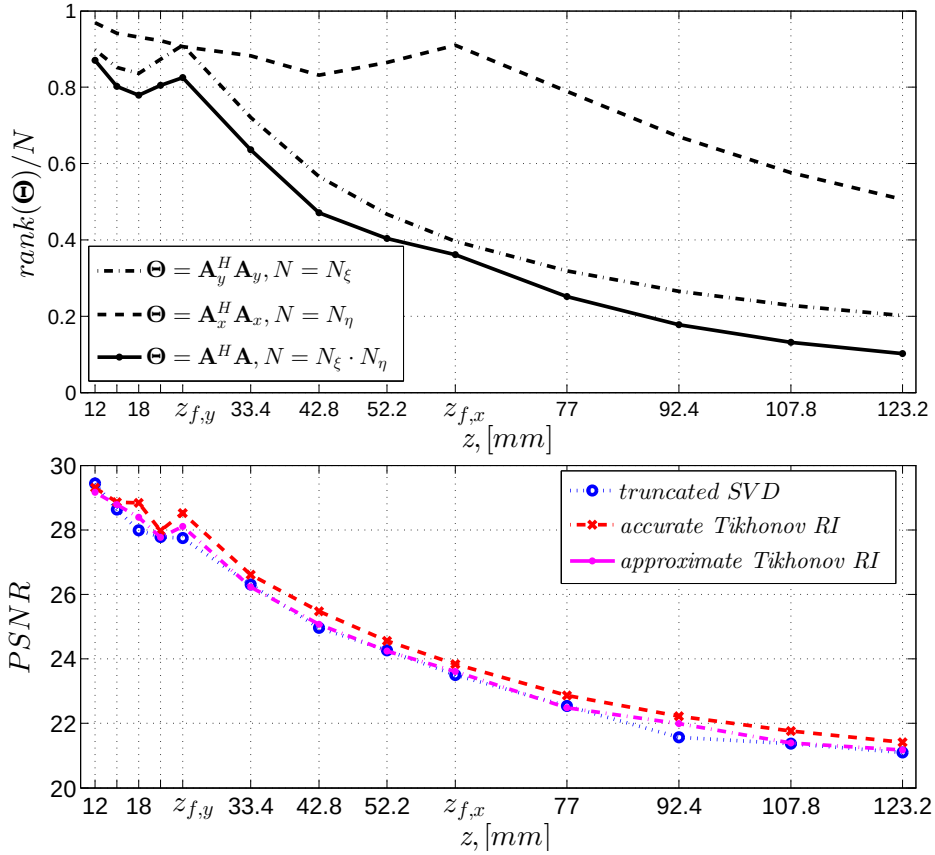

Figure 3.8: The amplitude reconstruction quality in PSNR (bottom image) versus *rank* for $\tau_\varepsilon = 0.02$ (top image) of the transform matrices $\mathbf{A}_y^H\mathbf{A}_y$, $\mathbf{A}_x^H\mathbf{A}_x$ and $\mathbf{A}^H\mathbf{A}$ for rectangular pixels of the same size at the object and sensor plane 8×5 (μm). The results are calculated by the *truncated SVD*, Eq.(3.55); Tikhonov *accurate* (Eq. (3.65), μ^2=0.0015) and *approximate* regularized inverse (Eq. (3.66), μ=0.01) for $z \in [\frac{z_{f,y}}{2}, 2{\cdot}z_{f,x}]$. $z_{f,y}$ =24.1mm, $z_{f,x}$ =61.6mm, Baboon test-image (512×512 pixels), noisy measurement data σ=0.01.

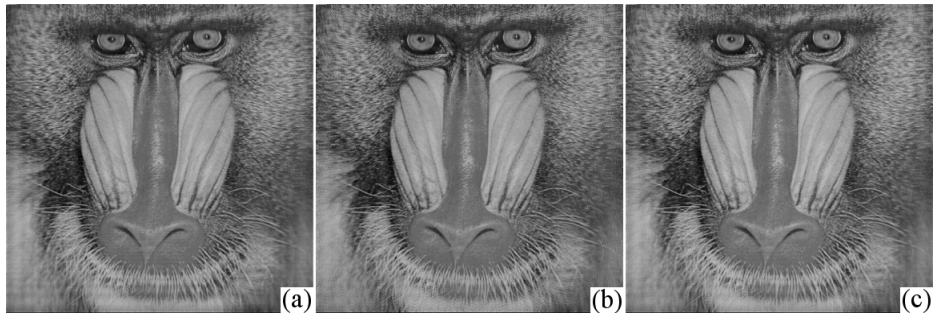

Figure 3.9: Amplitude reconstruction by (a) the truncated SVD, RMSE=0.052, $\tau_x = \tau_y$=429, (b) the accurate Tikhonov RI, RMSE=0.047, and (c) the approximate Tikhonov RI, RMSE=0.049 for square pixels $\Delta_\xi = \Delta_\eta = \Delta_x = \Delta_y = 7.4\mu m$. The results are given for AM, Baboon test-image (512×512 pixels), $z = 1.15 \cdot z_f$ noisy data σ=0.01.

The one-to-one relation between $rank(\mathbf{A}^H\mathbf{A})$ and the reconstruction accuracy in PSNR in Fig. 3.7 is obvious, so we take $z_f = \min(z_{f,x}, z_{f,y})$ [**P1**, cf. Eq. (51)] corresponding to the best accuracy in the interval $[z_{f,y}, z_{f,x}]$. The similar behavior can be seen for noisy data, $\sigma = 0.01$: see in Fig. 3.8.

Recall that in case of $\sigma = 0$ we calculate *rank* for the tolerance $\tau_\varepsilon = 10^{-12}$ and take a quite small regularization parameter $\mu = 10^{-12}$. For noisy data $\sigma = 0.01$ the numerical rank is calculated regarding to the essentially larger tolerance $\tau_\varepsilon = 0.02$ for all z. Analogically, the regularization parameter is taken much larger and different in the accurate and approximate model of the Tikhonov regularized inverse: $\mu^2 = 0.0015$ and $\mu = 0.01$, respectively. If we take, say, $\mu = 0.0387$ for the approximate Tikhonov scheme, the reconstruction accuracy will be systematically worse up to 20% in PSNR.

The curves corresponding to the approximate solution of the Tikhonov regularization (3.66) and the regularization by truncation (3.55) are almost completely merged in Figs. 3.7 and 3.8 with a slight superiority (about 5% in RMSE for $\sigma = 0.01$) in M–DDT. Nevertheless, the reconstructing imaging of the Tikhonov RI in general is better (see Fig. 3.9), and the operation with the regularization parameter is much simpler and computationally efficient comparing with the calculation of SVD and choice of a proper number of singular values for the regularization by truncation.

Table 3.1: The reconstruction accuracy (in PSNR) of the object amplitude (AM, Baboon test-image, 512×512 pixels) found by (column-wise, from left to right) the truncated SVD, the accurate and approximate Tikhonov RI for rectangular pixels.

				PSNR [dB]		
z	σ	τ_y	τ_x	Eq. (3.55)	Eq. (3.65)	Eq. (3.66)
$z = z_{f,y}$	$\sigma = 0$	512	476	39.71	**41.79**	39.75
$z = z_{f,y}$	$\sigma = 0.01$	466	464	27.73	**28.55**	28.12
$z = z_{f,x}$	$\sigma = 0$	217	512	25.11	**25.44**	25.12
$z = z_{f,x}$	$\sigma = 0.01$	203	466	23.49	**23.86**	23.62

The reconstruction imaging of the object amplitudes by the truncated SVD, accurate and approximate Tikhonov RI in the key points $z = z_{f,y}$ and $z = z_{f,x}$ both for noiseless and noisy data is found to be very close (for $z = z_{f,x}$ becomes worse comparing with the results for $z = z_{f,y}$ due to some blurring regarding to y direction (columns) of these images). Thus, we limit ourself by the reconstruction accuracy presented in Table 3.1. In this Table we also present the numbers of the used singular values τ_y and τ_x (for the regularization by truncation), computed according to Eqs. (3.45) for the mentioned experimentally found tolerance τ_ε. Obviously the best result is in favor of the accurate Tikhonov RI.

The comparison of the amplitude reconstructions by the mentioned techniques for AM, square pixels and noisy data σ=0.01 but for $z = 1.15 \cdot z_f$ is illustrated in Fig. 3.9. Here, it can be convinced in a better imaging of the Tikhonov RI with respect to the regularization by truncation. The use of the approximate solution in **P1**–**P2** is dictated by two main reasons. Firstly, the approximate RI is computationally simpler: the straightforward inverse of the huge matrix $\mathbf{A}^H\mathbf{A}$ requires computing of SVD. Secondly, it is found that (depending on the choice of the proper μ) there is no crucial difference in imaging between the accurate and approximate RI, and the reconstruction accuracy in RMSE by Eq. (3.65) is the greatest 5% better than by Eq. (3.66) for $\sigma = 0.01$ (20% for $\sigma = 0$) in case of $z = z_{f,y}$ and this otherness decays not exceeding 4% (6%).

3.7 Choosing the Tikhonov regularization parameter

The regularization parameter μ in **P1**–**P2** and [114, 115] is chosen experimentally just for simplicity. However, it is well known that there are many parameter-choice strategies, which are based on either an estimate of the norm of the perturbation $||\mathbf{u}_z - \mathbf{A}\widehat{\mathbf{u}}_0||_2 = ||\boldsymbol{\varepsilon}||_2$ (*Morozov discrepancy principle*, MDP [191, 156]) or the extraction of some additional information from the given residual and regularization errors: e.g., generalized cross validation [75], L-curve [93], U-curve [123], quasi-optimality criterion [95], normalized cumulative periodogram [94].

MDP

If the complex-valued measurements are given, we could evaluate the noise level $\hat{\sigma}$ using, e.g., the Daubechies wavelets [66, cf. Eqs. (9), (10)]: the expectation $E\langle\|\boldsymbol{\varepsilon}\|^2\rangle = N_x N_y \hat{\sigma}^2$ [109, cf. Eq. (2.14)]. For the same image and pixel sizes at the object and sensor planes in some cases[8][109, §2.3, Theorem 2.6] the regularization parameter μ can be found as the unique zero of the following function:

[8] The regularization parameter μ is calculated provided $\lim_{\mu\to 0} ||\mathbf{u}_z - \mathbf{A}\mathbf{A}_\mu^{-1}\mathbf{u}_z||_2^2 \le ||\mathbf{u}_z - \mathbf{A}\mathbf{A}_\mu^{-1}\mathbf{u}_z||_2^2 \le ||\mathbf{u}_z||_2^2$ (see Eq. (3.65) for $\mathbf{A}_\mu^{-1}$).

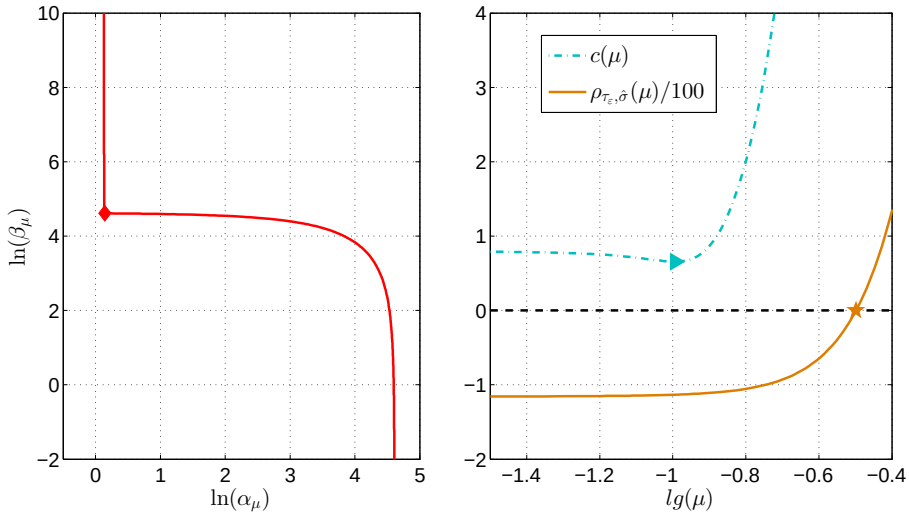

Figure 3.10: Choosing the regularization parameter μ by (left image) L-curve with respect to the maximum curvature in the left corner, and by (right image) NCP (the minimum of the function $c(\mu)$) or MDP (zero of the function $\rho_{\tau_\varepsilon,\hat{\sigma}}(\mu)$). The corresponding optimal μ are marked by bold geometrical elements. In the left image the line of the L-curve going upward corresponds to smaller μ, and the curve to the right corresponds to overregularized solutions with larger μ.

$$\rho_{\tau_\varepsilon,\hat{\sigma}}(\mu) = \sum_{s=1}^{rank(\mathbf{A}^H\mathbf{A})} \left(\frac{\boldsymbol{\chi}^2[s]}{\boldsymbol{\chi}^2[s]+\mu^2} ((\boldsymbol{\Lambda}_y^H \otimes \boldsymbol{\Lambda}_x^H)\mathbf{u}_z)[s] \right)^2 + \tag{3.68}$$
$$+ \sum_{s=rank(\mathbf{A}^H\mathbf{A})+1}^{N_x N_y} \left((\boldsymbol{\Lambda}_y^H \otimes \boldsymbol{\Lambda}_x^H)\mathbf{u}_z)[s] \right)^2 - N_x N_y \hat{\sigma}^2,$$

where the singular values in decreasing order of $\mathbf{A}^H\mathbf{A}$ are represented as the following vector $\boldsymbol{\chi} = \text{vec}\{\boldsymbol{\chi}_x \cdot \boldsymbol{\chi}_y^T\} = \text{vec}\{\boldsymbol{\chi}_y \cdot \boldsymbol{\chi}_x^T\}$. Recall $\boldsymbol{\chi}_y$ and $\boldsymbol{\chi}_x$ are the column vectors of the singular values of $\mathbf{A}_y^H\mathbf{A}_y$ and $\mathbf{A}_x^H\mathbf{A}_x$, respectively. The curve of the function $\rho_{\tau_\varepsilon,\hat{\sigma}}(\mu)$ and the optimal μ by MDP are presented in Fig. 3.10.

Since it is difficult to isolate the impact of the diffraction propagation and accurately estimate the measurement noise $\hat{\sigma}$, then the first type of parameter-choice methods, discrepancy principle based approach is not suitable. It is found that MDP works well only for small noise level (in our synthetic tests $\sigma < 0.02$) and small propagation distances, say $z < 1.5 \cdot z_f$. Moreover, the criterion function (3.68) depends on the numerical rank $rank(\mathbf{A}^H\mathbf{A})$ or, equivalently, on the proper choice of the tolerance τ_ε.

Further we present certain methods of the second type of the methods for choosing regularization parameters, which is found to enable a good estimate of

μ both for the noiseless and noisy data. It should be emphasized that all these criteria could be easily computed in parallel.

GCV

Generalized cross validation (GCV) is based on the philosophy that if an arbitrary element of $\mathbf{u}_z$ is left out, then a regularized solution should predict this observation well. The GCV estimate of the regularization parameter μ can be taken from the measurement data by minimization of the GCV criterion function [75, 95, 180]

$$\Gamma(\mu) = \frac{||\mathbf{A}\mathbf{A}_{\mu}^{-1}\mathbf{A}^H\mathbf{u}_z - \mathbf{u}_z||_2^2}{trace(\mathbf{A}\mathbf{A}_{\mu}^{-1}\mathbf{A}^H - \mathbf{I})^2} = \frac{||\mathbf{c} \circ \mathrm{vec}\{\mathbf{\Lambda}_x^H\mathbf{U}_z\mathbf{\Lambda}_y^*\}||_2^2}{(\mathrm{sum}(\mathbf{c}))^2}, \tag{3.69}$$

where $\mathbf{A}_{\mu}^{-1}$ is defined in Eq. (3.65), *trace* means the trace of a square matrix defined by a sum of the elements on the main diagonal. $\mathbf{c}$ in Eq. (3.69) is a vector constructed from the diagonal elements of the matrix

$$\mathrm{diag}(\mathbf{c}) = (\mathbf{D}_y \otimes \mathbf{D}_x)((\mathbf{D}_y^T\mathbf{D}_y \otimes \mathbf{D}_x^T\mathbf{D}_x) + \mu^2\mathbf{I})^{-1}(\mathbf{D}_y^T \otimes \mathbf{D}_x^T) - \mathbf{I}.$$

The result of choosing of the regularization parameter μ by minimization of the GCV criterion function $\Gamma(\mu)$ is presented in Fig. 3.11.

L-curve

Perhaps the most convenient graphical tool for analysis of discrete ill-posed problems is the so-called *L-curve*, which is a plot (for all valid regularization parameters μ) of the norm $||\mathbf{A}_{\mu}^{-1}\mathbf{A}^H\mathbf{u}_z||_2$ of the regularized solution versus the corresponding residual norm $||\mathbf{u}_z - \mathbf{A}\mathbf{A}_{\mu}^{-1}\mathbf{A}^H\mathbf{u}_z||_2$. It is known that under certain assumptions the L-curve

$$(||\mathbf{u}_z - \mathbf{A}\mathbf{A}_{\mu}^{-1}\mathbf{A}^H\mathbf{u}_z||_2,\ ||\mathbf{A}_{\mu}^{-1}\mathbf{A}^H\mathbf{u}_z||_2 = (\alpha_{\mu}, \beta_{\mu})$$

for Tikhonov regularization (3.65) has two characteristic parts: a *horizontal* part, where the regularized solution $\hat{\mathbf{u}}_0$ is dominated by regularization errors and almost *vertical* part, where $\hat{\mathbf{u}}_0$ is dominated by residual errors. In this way, the L-curve clearly displays the compromise between minimization of these two quantities, which is the heart of any regularization method [91, 95, 109]. In many cases it is advantageous to consider the L-curve in a log-log scale $(\ln\alpha_{\mu}, \ln\beta_{\mu})$. Moreover, the behavior of the L-curve is easily seen in such a scale. The optimal value of μ in terms of the L-curve method is thought to be chosen corresponding to the point of maximum curvature, as near the corner as possible (see Fig. 3.10). Any one-dimensional optimization routine can be used to locate the value of that corresponds to the maximum curvature[9]. This point can be easily found numerically by minimizing the curvature function of the L-curve [93, cf. Eq. (8)]

$$\kappa(\mu) = \frac{\dot{\alpha_{\mu}}\ddot{\beta_{\mu}} - \ddot{\alpha_{\mu}}\dot{\beta_{\mu}}}{\left(\dot{\alpha_{\mu}}^2 + \dot{\beta_{\mu}}^2\right)^{3/2}}, \tag{3.70}$$

[9] It can be, e.g., *corner* routine in [95].

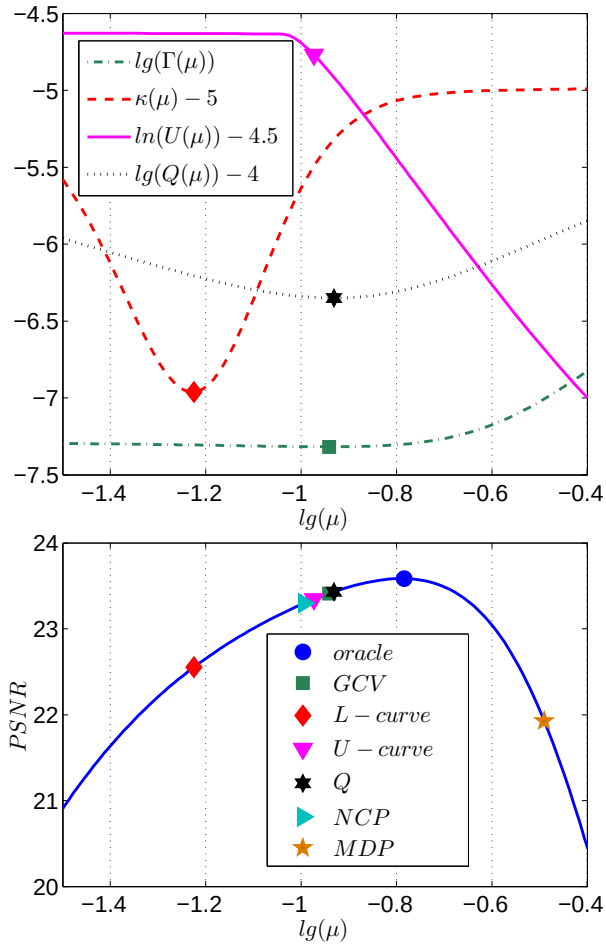

Figure 3.11: The optimal results of different parameter-choice methods and the corresponding reconstruction accuracy by the chosen μ marked by bold geometrical elements. The reconstruction quality is given in PSNR for AM (Lena test-image), $z = 1.5 \cdot z_f$, noisy data $\sigma = 0.03$. The curve of NCP and MDP criterion functions are given before in Fig. 3.10.

where the accents $\dot{}$ and $\ddot{}$ in Eq. (3.70) denote the numerical differentiation operations of the first and second order, respectively, with respect to the regularization parameter μ. The result of the minimization of this criterion function is depicted in Fig. 3.11.

U-curve

Following [123, cf. Eq. (9)], the U-curve is defined as $U(\mu) = \frac{1}{\alpha_\mu} + \frac{1}{\beta_\mu}$ with three characteristic parts: the "vertical"parts corresponding to the regularization parameter, for which α_μ and β_μ are dominated by each other, and a "horizontal"

part, which corresponds to the regularization parameter, where α_μ and β_μ are close to each other. In our experiments we choose the regularization parameter μ considering the U-curve in the log scale

$$\ln U(\mu) = \ln(\alpha_\mu + \beta_\mu) - \ln(\alpha_\mu \beta_\mu). \tag{3.71}$$

The behavior of such a $\ln U$-curve is presented in Fig. 3.11. In our case $\ln U(\mu)$ has a large horizontal part for small μ and then U-like curve to the right for relatively large μ with further very rapid increasing of $\ln U(\mu)$. In Fig. 3.11 we present only a left part of this U-like curve. Following the L-curve method we are looking for a proper μ in the corner between the large horizontal part of $\ln U(\mu)$ and the left vertical part, namely: we take the point of maximum curvature[9].

Quasi-optimality criterion

Quasi-optimality criterion (Q) [92, 156] means that the regularization parameter μ is calculated by minimizing the following function [95, cf. Eq. (2.64)]

$$Q(\mu) = \left(\sum_{s=1}^{N_x N_y} \left(\frac{\boldsymbol{\chi}^2[s]}{\boldsymbol{\chi}^2[s] + \mu^2} \cdot \frac{\mu^2}{\boldsymbol{\chi}^2[s] + \mu^2} ((\boldsymbol{\Lambda}_y^H \otimes \boldsymbol{\Lambda}_x^H)\mathbf{u}_z)[s] \right)^2 \right)^{1/2}. \tag{3.72}$$

It is shown in Fig. 3.11 that the minimum of the criterion function $Q(\mu)$ can be easily found, but only in a reasonable range of values, say $\mu \in [10^{-10}, 1]$ as it is emphasized in **P1.** For larger values of the regularization parameter, say $\mu > 1$, the curve of $Q(\mu)$ has a local maximum and then decreases monotonically.

NCP

The normalized cumulative periodogram (NCP) [95] is basically a cumulated power spectrum, and its computation requires one fast Fourier transform per residual vector $(\mathbf{u}_z - \mathbf{A}\mathbf{A}_\mu^{-1}\mathbf{A}^H\mathbf{u}_z)$. The NCP criterion function is calculated according to [94, Eq. (3.8)]. The expected NCP for white noise is a straight line, and we use the minimum distance from the NCP to a straight line denoted by $c(\mu)$ as the criterion to be minimize in order to choose the regularization parameter μ (see Fig. 3.10). This criterion is found to work unstable for relatively large distances $z > 2 \cdot z_f$ and large amount of noise, say $\sigma = 0.05$, thus we recommend to use in general the latter four mentioned methods: GCV, L- and U-curves, and quasi-optimality.

3.8 Conclusions

Here the developed two-matrix model for the accurate discrete diffraction propagation is presented. The contribution of the author of this thesis is the analysis of M–DDT (originated in **P1**), its properties and resulting reconstruction quality for different parameters of the optical system: the size of the object and given measurements, pixel size, propagation distances z, etc. It is of importance because M–DDT (as well as F–DDT) is used in our phase-retrieval algorithms **P3**–**P6**. Generally, M–DDT (F–DDT) may be employed in many application areas where

the precise discrete-to-discrete model is dictated by the use of digital devices (in SLM–CCD setups): e.g., for the wave field synthesis [111, 112] or holographic projection [125, 126].

In Section 3.5.3 we refine certain aspects related to the straightforward approach of the backward propagation for ill-posed matrices using the regularization by truncation. It is shown that in case of noiseless or a small amount of noise the truncated SVD is a good alternative for relatively fast implementation of the inverse of M–DDT, if the matrices of the eigenvectors are given. However, since the proper numerical rank can not be accurately determined, and due to the use of time-consuming SVD we typically use the Tikhonov RI model, which gives, in addition, a better reconstruction accuracy, especially for large z and noisy data.

Figures 3.7 and 3.8 clarify our choice of a single in-focus distance in case of rectangular images or pixels at the object and sensor planes: $z_f = \min(z_{f,x}, z_{f,y})$ [**P1**, Eq. (51)].

Here we present the accurate M–DDT propagation model in the Kronecker product form and visually explanation our suggestion to use the approximate Tikhonov RI in **P1**. The accurate model systematically gives a better reconstruction accuracy, but it is very difficult in use due to a very high dimension of the transform matrix $\mathbf{A}$.

It is also shown that the potential reconstruction accuracy can be predicted by the numerical rank or conditioning of individual matrices related to the transform of rows and columns of images (Eqs. (3.47)). It is connected to our further prediction analysis via a sum of such individual transform matrices in Section 4.3.

Finally, in Section 3.7 we consider the choosing of the Tikhonov regularization parameter μ : it is found that the conventional methods work quite well for the interferometric model where (noisy) complex-valued measurements are given. The problem consists of the noise level and ill-posedness of the transform matrix. In general case GCV, L-/U-curve or quasi-optimal methods enables a proper choice of μ. However, the situation is dramatically different in case of phase-retrieval when the phase is not given and we deal with a number of different sensor planes. This case of the parameter choosing is out of scope of this thesis but is our further work to be done.

Chapter 4

Multi-plane iterative phase retrieval

It has been mentioned that a conventional commodity sensor detects only the intensity of the light wave field and the phase is lost in this physical measurements. In practice we have no complex-valued observation $\mathbf{u}_z$ in the single plane discrete diffraction model (Fig. 3.1), and the object $\mathbf{u}_0$ can not be estimated straightforward by the backward wave field propagation according to, e.g., the conventional propagation models (see Section 2.2) or by the inverse of M–DDT from Section 3.5. Following the idea of the numerical recalculation of the object wave field from a number of intensity observations from Section 2.4, in this Chapter we consider developed computational *parallel iterative** multi-plane phase-retrieval algorithms, initially with no incorporate object filtering, as they were improved. In Section 4.2 the initial multi-plane scenario of phase retrieval, the MF–DDT algorithm is presented. Then, in Section 4.4 the augmented Lagrangian based parallel phase-retrieval algorithm and its modification for the known object structure: for the amplitude- (Section 4.4.3, the AL–A algorithm) and phase-only (Section 4.4.4 and 4.4.5, the gradient descent and Gauss–Newton AL–Ph algorithms) object to be reconstructed.

4.1 Propagation models

A volumetric wave field is generated by a single transverse object wave field $u_0(\xi, \eta)$ (see Fig. 2.2), however the 3D wave field is given only in a number of noisy intensity observations $\{|u_r(x,y)|^2\}_{r=1}^K$, at K different sensor planes parallel to the object plane at distances $z_r = z_1 + (r-1)\cdot\Delta_z$ from it. Here z_1 is the distance between the object and the first sensor plane, Δ_z is a fixed distance between the observation planes. We need to recover the phase in $\{u_r(x,y)\}_r$ and then reconstruct the complex-valued object $\hat{u}_0$ using these complex-valued estimates $\widehat{u}_r$, $r = 1, ...K$.

Again, it is assumed that the wave field distributions at the object and sensor planes are pixelated, i.e. they are pixel-wise invariant. Thus, we arrive at a discrete-to-discrete model but now with a number of wave field distributions as

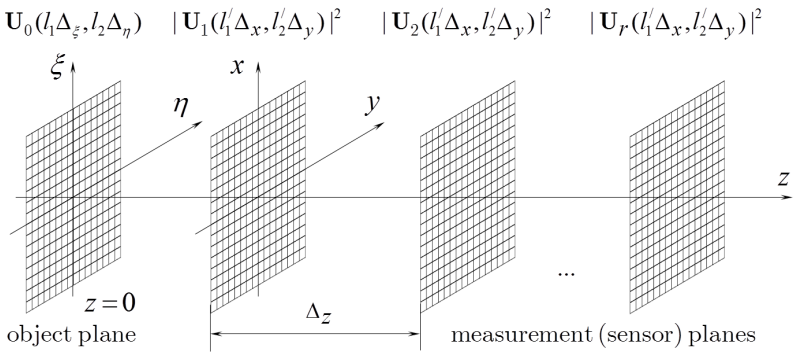

Figure 4.1: Discrete model of the multi-plane phase retrieval. $\mathbf{U}_0[l_1, l_2]$ and $\mathbf{U}_r[l_1', l_2']$ $(r = 1, ...K)$ are discrete 2D complex amplitudes at the object and measurement planes, respectively (cf. Fig. 2.2). Δ_z is a fixed distance between the measurement planes.

it is illustrated in Fig. 4.1. The link between the wave field distributions at the object and sensor planes is given in the following general form

$$\mathbf{u}_r = \mathbf{A}_r \cdot \mathbf{u}_0, \quad r = 1, ...K, \tag{4.1}$$

where the column vectors $\mathbf{u}_0$ and $\mathbf{u}_r$ denote the input and output of the coherent imaging system and $\mathbf{A}_r$ is a transform matrix described the forward wave field propagation from the object to the r-th sensor plane **P4**. Let us consider the discrete diffraction propagation model used to calculate the sensor plane wave field distributions $\mathbf{u}_r$.

4.1.1 Free space propagation

Let $\mathbf{M}_r$ be a discrete 2D distribution of the transfer function corresponding to the free space diffraction propagation to the distance z_r. It can be computed as the sampled version of the conventional ASD H_r or the Fresnel transfer function G_r; via the Fourier transform of the RS [196] or Fresnel diffraction kernels (with or without averaging, see Section 3.2.3). Following the propagation model (3.36) the result of the free space forward wave field propagation of the single size can be represented as follows

$$\mathbf{u}_r = \mathrm{vec}\{F^{-1}\{F\{\mathbf{U}_0\} \circ \mathbf{M}_r\}\}, \quad r = 1, ...K. \tag{4.2}$$

Note that in case of the double size $\mathbf{M}_r$ and realization via FFT (e.g., using F–DDT as in **P4**–**P5**, [149]) the difference consists of the zero-padding of the object $\mathrm{ZP}_{N_x' \times N_y'}\{\mathbf{U}_0\}$ and extraction of the center part of the resulting sensor plane distribution according to Eqs. (3.25)–(3.28). The image size at the object plane is taken as a multiple of 2 and the size of the sensor plane is defined by Eqs. (3.38); $N_1 = N_x' + N_\xi$, $N_2 = N_y' + N_\eta$.

The forward wave field propagation can be also calculated by M–DDT (see Eqs. (3.16)–(3.17) in Section 3.2.1) what enables the accurate pixel-to-pixel mapping $\mathbf{u}_0$ to $\mathbf{u}_r$ for images and pixels of different sizes at the object and the r-th sensor

planes. Again we obtain a single transform matrix in the form of the Kronecker product

$$\mathbf{u}_r = \mathbf{A}_r \cdot \mathbf{u}_0, \;\; \mathbf{A}_r = \mathbf{X}_r \otimes \mathbf{Y}_r, \qquad r = 1, ...K, \tag{4.3}$$

where $\mathbf{Y}_r$ and $\mathbf{X}_r$ are the averaged M–DDT transform matrices with respect to y (columns) and x (rows) directions of the object image. These transform matrices are calculated according to Eqs. (3.14)–(3.13), but, in contrast to what we have in Section 3.2.1, for different propagation distances z_r. It is emphasized by the additional subindices r of the transform matrices.

4.1.2 Observation model

Assume that we make a set of K experiments, and therefore a number of intensity measurements at the sensor planes are given. Then, we can formulate the phase problem to be solved as follows: *reconstruct the complex-valued object distribution* $\mathbf{u}_0$ *using the noisy intensity observations* $\{\mathbf{o}_r\}_r$, which can be represented by the following vector-matrix notation[1]

$$\mathbf{o}_r = |\mathbf{u}_r|^2 + \boldsymbol{\varepsilon}_r, \qquad r = 1, ...K, \tag{4.4}$$

where, in contrast to Eq. (3.41), the noise is assumed to be *real-valued* i.i.d. zero-mean Gaussian (for simplicity and referring to the central limit theorem) with the variance σ_r^2, $\boldsymbol{\varepsilon}_r[l'] \sim \mathcal{N}(0, \sigma_r^2)$, independent for different r. The error $\boldsymbol{\varepsilon}_r$ is considered as a result of various small degradation factors such as sensor noise. Note that it can be also used more complex distributions for $\boldsymbol{\varepsilon}_r$, such as Poissonian or mixed Poissonian–Gaussian [66].

4.2 Multiple plane Frequency DDT (MF–DDT)

As it is mentioned in Section 2.4, the stability and convergence of the iterative phase-retrieval algorithms as well as the accuracy of the resulting solutions are not guaranteed in case of presence of noise. In **P3** and [146] we developed our initial multi-plane iterative phase-retrieval techniques which enables a significantly improvement of the reconstruction quality by the aggregation of a number of the object estimates computed in the parallel phase-retrieval procedure.

In Section 2.4.3 we discuss the reconstruction of the volumetric wave field by the circular wave field propagation from one sensor plane to another one as it is presented in [8, Fig. 2]. Then, Eq. (2.12), describing the modern successive SBMIR phase-retrieval algorithm, can be rewritten in our vector-matrix notations as follows

$$\widehat{\mathbf{u}}_{\chi(t+1)} = \mathbf{A}_{\chi(t+1),\chi(t)} \cdot \left[\frac{\sqrt{\mathbf{o}_{\chi(t)}}}{|\widehat{\mathbf{u}}_{\chi(t)}|} \circ \widehat{\mathbf{u}}_{\chi(t)} \right], \qquad t = 1, 2, ... \tag{4.5}$$

where $\mathbf{A}_{\chi(t+1),\chi(t)}$ is the transform matrix of the wave field propagation from the $\chi(t)$-th to $\chi(t+1)$-th sensor plane, and the index of the sensor plane is defined

[1] In order to avoid negative values of $\mathbf{o}_r[l']$, in our numerical simulations we generate the observations as $\mathbf{o}_r[l'] = \max(|\mathbf{u}_r[l']|^2 + \boldsymbol{\varepsilon}_r[l'], c_0)$, where c_0 is a small positive DC constant (typically $c_0 = 10^{-4}$).

by Eq. (2.13). The operation in the square brackets of Eq. (4.5) is element-wise, i.e. $\frac{\sqrt{\mathbf{o}_{\chi(t)}}}{|\widehat{\mathbf{u}}_{\chi(t)}|}$ is a vector obtained by the element-wise division of the vector of the amplitude obtained from the given noisy intensity $\sqrt{\mathbf{o}_{\chi(t)}}$ at the $\chi(t)$-th sensor plane by the calculated amplitude $|\widehat{\mathbf{u}}_{\chi(t)}|$. Thus, $\left[\frac{\sqrt{\mathbf{o}_{\chi(t)}}}{|\widehat{\mathbf{u}}_{\chi(t)}|} \circ \widehat{\mathbf{u}}_{\chi(t)}\right]$ is a vector computed by means of a replacement of the module of $\widehat{\mathbf{u}}_{\chi(t)}$ by $\sqrt{\mathbf{o}_{\chi(t)}}$, keeping the calculated phase at that plane. Moreover, the initial guess for the phase can also be a random vector.

In contrast to successive phase-retrieval algorithms, we focus on the object plane. A multi-plane variation of GS is derived from the LS estimation of $\mathbf{u}_0$ assuming that complex-valued wave field estimates at the sensor plane $\mathbf{u}_r$ are available. Following the variational maximum likelihood (ML) approach for the Gaussian noise distribution in the observation model (4.4), the object reconstruction is formulated by the following criterion function to be minimized (cf. Eq. (3.64))

$$\mathcal{J} = \sum_{r=1}^{K} \frac{1}{\sigma_r^2} ||\mathbf{u}_r - \mathbf{A}_r \cdot \mathbf{u}_0||_2^2 + \mu \cdot ||\mathbf{u}_0||_2^2, \tag{4.6}$$

where σ_r^2 is the variance of the noise at the r-th sensor plane. The quadratic term in Eq. (4.6) appears as the minus logarithm of the Gaussian likelihood function corresponding to the propagation model (4.1). The following penalty term is the regularization including prior information on the object distribution $\mathbf{u}_0$ to be reconstructed. The regularization parameter μ in Eq. (4.6) defines a balance between the residual error of the propagation model and a priori given by the penalty. Numerous forms for the penalty are used in literature on digital image processing derived from speculations varying from probabilistic modeling of image distribution priors to heuristic constructions [91, 109], but in **P3**–**P5** and [146, 147] we again use a simple but efficient quadratic Tikhonov's penalty [219] as for M–DDT.

In **P3** we originate the *Multiple plane Frequency DDT* ($MF-DDT$) phase-retrieval algorithm. In MF–DDT the wave fields at all measurement planes are

---

Algorithm: $MF-DDT$
Input: $\{\mathbf{o}_r\}_{r=1}^K$
Initialization: $\mathbf{u}_0^0$
Repeat for $t = 0, 1, 2, ...$
Repeat for $r = 1, ...K$
1. Forward propagation:
$\mathbf{u}_r^t = \mathbf{A}_r \cdot \mathbf{u}_0^t$
End on r
2. Object update:
$\mathbf{u}_0^{t+1} = \left(\sum_{r=1}^K \frac{1}{\sigma_r^2} \mathbf{A}_r^H \mathbf{A}_r + \mu \cdot \mathbf{I}\right)^{-1} \cdot \sum_{r=1}^K \frac{1}{\sigma_r^2} \mathbf{A}_r^H \cdot \left[\frac{\sqrt{\mathbf{o}_r}}{|\mathbf{u}_r^t|} \circ \mathbf{u}_r^t\right] =$
$= \sum_{r=1}^K \frac{1}{\sigma_r^2} \mathbf{A}_\mu^{-1} \mathbf{A}_r^H \cdot \left[\frac{\sqrt{\mathbf{o}_r}}{|\mathbf{u}_r^t|} \circ \mathbf{u}_r^t\right]$
End on t

---

computed by the free space forward diffraction propagation (Step 1) using M–DDT or F–DDT. The object update (Step 2) is computed from the minimum condition $\frac{\partial}{\partial \mathbf{u}_0^*}\mathcal{J} = \sum_{r=1}^{K} \frac{1}{\sigma^2}[\mathbf{A}_r^H \mathbf{A}_r \mathbf{u}_0 - \mathbf{A}_r \mathbf{u}_r] + \mu \cdot \mathbf{u}_0 = 0$. The amplitude is kept to be equal to the square root of the noisy intensity from the sensor plane observation similar to SBMIR (4.5) and the phase is iteratively replaced.

Note that the object wave field reconstruction in MF–DDT can be interpreted as the summation of K object estimates calculated by the backward propagation of $\{\mathbf{u}_r^t\}_r$ with the transform matrices $\mathbf{A}_\mu^{-1}\mathbf{A}_r^H$. In contrast to Eq. (3.65), we calculate the inverse of a sum of the averaged transform matrices $\mathbf{A}_r^H\mathbf{A}_r$,

$$\mathbf{A}_\mu^{-1} = \left(\sum_{r=1}^{K} \frac{1}{\sigma_r^2}\mathbf{A}_r^H\mathbf{A}_r + \mu \cdot \mathbf{I}\right)^{-1}, \tag{4.7}$$

where $K \geq 1$ and the size of the matrix $\mathbf{A}_\mu^{-1}$ is $N_x N_\xi \times N_y N_\eta$.

In case of well conditioning and invertibility of the propagation transform matrices (e.g., for small distances $z_1 < z_f$ or if we use ASD instead of M–DDT) $\mathbf{A}_r^H\mathbf{A}_r = \mathbf{I}$ and no regularization is required, $\mu = 0$. If $\sigma_r^2 = \sigma^2\ \forall r$, then $\mathbf{A}_\mu^{-1} = \frac{\sigma^2}{K}$ $\forall r$ and the MF–DDT algorithm has much simpler form [**P4**, cf. Eq. (5)]

$$\begin{aligned} \mathbf{u}_r^t &= \mathbf{A}_r \cdot \mathbf{u}_0^t, \quad t = 0, 1, ... \\ \mathbf{u}_0^{t+1} &= \frac{1}{K}\sum_{r=1}^{K} \mathbf{A}_r^H \cdot \left[\frac{\sqrt{\mathbf{o}_r}}{|\mathbf{u}_r^t|} \circ \mathbf{u}_r^t\right]. \end{aligned} \tag{4.8}$$

4.3 Conditioning and reconstruction accuracy

It is found that the quality of phase retrieval can be indicated by the numerical rank ($rank(\sum_{r=1}^{K} \mathbf{A}_r^H\mathbf{A}_r)$) or conditioning number ($cond(\sum_{r=1}^{K} \mathbf{A}_r^H\mathbf{A}_r)$) of a sum of averaged transform matrices analogically to the way it is presented in Section 3.5.2. The interesting point is that despite the decrease of $rank(\sum_{r=1}^{K} \mathbf{A}_r^H\mathbf{A}_r)$, $K > 1$, the behaviour of *rank* or *cond* for $z_1 > z_f$ looks similar to what we have for K=1. For $z_1 < z_f$, however, *rank* takes its maximum value (see Fig. 4.2 and Fig. 4.4, for K=5), and *cond* significantly decreases (see Fig. 4.3 and Fig. 4.5). As before, larger *rank* or smaller *cond* corresponds to a better reconstruction accuracy: see [**P4,** Fig. 2 and Table 1] for $z = \frac{1}{2} \cdot z_f$ and $K = \{3, 5, 10\}$.

In general, due to the very large dimension of the transform matrices $\mathbf{A}_r$, it is difficult to calculate *rank* or *cond* for the sum of $\mathbf{A}_r^H\mathbf{A}_r \in \mathbb{C}^{N_\xi N_\eta \times N_\xi N_\eta}$. However, we have found that $rank(\sum_{r=1}^{K} \mathbf{X}_r^H\mathbf{X}_r) \cdot rank(\sum_{r=1}^{K} \mathbf{Y}_r^H\mathbf{Y}_r)$ can be used as a good evaluation of $rank(\sum_{r=1}^{K} \mathbf{A}_r^H\mathbf{A}_r)$. Indeed, since $rank(\mathbf{X}_r \otimes \mathbf{Y}_r) = rank(\mathbf{X}_r) \cdot rank(\mathbf{Y}_r)$ [99] and

$$\begin{aligned} &\sum_{r=1}^{K} \mathbf{A}_r^H\mathbf{A}_r = \sum_{r=1}^{K} (\mathbf{X}_r^H\mathbf{X}_r \otimes \mathbf{Y}_r^H\mathbf{Y}_r) = \\ &= \left(\sum_{r=1}^{K} \mathbf{X}_r^H\mathbf{X}_r\right) \otimes \left(\sum_{r=1}^{K} \mathbf{Y}_r^H\mathbf{Y}_r\right) - \sum_{\substack{s,r=1 \\ s\neq r}}^{K} (\mathbf{X}_s^H\mathbf{X}_s \otimes \mathbf{Y}_r^H\mathbf{Y}_r), \end{aligned} \tag{4.9}$$

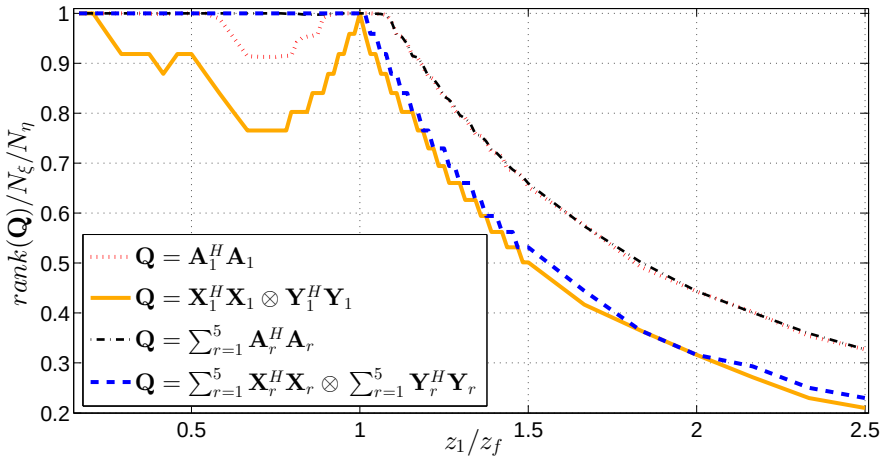

Figure 4.2: Comparison of the numerical ranks of the averaged matrices $\sum_{r=1}^{K} \mathbf{A}_r^H\mathbf{A}_r$ and $\sum_{r=1}^{K} \mathbf{X}_r^H\mathbf{X}_r \otimes \sum_{r=1}^{K} \mathbf{Y}_r^H\mathbf{Y}_r$ for $K = \{1, 5\}$, $\Delta_z = 0.5\ \mu m$, $z_f = 4.1\ mm$, square images ($N_\xi = N_\eta = 48$) and pixels ($\Delta_\xi = \Delta_\eta = 6.7\ \mu m$) of the same size at the object and sensor planes.

then $rank(\sum_{r=1}^{K} \mathbf{A}_r^H\mathbf{A}_r)$ can be bounded as

$$rank\left(\sum_{r=1}^{K} \mathbf{X}_r^H\mathbf{X}_r\right) rank\left(\sum_{r=1}^{K} \mathbf{Y}_r^H\mathbf{Y}_r\right) \leq rank\left(\sum_{r=1}^{K} \mathbf{A}_r^H\mathbf{A}_r\right) + \quad (4.10)$$

$$+ rank\left(\sum_{\substack{s,r=1 \\ s\neq r}}^{K} (\mathbf{X}_s^H\mathbf{X}_s \otimes \mathbf{Y}_r^H\mathbf{Y}_r)\right) \leq \sum_{r=1}^{K} rank(\mathbf{X}_r^H\mathbf{X}_r) rank(\mathbf{Y}_r^H\mathbf{Y}_r),$$

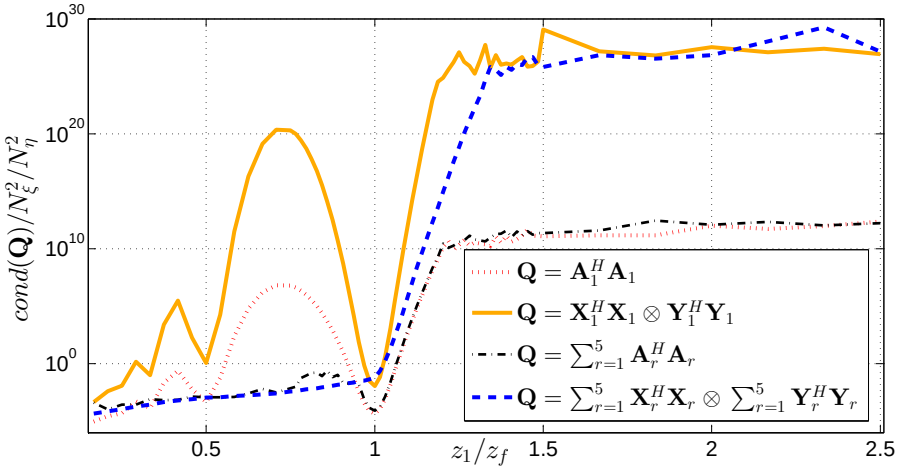

Figure 4.3: Comparison of the conditioning number of the averaged matrices $\sum_{r=1}^{K} \mathbf{A}_r^H\mathbf{A}_r$ and $\sum_{r=1}^{K} \mathbf{X}_r^H\mathbf{X}_r \otimes \sum_{r=1}^{K} \mathbf{Y}_r^H\mathbf{Y}_r$ for $K = \{1, 5\}$ and the same settings as in Fig. 4.2.

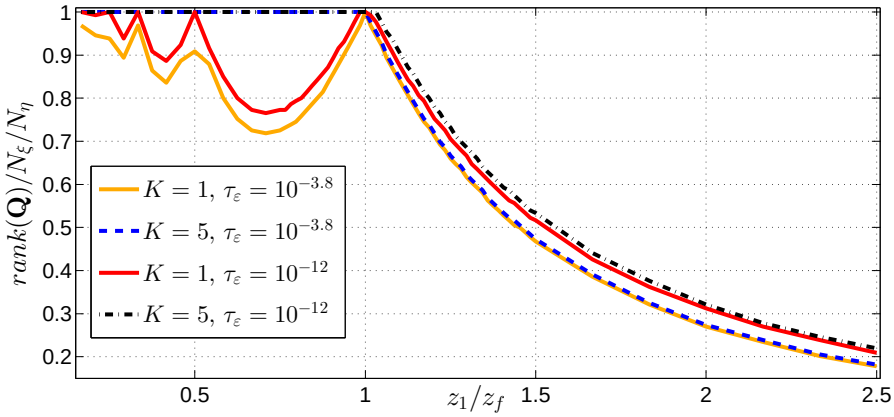

Figure 4.4: Comparison of the numerical ranks of the averaged matrices $\mathbf{Q} = \sum_{r=1}^{K} \mathbf{X}_r^H \mathbf{X}_r \otimes \sum_{r=1}^{K} \mathbf{Y}_r^H \mathbf{Y}_r$ computed by different tolerances $\tau_\varepsilon = 10^{-12}$ and $\tau_\varepsilon = 10^{-3.8}$ for $K = \{1, 5\}$. Here $\Delta_z = 2\ \mu m$, $z_f = 21.6\ mm$, square images ($N_\xi = N_\eta = 256$) and pixels ($\Delta_\xi = \Delta_\eta = 6.7\ \mu m$) of the same size at the object and sensor planes (see **P4**).

In practice

$$rank\left(\sum_{r=1}^{K} \mathbf{X}_r^H \mathbf{X}_r\right) rank\left(\sum_{r=1}^{K} \mathbf{Y}_r^H \mathbf{Y}_r\right) - rank\left(\sum_{\substack{s,r=1 \\ s \neq r}}^{K} (\mathbf{X}_s^H \mathbf{X}_s \otimes \mathbf{Y}_r^H \mathbf{Y}_r)\right) \quad (4.11)$$

is often negative and therefore Eq. (4.11) is useless as the lower bound for $rank(\sum_{r=1}^{K} \mathbf{A}_r^H \mathbf{A}_r)$.

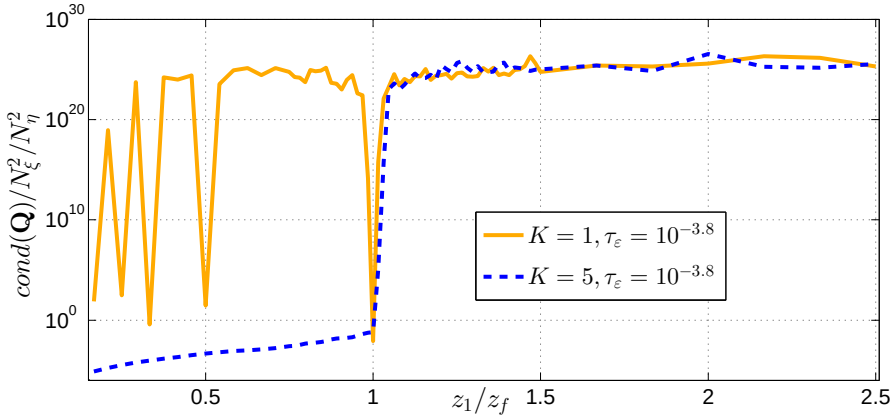

Figure 4.5: Conditioning number of the averaged matrices $\mathbf{Q} = \sum_{r=1}^{K} \mathbf{X}_r^H \mathbf{X}_r \otimes \sum_{r=1}^{K} \mathbf{Y}_r^H \mathbf{Y}_r$ for $K = \{1, 5\}$ and settings similar to Fig. 4.4.

Thus, we omit the second term and arrive at

$$rank\left(\sum_{r=1}^{K}\mathbf{X}_r^H\mathbf{X}_r\right)rank\left(\sum_{r=1}^{K}\mathbf{Y}_r^H\mathbf{Y}_r\right)\leq rank\left(\sum_{r=1}^{K}\mathbf{A}_r^H\mathbf{A}_r\right). \tag{4.12}$$

Fig. 4.2 demonstrate the use of Eq. (4.12). In Fig. 4.3 it is shown that an inequality similar to Eq. (4.12) can be used for the conditioning numbers with respect to the individual transform matrices $\mathbf{X}_r^H\mathbf{X}_r$ and $\mathbf{Y}_r^H\mathbf{Y}_r$ too.

Since for $z = z_f$ the transform matrices should be well-posed and no regularization should be required, then the tolerance τ_ε used for the calculation of *rank* is taken with respect to $z = z_f$ as follows

$$\tau_\varepsilon = \max_{\tau_\varepsilon}(\tau_\varepsilon : rank(\mathbf{X}_1^H\mathbf{X}_1)\cdot rank(\mathbf{Y}_1^H\mathbf{Y}_1) = N_\xi \cdot N_\eta). \tag{4.13}$$

In Fig. 4.4 we present the comparison of the computed numerical ranks for the tolerance $\tau_\varepsilon = 10^{-3.8}$ found according to Eq. (4.13) and $\tau_\varepsilon = 10^{-12}$ as before in our experiments with the M-DDT matrices in Chapter 3.5. It can be seen that for smaller tolerance $rank(\sum_{r=1}^{K}\mathbf{X}_r^H\mathbf{X}_r \otimes \sum_{r=1}^{K}\mathbf{Y}_r^H\mathbf{Y}_r)$ becomes only slightly larger but it may lead to an uncertainty in the behavior of the numerical rank in the case when the propagation distance is near z_f or $z < z_f$. For instance, we have mentioned that for say $z = 1.05 \cdot z_f$ there is no perfect reconstruction so *rank* should indicate that.

A proper selection of the regularization parameter μ is an important point of the variation formulation in inverse imaging. However, it is difficult to use the straightforward parameter-choice methods, like the L-curve or U-curve mentioned in Section 3.7 for the multiple plane phase-retrieval scenario. Moreover, it is hard to realize the direct computation of the inverse of $\mathbf{A}_\mu^{-1}$ (Eq. (4.7)) due to its very large dimension. Thus, the Tikhonov parameter μ in **P3**–**P5** and [146, 147] is chosen experimentally, and the analysis of the choosing the regularization parameter is beyond the scope of this thesis.

4.4 Augmented Lagrangian technique

It is found that in case of noiseless data ($\sigma = 0$) or small amount of noise (say, $\sigma = 0.01$) the parallel MF–DDT phase-retrieval algorithm gives a better reconstruction accuracy comparing with the successive one by example of SBMIR (more details are given in **P3** and [146]). However, the situation is dramatically different in general case with a significant noise level of the intensity observations $\sigma > 0.01$ and $z > z_f$ resulting in strongly ill conditioning of the diffraction propagation operators.

The regularization only is found not to be enough[2] – some additional constants related to both the wave field amplitude and phase (or to the real and imaginary parts) are required in order to balance the accurate forward wave field propagation and fitting to the given observations.

[2] Proper regularization parameters for MF–DDT and the augmented Lagrangian based phase-retrieval algorithm are chosen experimentally. The corresponding Matlab code for phase retrieval is available on the project web page [1].

4.4.1 Variational formulation of phase retrieval

Let us consider the variational ML formulation of the augmented Lagrangian based phase-retrieval algorithm with respect to noisy measurements. The straightforward setting for the Gaussian noise distributions in the observation model (4.4) results in the following criterion (cf. Eq. (4.6))

$$\mathcal{J} = \sum_r \frac{1}{2\sigma_r^2} ||\mathbf{o}_r - |\mathbf{u}_r|^2||_2^2 + \mu \cdot ||\mathbf{u}_0||_2^2, \tag{4.14}$$

where the first summand is the quadratic fidelity term corresponding to the observation model (see **P4** for metrics for the fidelity terms) and the second term is the Tikhonov regularization. Using this new criterion (4.14) we require the accurate forward wave field propagation (4.1), and formulate the object reconstruction as the following constrained optimization

$$\begin{aligned} &\widehat{\mathbf{u}}_0 = \arg\min_{\mathbf{u}_0} \sum_{r=1}^{K} \frac{1}{2\sigma_r^2} ||\mathbf{o}_r - |\mathbf{u}_r|^2||_2^2 + \mu \cdot ||\mathbf{u}_0||_2^2 \\ &\text{subject to } \mathbf{u}_r = \mathbf{A}_r \cdot \mathbf{u}_0, \quad r = 1, ...K. \end{aligned} \tag{4.15}$$

The regularization parameter μ in Eq. (4.15) defines a balance between the prior information on the object and the fitting of calculated intensities of the wave fields at the sensor planes to the given observations. If $\mu = 0$ the solution $\hat{\mathbf{u}}_0$ minimizes $\sum_r \frac{1}{2\sigma_r^2} ||\mathbf{o}_r - |\mathbf{u}_r|^2||_2^2$ ignoring the fact that the data $\{\mathbf{o}_r\}_r$ are noisy. It can result in noisy and non-smooth $\hat{\mathbf{u}}_0$. If $\mu > 0$ and (comparatively) large, then the noise effects are well suppressed but the solution $\hat{\mathbf{u}}_0$ can be oversmoothed and important features lost. The additional constraint corresponds to the forward propagation of the object to different sensor planes. The constrained optimization problem (4.15) can be represented using the augmented Lagrangian [98, 185] so the criterion (with complex-valued variables) to be minimized is of the form

$$\begin{aligned} &\mathcal{J}_{AL}(\{\mathbf{o}_r\}, \mathbf{u}_0, \{\mathbf{u}_r\}, \{\mathbf{\Lambda}_r\}) = \sum_{r=1}^{K} \frac{1}{\sigma_r^2} [\frac{1}{2} ||\mathbf{o}_r - |\mathbf{u}_r|^2||_2^2 + \\ &+ \frac{1}{\gamma_r} ||\mathbf{u}_r - \mathbf{A}_r \cdot \mathbf{u}_0||_2^2 + \frac{2}{\gamma_r} \operatorname{Re}\{\mathbf{\Lambda}_r^H (\mathbf{u}_r - \mathbf{A}_r \cdot \mathbf{u}_0)\}] + \mu \cdot ||\mathbf{u}_0||_2^2, \end{aligned} \tag{4.16}$$

where $\{\mathbf{\Lambda}_r\} \in \mathbb{C}^{N_x N_y}$ are the Lagrange multipliers. We refer to [162, Chapters 15–17] for more details on the theory of the augmented Lagrangian method.

In Eq. (4.16) the constraint $\mathbf{u}_r - \mathbf{A}_r \cdot \mathbf{u}_0 = 0$ is used both in the quadratic and linear terms with the positive penalty coefficients $\frac{1}{\gamma_r}$. If we keep only the quadratic terms the augmented Lagrangian becomes the penalty criterion. As a rule it leads to computational difficulties because this criterion can be very ill conditioned. If we keep only the linear term the augmented Lagrangian becomes the standard Lagrangian. However, the saddle point of this standard Lagrangian is unstable. It results in the problems of numerical solutions. The stability of the saddle point of the augmented Lagrangian is one of the principal advantages of this criterion [74]. Note that the linear terms $\frac{1}{\gamma_r} \mathbf{\Lambda}_r^H (\mathbf{u}_r - \mathbf{A}_r \cdot \mathbf{u}_0)$ and $\frac{1}{\gamma_r} \mathbf{\Lambda}_r^T (\mathbf{u}_r - \mathbf{A}_r \cdot \mathbf{u}_0)^*$

in $\mathcal{J}_{AL}$ are mutually conjugate, i.e. we control the real and imaginary part of the discrepancy $\mathbf{u}_r - \mathbf{A}_r \cdot \mathbf{u}_0$.

4.4.2 Augmented Lagrangian algorithm (AL)

A search of this saddle point requires the minimization of the criterion (4.16) on $\mathbf{u}_0$ and $\{\mathbf{u}_r\}$, and maximization on the vectors of the Lagrange multipliers $\{\mathbf{\Lambda}_r\}$. The optimization of the AL criterion can be realized by partitioning of the variables $\mathbf{u}_0$ and $\{\mathbf{u}_r\}$ into several blocks according to their roles following the *alternating direction method of multipliers* (ADMM, see, e.g., [2, 46]) and optimizing of (4.16) with respect to each block by fixing all other blocks at each inner iteration [19] as in the following algorithm

$$
\begin{aligned}
&\textbf{Repeat for } t = 1, 2, ... \\
&\textbf{Repeat for } r = 1, ...K \\
&\mathbf{u}_r^{t+1} = \arg\min_{\mathbf{u}_r} \mathcal{J}_{AL}(\mathbf{o}_r, \mathbf{u}_0^t, \mathbf{u}_r, \mathbf{\Lambda}_r^t) \\
&\mathbf{\Lambda}_r^{t+1} = \mathbf{\Lambda}_r^t + \alpha_r \cdot (\mathbf{u}_r^t - \mathbf{A}_r \cdot \mathbf{u}_0^t) \\
&\textbf{End on } r \\
&\mathbf{u}_0^{t+1} = \arg\min_{\mathbf{u}_o} \mathcal{J}_{AL}(\{\mathbf{o}_r\}, \mathbf{u}_0, \{\mathbf{u}_r^{t+1}\}, \{\mathbf{\Lambda}_r^t\}) \\
&\textbf{End on } t
\end{aligned}
\tag{4.17}
$$

It leads to the iterative parallel augmented Lagrangian (AL) based algorithm [**P4**, cf. Eqs. (21)] presented below.

Algorithm: *AL*
Input: $\{\mathbf{o}_r\}_{r=1}^K$
Initialization: $\mathbf{u}_0^0$, $\{\mathbf{\Lambda}_r^0\}_{r=1}^K$
Repeat for $t = 0, 1, 2, ...$
Repeat for $r = 1, ...K$
1. Forward propagation:
$\mathbf{u}_r^{t+1/2} = \mathbf{A}_r \cdot \mathbf{u}_0^t$
2. Fitting to observations:
$\mathbf{u}_r^{t+1}[l'] = \mathcal{G}(\mathbf{o}_r[l'], \mathbf{u}_r^{t+1/2}[l'], \mathbf{\Lambda}_r^t[l'])\ \forall l'$
3. Lagrange multipliers update:
$\mathbf{\Lambda}_r^{t+1} = \mathbf{\Lambda}_r^t + \alpha_r \cdot (\mathbf{u}_r^{t+1} - \mathbf{u}_r^{t+1/2})$
End on r
4. Object update:
$\mathbf{u}_0^{t+1} = \left(\sum_{r=1}^K \frac{1}{\gamma_r \sigma_r^2} \mathbf{A}_r^H \mathbf{A}_r + \mu \cdot \mathbf{I}\right)^{-1} \cdot \sum_{r=1}^K \frac{1}{\gamma_r \sigma_r^2} \mathbf{A}_r^H \cdot (\mathbf{u}_r^{t+1} + \mathbf{\Lambda}_r^t)$
End on t

Note that the optimization on the Lagrange multipliers $\{\mathbf{\Lambda}_r^t\}$ in Eqs. (4.17) is produced in the gradient direction $\partial \mathcal{J}_{AL} / \partial \mathbf{\Lambda}_r^* = 0$. The updating step $\alpha_r \in [0, 1]$ [162] is taken to improve the convergence of AL. The derivation of the augmented Lagrangian based phase-retrieval algorithm, namely: the optimization of $\mathcal{J}_{AL}$ on

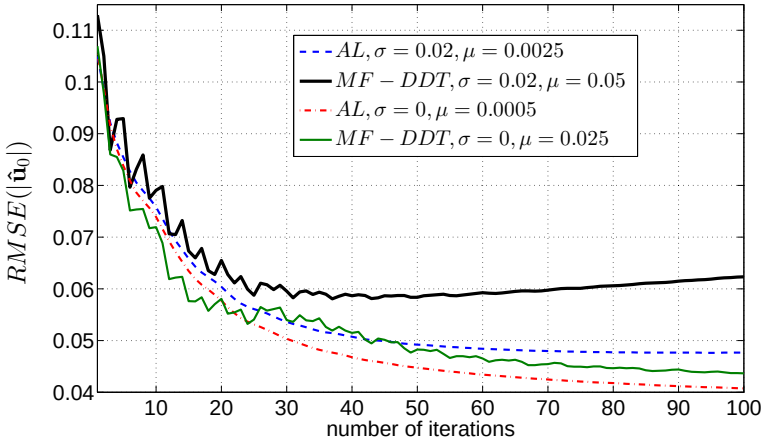

Figure 4.6: Convergence of the MF–DDT **P3** and AL **P4** algorithms in case of the amplitude reconstruction from noisy ($\sigma = 0.02$) and noiseless intensity observations for $z = 2 \cdot z_f$. The RMSE (solid) curves for MF–DDT are erratic, and for noisy data RMSE starts to monotonically increase (thick solid curve), i.e. MF–DDT diverges.

Figure 4.7: Amplitude reconstruction by MF–DDT and AL (100 iterations) from noisy and noiseless measurement data for $z = 2 \cdot z_f$, $K = 5$, AM. The first row corresponds to the amplitude estimates reconstructed from noisy data ($\sigma = 0.02$) by (a) AL **P4**, $\mu = 0.0025$, RMSE($|\hat{\mathbf{u}}_0|$)=0.048 and (b) MF–DDT **P3**, $\mu = 0.05$, RMSE($|\hat{\mathbf{u}}_0|$)=0.062. In the second row there are results obtained from noiseless observations: (c) AL, $\mu = 0.0005$, RMSE($|\hat{\mathbf{u}}_0|$)=0.041 and (d) MF–DDT, $\mu = 0.025$, RMSE($|\hat{\mathbf{u}}_0|$)=0.044.

$\mathbf{u}_0$ and $\mathbf{u}_r$ according to the minimum condition $\partial \mathcal{J}_{AL}/\partial \mathbf{u}_0^* = 0$ and $\partial \mathcal{J}_{AL}/\partial \mathbf{u}_r^* = 0$, respectively, is presented in Appendices A.1 and A.2.

The initialization concerns the object (e.g., $\mathbf{u}_0^0[l] = \frac{1}{2}$) and Lagrange multipliers vectors (e.g., $\mathbf{\Lambda}_r^0[l] = 0$). In Step 1 of AL we calculate the forward propagation of the object estimate $\mathbf{u}_0^t$ to K sensor planes. Step 2 gives the updates $\mathbf{u}_r^{t+1}$ to "reconcile" the estimates $\mathbf{u}_r^{t+1/2}$ numerically with the observations $\mathbf{o}_r$. The operator defining this update $\mathbf{u}_r^{t+1}$ is denoted by $\mathcal{G}$ and described by Eqs. (A.4)–(A.6). Step 3 returns the update for the Lagrange multipliers $\mathbf{\Lambda}_r^{t+1}$ similar to what we have in Eqs. (4.17). Step 4 gives the update for the object wave field calculated from the corrected image estimates $\mathbf{u}_r^{t+1}$ and the Lagrange multipliers $\mathbf{\Lambda}_r^t$. Note that Step 4 has the structure that is typical for the parallel algorithm: the multiple estimates of $\mathbf{u}_0$ obtained from K sensor planes are aggregated into the final update for the object reconstruction.

It can be seen that the main difference of the AL algorithm from MF–DDT consists of the the estimation of the wave fields at the sensor plane[3] (Step 2 of AL). In Figs. 4.6 and 4.7 the comparison of the amplitude reconstruction quality obtained by MF–DDT and AL phase-retrieval algorithms **P4**, [147] for $z = 2 \cdot z_f$ and the synthetic noisy with $\sigma = 0.02$ are presented. The forward and backward propagations are always performed using F–DDT with averaging. It is obvious that the reconstruction imaging is in favour of AL for both noisy and noiseless data (left column in Fig. 4.7). Here we would like to emphasize the divergence of MF–DDT (thick curve, Fig. 4.6) in case of larger amount of noise and strong ill-posedness of the transform matrix. Moreover, it is found that for larger z or σ the reconstruction imaging becomes even worse (cf. Fig. 4.7(b)). Thus, AL, as our further development of the parallel phase-retrieval algorithm, becomes significant more powerful tool for the object wave field reconstruction from noisy data and large propagation distances.

The discussion about the object reconstruction quality by the AL algorithm for AM and PM and comparison of AL with SBMIR are presented in [**P4**, Section 3] and [147, Section 4]. Evidently that a priori information on the object can significantly improve the reconstruction quality, and further we consider some modification of the AL algorithm developed especially for known object structures, for AM and PM.

4.4.3 AL for amplitude object (AL–A)

Note that the object estimation in the AL algorithm is presented for an arbitrary, complex-valued object (3.1) by means that no prior information on its structure is given. In many cases the object phase is known (say, the phase is constant in a thin glass transparency), and the only unknown variable is the object amplitude.

For the amplitude modulation of the object (AM) $\mathbf{u}_0 = \mathbf{a}_0$, $\boldsymbol{\phi}_0[l] = 0$ the analytical solution of the object update (Step 4 of AL) is defined by $\partial \mathcal{J}_{AL}/\partial \mathbf{a}_0 = 0$,

[3] In [118, Appendix B] it is shown that for small noise level σ and/or large γ_r (i.e. the strong domination of the fidelity terms related to the forward propagation) the updating of $\mathbf{u}_r^t$ can be significantly simplified: $\{\mathbf{u}_r^t\}$ can be computed by the replacement of the amplitude estimates with the given (noisy) measurements as in MF–DDT or SBMIR. Figs. 4.6 and 4.7 for $\sigma = 0$ prove our words that this modification may be used only for well-posed transform matrices or, at least, for distances close to z_f.

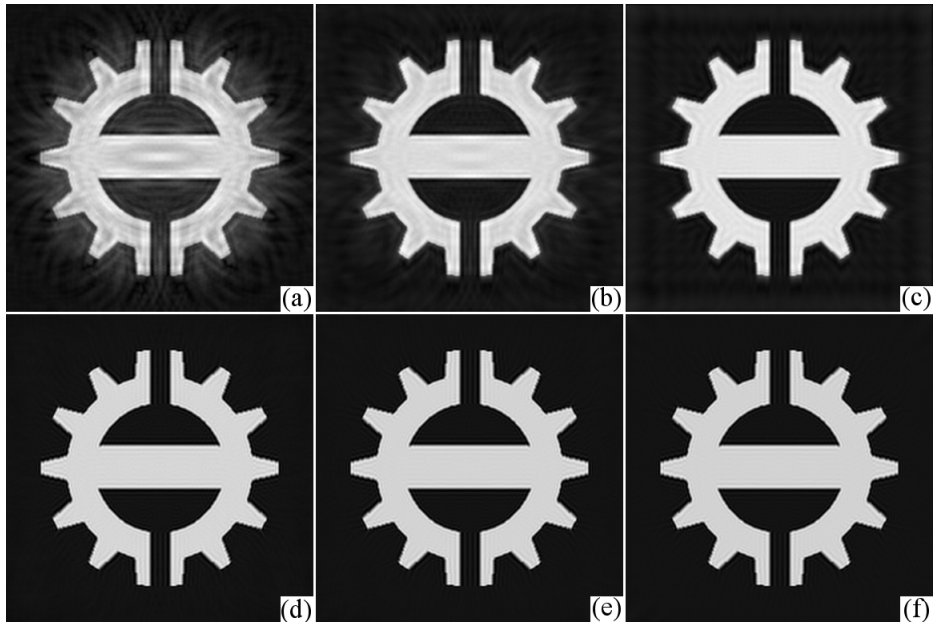

Figure 4.8: Amplitude reconstruction by (a-c) the AL phase-retrieval algorithm and by (d-f) its modification AL–A developed for AM (see Eq. (4.18)). The amplitude estimates are given for $z = 2 \cdot z_f$, $\sigma = 0$, $\mu = 0.005$ and different number of observations (from left to right) $K = \{3, 5, 10\}$. Reconstruction accuracy for (a/b/c) is PSNR=18.7/22.8/24; and for (d/e/f) PSNR=26/26.1/26.2.

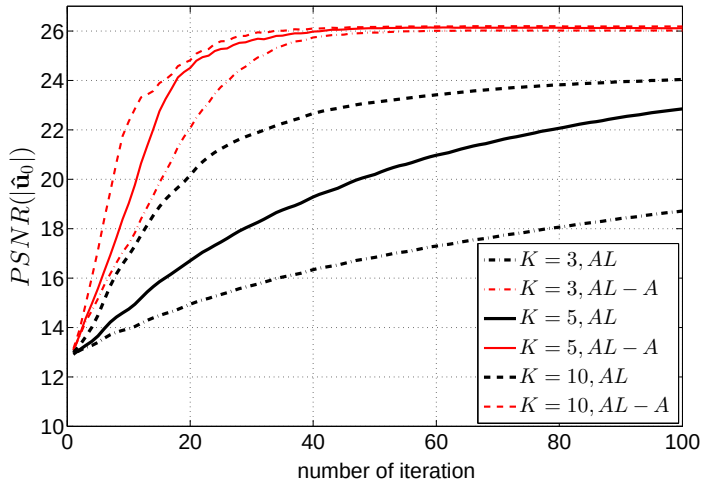

Figure 4.9: Convergence rate of the AL and AL–A phase-retrieval algorithms for $z = 2 \cdot z_f$ and $K = \{3, 5, 10\}$ for the experiments described in [**P4**, Fig. 2 and Table 1].

namely the optimal solution of the amplitude estimate is

$$\mathbf{a}_0^{t+1} = \left(\sum_{r=1}^{K} \frac{1}{\gamma_r \sigma_r^2} \mathrm{Re}\{\mathbf{A}_r^H \mathbf{A}_r\} + \mu \cdot \mathbf{I} \right)^{-1} \cdot \sum_{r=1}^{K} \frac{1}{\gamma_r \sigma_r^2} \mathrm{Re}\{\mathbf{A}_r^H (\mathbf{u}_r^{t+1} + \mathbf{\Lambda}_r^t)\}. \quad (4.18)$$

The derivation of Eq. (4.18) is given in Appendix A.2.1. Practically, the only difference is that at each iteration we should keep only the real part of the object estimate $\mathbf{u}_0^{t+1}$ and the imaginary part (object phase) should be always set equal to zero. Thus, we arrive at the modification of the AL algorithm for AM, denoted by $AL - A$.

Algorithm: $AL - A$
Input: $\{\mathbf{o}_r\}_{r=1}^K$
Initialization: $\mathbf{a}_0^0$, $\{\mathbf{\Lambda}_r^0\}_{r=1}^K$
Repeat for $t = 0, 1, 2, ...$
Repeat for $r = 1, ...K$
1. Forward propagation:
$\mathbf{u}_r^{t+1/2} = \mathbf{A}_r \cdot \mathbf{a}_0^t$
2. Fitting to observations:
$\mathbf{u}_r^{t+1}[l'] = \mathcal{G}(\mathbf{o}_r[l'], \mathbf{u}_r^{t+1/2}[l'], \mathbf{\Lambda}_r^t[l'])\ \forall l'$
3. Lagrange multipliers update:
$\mathbf{\Lambda}_r^{t+1} = \mathbf{\Lambda}_r^t + \alpha_r \cdot (\mathbf{u}_r^{t+1} - \mathbf{u}_r^{t+1/2})$
End on r
4. Object amplitude update:
$\mathbf{a}_0^{t+1} = \left(\sum_{r=1}^K \frac{1}{\gamma_r \sigma_r^2} \mathrm{Re}\{\mathbf{A}_r^H \mathbf{A}_r\} + \mu \cdot \mathbf{I} \right)^{-1} \cdot \sum_{r=1}^K \frac{1}{\gamma_r \sigma_r^2} \mathrm{Re}\{\mathbf{A}_r^H (\mathbf{u}_r^{t+1} + \mathbf{\Lambda}_r^t)\}$
End on t

In contrast to AL, the initialization concerns (except the Lagrange multipliers) the object amplitude only (e.g., $\mathbf{a}_0^0[l] = \frac{1}{2}$ as before), i.e. we care only about the object amplitude.

The visual comparison of the reconstruction quality by AL and AL–A is presented in Fig. 4.8: the top row corresponds to the AL amplitude reconstructions for $z = 2 \cdot z_f$ and different number of observations $K = \{3, 5, 10\}$. In the bottom row we present the object amplitudes obtained by AL–A. It can be seen that the AL–A results look much better than what we have by AL, but they are almost identical in spite of various K. The convergence (in PSNR) for these settings for both AL and AL–A are illustrated in Fig. 4.9. It is found that numerically the reconstruction accuracy of AL–A is approximately two-three times better in RMSE comparing with AL. Moreover the convergence of AL–A is much faster: here 50 iterations is enough while the AL reconstruction even after 100 iterations demonstrate worse imaging. All these results are computed for the Tiknonov regularization parameter $\mu = 0.005$. Note also that even for insufficient $K = 3 < 4$ (see Section 2.4.2) the AL–A gives a good reconstruction quality.

4.4.4 AL for phase object (AL–Ph): gradient descent algorithm

Let us consider the phase-only object wave field, i.e. the object of the form $\mathbf{u}_0 = a \cdot \exp(i\boldsymbol{\phi}_0)$, where $a \in \mathbb{R}^+$ is a (in general unknown) scalar variable. In out experiments it is typically equal to 1.

Let us assume for a moment that a is known. Then, the minimum condition on $\boldsymbol{\phi}_0$ for $\mathcal{J}_{AL}$ can be presented as follows (see Eq. (A.16) in Appendix A.2.2)

$$\frac{\partial}{\partial \boldsymbol{\phi}_0}\mathcal{J}_{AL} = 2\,\mathrm{Im}\{(a \cdot e^{-i\boldsymbol{\phi}_0}) \circ \sum_{r=1}^{K} \frac{1}{\gamma_r \sigma_r^2}\mathbf{A}_r^H(\mathbf{A}_r(a \cdot e^{i\boldsymbol{\phi}_0}) - \mathbf{u}_r - \boldsymbol{\Lambda}_r)\} = 0. \quad (4.19)$$

The update of the object phase at the t-th iteration is performed by the iterative gradient descent algorithm due to a huge dimension of the transform matrices. Provided the initial guess $\boldsymbol{\phi}_{0,t}^0 = \boldsymbol{\phi}_0^t$ the object phase is calculated as follows

$$\begin{aligned}
&\textbf{Repeat for } s = 0, 1, 2, \ldots S-1 \quad (4.20)\\
&\mathbf{u}_{0,t+1/2}^s = a \cdot \exp(i\boldsymbol{\phi}_{0,t}^s)\\
&\Delta\boldsymbol{\phi}_{0,t}^s = 2\,\mathrm{Im}\{(\mathbf{u}_{0,t+1/2}^s)^* \circ \sum_{r=1}^{K} \frac{1}{\gamma_r \sigma_r^2}\mathbf{A}_r^H(\mathbf{A}_r(\mathbf{u}_{0,t+1/2}^s) - \mathbf{u}_r^{t+1} - \boldsymbol{\Lambda}_r^t)\}\\
&\boldsymbol{\phi}_{0,t}^{s+1} = \boldsymbol{\phi}_{0,t}^s - \beta \cdot \Delta\boldsymbol{\phi}_{0,t}^s\\
&\textbf{End on } s
\end{aligned}$$

where $\mathbf{u}_{0,t+1/2}^s$ is the auxiliary estimate of the object, $\Delta\boldsymbol{\phi}_{0,t}^s$ is here the phase gradient. The result of Eqs. (4.20) for the t-th iteration is the object phase estimate at the $(t+1)$-th iteration, in terms of Eq. (4.20) $\mathbf{u}_0^{t+1} = a \cdot \exp(i\boldsymbol{\phi}_{0,t}^S)$. In **P5** the number of iterations S and the updating step β are fixed for simplicity. Since the fixed updating step may result in divergence of the algorithm, β could be also defined as, e.g., a fractional step, i.e. the step size in the process of descent is divided into a certain value.

If the magnitude of the object a is known, we use its true value, denoted in **P5** as "a_0", i.e. $\mathbf{u}_0^{t+1} = \mathrm{a}_0 \cdot \exp(i\boldsymbol{\phi}_{0,t}^S)$. If the scalar a is unknown, then the amplitude estimate is calculated after the update of the phase as

$$\begin{aligned}
\chi &= \sum_{r=1}^{K} \frac{1}{\gamma_r \sigma_r^2}||\mathbf{A}_r \exp(i\boldsymbol{\phi}_{0,t}^S)||_2^2 + \mu \cdot N_\xi N_\eta, \quad (4.21)\\
a^{t+1} &= \frac{1}{\chi}\sum_{r=1}^{K} \frac{1}{\gamma_r \sigma_r^2}\,\mathrm{Re}\{(\exp(-i\boldsymbol{\phi}_{0,t}^S))^T \cdot \mathbf{A}_r^H(\mathbf{u}_r^{t+1} + \boldsymbol{\Lambda}_r^t)\}.
\end{aligned}$$

The derivation is presented in Appendix A.2.2. Thus, the object estimate is therefore of the form $\mathbf{u}_0^{t+1} = a^{t+1} \cdot \exp(i\boldsymbol{\phi}_{0,t}^S)$.

Eqs. (4.20)–(4.21) define the modification of the AL algorithm for PM denoted by $AL - Ph$ with the conventional gradient descent method for the estimation of the object phase. The initialization concerns both the object amplitude (e.g., $a^0 = \frac{1}{2}$, if a_0 is unknown) and the phase (it could be, e.g., a random or zero vector).

Algorithm: $AL-Ph$, gradient descent
Input: $\{\mathbf{o}_r\}_{r=1}^K$
Initialization: $\boldsymbol{\phi}_{0,1}^0 \equiv \boldsymbol{\phi}_{0,0}^S$, a^0, $\{\boldsymbol{\Lambda}_r^0\}_{r=1}^K$
Repeat for $t = 0, 1, 2, ...$
$\widehat{a} = \begin{cases} \mathrm{a}_0, & \text{if } \mathrm{a}_0 \text{ is given} \\ a^t, & \text{otherwise} \end{cases}$
Repeat for $r = 1, ...K$
1. Forward propagation:
$\mathbf{u}_r^{t+1/2} = \mathbf{A}_r \cdot [\widehat{a} \cdot \exp(i\boldsymbol{\phi}_{0,t}^S)]$
2. Fitting to observations:
$\mathbf{u}_r^{t+1}[l'] = \mathcal{G}(\mathbf{o}_r[l'], \mathbf{u}_r^{t+1/2}[l'], \boldsymbol{\Lambda}_r^t[l'])\ \forall l'$
3. Lagrange multipliers update:
$\boldsymbol{\Lambda}_r^{t+1} = \boldsymbol{\Lambda}_r^t + \alpha_r \cdot (\mathbf{u}_r^{t+1} - \mathbf{u}_r^{t+1/2})$
End on r
4. Object phase update:
$\boldsymbol{\phi}_{0,t+1}^0 = \boldsymbol{\phi}_{0,t}^S$
Repeat for $s = 0, 1, 2, ...S-1$
$\mathbf{u}_{0,t+1}^s = \widehat{a} \cdot \exp(i\boldsymbol{\phi}_{0,t+1}^s)$
$\Delta\boldsymbol{\phi}_{0,t}^s = 2\,\mathrm{Im}\{(\mathbf{u}_{0,t+1}^s)^* \circ \sum_{r=1}^K \frac{1}{\gamma_r\sigma_r^2}\mathbf{A}_r^H(\mathbf{A}_r \cdot \mathbf{u}_{0,t+1}^s - \mathbf{u}_r^{t+1} - \boldsymbol{\Lambda}_r^t)\}$
$\boldsymbol{\phi}_{0,t+1}^{s+1} = \boldsymbol{\phi}_{0,t+1}^s - \beta \cdot \Delta\boldsymbol{\phi}_{0,t}^s$
End on s
5. Amplitude recalculation, if a_0 is not given
$\chi = \sum_{r=1}^K \frac{1}{\gamma_r\sigma_r^2}||\mathbf{A}_r \exp(i\boldsymbol{\phi}_{0,t+1}^S)||_2^2 + \mu \cdot N_\xi N_\eta$
$a^{t+1} = \frac{1}{\chi}\ \sum_{r=1}^K \frac{1}{\gamma_r\sigma_r^2}\,\mathrm{Re}\{(\exp(-i\boldsymbol{\phi}_{0,t+1}^S))^T \cdot \mathbf{A}_r^H(\mathbf{u}_r^{t+1} + \boldsymbol{\Lambda}_r^t)\}$
End on t

In **P5** we present the comparison of the wave field reconstruction of AL–Ph (gradient descent) with AL and SBMIR. The AL–Ph algorithm demonstrates faster convergence [**P5**, cf. Fig. 3] and significantly better reconstruction accuracy, especially by example of the smooth *Mexican Hat* object [**P5**, cf. Fig. 5]. The convergence of the object magnitude in case of a_0={0.85, 1, 1.25} is illustrated in [**P5**, Fig. 4]. It is found that a larger number of observations K leads to a faster convergence, but results in significant oscillations around a_0. Moreover, these oscillations are larger for larger a_0.

4.4.5 AL for phase object (AL–Ph): Gauss–Newton algorithm

The Gauss–Newton (GN) method is a modification of the well-known Newton–Raphson method used to solve (non-linear) LS problems, in particular for optimization of criterion functions. Unlike Newton's method, the GN algorithm has the advantage that second derivatives, which can be challenging to compute, are not required. Moreover, GN is essentially simpler because it is not so vulnerable to the initial guess as Newton's method. The GN algorithm of the object phase recovering is also iterative and follows from the linearization of the residual

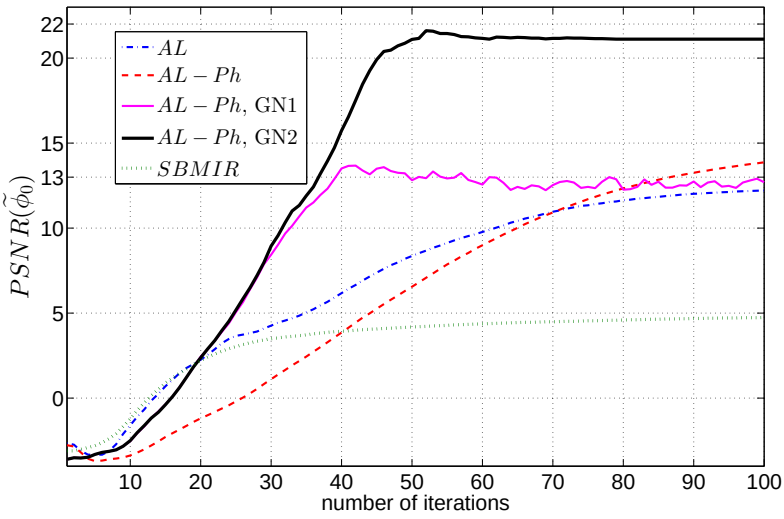

Figure 4.10: Convergence of the phase-retrieval algorithms used for the reconstruction of a phase-only object by AL (dashed-dotted curve); AL–Ph, gradient descent with the fixed updating step β (dashed curve, [**P5**, cf. Fig. 3]); AL–Ph, Gauss–Newton method with the fixed updating steps β and ζ (AL–Ph GN1, solid thin curve); AL–Ph, Gauss–Newton method with the fractional steps β and ζ (AL–Ph GN2, solid thick curve); and SBMIR ([8], dotted curve). These results are obtained for $z = 2 \cdot z_f$ and noisy measurements σ=0.05, PM with the known a_0=1, K=5, *chessboard* test-image. β and ζ in AL–Ph GN2 are divided by 2 and the number of iterations S and Q are doubled each 10 iterations. The curves of PSNR for GN1 and GN2 are overlapped up to the 30th iteration.

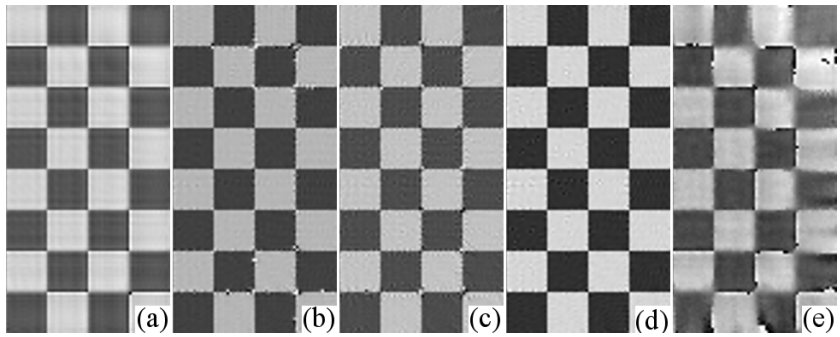

Figure 4.11: Fragments of the phase reconstruction obtained using different phase-retrieval algorithms: (a) by AL, PSNR=12.2, (b) by AL–Ph, gradient descent with the fixed updating step β, PSNR =13.9, (c) by AL–Ph, GN1 with the fixed updating steps β and ζ, PSNR=12.7, (d) by AL–Ph, GN2 with the fractional steps β and ζ, PSNR=21.1, (e) by SBMIR, PSNR=4.7. These results are given for $z = 2 \cdot z_f$ and noisy measurements σ=0.05, PM with the known a_0=1, K=5, *chessboard* test-image after 100 iterations, see Fig. 4.10, [**P5**, cf. Fig. 2].

$\mathbf{u}_r - \mathbf{A}_r \cdot \mathbf{u}_0$ in the AL criterion (4.16) as

$$\mathbf{u}_r - \mathbf{A}_r \cdot \mathbf{u}_0 \approx \mathbf{u}_r - \mathbf{A}_r \cdot [a \cdot \exp(i\boldsymbol{\phi}_0)] - \frac{\partial}{\partial \boldsymbol{\phi}_0}(\mathbf{A}_r \cdot [a \cdot \exp(i\boldsymbol{\phi}_0)]) \cdot \boldsymbol{\varphi}_0, \quad (4.22)$$

i.e. it is obtained by ignoring the second-order derivative terms (only the first two terms of the Taylor series are taken). Here $\boldsymbol{\varphi}_0$ is a small phase increment. Thus, the forward wave field propagation can be presented by (see Eq. (A.20))

$$\mathbf{u}_r = \mathbf{A}_r \cdot [a \cdot \exp(i\boldsymbol{\phi}_0)] + i\mathbf{A}_r \boldsymbol{\Gamma} \cdot \boldsymbol{\varphi}_0, \quad (4.23)$$

where $\boldsymbol{\Gamma}$ is the diagonal matrix with the object vector components in the main diagonal, $\boldsymbol{\Gamma} = \mathrm{diag}(a \cdot \exp(i\boldsymbol{\phi}_0)) \in \mathbb{C}^{N_\xi N_\eta \times N_\xi N_\eta}$. Then, the phase update in terms of the GN algorithm is of the form (cf. Eq. (4.20))

$$\boldsymbol{\phi}_0^{t+1} = \boldsymbol{\phi}_0^t + \beta \cdot \boldsymbol{\varphi}_0 = \boldsymbol{\phi}_0^t - \frac{\beta}{2} \cdot \boldsymbol{\Upsilon}^{-1} \cdot \frac{\partial}{\partial \boldsymbol{\phi}_0} \mathcal{J}_{AL} = \quad (4.24)$$

$$= \boldsymbol{\phi}_0^t - \beta \cdot \left(\sum_{r=1}^{K} \frac{1}{\gamma_r \sigma_r^2} \mathrm{Re}\{\boldsymbol{\Gamma}^T \mathbf{A}_r^T \mathbf{A}_r^* \boldsymbol{\Gamma}^*\} \right)^{-1} \times$$

$$\times \mathrm{Im}\{(\mathbf{u}_0^t)^* \circ \sum_{r=1}^{K} \frac{1}{\gamma_r \sigma_r^2} \mathbf{A}_r^H (\mathbf{A}_r \mathbf{u}_0^t - \mathbf{u}_r^{t+1} - \boldsymbol{\Lambda}_r^t)\},$$

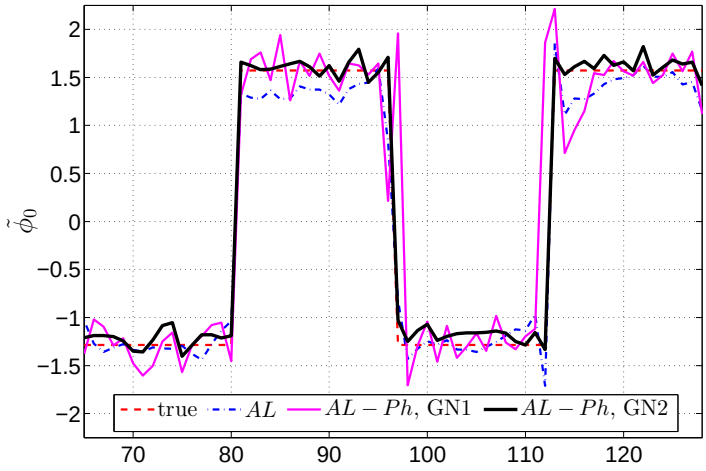

Figure 4.12: Cross-section of the reconstructed phases by (dashed-dotted curve) by AL, PSNR=12.2; by (solid thin curve) AL–Ph, GN1 with the fixed updating steps β and ζ, PSNR=12.7 and by (solid thick curve) AL–Ph GN2 with the fractional steps β and ζ, PSNR=21.1. The true phase is depicted by a dashed curve. These results are presented for experiments illustrated in Fig. 4.11.

where β is the updating step and the matrix

$$\boldsymbol{\Upsilon} = \sum_{r=1}^{K} \frac{1}{\gamma_r \sigma_r^2} \operatorname{Re}\{\boldsymbol{\Gamma}^T \mathbf{A}_r^T \mathbf{A}_r^* \boldsymbol{\Gamma}^*\} \in \mathbb{C}^{N_\xi N_\eta \times N_\xi N_\eta} \tag{4.25}$$

is a sort of approximation of the Hessian matrix, computed for $\boldsymbol{\Gamma} = \operatorname{diag}(a \cdot \exp(i\boldsymbol{\phi}_0^t))$. The phase increment $\boldsymbol{\varphi}_0$ in Eq. (4.24) is derived in Appendix A.3.

Due to a huge dimension of the matrix $\boldsymbol{\Upsilon}$ (Eq. (4.25)) we use an additional iterative procedure to compute the phase increment. Thus, we arrive at the following algorithm, which results in the update of the object phase estimate $\boldsymbol{\phi}_{0,t}$ at the t-th iteration

$$\begin{aligned}
&\textbf{Repeat for } s = 0, 1, 2, \ldots S-1 \\
&\mathbf{u}_{0,t}^s = a^t \cdot \exp(i\boldsymbol{\phi}_{0,t}^s) \\
&\Delta\boldsymbol{\phi}_{0,t}^s = \operatorname{Im}\{(\mathbf{u}_{0,t}^s)^* \circ \sum_{r=1}^{K} \frac{1}{\gamma_r \sigma_r^2} \mathbf{A}_r^H (\mathbf{A}_r \mathbf{u}_{0,t}^s - \mathbf{u}_r - \boldsymbol{\Lambda}_r)\} \\
&\boldsymbol{\Gamma}^s = \operatorname{diag}(a^t \cdot \exp(i\boldsymbol{\phi}_{0,t}^s)), \;\; \boldsymbol{\Upsilon}^s = \sum_{r=1}^{K} \frac{1}{\gamma_r \sigma_r^2} \operatorname{Re}\{(\boldsymbol{\Gamma}^s)^T \mathbf{A}_r^T \mathbf{A}_r^* (\boldsymbol{\Gamma}^s)^*\} \\
&\textbf{Repeat for } q = 0, 1, 2, \ldots Q-1 \\
&\boldsymbol{\varphi}_{0,t}^{q+1} = \boldsymbol{\varphi}_{0,t}^q - \zeta \cdot \left[\boldsymbol{\Upsilon}^s \cdot \boldsymbol{\varphi}_{0,t}^q + \Delta\boldsymbol{\phi}_{0,t}^s\right] \\
&\textbf{End on } q \\
&\boldsymbol{\phi}_{0,t}^{s+1} = \boldsymbol{\phi}_{0,t}^s + \beta \cdot \boldsymbol{\varphi}_{0,1}^Q \\
&\textbf{End on } s
\end{aligned} \tag{4.26}$$

where $\boldsymbol{\Gamma}^s$ and $\boldsymbol{\Upsilon}^s$ are the s-th iterations of the auxiliary (above mentioned) matrices, ζ is a new updating step for the estimate of the phase increment $\boldsymbol{\varphi}_{0,t}$. Together, Eqs. (4.21) and Eqs. (4.26) result in the AL–Ph phase-retrieval algorithm with the phase estimation by the Gauss–Newton method. Here we denote this algorithm "$AL-Ph, GN$" in order to distinguish it from the gradient descent implementation from Section 4.4.4.

Thus, the main difference of the GN version of AL–Ph from the gradient descent implementation consists of the calculation of the descent direction what may essentially improves the phase reconstruction quality and the convergence rate of the phase-retrieval algorithm, though the convergence of this algorithm is not guaranteed.

In Fig. 4.10 we present the convergence of AL, SBMIR and various modification of AL–Ph in case of the phase reconstruction from significantly noisy data ($\sigma = 0.05$) and ill-posed transform matrices ($z = 2 \cdot z_f$). The result by the AL–Ph algorithm with the fixed updating steps β and ζ is depicted with a solid thin curve and denoted by GN1. It can be seen that this algorithm demonstrates the fastest convergence, but after about 40 iterations the PSNR curve for this algorithm starts to be erratic with some tendency to decrease.

In order to overcome this problem we take in AL–Ph fractional steps: each 10 steps we divide β and ζ by 2 and double S and Q. The result for the fractional

Algorithm: $AL-Ph$, Gauss–Newton (GN)
Input: $\{\mathbf{o}_r\}_{r=1}^K$
Initialization: $\boldsymbol{\phi}_{0,1}^0 \equiv \boldsymbol{\phi}_{0,0}^S$, $\boldsymbol{\varphi}_{0,0}^Q = 0$, a^0, $\{\boldsymbol{\Lambda}_r^0\}_{r=1}^K$
Repeat for $t = 0, 1, 2, ...$
$\widehat{a} = \begin{cases} \mathrm{a}_0, & \text{if } \mathrm{a}_0 \text{ is given} \\ a^t, & \text{otherwise} \end{cases}$
Repeat for $r = 1, ...K$
1. Forward propagation:
$\mathbf{u}_r^{t+1/2} = \mathbf{A}_r \cdot [\widehat{a} \cdot \exp(i\boldsymbol{\phi}_{0,t}^S)]$
2. Fitting to observations:
$\mathbf{u}_r^{t+1}[l'] = \mathcal{G}(\mathbf{o}_r[l'], \mathbf{u}_r^{t+1/2}[l'], \boldsymbol{\Lambda}_r^t[l'])\ \forall l'$
3. Lagrange multipliers update:
$\boldsymbol{\Lambda}_r^{t+1} = \boldsymbol{\Lambda}_r^t + \alpha_r \cdot (\mathbf{u}_r^{t+1} - \mathbf{u}_r^{t+1/2})$
End on r
$\boldsymbol{\phi}_{0,t+1}^0 = \boldsymbol{\phi}_{0,t}^S$
Repeat for $s = 0, 1, 2, ...S-1$
4. Calculation of the phase gradient:
$\Delta\boldsymbol{\phi}_{0,t}^s = \mathrm{Im}\{(\widehat{a} \cdot \exp(-i\boldsymbol{\phi}_{0,t+1}^s)) \circ \sum_{r=1}^K \frac{1}{\gamma_r\sigma_r^2}\mathbf{A}_r^H \times$
$\times(\mathbf{A}_r(\widehat{a} \cdot \exp(i\boldsymbol{\phi}_{0,t+1}^s)) - \mathbf{u}_r^{t+1} - \boldsymbol{\Lambda}_r^t)\}$
5. Calculation of the phase increment:
$\boldsymbol{\varphi}_{0,t+1}^0 = \boldsymbol{\varphi}_{0,t}^Q$
$\boldsymbol{\Gamma}^s = \mathrm{diag}(a^t \cdot \exp(i\boldsymbol{\phi}_{0,t}^s))$, $\boldsymbol{\Upsilon}^s = \sum_{r=1}^K \frac{1}{\gamma_r\sigma_r^2}\mathrm{Re}\{(\boldsymbol{\Gamma}^s)^T\mathbf{A}_r^T\mathbf{A}_r^*(\boldsymbol{\Gamma}^s)^*\}$
Repeat for $q = 0, 1, 2, ...Q-1$
$\boldsymbol{\varphi}_{0,t+1}^{q+1} = \boldsymbol{\varphi}_{0,t+1}^q - \zeta \cdot \left[\boldsymbol{\Upsilon}^s \cdot \boldsymbol{\varphi}_{0,t+1}^q + \Delta\boldsymbol{\phi}_{0,t}^s\right]$
End on q
6. Update of the object phase:
$\boldsymbol{\phi}_{0,t+1}^{s+1} = \boldsymbol{\phi}_{0,t+1}^s + \beta \cdot \boldsymbol{\varphi}_{0,t+1}^Q$
End on s
7. Update of the object amplitude, if a_0 is not given
$\chi = \sum_{r=1}^K \frac{1}{\gamma_r\sigma_r^2}||\mathbf{A}_r \exp(i\boldsymbol{\phi}_{0,t+1}^S)||_2^2 + \mu \cdot N_\xi N_\eta$
$a^{t+1} = \frac{1}{\chi}\sum_{r=1}^K \frac{1}{\gamma_r\sigma_r^2}\mathrm{Re}\{(\exp(-i\boldsymbol{\phi}_{0,t+1}^S))^T \cdot \mathbf{A}_r^H(\mathbf{u}_r^{t+1} + \boldsymbol{\Lambda}_r^t)\}$
End on t

steps is marked by a solid thick curve and denoted by GN2. This modification enables much better (about two times better) reconstruction accuracy of the object phase: RMSE=0.232 for the fixed steps and RMSE=0.088 for fractional steps after 100 iterations. The reconstruction imaging is also in favor of AL–Ph GN2 with fractional steps: it can be convinced in better imaging of this algorithm in Fig. 4.11 and Fig. 4.12, where the fragments of the reconstructed phases and corresponding cross-sections are illustrated. Note that AL results in a smoothed phase estimate and the use of fixed updating steps in AL–Ph GN1 leads to strong errors on the border of the *chessboard* test-image. In general, the result of AL–Ph GN2 is more contrast.

Since the optimization criterion in the AL based algorithm is nonconvex, the

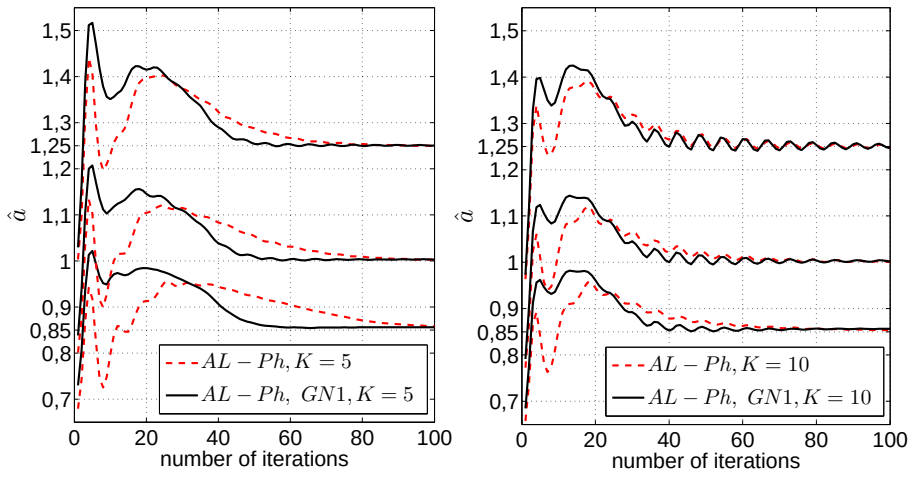

Figure 4.13: Convergence of the object magnitude recovering by (dashed curve) AL–Ph, gradient descent [**P5**, cf. Fig. 4] and by (solid curve) AL–Ph, GN1. These results are given for PM with unknown a_0={0.85,1,1.25}, $z = 2 \cdot z_f$, noisy measurements σ=0.05, *chessboard* test-image and different number of observations: (left image) K=5, (right image) K=10.

result is strongly depends on the initial guess of the algorithm. According to our experiments, AL–Ph GN2 with fractional updating steps demonstrates the best reconstruction accuracy for various initial guesses. However, the computational complexity of the Gaussian–Newton AL–Ph algorithm is significantly higher comparing with the original AL or the gradient descent AL–Ph algorithm. The crucial point is that due to very high dimension of the matrix $\boldsymbol{\Upsilon}$ (Eq. (4.25)) we use an additional loop for the calculation of the phase increment: in particular, at each s-th step (see Eq. (4.26)) we perform $K \cdot N_\xi^2 N_\eta^2 + Q \cdot N_x N_y N_\xi^2 N_\eta^2$ multiplications and additions to calculate $\boldsymbol{\Upsilon}^s$ and, in addition, $Q \cdot N_\xi^2 N_\eta^2$ operations to find $\boldsymbol{\Upsilon}^s \cdot \boldsymbol{\varphi}_{0,t+1}^q$. The computational time (in averaged for one iteration) for the AL and AL–Ph algorithms is presented in Table 4.1. These results are obtain by Monte Carlo simulation with averaging over 50 samples.

It can be seen a linear growth of the computational time with respect to the

Table 4.1: Computational time (in seconds for one iteration) for AL, the gradient descent AL–Ph and Gauss–Newton AL–Ph (AL–Ph GN1 with the fixed updating steps) algorithms.

		Algorithms		
$N_\xi \times N_\eta$	K	AL	AL–Ph	AL–Ph GN1
128×128	5	0.15	0.6	5.1
128×128	10	0.28	1.2	10.6
256×256	5	0.6	3.75	35
256×256	10	1.25	7.35	68.6

dimension of the problem. Note, however, that the computational time for AL–Ph increases faster than for AL because of additional loops. Moreover, this time may increase in times in case of the fractional updating steps.

In Fig. 4.13 we illustrate the convergence of the gradient descent AL–Ph and AL–Ph GN1 (with fixed updating steps) algorithms in case of recovering the object magnitude $\widehat{a}$ for PM, $\mathrm{a}_0 = \{0.85, 1, 1.25\}$. The GN1 version of the phase-retrieval algorithm gives better convergence rate for both $K = 5$ and $K = 10$ comparing with the gradient descent AL–Ph **P5**. However, it can be also seen that the oscillations around a_0 are more significant for GN1.

4.5 Conclusions

In this Chapter we firstly consider our initial development of the parallel iterative MF–DDT phase-retrieval algorithm **P3** with simultaneous aggregating of a number of object estimates and therefore noise suppressing. The replacement of the computed amplitudes of the wave field at the sensor planes by ones obtained from measurements is used analogically to the successive SBMIR phase-retrieval algorithm. Further we reformulate the optimization problem: provided the accurate forward diffraction propagation we are looking for the fit of the calculated intensity of the sensor plane wave field distribution to the observation. It results in the augmented Lagrangian phase-retrieval algorithm originated in **P4**. The use of a priori information on the object is firstly presented in **P5** by example of the modification of the AL algorithm for PM. The AL–Ph phase-retrieval algorithm demonstrates a significant improvement of the reconstruction accuracy (about two times in RMSE). In this text we gather all of these algorithms together and present them in order of their development. Note that in Chapter 4 we have no additional object filtering.

In Section 4.3 it is shown that the potential object reconstruction accuracy from K wave field estimates at the sensor planes can be indicated by the rank of the sums of individual matrices $rank(\sum_{r=1}^{K} \mathbf{X}_r^H \mathbf{X}_r) \cdot rank(\sum_{r=1}^{K} \mathbf{Y}_r^H \mathbf{Y}_r)$, where the transform matrix of the diffraction propagation to the distance z_r is $\mathbf{A}_r = \mathbf{X}_r \otimes \mathbf{Y}_r$. This handy tool can clarify the resulting good imaging by AL for $z = \frac{1}{2} \cdot z_f$ and $z = z_f$: compare the maximum value of the numerical rank in Fig. 4.4 with very good reconstruction quality in [**P4**, cf. Fig.2, Table 1].

In Section 4.4.3 we introduce the modification of the AL algorithm developed for the amplitude-only object denoted by AL–A. Figure 4.9 demonstrate a better convergence rate and reconstruction accuracy (about 50% in RMSE for K=5). In Section 4.4.5 we present the modification of AL for the phase-only object, where the phase update is computed by the Gauss–Newton method (this algorithm is denoted by AL–Ph GN). It is shown that AL–Ph GN converges much faster comparing with the gradient descent based AL–Ph algorithm or the AL algorithms (especially with fractional updating steps, see Fig. 4.10) and gives much sharper, contrast object phase reconstruction (see Fig. 4.11).

Chapter 5

Phase retrieval with sparse object regularization

It is found **P3** that the spatially adaptive regularization (realized via BM3D filter [34, 35]) results in a significant improvement in imaging. Thus, *sparse modeling* is decided to be incorporated into the AL phase-retrieval algorithm because of high performance and flexibility of this technique [48]. Sparse modeling of the object is recognized to allow overcoming the loss of information related to the ill-posedness of forward propagation operators, wiping out different corrupting artifacts, filtering noise, and therefore enhancing the resulting quality. In this Chapter we consider the improvement of the reconstruction accuracy and imaging by the incorporate separate filtering of the object amplitude and phase (numerical experiments and some additional information can be found in **P5**–**P6**, [149]). Moreover, here we also discuss the use of the object sparse modeling in a more sophisticated phase-retrieval method with compensation of distortions arising sue to the forward diffraction propagation in the 4f optical system **P7**.

5.1 Observation models

In Section 2.2 we consider the forward wave field propagation computed via the RS and Fresnel diffraction integral, by the ASD or Fresnel transfer functions, and the result of the free space diffraction propagation, precisely the intensity measurements of diffraction patterns are (fairly) obtained at different distances from the object. Despite the simplicity of the mathematical apparatus of the free-space setup, in practise the optical system is bulky and expensive due to the use of a motorized sensor. In addition, the recording process of intensity measurements is relatively slow due to the movement of the sensor.

Note that the transfer function of ASD (Eq. (1.44)) or its Fresnel approximation (Eq. (1.67)) describes a pure phase modulation. It is shown in [4, 53] that a 4f configuration can be used to imitate the lensless optical system for the multi-plane phase-retrieval scenario. The forward wave field propagation, presented in Fig. 2.2, can be realized by the phase modulation of the Fourier transform of the

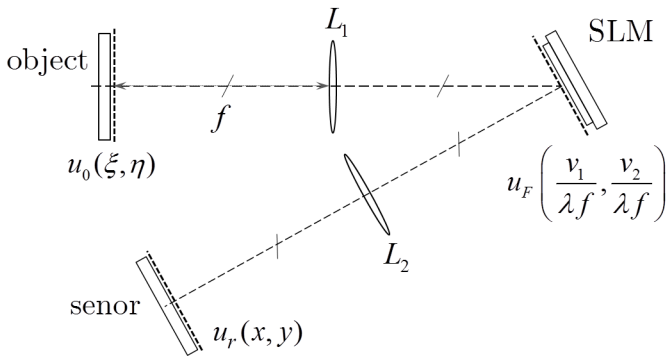

Figure 5.1: Experimental 4f optical setup for measurement recording [53]. The lenses L_1 and L_2 in the 4f configuration provides an accurate propagation of the transverse object wave field $u_0(\xi,\eta)$ to the parallel observation (sensor) plane giving the wave field $u_r(x,y)$. An optical mask with the complex-valued transmittance $\mathcal{M}_r(\frac{v_1}{\lambda f},\frac{v_2}{\lambda f})$ located at the Fourier plane (a phase modulating SLM) enables linear filter operations.

object wave field using the phase-only LC-SLM placed in the Fourier domain of the 4f optical system as it is illustrated in Fig. 5.1. The principal feature is that in this case the sensor plane is immobile and fixed at the distance $4f$ from the object plane.

5.1.1 4f configuration in phase-retrieval scenario

The lenses L_1 and L_2 with the focal length f arranged in the 4f configuration provides an accurate propagation of the object wave field $u_0(\xi,\eta)$ to the parallel measurement plane. Let us consider an ideal optical path with no distortions/aberrations. It can be shown (see Appendix B.1) that the wave field at the Fourier plane (at the back focal plane of the first lens L_1) is given as follows

$$u_F\left(\frac{v_1}{\lambda f},\frac{v_2}{\lambda f}\right)=\frac{e^{i2kf}}{i\lambda f}\mathcal{F}\{u_0(\xi,\eta)\}\left(\frac{v_1}{\lambda f},\frac{v_2}{\lambda f}\right), \tag{5.1}$$

where $v=(v_1,v_2)\in\mathbb{R}^2$ are the spatial frequencies. If the optical mask (SLM) inserted at the Fourier plane has the complex-valued transmittance $\mathcal{M}_r(\frac{v_1}{\lambda f},\frac{v_2}{\lambda f})$, then the output of the optical system is defined as

$$\begin{aligned} u_r(x,y) &= \frac{e^{i2kf}}{i\lambda f}\mathcal{F}\{u_F\left(\frac{v_1}{\lambda f},\frac{v_2}{\lambda f}\right)\cdot\mathcal{M}_r\left(\frac{v_1}{\lambda f},\frac{v_2}{\lambda f}\right)\}(-x,-y)= \\ &= -e^{i4kf}\cdot\{u_0\circledast\mathcal{F}\{\mathcal{M}_r\left(\frac{v_1}{\lambda f},\frac{v_2}{\lambda f}\right)\}\}(-x,-y),\ r=1,...K. \end{aligned} \tag{5.2}$$

Depending on the used optical masks $\{\mathcal{M}_r(\frac{v_1}{\lambda f},\frac{v_2}{\lambda f})\}$, a number of various wave field distributions $\{u_r\}_{r=1}^K$ can be generated at the sensor plane corresponding to different complex-valued transmittances. For instance, the imitation of the free space propagation via the Fourier transform of complex amplitudes of the object

and the sensor plane wave field distributions is of the form [118]

$$U_r\left(\frac{v_1}{\lambda f},\frac{v_2}{\lambda f}\right)=-e^{i4kf}\cdot U_0\left(-\frac{v_1}{\lambda f},-\frac{v_2}{\lambda f}\right)\cdot\mathcal{M}_r\left(-\frac{v_1}{\lambda f},-\frac{v_2}{\lambda f}\right),\tag{5.3}$$

where $r=1,...K$ and, taking into account that the Fourier transforms are given in a scaled spatial coordinates[1], the optical mask corresponding to ASD is [53]

$$\mathcal{M}_r\left(\frac{v_1}{\lambda f},\frac{v_2}{\lambda f}\right)=\exp\left(ikz_r\sqrt{1-\frac{v_1^2}{f^2}-\frac{v_2^2}{f^2}}\right)\tag{5.4}$$

for various distances z_r of the wave field propagation.

5.1.2 Discrete modeling of 4f configuration

The discrete model of Eqs. (5.1)–(5.2) provided the sampling conditions

$$\frac{1}{N_\xi}=\frac{\Delta_1\Delta_\xi}{\lambda f},\quad \frac{1}{N_\eta}=\frac{\Delta_2\Delta_\eta}{\lambda f},\quad \frac{1}{N_1}=\frac{\Delta_1\Delta_x}{\lambda f},\quad \frac{1}{N_2}=\frac{\Delta_2\Delta_y}{\lambda f},\tag{5.5}$$

can be represented in the form

$$\mathbf{u}_r=-e^{i4kf}\cdot\mathrm{vec}\{F\{F\{\mathbf{U}_0\}\circ\mathbf{M}_r\}\},\quad r=1,...K.\tag{5.6}$$

The 2D transfer function $\mathbf{M}_r$ in Eq. (5.6) by means of the real optical mask (see Eq. (B.10) in Appendix B.2) is very different from what is used in the free space propagation model (Eq. (4.2)) due to a finite size of the used phase modulating LC-SLM and the fact that the active area of SLM cells is, in general, smaller than the full size of a pixel (i.e. the fill factor is not 100%). Further the discrete models of the diffraction propagation in 4f configuration (5.6) is applied in order to obtain the required vectors of intensity measurements $\{\mathbf{o}_r\}$ (see Eq.(4.4)).

For simplicity, we use Eq. (B.9) for both the synthetic numerical experiments (in **P6**, [149]) and processing of experimental data from the 4f optical system with a phase modulating LC-SLM in the Fourier domain (in **P6**–**P7**). In the second case the changes from the theoretically predicted result of the wave field propagation and nonidealities related to, e.g., the bandlimitedness of the transfer function or various distortions in the optical path of the used coherent imaging system (Fig. 5.1) are considered as disturbances in the optical path[2] to be estimated and compensated.

5.2 Sparse modeling and BM3D filtering

According to the sparsity hypothesis it is assumed that the object amplitude $\mathbf{a}_0\in\mathbb{R}^n$ and phase $\boldsymbol{\phi}_0\in\mathbb{R}^n$ can be separately approximated with small numbers of non-zero components of basis functions ($n=N_\xi N_\eta$). Note that there is no prior information on the object modulation as before in AL–A (Section 4.4.3)

[1] Substituting $\frac{v_1}{\lambda f}=\eta_1$, $\frac{v_1}{\lambda f}=\eta_1$ in Eq. (1.48) we obtain Eq. (5.4).

[2] The problem of disturbances compensation is discussed in Section 5.3.

and AL–Ph (see Sections 4.4.4, **P5** and Section 4.4.5). In addition, the ideal basis functions for the object approximation are unknown a priori as well, and they are selected from a given set of potential bases (dictionaries). In general, sparse image approximation can be given in the synthesis or analysis form as follows:

$$\begin{array}{cc} \boldsymbol{\theta}_a = \boldsymbol{\Phi}_a \cdot |\mathbf{u}_0|, \quad \boldsymbol{\theta}_\phi = \boldsymbol{\Phi}_\phi \cdot \mathcal{W}^{-1}\{\arg\{\mathbf{u}_0\}\}, & \text{(analysis)} \\ \mathbf{a}_0 = \boldsymbol{\Psi}_a \cdot \boldsymbol{\theta}_a, \quad \boldsymbol{\phi}_0 = \boldsymbol{\Psi}_\phi \cdot \boldsymbol{\theta}_\phi, & \text{(synthesis)} \end{array} \tag{5.7}$$

where $\boldsymbol{\Psi}_a$,$\boldsymbol{\Psi}_\phi$ and $\boldsymbol{\Phi}_a$, $\boldsymbol{\Phi}_\phi$ are the frame transform matrices, and the vector $\boldsymbol{\theta}_a$, $\boldsymbol{\theta}_\phi \in \mathbb{R}^m$ can be considered as a spectrum in a parametric data adaptive approximation ($m \gg n$). Recall that $\mathcal{W}$ denotes the wrapping operator (see Eq. (1)) and, hence, $\mathcal{W}^{-1}$ in Eqs. (5.7) is an unwrapping operator (which can be realized by, e.g., [44, 222]).

As it is mentioned in Chapter 3 here and in **P5**–**P7**, [149] the recovered object argument is assumed to be in the interval $[-\pi, \pi)$ and therefore no unwrapping procedure is required; thus, the wrapping/unwrapping operators are hereafter omitted.

Subindices $_a$ and $_\phi$ in Eqs. (5.7) are shown for the amplitude and phase, respectively. It is recognized that, in contrast to classical orthonormal bases (m=n), overcomplete frames based modeling ($m \gg n$) is a much more efficient for imaging [48, 89] and results in a better wave field reconstruction accuracy.

The sparsity of approximation is characterized by either the ℓ_0 or ℓ_1 norms. A smaller value of the norm means a higher sparsity of approximation. Note that results obtained by ℓ_0 or ℓ_1 norms are shown to be closed to each other [42], what allows replacing the nonconvex ℓ_0 norm by the convex ℓ_1 norm in many variational settings. The main intention is to find sparsest (shortest) models for phase and amplitude with smallest values of the ℓ_0 or ℓ_1 norms. The separate sparse modeling for the object phase and amplitude is realized via the powerful BM3D-frame filter, specified for denoising and other imaging problems [37, 38, 117].

Taking into account the sparse modeling for the object amplitude and phase, the wave field reconstruction is performed by minimization of the following criterion [**P6**, Eq. (7)]

$$\mathcal{J} = \sum_{r=1}^{K} \frac{1}{2\sigma^2} ||\mathbf{o}_r - |\mathbf{u}_r|^2||_2^2 + \tau_a \cdot ||\boldsymbol{\theta}_a||_p + \tau_\phi \cdot ||\boldsymbol{\theta}_\phi||_p \text{ subject to} \tag{5.8}$$

$$\mathbf{u}_r = \mathbf{A}_r \cdot \mathbf{u}_0,\ r = 1, ...K, \quad \text{(forward propagation)} \tag{5.9}$$

$$\boldsymbol{\theta}_a = \boldsymbol{\Phi}_a \cdot |\mathbf{u}_0|,\ \boldsymbol{\theta}_\phi = \boldsymbol{\Phi}_\phi \cdot \arg\{\mathbf{u}_0\}, \quad \text{(analysis)} \tag{5.10}$$

$$\mathbf{a}_0 = \boldsymbol{\Psi}_a \cdot \boldsymbol{\theta}_a,\ \boldsymbol{\phi}_0 = \boldsymbol{\Psi}_\phi \cdot \boldsymbol{\theta}_\phi, \quad \text{(synthesis)} \tag{5.11}$$

where regularization terms for phase and amplitude are taken using the ℓ_p norms ($p = \{0, 1\}$). The positive parameters τ_a and τ_φ in Eq. (5.8) define a balance between the fitting of the calculated $|\mathbf{u}_r|^2$ to the given observation $\mathbf{o}_r$, smoothness of the wave field reconstruction and the complexity of the used model: cardinality of spectra $\boldsymbol{\theta}_a$, $\boldsymbol{\theta}_\phi$ of the object amplitude and phase.

5.2.1 Multi-objective optimization

It is shown in [38] that a multi-objective optimization can be much more efficient than the minimization of the single criterion $\mathcal{J}$ from Eqs. (5.8)–(5.11) due to a simpler implementation (filtering and inverse procedure are decoupled) and resulting better reconstruction quality[3]. Thus, instead of the constrained minimization of (5.8)–(5.11) we arrive at the unconstrained minimization of two criterion functions $\mathcal{J}_1$ and $\mathcal{J}_2$ with changing the constraints for sparse modeling by the quadratic penalties with positive weights

$$\mathcal{J}_1(\{\mathbf{o}_r\}, \mathbf{u}_0, \{\mathbf{u}_r\}, \{\mathbf{\Lambda}_r^t\}, \mathbf{v}_0) = \sum_{r=1}^{K} \frac{1}{\sigma^2}[\frac{1}{2}||\mathbf{o}_r - |\mathbf{u}_r|^2||_2^2 + \tag{5.12}$$
$$+\frac{1}{\gamma_r}||\mathbf{u}_r - \mathbf{A}_r \cdot \mathbf{u}_0||_2^2 + \frac{2}{\gamma_r}\,\mathrm{Re}\{\mathbf{\Lambda}_r^H \cdot (\mathbf{u}_r - \mathbf{A}_r \cdot \mathbf{u}_0)\} + \frac{1}{\gamma_0}||\mathbf{u}_0 - \mathbf{v}_0||_2^2,$$

$$\mathcal{J}_2(\boldsymbol{\theta}_a, \boldsymbol{\theta}_\phi, \mathbf{u}_0) = \tau_a \cdot ||\boldsymbol{\theta}_a||_p + \frac{1}{2\gamma_a}||\boldsymbol{\theta}_a - \mathbf{\Phi}_a \cdot |\mathbf{u}_0|||_2^2 + \tag{5.13}$$
$$+\tau_{_\phi} \cdot ||\boldsymbol{\theta}_\phi||_p + \frac{1}{2\gamma_\phi}||\boldsymbol{\theta}_\phi - \mathbf{\Phi}_\phi \cdot \arg\{\mathbf{u}_0\}||_2^2,$$

where in Eq. (5.12) $\mathbf{v}_0 = \mathbf{\Psi}_a\boldsymbol{\theta}_a \circ \exp(i \cdot \mathbf{\Psi}_\phi\boldsymbol{\theta}_\phi)$ is an approximation of the complex-valued object distribution $\mathbf{u}_0$.

Note that in contrast to [118] and similar to AL we involve the quadratic and linear penalties related to the forward propagation model ($\mathbf{u}_r = \mathbf{A}_r \cdot \mathbf{u}_0$) with the same positive parameters $\frac{1}{\gamma_r}$. Thus, $\mathcal{J}_1$ becomes the augmented Lagrangian objective function at least with respect to this particular constraint.

The analysis and synthesis constraints in Eq. (5.10) and Eq. (5.11) are replaced by quadratic penalties with the corresponding positive parameters $\frac{1}{\gamma_a}$, $\frac{1}{\gamma_\phi}$ and $\frac{1}{\gamma_0}$ in Eq. (5.13) and Eq. (5.12), what is a standard tools to deal with constrained optimization [19]. Note also that the criterion $\mathcal{J}_2$ is separable with respect to $\boldsymbol{\theta}_a$ and $\boldsymbol{\theta}_\phi$, thus it can be rewritten as $\mathcal{J}_2 = \mathcal{J}_{2,a} + \mathcal{J}_{2,\phi}$, where

$$\begin{aligned} \mathcal{J}_{2,a}(\boldsymbol{\theta}_a, |\mathbf{u}_0|) &= \tau_a \cdot ||\boldsymbol{\theta}_a||_p + \frac{1}{2\gamma_a}||\boldsymbol{\theta}_a - \mathbf{\Phi}_a \cdot |\mathbf{u}_0|||_2^2, \\ \mathcal{J}_{2,\phi}(\boldsymbol{\theta}_\phi, \arg\{\mathbf{u}_0\}) &= \tau_{_\phi} \cdot ||\boldsymbol{\theta}_\phi||_p + \frac{1}{2\gamma_\phi}||\boldsymbol{\theta}_\phi - \mathbf{\Phi}_\phi \cdot \arg\{\mathbf{u}_0\}||_2^2. \end{aligned} \tag{5.14}$$

It is recognized [38, 117] that the minimization of $\mathcal{J}_1$ on $\mathbf{u}_0$ in general results in increasing of $\mathcal{J}_2$ and vice versa, optimization of $\mathcal{J}_2$ with respect to spectra $\boldsymbol{\theta}_a$ and $\boldsymbol{\theta}_\phi$ increases $\mathcal{J}_1$. This problem can be interpreted in terms of the game theory as a noncooperative interaction between the players. A compromise in this selfish behavior can be found in the fixed point $(\mathbf{u}_0^\star, \boldsymbol{\theta}_a^\star, \boldsymbol{\theta}_\phi^\star)$ of the optimization called *generalized Nash equilibrium* [50, 110, 129]. Then, the complex-valued object wave

[3] Note that in [38] different models, such as analysis- and synthesis-only based object reconstructions, are considered.

field is reconstructed using decoupling of the inverse procedure and BM3D-frame filtering of the object amplitude and phase as [**P6**, cf. Eq. (10)]

$$\begin{cases} \boldsymbol{\theta}_a^\star = \arg\min\limits_{\boldsymbol{\theta}_a} \mathcal{J}_{2,a}(\boldsymbol{\theta}_a, |\mathbf{u}_0^\star|) \\ \boldsymbol{\theta}_\phi^\star = \arg\min\limits_{\boldsymbol{\theta}_\phi} \mathcal{J}_{2,\phi}(\boldsymbol{\theta}_\phi, \arg\{\mathbf{u}_0^\star\}) \\ \mathbf{v}_0^\star = \boldsymbol{\Psi}_a \boldsymbol{\theta}_a^\star \circ \exp(i \cdot \boldsymbol{\Psi}_\varphi \boldsymbol{\theta}_\varphi^\star) \\ \mathbf{u}_0^\star = \arg \min\limits_{\mathbf{u}_0, \{\mathbf{u}_r\}} \max\limits_{\{\boldsymbol{\Lambda}_r\}} \mathcal{J}_1(\{\mathbf{o}_r\}, \mathbf{u}_0, \{\mathbf{u}_r\}, \{\boldsymbol{\Lambda}_r^t\}, \mathbf{v}_0^\star) \end{cases}. \tag{5.15}$$

Taking into account Eq. (4.17), the problem (5.15) can be realized with the following iterative algorithm

Repeat for $t = 0, 1, 2, ...$

$$\boldsymbol{\theta}_a^t = \arg\min_{\boldsymbol{\theta}_a} \mathcal{J}_{2,a}(\boldsymbol{\theta}_a, |\mathbf{u}_0^t|) \tag{5.16}$$

$$\boldsymbol{\theta}_\phi^t = \arg\min_{\boldsymbol{\theta}_\phi} \mathcal{J}_{2,\phi}(\boldsymbol{\theta}_\phi, \arg\{\mathbf{u}_0^t\}) \tag{5.17}$$

$$\mathbf{v}_0^{t+1} = \boldsymbol{\Psi}_a \boldsymbol{\theta}_a^t \circ \exp(i \cdot \boldsymbol{\Psi}_\phi \boldsymbol{\theta}_\phi^t) \tag{5.18}$$

Repeat for $r = 1, ...K$

$$\mathbf{u}_r^{t+1} = \arg\min_{\mathbf{u}_r} \mathcal{J}_1(\mathbf{o}_r, \mathbf{u}_0^t, \mathbf{u}_r, \boldsymbol{\Lambda}_r^t, \mathbf{v}_0^{t+1}) \tag{5.19}$$

$$\boldsymbol{\Lambda}_r^{t+1} = \boldsymbol{\Lambda}_r^t + \alpha_r \cdot (\mathbf{u}_r^t - \mathbf{A}_r \cdot \tilde{\mathbf{u}}_0^t) \tag{5.20}$$

End on r

$$\mathbf{u}_0^{t+1} = \arg\min_{\mathbf{u}_o} \mathcal{J}_1(\{\mathbf{o}_r\}, \mathbf{u}_0, \{\mathbf{u}_r^{t+1}\}, \{\boldsymbol{\Lambda}_r^t\}, \mathbf{v}_0^{t+1}) \tag{5.21}$$

End on t

Depending on the chosen ℓ_0 or ℓ_1 norm in $\mathcal{J}_2$ the so-called *hard* or *soft* thresholding, respectively, is appeared in the calculation of the spectrum for the object amplitude $\boldsymbol{\theta}_a^t$ and phase $\boldsymbol{\theta}_\phi^t$ in Eqs. (5.16) and (5.17). Indeed, in Eqs. (5.14) we consider the optimization problem with respect to $\boldsymbol{\theta}_a$ or $\boldsymbol{\theta}_\phi$ in the following

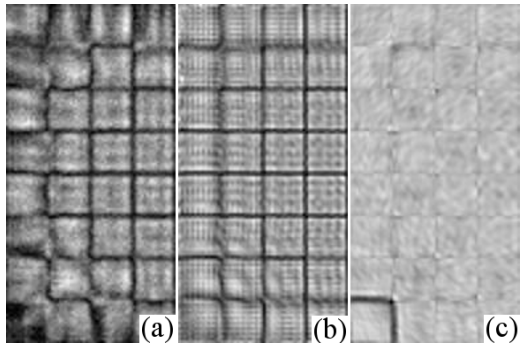

Figure 5.2: Fragments of the reconstructed object amplitude (128×64) computed using (a) SBMIR, RMSE=0.35, (b) AL, RMSE=0.23 and (c) D–AL, RMSE=0.026. The results are presented for synthetic data with the true object amplitude $\mathbf{a}_0[l] = 1$.

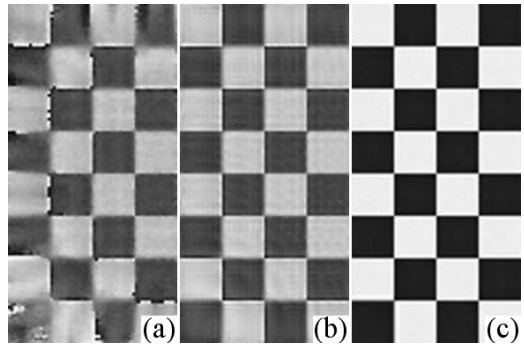

Figure 5.3: Fragments of the reconstructed object phase (128×64) computed using (a) SBMIR, RMSE=0.58, (b) AL, RMSE=0.26 and (c) D–AL, RMSE=0.036. The results are presented for synthetic data, PM, *chessboard* test-image.

general form

$$\tau \cdot ||\boldsymbol{\theta}||_p + \frac{1}{2\gamma}||\boldsymbol{\theta} - \mathbf{b}||_2^2 \to \min_{\boldsymbol{\theta}} \tag{5.22}$$

for the vectors $\boldsymbol{\theta}, \mathbf{b} \in \mathbb{R}^m$. For $p \leq 1$ the ℓ_p-norm is nondifferentiable, which makes optimization on $\boldsymbol{\theta}$ nontrivial. Nevertheless, for $p = 0$ and $p = 1$, there are known analytical solutions, which can be found using convex optimization for $p = 1$ or just from the analysis of the criterion function for $p = 0$ [48]

$$\boldsymbol{\theta} = \Im h_{\tau\gamma}(\mathbf{b}) = \begin{cases} sign(\mathbf{b}) \cdot \max(|\mathbf{b}| - \tau\gamma, 0), & \text{for } \ell_1\text{-norm} \\ \mathbf{b} \circ \mathbf{1}(|\mathbf{b}| \geq \sqrt{2\tau\gamma}), & \text{for } \ell_0\text{-norm} \end{cases}, \tag{5.23}$$

where $\mathbf{1}(\cdot)$ stands for the indicator function (Eq. (10)).

In this thesis as well as in **P6**–**P7**, [149] the object reconstruction in performed using the soft thresholding, i.e. we use sparse modeling with respect to the ℓ_1-norm, because it result in less oversmoothing and hence less loss of small details of the object.

Eqs. (5.16)–(5.17) enable the spectrum estimates of the object amplitude and phase by thresholding $\boldsymbol{\theta}_a^t = \Im h_{\tau_a\gamma_a}(\boldsymbol{\Phi}_a \cdot |\mathbf{u}_0^t|)$ and $\boldsymbol{\theta}_\phi^t = \Im h_{\tau_\phi\gamma_\phi}(\boldsymbol{\Phi}_\phi \cdot \arg\{\mathbf{u}_0^t\})$, respectively, in the BM3D-frame domain with the corresponding thresholds $\tau_a\gamma_a$ and $\tau_\phi\gamma_\phi$ [**P6**, Eqs. (14)]. Eq. (5.18) corresponds to the synthesis of the object approximation $\mathbf{v}_0^t$ from the calculated spectra $\boldsymbol{\theta}_a^t$ and $\boldsymbol{\theta}_\phi^t$. Together the operations (of analysis, thresholding and synthesis) in Eqs. (5.16)–(5.18) related to the optimization of $\mathcal{J}_2$ can be rewritten more compact as follows

$$\begin{aligned} \mathbf{a}_0^{t+1/2} &= BM3D_a(|\mathbf{u}_0^t|), \\ \boldsymbol{\phi}_0^{t+1/2} &= BM3D_\phi(\arg\{\mathbf{u}_0^t\}), \\ \mathbf{v}_0^t &= \mathbf{a}_0^{t+1/2} \circ \exp(i \cdot \boldsymbol{\phi}_0^{t+1/2}), \end{aligned} \tag{5.24}$$

where $BM3D(\cdot)$ denotes hereafter the processing by the BM3D-frame filter, and the corresponding subindices $_a$ and $_\phi$ emphasize that the filtering is performed

with different parameters and different transform matrices $\mathbf{\Psi}_a$, $\mathbf{\Psi}_\phi$ and $\mathbf{\Phi}_a$, $\mathbf{\Phi}_\phi$ for the amplitude and phase, respectively. In our implementation the analysis and synthesis operations, the thresholding and calculation of the frame transform matrices $\mathbf{\Psi}$ and $\mathbf{\Phi}$ are integrated in a single block of the BM3D filter.

The optimization steps for $\mathcal{J}_1$ in Eqs. (5.19)–(5.21) related to the calculation of the complex-valued wave field estimates $\{\mathbf{u}_r^{t+1}\}$ at the sensor planes, updating of the Lagrange multipliers $\{\mathbf{\Lambda}_r^{t+1}\}$ and the object $\mathbf{u}_0^{t+1}$ are similar to what we have for the AL algorithm (see Appendix A.1 and Appendix A.2 taking into account that $\frac{\partial}{\partial \mathbf{u}_0^*}\mathcal{J}_1 = \sum_{r=1}^K \frac{1}{\gamma_r \sigma_r^2}\mathbf{A}_r^H\mathbf{A}_r\mathbf{u}_0 + \frac{1}{\gamma_0}\cdot\mathbf{u}_0 - \sum_{r=1}^K \frac{1}{\gamma_r\sigma_r^2}\mathbf{A}_r^H\cdot(\mathbf{u}_r+\mathbf{\Lambda}_r) + \frac{1}{\gamma_0}\mathbf{v}_0 = 0$).

5.2.2 Decoupled augmented Lagrangian (D–AL) algorithm

Eqs. (5.24) and solutions of Eqs. (5.19)–(5.21) result in the iterative algorithm called *Decoupled Augmented Lagrangian* $(D-AL)$ because of decoupling the incorporated BM3D-frame object pre-filtering in Step 1 and the inverse procedure of the object wave field reconstruction from the noisy observations and filtered object approximation $\mathbf{v}_0^t$ in Step 6.

Note that the initialization here consists not only of the Lagrange multipliers but also of a proper object estimate. Besides, the object initialization is not trivial since a balance between the denoising and a "freedom" for the further enhancement of the object reconstruction by filtering. It is shown [**P6**, Fig. 2] that lack of

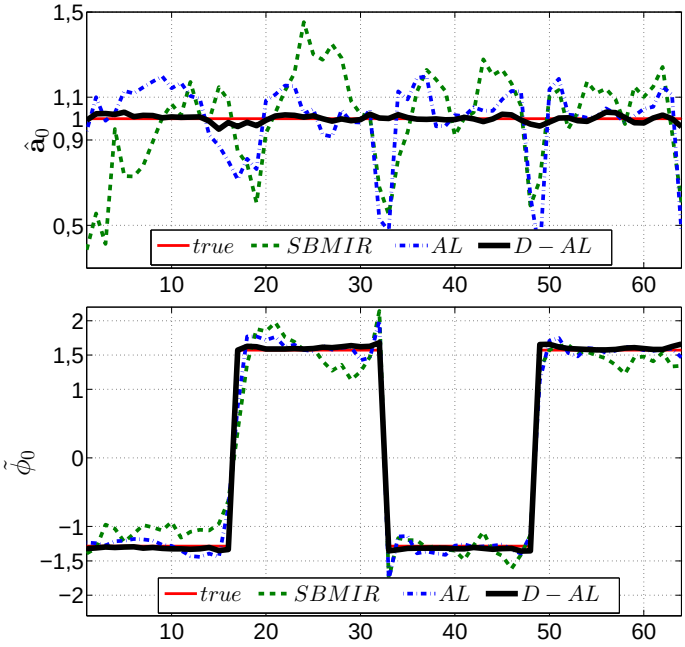

Figure 5.4: Cross-sections of the reconstructed object amplitude (top image) and object phase (bottom image) for the results presented in Figs. 5.2 and 5.3, respectively. Thick curve corresponds to D–AL, dashed curve – to SBMIR and dashed-dotted curve – to AL.

Algorithm: $D-AL$
Input: $\{\mathbf{o}_r\}_{r=1}^{K}$
Initialization: $\mathbf{u}_0^0$, $\{\mathbf{\Lambda}_r^0\}$
Repeat for $t = 0, 1, 2...$
1. BM3D filtering:
$\mathbf{a}_0^{t+1/2} = BM3D_a(|\mathbf{u}_0^t|)$,
$\boldsymbol{\phi}_0^{t+1/2} = BM3D_\phi(\arg\{\mathbf{u}_0^t\})$
2. Object approximation synthesis:
$\mathbf{v}_0^{t+1} = \mathbf{a}_0^{t+1/2} \circ \exp(i \cdot \boldsymbol{\phi}_0^{t+1/2})$
Repeat for $r = 1, ...K$
3. Forward propagation:
$\mathbf{u}_r^{t+1/2} = \mathbf{A}_r \cdot \mathbf{u}_0^t$
4. Fitting to observations:
$\mathbf{u}_r^{t+1}[l'] = \mathcal{G}(\mathbf{o}_r[l'], \mathbf{u}_r^{t+1/2}[l'], \mathbf{\Lambda}_r^t[l'])\ \forall l'$
5. Lagrange multipliers update:
$\mathbf{\Lambda}_r^{t+1} = \mathbf{\Lambda}_r^t + \alpha_r \cdot (\mathbf{u}_r^{t+1} - \mathbf{u}_r^{t+1/2})$
End on r
6. Object update:
$\mathbf{u}_0^{t+1} = \left(\sum_{r=1}^{K} \frac{1}{\gamma_r \sigma_r^2} \mathbf{A}_r^H \mathbf{A}_r + \frac{1}{\gamma_0} \cdot \mathbf{I}\right)^{-1} \cdot \sum_{r=1}^{K} \frac{1}{\gamma_r \sigma_r^2} \mathbf{A}_r^H \cdot (\mathbf{u}_r^{t+1} + \mathbf{\Lambda}_r^t) + \frac{1}{\gamma_0} \mathbf{v}_0^{t+1}$
End on t

preprocessing (too noisy initial $\mathbf{u}_0^0$) results in a deterioration of the convergence rate and as a result noisy reconstruction corrupted by diffraction artifacts ("waves" on border of the geometrical elements [**P6**, Fig. 3]). Excess of preprocessing leads, in most cases, to oversmoothed reconstructions and loss of small components.

It is shown by multiple numerical simulations that the D–AL algorithm enables an essential enhancement of the reconstruction quality for both the reconstruction the amplitude- (see **P6** for details) or phase-only objects [149] from noisy observation data. In particular, in Figs. 5.2 and 5.3 we present the comparison of the object amplitude and phase reconstruction for PM obtained by SBMIR, AL and D–AL. In Fig. 5.4 the corresponding cross-section of the amplitude and phase estimates is illustrated. It is obvious that the reconstruction imaging is in favor of D–AL. For syntactic data the reconstruction accuracy of D–AL, even without prior information on the object modulation, is up to ten times better (in RMSE) comparing with AL or SBMIR. Nevertheless, it is difficult to obtain good imaging in case of experimental data, when the measurements are essentially corrupted and such distortions can not be represented via simple i.i.d. additive Gaussian noise.

5.3 Sparse reconstruction with background compensation in 4f configuration

In a real optical system the intensity observations are very different from theoretical results and the observation model can not be described by Eqs. (4.1) with the additive Gaussian (or Poissonian–Gaussian) noise. The systematic distortions

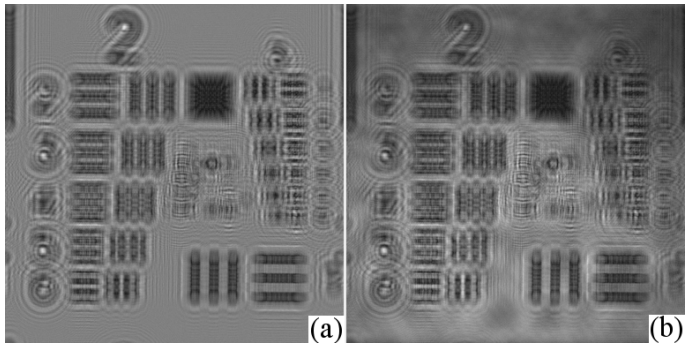

Figure 5.5: Influence of the distortions in the coherent imaging system on the intensity observations. Simulations of the corrupting effect: (a) noisy intensity with no distortions, $\sigma = 0.02$ and (b) intensity observation with realistic synthetic degradations.

appear due to many factors such as non-ideality of optical system (misalignment, misfocusing, aberrations), dust on optical elements, reflections, vibration to name just a few. In Fig. 5.5 we present the result of a realistic distortions arising in the optical path of a coherent imaging system[4] on the imaging of the intensity measurements at the sensor plane. Evidently the wave field reconstructions obtained by phase-retrieval algorithms from such disturbed data are traditionally noisy, blurred and corrupted. Imaging of the reconstructed objects even using strong filtering (e.g., by BM3D-frame filter with large thresholding parameters for the object amplitude and phase, soft or hard thresholding) is poor: see [**P6**, Figs. 5 and 6]. Moreover, the reconstruction from the experimental data is very sensitive to disturbing factors in case of ill-posedness of the diffraction propagation transform matrices. In particular, one of the strongest sources of disturbances in the used 4f optical system [53] imitating the forward free space wave propagation is the phase modulating LC-SLM (realizing different optical masks, Eq. (B.10)) because of its location in the Fourier domain.

5.3.1 Cumulative disturbance model in imaging system

Let $u_0(\xi,\eta)$ be a *true* 2D object wave field at the entrance pupil of the optical system. Taking into consideration the non-ideality of the optical system, we introduce a disturbed object wave field $\widetilde{u}_0(\xi,\eta)$ as a product of a typically unknown *background* (cumulative distortion) wave field $u_B(\xi,\eta)$ by the true object wave field $u_0(\xi,\eta)$ as

$$\widetilde{u}_0(\xi,\eta) = u_0(\xi,\eta)\cdot u_B(\xi,\eta), \tag{5.25}$$

where the diacritic $\widetilde{\ }$ emphasizes the difference of the disturbed object $\widetilde{u}_0$ from the ideal one u_0. The phase-retrieval techniques mentioned in Chapter 4 are able to give the reconstruction of the disturbed wave field $\widetilde{u}_0(\xi,\eta)$ only and not able to separate the background in order to estimate the true wave field $u_0(\xi,\eta)$.

[4] The presented disturbances are simulated by the data obtained from the 4f optical system presented in Fig. 5.1.

Taking into account the used vector-matrix notation and the distortions in the real optical system (Eq. (5.25)), the forward wave field propagation model from the object to the sensor plane can be given in the form (cf. Eq. (4.1))

$$\mathbf{u}_r = \mathbf{A}_r \cdot \widetilde{\mathbf{u}}_0,\ r = 1, ...K, \tag{5.26}$$

where

$$\widetilde{\mathbf{u}}_0 = \mathbf{u}_0 \circ \mathbf{u}_B \tag{5.27}$$

is a complex-valued column vector, corresponding to the disturbed object discrete 2D wave field distribution, $\mathbf{u}_0$ is a complex-valued true object wave field. All essential nonidealities and differences of the observation obtained by real optical masks $\mathbf{M}_r$ (see Eqs. (B.10)) from the ideal one (Eq. (B.9)) are considered as components of the complex-valued background $\mathbf{u}_B$ to be estimated and compensated.

5.3.2 SPAR–BC algorithm

In order to filter the above mention disturbances of the optical path out, we develop two step phase-retrieval algorithm. Firstly, we perform special calibration procedure: record a set of observation data $\{\mathbf{o}_r^B\}$ imitating the diffraction propagation of the free space object (test-image $\mathbf{u}_0[l] = 1\ \forall l$) by

$$\mathbf{o}_r^B = |\mathbf{A}_r \cdot \mathbf{u}_B|^2 + \boldsymbol{\varepsilon}_r,\ r = 1, ...K, \tag{5.28}$$

where $\widetilde{\mathbf{u}}_0 = \mathbf{u}_B$, and then estimate the vector of the background $\widehat{\mathbf{u}}_B$ from these intensity measurements. The error vector $\boldsymbol{\varepsilon}_r$ in Eq. (5.28) describes the additive Gaussian zero-mean noise of a small level (e.g., sensor noise, $\boldsymbol{\varepsilon}_r[l'] \sim \mathcal{N}(0, \sigma_r^2)$). Then, we record a set of intensity measurements $\{\mathbf{o}_r\}_r$ for the investigating object $\mathbf{u}_0$ according to

$$\mathbf{o}_r = |\mathbf{A}_r \cdot (\mathbf{u}_0 \circ \mathbf{u}_B)|^2 + \boldsymbol{\varepsilon}_r,\ r = 1, ...K, \tag{5.29}$$

and reconstruct the object $\widehat{\mathbf{u}}_0$, namely: both the object amplitude $\widehat{\mathbf{a}}_0$ and phase $\widehat{\boldsymbol{\phi}}_0$, using the computed background $\widehat{\mathbf{u}}_B$.

At first glance, this problem looks trivial: one may find $\widehat{\mathbf{u}}_B$ and an estimate for the disturbed object $\widetilde{\mathbf{u}}_0$ and then recalculate the object as $\widehat{\mathbf{u}}_0[l] = \widetilde{\mathbf{u}}_0[l]/\widehat{\mathbf{u}}_B[l]$. However, a priori information about the object, which could be used in sparse modeling, concerns the true object wave field $\mathbf{u}_0$ but not the disturbed one $\widetilde{\mathbf{u}}_0$. Hence, the iterative recalculation of the object estimate ($\mathbf{u}_0^t[l] = \widetilde{\mathbf{u}}_0^t[l]/\widehat{\mathbf{u}}_B[l]$, $t = 0, 1, 2, ...$) is required, and the structure of the resulting phase-retrieval algorithm is therefore essentially different from the trivial guess. More details can be found in **P7**.

Background reconstruction

Since no prior information on the background is given, it is straightforward to reconstruct $\widehat{\mathbf{u}}_B$ from $\{\mathbf{o}_r^B\}$ as before

$$\widehat{\mathbf{u}}_B = \arg \min_{\mathbf{u}_B, \{\mathbf{u}_r\}} \max_{\{\boldsymbol{\Lambda}_r\}} \mathcal{J}_{AL}(\{\mathbf{o}_r^B\}, \mathbf{u}_B, \{\mathbf{u}_r\}, \{\boldsymbol{\Lambda}_r\}) \tag{5.30}$$

by the AL algorithm. While $\widetilde{\mathbf{u}}_0 = \mathbf{u}_B$, then $\mathbf{u}_r = \mathbf{A}_r \cdot \mathbf{u}_B$, $r = 1, ...K$ in Eq. (5.30), and $\mathbf{u}_B$ is one of the arguments of the AL criterion function. This stage is shown in the upper block of Fig. 5.6 highlighted by a dashed line.

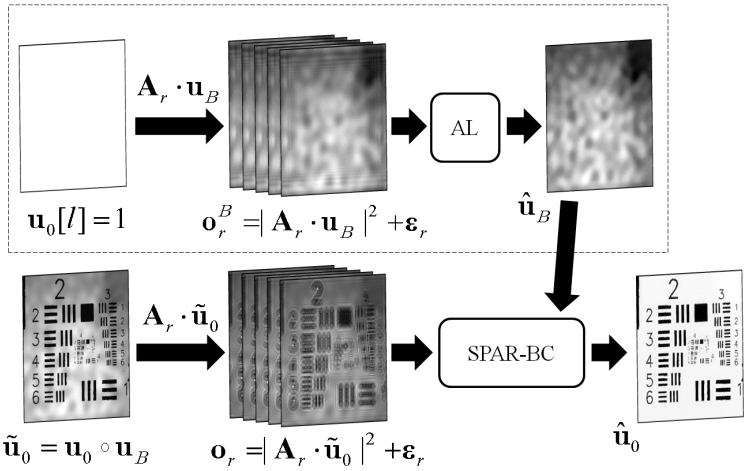

Figure 5.6: Two-steps phase retrieval with background compensation. The upper block highlighted by a dashed line represents the background calibration procedure, where the complex-valued estimate $\widehat{\mathbf{u}}_B$ is found by AL (or D–AL). The reconstruction of the (true) object $\widehat{\mathbf{u}}_0$ using the background compensation by the SPAR–BC algorithm is under the calibration procedure block.

Sparse modeling of the true object

Since the prior information is given for the true object, then, taking into account the sparse modeling for the true object amplitude and phase from Section 5.2, the wave field reconstruction is performed by minimization of the following criterion

$$\mathcal{J} = \sum_{r=1}^{K} \frac{1}{2\sigma^2} ||\mathbf{o}_r - |\mathbf{u}_r|^2||_2^2 + \tau_a \cdot ||\boldsymbol{\theta}_a||_p + \tau_\phi \cdot ||\boldsymbol{\theta}_\phi||_p \text{ subject to} \quad (5.31)$$

$$\mathbf{u}_r = \mathbf{A}_r \cdot \widetilde{\mathbf{u}}_0,\ r = 1, ...K, \quad \text{(forward propagation)} \quad (5.32)$$

$$\widetilde{\mathbf{u}}_0 = \mathbf{u}_0 \circ \mathbf{u}_B, \quad \text{(disturbed object)} \quad (5.33)$$

$$\boldsymbol{\theta}_a = \boldsymbol{\Phi}_a \cdot |\mathbf{u}_0|,\ \boldsymbol{\theta}_\phi = \boldsymbol{\Phi}_\phi \cdot \arg\{\mathbf{u}_0\}, \quad \text{(true object analysis)} \quad (5.34)$$

$$\mathbf{a}_0 = \boldsymbol{\Psi}_a \cdot \boldsymbol{\theta}_a,\ \boldsymbol{\phi}_0 = \boldsymbol{\Psi}_\phi \cdot \boldsymbol{\theta}_\phi, \quad \text{(true object synthesis)} \quad (5.35)$$

where, in contrast to D–AL **P6**, the distortions arising due to the forward wave propagation are involved in the forward wave field propagation model (Eq. (5.32)). Following the multi-objective optimization, instead of the constrained optimization the criterion $\mathcal{J}$ (Eqs. (5.31)–(5.35)) we arrive at the alternating minimization of two criteria: $\mathcal{J}_1$ with respect to the disturbed object $\widetilde{\mathbf{u}}_0 = \mathbf{u}_0 \circ \mathbf{u}_B$ and $\mathcal{J}_2 = \mathcal{J}_{2,a} + \mathcal{J}_{2,\phi}$ with respect to the spectra of the true object.

$$\mathcal{J}_1(\{\mathbf{o}_r\}, \widetilde{\mathbf{u}}_0, \{\mathbf{u}_r\}, \{\boldsymbol{\Lambda}_r^t\}, \mathbf{v}_0) = \sum_{r=1}^{K} \frac{1}{\sigma^2} [\frac{1}{2} ||\mathbf{o}_r - |\mathbf{u}_r|^2||_2^2 + \quad (5.36)$$

$$+ \frac{1}{\gamma_r} ||\mathbf{u}_r - \mathbf{A}_r \cdot \widetilde{\mathbf{u}}_0||_2^2 + \frac{2}{\gamma_r} \mathrm{Re}\{\boldsymbol{\Lambda}_r^H \cdot (\mathbf{u}_r - \mathbf{A}_r \cdot \widetilde{\mathbf{u}}_0)\} + \frac{1}{\gamma_0} ||\widetilde{\mathbf{u}}_0 - \widetilde{\mathbf{v}}_0||_2^2,$$

where $\widetilde{\mathbf{v}}_0 = \mathbf{v}_0 \circ \mathbf{u}_B$ stands for the approximation of the disturbed object. Since the criterion function $\mathcal{J}_2$ is defined with respect to the true object, thus the preparatory background compensation $\mathbf{u}_0[l] = \widetilde{\mathbf{u}}_0[l]/\mathbf{u}_B[l]$ should be performed.

$$\mathcal{J}_{2,a}(\boldsymbol{\theta}_a, |\mathbf{u}_0|) = \tau_a \cdot ||\boldsymbol{\theta}_a||_p + \frac{1}{2\gamma_a}||\boldsymbol{\theta}_a - \boldsymbol{\Phi}_a \cdot \left|\frac{\widetilde{\mathbf{u}}_0}{\mathbf{u}_B}\right||_2^2, \tag{5.37}$$

$$\mathcal{J}_{2,\phi}(\boldsymbol{\theta}_\phi, \arg\{\mathbf{u}_0\}) = \tau_\phi \cdot ||\boldsymbol{\theta}_\phi||_p + \frac{1}{2\gamma_\phi}||\boldsymbol{\theta}_\phi - \boldsymbol{\Phi}_\phi \cdot \arg\left\{\frac{\widetilde{\mathbf{u}}_0}{\mathbf{u}_B}\right\}||_2^2, \tag{5.38}$$

where $\frac{\widetilde{\mathbf{u}}_0}{\mathbf{u}_B}$ is the element-wise division similar to what we have in Eq. (4.5).

Using the compact form of Eqs. (5.24), we arrive at the phase-retrieval algorithm with sparse modeling of the true object and the iterative background compensation. This algorithm introduced in **P7** (initially for a binary amplitude object) is named *Sparse Phase Amplitude Reconstruction with Background Compensation* or $SPAR-BC$.

Algorithm: $SPAR-BC$
Input: $\{\mathbf{o}_r^B\}_{r=1}^K$, $\{\mathbf{o}_r\}_{r=1}^K$
Initialization: $\widehat{\mathbf{u}}_B$, $\widetilde{\mathbf{u}}_0^0$, $\{\boldsymbol{\Lambda}_r^0\}$
Repeat for $t = 0, 1, 2...$
1. Object update (background compensation):
$\mathbf{u}_0^t[l] = \widetilde{\mathbf{u}}_0^t[l]/\widehat{\mathbf{u}}_B[l]$
2. BM3D filtering:
$\mathbf{a}_0^{t+1/2} = BM3D_a(|\mathbf{u}_0^t|)$,
$\boldsymbol{\phi}_0^{t+1/2} = BM3D_\phi(\arg\{\mathbf{u}_0^t\})$
3. Object approximation synthesis:
$\mathbf{v}_0^{t+1} = \mathbf{a}_0^{t+1/2} \circ \exp(i \cdot \boldsymbol{\phi}_0^{t+1/2})$
Repeat for $r = 1, ...K$
4. Forward propagation:
$\mathbf{u}_r^{t+1/2} = \mathbf{A}_r \cdot \widetilde{\mathbf{u}}_0^t$
5. Fitting to observations:
$\mathbf{u}_r^{t+1}[l'] = \mathcal{G}(\mathbf{o}_r[l'], \mathbf{u}_r^{t+1/2}[l'], \boldsymbol{\Lambda}_r^t[l'])\ \forall l'$
6. Lagrange multipliers update:
$\boldsymbol{\Lambda}_r^{t+1} = \boldsymbol{\Lambda}_r^t + \alpha_r \cdot (\mathbf{u}_r^{t+1} - \mathbf{u}_r^{t+1/2})$
End on r
7. Disturbed object update:
$\widetilde{\mathbf{u}}_0^{t+1} = \left(\sum_{r=1}^K \frac{1}{\gamma_r \sigma_r^2}\mathbf{A}_r^H\mathbf{A}_r + \frac{1}{\gamma_0} \cdot \mathbf{I}\right)^{-1} \times$
$\times \sum_{r=1}^K \frac{1}{\gamma_r \sigma_r^2}\mathbf{A}_r^H \cdot (\mathbf{u}_r^{t+1} + \boldsymbol{\Lambda}_r^t) + \frac{1}{\gamma_0} \cdot (\widehat{\mathbf{u}}_B \circ \mathbf{v}_0^{t+1})$
End on t

This second stage of the object reconstruction is illustrated in the flowchart of SPAR–BC in Fig. 5.6 under the mentioned block for the background estimation.

The initialization concerns the calculation not only of the background estimation $\widehat{\mathbf{u}}_B$ and Lagrange multipliers (e.g., $\boldsymbol{\Lambda}_r^0[k] = 0$), but also the initial guess for the disturbed object $\widetilde{\mathbf{u}}_0^0$, found, e.g., by AL or D–AL. Note that the output of

the SPAR–BC phase-retrieval algorithm is not the estimate of the disturbed $\widetilde{\mathbf{u}}_0$ (Step 7), but the estimate of the true object wave field $\mathbf{u}_0$ by the background compensation calculated in Step 1.

5.3.3 SPAR–BC for binary amplitude object

In **P7** we consider the reconstruction of a binary object with the amplitude given in the form

$$\mathbf{a}_0[l] = |\mathbf{u}_0[l]| = \begin{cases} \beta_1, \text{ for } l \in X_1, \\ \beta_0, \text{ for } l \in X_0, \end{cases}, \tag{5.39}$$

where $\beta_0 \in \mathbb{R}^+$ and $\beta_1 \in \mathbb{R}^+$ stand for the lower and upper levels of the object amplitude signal, respectively. The set X_1 defines the indices of the upper level and the set X_0 defines the indices of the lower level, $X_0 \cup X_1 = \{l : l = \{1, 2, ...N_\xi N_\eta\}\}$. Both these levels β_0, β_1 and the sets X_0, X_1 are unknown and should be reconstructed.

We incorporate the knowledge about the object amplitude (Eq. (5.39)) in the criterion $\mathcal{J}_{2,a}$ as an additional constraint. To deal with such a new criterion, a special modification of the filtering procedure is developed targeted on an essential improvement of the reconstruction of the binary object amplitude. The BM3D filtering (Step 2 of SPAR–BC) is replaced by

$$\begin{aligned} \mathbf{a}_0^{t+1/3} &= BM3D_a(|\mathbf{u}_0^t| - \beta_0^t) + \beta_0^t \\ \mathbf{a}_0^{t+1/2} &= BM3D_a(\mathbf{a}_0^{t+1/3} - \beta_1^t) + \beta_1^t \end{aligned} \tag{5.40}$$

where the estimates of the lower β_0^t and upper levels β_1^t are calculated as medians of $\mathbf{a}_0^t = |\mathbf{u}_0^t|$ over the corresponding subsets $X_0^t = \{\mathbf{a}_0^t : 0 \le \mathbf{a}_0^t \le \rho^t\}$ and $X_1^t = \{\mathbf{a}_0^t : \mathbf{a}_0^t > \rho^t\}$

$$\begin{aligned} \beta_0^t &= \text{median}_{\mathbf{a}_0^t \in X_0^t}(\mathbf{a}_0^t), \\ \beta_1^t &= \text{median}_{\mathbf{a}_0^t \in X_1^t}(\mathbf{a}_0^t) \end{aligned} \tag{5.41}$$

For estimation of subsets X_0^t and X_1^t, corresponding to small and large values of $\mathbf{a}_0^t$, we use the thresholding parameter ρ^t calculated using the Otsu algorithm [170]. In the procedures (5.40), successive subtractions of β_0^t and β_1^t makes the image flatter first in the area of low values of binary amplitude signal and after that in the area of its high values. Experiments show that this flattening enables much more efficient filtering of artifacts for the estimate of $\mathbf{a}_0$ in case of binary object.

For the phase filtering we make the flattening procedure simpler because for the considered $\mathbf{u}_0$ the phase should be zero. The median of the object phase is calculated only ones as $\boldsymbol{\varphi}_0^t = \text{median}(\arg\{\mathbf{u}_0^t\})$ without partitioning in two subsets as for the object amplitude. Finally, the BM3D-frame filtering and update of the object approximation (Steps 2 and 3 in SPAR–BC) are replaced by

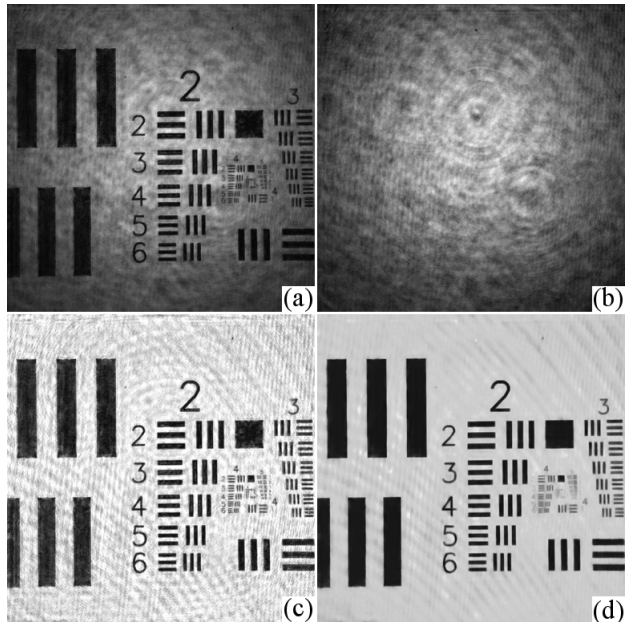

Figure 5.7: Sparse object reconstruction with background compensation by SPAR–BC. Fragments of (a) the AL amplitude estimate of the disturbed object $|\widetilde{\mathbf{u}}_0^0|$ used as the initial guess for SPAR–BC; (b) the AL amplitude estimate of the background $|\mathbf{u}_B|$; (c) the initial guess for the object amplitude $|\mathbf{u}_0^0|$ computed by background compensation; (d) the resulting reconstruction of the object amplitude $|\widehat{\mathbf{u}}_0|$.

$$
\begin{aligned}
\mathbf{a}_0^{t+1/3} &= BM3D_a(|\mathbf{u}_0^t| - \beta_0^t) + \beta_0^t \\
\mathbf{a}_0^{t+1/2} &= BM3D_a(\mathbf{a}_0^{t+1/3} - \beta_1^t) + \beta_1^t \\
\boldsymbol{\phi}_0^{t+1/2} &= BM3D_\phi(\arg\{\mathbf{u}_0^t\} - \boldsymbol{\varphi}_0^t) \\
\mathbf{v}_0^{t+1} &= \mathbf{a}_0^{t+1/2} \circ \exp(i \cdot (\boldsymbol{\phi}_0^{t+1/2} + \boldsymbol{\varphi}_0^t))
\end{aligned}
\tag{5.42}
$$

The results of the object reconstruction from experimental data by SPAR–BC are obtained using this modified BM3D-frame filtering: in practice, Step 2 of SPAR–BC is defined exactly by Eqs. (5.42).

In Fig 5.7 we illustrate some results obtained by the SPAR–BC algorithm from experimental data. In Figs. 5.7(a) and 5.7(b) the initial data of this algorithm are presented: the amplitude estimates of the disturbed object $|\widetilde{\mathbf{u}}_0^0|$ and the background $|\mathbf{u}_B|$, respectively. The result of the background compensation, i.e. the initial guess of the object amplitude calculated by $|\mathbf{u}_0^0[l]| = |\widetilde{\mathbf{u}}_0^0[l]|/|\widehat{\mathbf{u}}_B[l]|$ is demonstrated in Fig. 5.7(c). The resulting object amplitude computed by iterative background compensation and BM3D-frame filtering is illustrated in Fig. 5.7(d). Please, compare visual quality of the object amplitude reconstructions shown Fig. 5.7(c) and 5.7(d). Since we have no true complex-valued background, it is impossible to obtain directly good imaging of the object. The iterative BM3D filtering

allows to consistently wiping out the artifacts related to the inaccurate background reconstruction. In general, the SPAR–BC reconstruction in Figs. 5.7(d) looks very close to the original binary object.

5.4 Discussion and further work

As it is mentioned in Section 2.4, in the parallel phase retrieval we deal with nonconvex optimization problem, thus, strictly speaking, there is no guarantee of the uniqueness of the resulting solution, and there could be some problems with the convergence of the phase-retrieval algorithm (very low convergence rate [**P6** cf. Fig. 2], stagnation, etc.). Nevertheless the developed AL based algorithms can be considered as heuristic greedy algorithms giving local optima (AL, AL–A, AL–Ph) [162] or stationary, fixed points (D–AL and SPAR–BC) [38]. The accurate derivation of the convergence of the algorithms in case of nonconvex nonsmooth criterion function is beyond the scope of this thesis. However, our multiple numerical experiments with synthetic and experimental data show that these AL based phase-retrieval algorithms have a good convergence rate and reconstruction quality (see more details in **P4**–**P7**), in many cases better comparing with the state-of-the-art algorithms such as SBMIR [7, 8, 178]. The use and incorporation of a priori information on the object to the algorithms (see AL–A, AL–Ph **P5** and SPAR–BC **P7**) significantly improves the reconstruction accuracy and enhances imaging even more.

Note that the considered AL based algorithms are quite time consuming because of the large dimension of the images and use of a number of sensor planes (in our experiments typically K=5). However, the computational performance can be significantly improved using the advantage of the parallel processing: components of the vectors $|\mathbf{u}_0^t|$ and $|\mathbf{u}_r^t|$, $|\mathbf{\Lambda}_r^t|$ (for different r) can be found independently at each t-th iteration of our algorithms. It is shown in **P6** that our implementation of D–AL on a graphic processing unit[5] (GPU) gives an essential acceleration from two up to 10 times and more.

The algorithm parameters such as the Tikhonov regularization parameter μ, penalty coefficients γ_r for the Lagrange multipliers[6], penalty coefficients for the additional constraints for the object analysis and synthesis in the BM3D domain γ_a , γ_ϕ and threshold parameters τ_a, τ_ϕ are found in our numerical simulations manually, by minimizing RMSE$(\gamma_r, \mu, K, \Delta_z, z_1, \sigma_r)$ for AL (see, e.g., [**P4**, Fig. 3]) ; or more general – by minimizing RMSE$(\gamma_r, \tau_a\gamma_a, \tau_\phi\gamma_\phi, \gamma_0, K, \Delta_z, z_1, \sigma_r)$ for D–AL [149] and SPAR–BC, just because these parameters are interconnected. Indeed, for a certain propagation distance z_1 and distance between the sensor planes Δ_z RMSE curve decreases starting from certain K. Larger number of used observations means that we involve more blurred measurements. Despite a small deviation in the numerical ranks (see Fig. 4.4), we use more and more ill-posed transform matrices corresponding to larger z_r. In addition, the choice of the parameters also depends on the noise level in the given intensity measurements σ_r, the type and size of the object (relative size of the important components of the

[5] The BM3D-frame filter used in this work is realized on a central processing unit (CPU).

[6] In our works **P6**–**P7** and [149] small object details are recovered with slowly updating Lagrange multipliers.

object). It is difficult to use the conventional parameter-choice methods (e.g., to find the Tikhonov regularization parameter μ, see Section 3.7) for the multi-plane phase-retrieval: more sophisticated tools to find proper parameters [108, 186] are required.

Thus, in our papers **P4**–**P7**, [149] we present rather our recommendations for the values of the algorithm parameters. In case of the use of real experimental data we rely on the results of numerical simulations. Our further work concerns the adaptive selection of the parameter as well as an automatic tuning of the filtering for noisy experimental data.

5.4.1 Synthetic background in SPAR–BC: object "restoration"

The discussion about the object reconstruction of a binary amplitude-only object with background compensating is presented in Sections 5.3.2 – 5.3.3 and in our recent paper **P7**. However, the presented results are obtained in case of additional experiments for the background estimation. But, what if these is no background estimation? In Fig. 5.8 we illustrate our numerical experiment of phase retrieval by SPAR–BC with a synthetic background used to imitate the distortions in the optical path. The results are shown for the same parameter setting of the imaging system as in **P7**, including the size of the images and pixels' sizes.

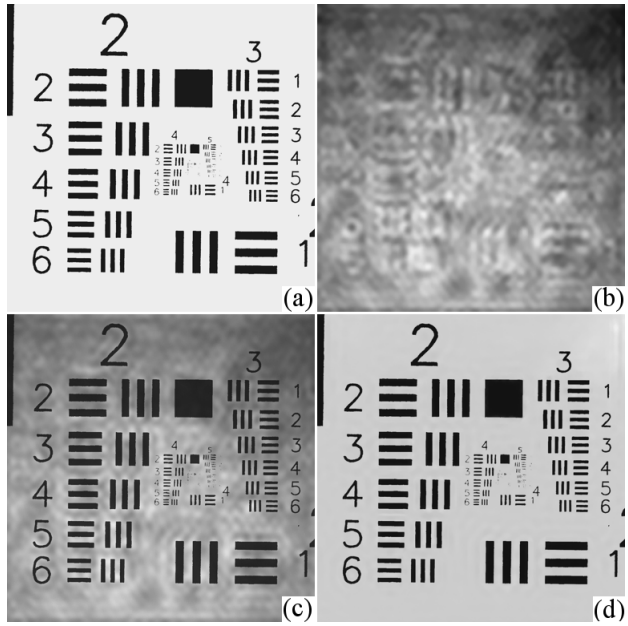

Figure 5.8: Numerical simulation to illustrate the influence of background compensating on the reconstruction imaging. (a) The true binary amplitude object. (b) The amplitude of a synthetic complex-valued background $|\mathbf{u}_B|$. (c) The amplitude estimate of the disturbed object found by AL, RMSE=0.4. (d) The reconstructed true object amplitude $\widehat{\mathbf{a}}_0$ obtained by SPAR–BC, RMSE=0.043.

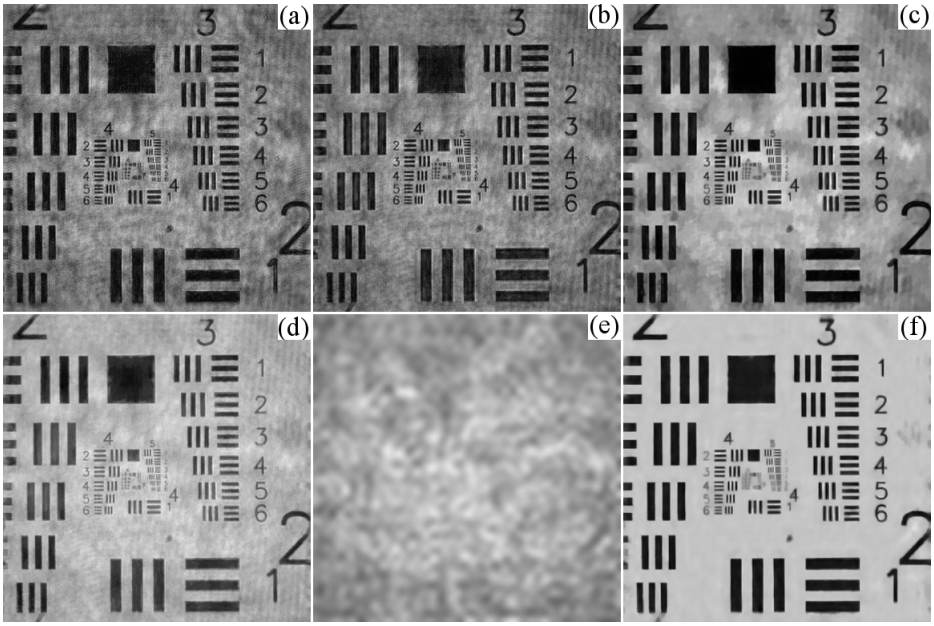

Figure 5.9: Amplitude reconstructions from experimental data (1024×1024 pixels, see **P6** for settings parameters) by (a) SBMIR [7, 8]; (b) AL, **P4**; (c) D–AL, with original BM3D filtering, $\tau_a\gamma_a$=0.05 [**P6**, Fig. 5]; (d) D–AL, with the modified BM3D filtering, Eqs. (5.42), $\tau_a\gamma_a$=0.02. (e) The amplitude of the synthetic smooth background constructed by inpainting of geometrical elements of the AL amplitude reconstruction. (f) The object amplitude estimate found by SPAR–BC with the synthetic background.

In Fig. 5.8(a) the true binary amplitude object $\mathbf{u}_0 = \mathbf{a}_0$ is shown. The amplitude of the synthetic background $|\mathbf{u}_B|$ generated based on experimental data is depicted in Fig. 5.8(b). In order to construct the synthetic complex-valued background we use the experimental measurement data, which result in the object reconstruction presented in [4, Fig. 7]. Firstly, we reconstruct the disturbed object by AL. Then, the complex-valued background $\mathbf{u}_B$ is computed from this object estimate with inpainting of the regions of geometrical elements (for the amplitude and phase, separately) by Criminisi's algorithm [30].

Here it should be mentioned that the results of the forward wave field propagation (examples of the intensity measurements) of the ideal amplitude-only object ($|\mathbf{A}_r \cdot \mathbf{a}_0|^2$) and the disturbed complex-valued object using this synthetic complex-valued background ($|\mathbf{A}_r \cdot (\mathbf{a}_0 \circ \mathbf{u}_B)|^2$) are given in Figs. 5.5(a) and 5.5(b), respectively.

In Fig. 5.8(c) we demonstrate the AL reconstruction of the disturbed object amplitude from corrupted and noisy intensity observations ($\sigma_r = 0.02$ for all $r = 1, ...5$, see Fig. 5.5(b), Eq. (5.29)). In Fig. 5.8(d) we present the reconstructed "true" object amplitude $\widehat{\mathbf{a}}_0$ from the same noisy data computed by SPAR–BC ($\tau_a\gamma_a$=0.05, $\tau_\phi\gamma_\phi$=0.3) with compensation of the synthetic background. These presented reconstructions are obtained by 100 iterations. It is obvious that the sparse reconstruction with background compensation enables a

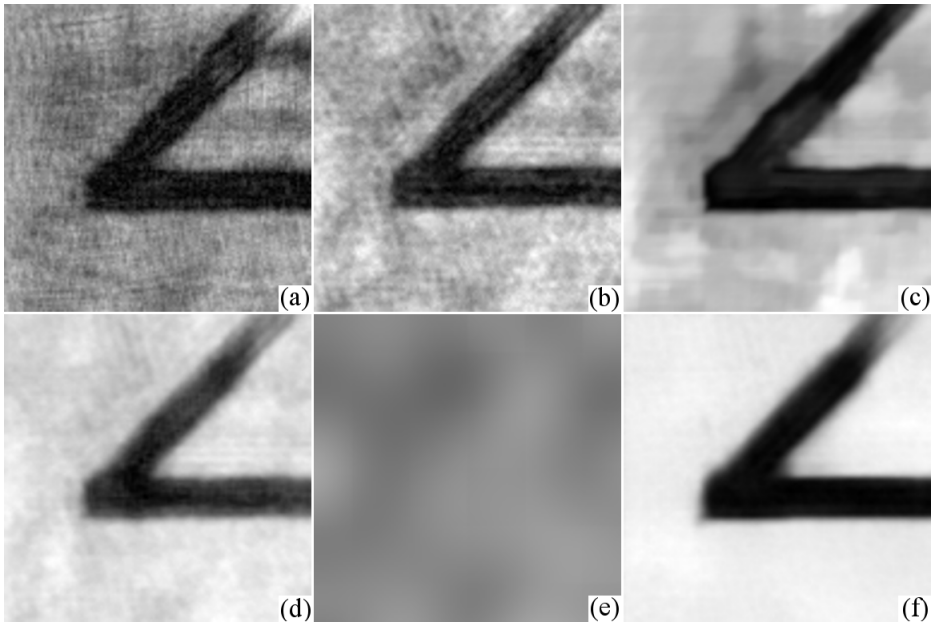

Figure 5.10: The corresponding top left fragments of the images (of the size 128 × 128) illustrated in Fig. 5.9.

significant improvement of the reconstruction accuracy (in our numerical simulations – up to in order of amplitude in RMSE) and imaging enhancement in case of strong corruption of the given observations. The background estimate "undertakes" strong fluctuations, which would be difficult to compensate by filtering.

However, it is much more important that the previously unsuccessful object reconstructions can be significantly improved either by the additional calibration procedure (if the used optical system with the same settings is available), as in the original SPAR–BC algorithm, or by the synthetic background generated from the reconstructed disturbed object.

In Fig. 5.9 some examples of the amplitude object reconstruction by different phase-retrieval methods are shown. The presented results are 1024×1024 pixels large and obtain from the experimental date of the optical system with parameters discussed in **P6**. Figures 5.9(a) – 5.9(d) illustrate the amplitude estimates computed by SBMIR, AL, D–AL **P6** and D–AL with the modified BM3D filtering according to Eqs. (5.42), respectively. D–AL is computed with soft thresholding. In Fig. 5.9(e) we present the amplitude of a synthetic background constructed again by inpainting of the AL object reconstruction (separately, the amplitude and phase) and further smoothing by the BM3D filter. In Fig. 5.9(f) we demonstrate the reconstructed object amplitude obtained by SPAR–BC using this synthetic background. We call such a modification of the SPAR–BC algorithm, where only measurements for the object are required $\{\mathbf{o}_r\}$, *object "restoration"* by analogy with the restoration of old photos that have lost their imaging quality with time. It can be seen that this procedure suppresses remaining noise (cf. 5.9 (d)), of

cause, with some oversmoothing, but with no strong degradations (cf. 5.9(c)). In Fig. 5.10 top left fragments of the mentioned images illustrated in Fig. 5.9 of the size 128×128 pixels are presented.

The main point is the selection of geometric elements on the AL object reconstruction. It can be made manually or using the conventional Otsu algorithm [170], while it is originated especially for binarization of gray-scale images.

5.4.2 Exploitation of parallel AL based algorithms

The resulting parallel multi-plane AL based algorithms may be used for various application, where a good imaging of the complex-valued wave field is required: in optical nondestructive testing, in microscopy to analyse, e.g., blood cells (a live blood specimen) or in astronomy for, say, the James Webb space telescope. In our works **P6**–**P7** we present the results of the object reconstruction only by phase retrieval. Our further work concerns also the comparison of the obtained results with the holographic approach especially using the accurate M–DDT technique. Also we are planning to implement the SPAR–BC algorithm for smooth amplitude and phase objects.

In addition, it is shown in **P7** that the modified BM3D filtering (Eqs. (5.42)) works as a classifier for the noisy binary object estimate. The estimate of the amplitude levels are found using the Otsu method, but the BM3D filtering shifts the value of the pixel $\mathbf{a}_0^t[l]$ to one of these two levels β_0^t or β_1^t depending on the local neighborhood. Thus, such a modification can be used as an advanced tool for binarization of noisy and corrupted objects.

Appendix A: Derivations of AL algorithms

Here we provide some details of optimization of the AL criteria on $\{\mathbf{u}_r\}$ and $\mathbf{u}_0$ defining the proposed phase-retrieval algorithms.

A.1 Minimization of $\mathcal{J}_{AL}$ on $\mathbf{u}_r$

The AL criterion (cf. Eq. (4.16))

$$\mathcal{J}_{AL}(\{\mathbf{o}_r\},\mathbf{u}_0,\{\mathbf{u}_r\},\{\mathbf{\Lambda}_r\}) = \mu\cdot||\mathbf{u}_0||_2^2+\sum_{r=1}^{K}\frac{1}{\sigma_r^2}[\frac{1}{2}||\mathbf{o}_r-|\mathbf{u}_r|^2||_2^2+ \tag{A.1}$$

$$+\frac{1}{\gamma_r}||\mathbf{u}_r-\mathbf{A}_r\cdot\mathbf{u}_0||_2^2+\frac{1}{\gamma_r}\mathbf{\Lambda}_r^H(\mathbf{u}_r-\mathbf{A}_r\cdot\mathbf{u}_0)+\frac{1}{\gamma_r}\mathbf{\Lambda}_r^T(\mathbf{u}_r-\mathbf{A}_r\cdot\mathbf{u}_0)^*],$$

is additive with respect to the vectors $\mathbf{u}_r$ and their components. Thus, the minimization of $\mathcal{J}_{AL}$ on $\mathbf{u}_r$ can be produced separately for every r and l'. The minimum condition for $\mathbf{u}_r[l']$

$$\frac{\partial\mathcal{J}_{AL}}{\partial\mathbf{u}_r^*[l']}=\frac{1}{\sigma_r^2}(|\mathbf{u}_r[l']|^2-\mathbf{o}_r[l'])\cdot\mathbf{u}_r[l']+\frac{1}{\gamma_r\sigma_r^2}(\mathbf{u}_r[l']-\boldsymbol{\varsigma}_r[l']+\mathbf{\Lambda}_r[l'])=0 \tag{A.2}$$

results in

$$\mathbf{u}_r[l']=\frac{(\mathbf{A}_r\cdot\mathbf{u}_0)[l']-\mathbf{\Lambda}_r[l']}{\gamma_r(|\mathbf{u}_r[l']|^2-\mathbf{o}_r[l'])+1}=\frac{\boldsymbol{\varsigma}_r[l']}{\boldsymbol{\kappa}_r[l']}. \tag{A.3}$$

Taking the module from the left and right sides of Eq. (A.3) we arrive at the cubic equation with respect to $|\mathbf{u}_r[l']|$:

$$|\mathbf{u}_r[l']|^3+|\mathbf{u}_r[l']|\cdot\left(\frac{1}{\gamma_r}-\mathbf{o}_r[l']\right)-sign(\boldsymbol{\kappa}_r[l'])\cdot\frac{|\boldsymbol{\varsigma}_r[l']|}{\gamma_r}=0. \tag{A.4}$$

The last equation may have one or three real solutions. We are looking for a nonnegative one for $|\mathbf{u}_r[l']|$. Let us denote this solution for Eq. (A.4) as $|\mathbf{u}_r^{\dagger}[l']|$. If the nonnegative real-valued root of Eq. (A.4) is found, then the corresponding complex-valued estimate of the wave field at the sensor plane $\widehat{\mathbf{u}}_r[l']$ is calculated according to Eq. (A.3) as follows

$$\widehat{\mathbf{u}}_r[l']=\frac{(\mathbf{A}_r\cdot\mathbf{u}_0)[l']-\mathbf{\Lambda}_r[l']}{\gamma_r(|\mathbf{u}_r^{\dagger}[l']|^2-\mathbf{o}_r[l'])+1}. \tag{A.5}$$

For brevity, we denote the nonlinear algorithm giving the nonnegative real-valued root of Eq. (A.4) and computing Eq. (A.5) as

$$\widehat{\mathbf{u}}_r[l'] = \mathcal{G}(\mathbf{o}_r[l'], \mathbf{u}_r[l'], \mathbf{\Lambda}_r[l']). \tag{A.6}$$

It defines Step 2 of our AL based phase-retrieval algorithms. We refer to **P4** and [118] for more details.

A.2 Minimization of $\mathcal{J}_{AL}$ on $\mathbf{u}_0$

In these derivative calculations, the differentiation of a scalar by a vector results in a vector of derivatives: $\frac{\partial \mathcal{J}_{AL}}{\partial \mathbf{u}_0} = [\frac{\partial \mathcal{J}_{AL}}{\partial \mathbf{u}_0[1]}, ..., \frac{\partial \mathcal{J}_{AL}}{\partial \mathbf{u}_0[N_\xi N_\eta]}]^T$, provided that $\mathbf{u}_0 = [\mathbf{u}_0[1], ..., \mathbf{u}_0[N_\xi N_\eta]]^T$. The minimum condition $\frac{\partial \mathcal{J}_{AL}}{\partial \mathbf{u}_0^*} = 0$ gives the object estimate in the form

$$\widehat{\mathbf{u}}_0 = \left(\sum_{r=1}^{K} \frac{1}{\gamma_r \sigma_r^2} \mathbf{A}_r^H \mathbf{A}_r + \mu \cdot \mathbf{I} \right)^{-1} \cdot \sum_{r=1}^{K} \frac{1}{\gamma_r \sigma_r^2} \mathbf{A}_r^H (\mathbf{u}_r + \mathbf{\Lambda}_r), \tag{A.7}$$

what defines Step 4 of the AL algorithm.

Further we are looking for the object estimate in case of the amplitude (AM) and phase modulations (PM) of the object. The solutions are derived from the minimum conditions $\partial \mathcal{J}_{AL}/\partial \mathbf{a}_0 = 0$ and $\partial \mathcal{J}_{AL}/\partial \boldsymbol{\phi}_0 = 0$. Note that the very first fidelity term of Eq. (A.1) does not depend on the object, it depends neither on $\mathbf{a}_0 \in \mathbb{R}^{N_\xi N_\eta}$ nor on $\boldsymbol{\phi}_0 \in \mathbb{R}^{N_\xi N_\eta}$. Let us rewrite Eq. (A.1) as

$$\begin{aligned} & \widetilde{\mathcal{J}}_{AL}(\mathbf{u}_0, \{\mathbf{u}_r\}, \{\mathbf{\Lambda}_r\}) = \qquad (A.8) \\ = & \sum_{r=1}^{K} \frac{1}{\sigma_r^2} [\frac{1}{\gamma_r} ||\mathbf{u}_r - \mathbf{A}_r \cdot \mathbf{u}_0||_2^2 + \frac{2}{\gamma_r} \mathrm{Re}\{\mathbf{\Lambda}_r^H (\mathbf{u}_r - \mathbf{A}_r \cdot \mathbf{u}_0)\}] + \mu \cdot ||\mathbf{u}_0||_2^2 = \\ = & \sum_{r=1}^{K} \frac{1}{\sigma_r^2} [\frac{1}{\gamma_r} \mathcal{A}_r(\mathbf{u}_0, \mathbf{u}_r) + \frac{1}{\gamma_r} \mathcal{B}_r(\mathbf{u}_0, \mathbf{u}_r, \mathbf{\Lambda}_r)] + \mu \cdot ||\mathbf{u}_0||_2^2 \end{aligned}$$

and consider the optimization of $\widetilde{\mathcal{J}}_{AL}$ on $\mathbf{a}_0$ and $\boldsymbol{\phi}_0$ in parts.

A.2.1 Analytical solution: update of the object amplitude

The derivative of the scalar $\mathbf{u}_r^T \cdot \mathbf{A}_r^* \cdot \mathbf{u}_0^*$ with respect to the vector $\mathbf{a}_0$ is $(\mathbf{A}_r^H \mathbf{u}_r) \circ \exp(-i\boldsymbol{\phi}_0)$ because

$$\begin{aligned} & \frac{\partial}{\partial \mathbf{a}_0[l]} (\mathbf{u}_r^T \cdot \mathbf{A}_r^* \cdot \mathbf{u}_0^*) = \frac{\partial}{\partial \mathbf{a}_0[l]} \sum_{l'} \mathbf{u}_r[l'] \sum_{s} \mathbf{A}_r^*[l', s] \mathbf{u}_0^*[s] = \qquad (A.9) \\ & = \exp(-i\boldsymbol{\phi}_0[l]) \cdot \sum_{l'} \mathbf{u}_r[l'] \mathbf{A}_r^*[l', l] = (\mathbf{A}_r^H \mathbf{u}_r)[l] \cdot \exp(-i\boldsymbol{\phi}_0[l]), \end{aligned}$$

where $\mathbf{u}_0^* = \mathbf{a}_0 \circ e^{-i\boldsymbol{\phi}_0}$. Hence

$$\begin{aligned}
&\frac{\partial}{\partial \mathbf{a}_0}\mathcal{A}_r(\mathbf{u}_0, \mathbf{u}_r) = \qquad (A.10)\\
&= \frac{\partial}{\partial \mathbf{a}_0}||\mathbf{u}_r - \mathbf{A}_r \cdot \mathbf{u}_0||_2^2 = \frac{\partial}{\partial \mathbf{a}_0}[-\mathbf{u}_r^T \cdot \mathbf{A}_r^* \cdot \mathbf{u}_0^* - \mathbf{u}_0^T \cdot \mathbf{A}_r^T \cdot \mathbf{u}_r^* + \\
&+\mathbf{u}_0^T \cdot \mathbf{A}_r^T \cdot \mathbf{A}_r^* \cdot \mathbf{u}_0^*] = -[\mathbf{A}_r^H \mathbf{u}_r \circ \exp(-i\boldsymbol{\phi}_0) + (\mathbf{A}_r^H \mathbf{u}_r \circ \exp(-i\boldsymbol{\phi}_0))^*] + \\
&+\mathbf{A}_r^H \mathbf{A}_r \mathbf{u}_0 \circ \exp(-i\boldsymbol{\phi}_0) + (\mathbf{A}_r^H \mathbf{A}_r \mathbf{u}_0 \circ \exp(-i\boldsymbol{\phi}_0))^* = \\
&= 2\,\mathrm{Re}\{\mathbf{A}_r^H(\mathbf{A}_r\mathbf{u}_0 - \mathbf{u}_r) \circ \exp(-i\boldsymbol{\phi}_0)\}.
\end{aligned}$$

Analogically

$$\begin{aligned}
&\frac{\partial}{\partial \mathbf{a}_0}\mathcal{B}_r(\mathbf{u}_0, \mathbf{u}_r, \boldsymbol{\Lambda}_r) = \frac{\partial}{\partial \mathbf{a}_0} 2\,\mathrm{Re}\{\boldsymbol{\Lambda}_r^H \cdot (\mathbf{u}_r - \mathbf{A}_r \cdot \mathbf{u}_0)\} = \qquad (A.11)\\
&= \frac{\partial}{\partial \mathbf{a}_0}[-\boldsymbol{\Lambda}_r^T \cdot \mathbf{A}_r^* \cdot \mathbf{u}_0^* - \boldsymbol{\Lambda}_r^H \cdot \mathbf{A}_r \cdot \mathbf{u}_0] = -[\mathbf{A}_r^H \boldsymbol{\Lambda}_r \circ \exp(-i\boldsymbol{\phi}_0) + \\
&+ (\mathbf{A}_r^H \boldsymbol{\Lambda}_r \circ \exp(-i\boldsymbol{\phi}_0))^*] = -2\,\mathrm{Re}\{\mathbf{A}_r^H \boldsymbol{\Lambda}_r \circ \exp(-i\boldsymbol{\phi}_0)\}.
\end{aligned}$$

Together Eqs. (A.10)–(A.11) give the minimum condition with respect to $\mathbf{a}_0$ in the form

$$\begin{aligned}
&\frac{\partial}{\partial \mathbf{a}_0}\mathcal{J}_{AL} = \qquad (A.12)\\
&= \sum_{r=1}^{K} \frac{2}{\gamma_r \sigma_r^2}\,\mathrm{Re}\{\mathbf{A}_r^H(\mathbf{A}_r\mathbf{u}_0 - \mathbf{u}_r - \boldsymbol{\Lambda}_r) \circ \exp(-i\boldsymbol{\phi}_0)\} + 2\mu \cdot \mathbf{u}_0 \circ \exp(-i\boldsymbol{\phi}_0) = 0.
\end{aligned}$$

In case of AM ($\boldsymbol{\phi}_0[l] = 0\ \forall l$), we arrive at the following analytical solution

$$\mathbf{a}_0 = \left(\sum_{r=1}^{K} \frac{1}{\gamma_r \sigma_r^2}\,\mathrm{Re}\{\mathbf{A}_r^H \mathbf{A}_r\} + \mu \cdot \mathbf{I}\right)^{-1} \cdot \sum_{r=1}^{K} \frac{1}{\gamma_r \sigma_r^2}\,\mathrm{Re}\{\mathbf{A}_r^H(\mathbf{u}_r^{t+1} + \boldsymbol{\Lambda}_r^t)\}, \quad (A.13)$$

what determines the update of the object amplitude in Step 4 of the AL–A algorithm.

A.2.2 Analytical solution: update of the object phase

Let us consider the phase modulation of the object (PM) in the form $\mathbf{u}_0 = a \cdot e^{i\boldsymbol{\phi}_0}$, where a is unknown constant. Taking into account that $\mathbf{u}_0^* = a \cdot e^{-i\boldsymbol{\phi}_0}$, the derivative of $\mathcal{A}_r$ with respect to $\boldsymbol{\phi}_0$ results in

$$\begin{aligned}
&\frac{\partial}{\partial \boldsymbol{\phi}_0}\mathcal{A}_r(\mathbf{u}_0, \mathbf{u}_r) = \qquad (A.14)\\
&= i(\mathbf{A}_r^H \mathbf{u}_r \circ \mathbf{u}_0^*) - i(\mathbf{A}_r^H \mathbf{u}_r \circ \mathbf{u}_0^*)^* + i(\mathbf{u}_0^* \circ \mathbf{A}_r^H \mathbf{A}_r \mathbf{u}_0)^* - i(\mathbf{u}_0^* \circ \mathbf{A}_r^H \mathbf{A}_r \mathbf{u}_0) = \\
&= 2\,\mathrm{Im}\{\mathbf{u}_0^* \circ \mathbf{A}_r^H \mathbf{A}_r \mathbf{u}_0\} - 2\,\mathrm{Im}\{\mathbf{u}_0^* \circ \mathbf{A}_r^H \mathbf{u}_r\} = 2\,\mathrm{Im}\{\mathbf{u}_0^* \circ \mathbf{A}_r^H(\mathbf{A}_r\mathbf{u}_0 - \mathbf{u}_r)\}.
\end{aligned}$$

Analogically

$$\begin{aligned}
&\frac{\partial}{\partial \boldsymbol{\phi}_0}\mathcal{B}_r(\mathbf{u}_0, \mathbf{u}_r, \boldsymbol{\Lambda}_r) = \frac{\partial}{\partial \boldsymbol{\phi}_0}[-\boldsymbol{\Lambda}_r^T \mathbf{A}_r^* \mathbf{u}_0^* - \boldsymbol{\Lambda}_r^H \mathbf{A}_r \mathbf{u}_0] = \qquad (A.15)\\
&= i(\mathbf{A}_r^H \boldsymbol{\Lambda}_r \circ \mathbf{u}_0^*) - i(\mathbf{A}_r^H \boldsymbol{\Lambda}_r \circ \mathbf{u}_0^*)^* = -2\,\mathrm{Im}\{\mathbf{A}_r^H \boldsymbol{\Lambda}_r \circ \mathbf{u}_0^*\}.
\end{aligned}$$

Eq. (A.14) and Eq. (A.15) give the minimum condition with respect to $\boldsymbol{\phi}_0$ in the form

$$\frac{\partial}{\partial \boldsymbol{\phi}_0}\mathcal{J}_{AL} = 2\,\mathrm{Im}\{\mathbf{u}_0^* \circ \sum_{r=1}^{K} \frac{1}{\gamma_r \sigma_r^2}\mathbf{A}_r^H(\mathbf{A}_r\mathbf{u}_0 - \mathbf{u}_r - \boldsymbol{\Lambda}_r)\} = \tag{A.16}$$

$$= \quad 2\,\mathrm{Im}\{(a \cdot e^{-i\boldsymbol{\phi}_0}) \circ \sum_{r=1}^{K} \frac{1}{\gamma_r \sigma_r^2}\mathbf{A}_r^H(\mathbf{A}_r(a \cdot e^{i\boldsymbol{\phi}_0}) - \mathbf{u}_r - \boldsymbol{\Lambda}_r)\} = 0,$$

what determines the phase update in the gradient descent AL–Ph algorithm.

If the phase is defined, then the unknown scalar a is calculated from the condition $\frac{\partial}{\partial a}\mathcal{J}_{AL} = 0$ (cf. Eq. (A.12)) as

$$\chi = \sum_{r=1}^{K} \frac{1}{\gamma_r \sigma_r^2} ||\mathbf{A}_r \exp(i\boldsymbol{\phi}_0)||_2^2 + \mu \cdot N_\xi N_\eta, \tag{A.17}$$

$$a = \frac{1}{\chi}\sum_{r=1}^{K} \frac{1}{\gamma_r \sigma_r^2}\,\mathrm{Re}\{\exp(-i\boldsymbol{\phi}_0^T) \cdot \mathbf{A}_r^H(\mathbf{u}_r + \boldsymbol{\Lambda}_r)\}. \tag{A.18}$$

It gives Step 5 and Step 7 in the gradient descent and Gauss–Newton AL–Ph algorithms, respectively.

A.3 Approximate solution: Gauss–Newton AL–Ph algorithm

The object phase $\boldsymbol{\phi}_0$ can be also found using the iterative Gauss–Newton method derived from the linearization

$$\begin{aligned}
&\mathcal{A}_r(\mathbf{u}_0, \mathbf{u}_r) + \mathcal{B}_r(\mathbf{u}_0, \mathbf{u}_r, \boldsymbol{\Lambda}_r) = \\
&= ||\mathbf{u}_r - \mathbf{A}_r \cdot \mathbf{u}_0||_2^2 + 2\,\mathrm{Re}\{\boldsymbol{\Lambda}_r^H \cdot (\mathbf{u}_r - \mathbf{A}_r \cdot \mathbf{u}_0)\} \approx \\
&\approx \left(\mathbf{u}_r - \mathbf{A}_r\mathbf{u}_0 - \frac{\partial}{\partial \boldsymbol{\phi}_0}(\mathbf{A}_r\mathbf{u}_0) \cdot \boldsymbol{\varphi}_0\right)^H \cdot \left(\mathbf{u}_r - \mathbf{A}_r\mathbf{u}_0 - \frac{\partial}{\partial \boldsymbol{\phi}_0}(\mathbf{A}_r\mathbf{u}_0) \cdot \boldsymbol{\varphi}_0\right) + \\
&+2\,\mathrm{Re}\{\boldsymbol{\Lambda}_r^H \cdot (\mathbf{u}_r - \mathbf{A}_r\mathbf{u}_0 - \frac{\partial}{\partial \boldsymbol{\phi}_0}(\mathbf{A}_r\mathbf{u}_0) \cdot \boldsymbol{\varphi}_0)\} \triangleq \mathcal{S}_r(a, \boldsymbol{\phi}_0, \boldsymbol{\varphi}_0, \mathbf{u}_r, \boldsymbol{\Lambda}_r),
\end{aligned} \tag{A.19}$$

where $\boldsymbol{\varphi}_0 \in \mathbb{R}^{N_\xi N_\eta}$ is a small increment of the object phase. For PM of the form $\mathbf{u}_0 = a \cdot e^{i\boldsymbol{\phi}_0}$ it can be shown that the derivative of the vector $\mathbf{A}_r \cdot \mathbf{u}_0$ with respect to the vector $\boldsymbol{\phi}_0$ is

$$\frac{\partial}{\partial \boldsymbol{\phi}_0}(\mathbf{A}_r \cdot \mathbf{u}_0) = i\mathbf{A}_r\boldsymbol{\Gamma},\ \boldsymbol{\Gamma} = \mathrm{diag}(a \cdot \exp(i\boldsymbol{\phi}_0)) \tag{A.20}$$

as

$$\begin{aligned}
\frac{\partial}{\partial \boldsymbol{\phi}_0[l]}(\mathbf{A}_r \cdot \mathbf{u}_0) &= \frac{\partial}{\partial \boldsymbol{\phi}_0[l]}\sum_s \mathbf{A}_r[l', s](a \cdot \exp(i\boldsymbol{\phi}_0[s])) = \\
&= i\mathbf{A}_r[l', l] \cdot (a \cdot \exp(i\boldsymbol{\phi}_0[l]))\ \forall l'
\end{aligned} \tag{A.21}$$

Thus, we arrive at

$$\begin{aligned} & \mathcal{S}_r(a, \boldsymbol{\phi}_0, \boldsymbol{\varphi}_0, \mathbf{u}_r, \boldsymbol{\Lambda}_r) = \\ = \; & (\mathbf{u}_r - \mathbf{A}_r \cdot \mathbf{u}_0 - i\mathbf{A}_r\boldsymbol{\Gamma} \cdot \boldsymbol{\varphi}_0)^H (\mathbf{u}_r - \mathbf{A}_r \cdot \mathbf{u}_0 - i\mathbf{A}_r\boldsymbol{\Gamma} \cdot \boldsymbol{\varphi}_0) + \\ & + 2\,\mathrm{Re}\{\boldsymbol{\Lambda}_r^H \cdot (\mathbf{u}_r - \mathbf{A}_r \cdot \mathbf{u}_0 - i\mathbf{A}_r\boldsymbol{\Gamma} \cdot \boldsymbol{\varphi}_0)\}. \end{aligned} \tag{A.22}$$

The extremal condition $\frac{\partial}{\partial \boldsymbol{\varphi}_0} \sum_r \frac{1}{\gamma_r \sigma_r^2} \mathcal{S}_r = 0$ gives us the increment $\boldsymbol{\varphi}_0$. We take only those components of $\mathcal{S}_r$ which depend on $\boldsymbol{\varphi}_0$, i.e. further we use the criterion

$$\begin{aligned} \widetilde{\mathcal{S}}_r = & -\mathbf{u}_r^H \cdot i\mathbf{A}_r\boldsymbol{\Gamma} \cdot \boldsymbol{\varphi}_0 + \mathbf{u}_0^H \mathbf{A}_r^H \cdot i\mathbf{A}_r\boldsymbol{\Gamma} \cdot \boldsymbol{\varphi}_0 + \\ & + i\boldsymbol{\varphi}_0^T \cdot \boldsymbol{\Gamma}^H \mathbf{A}_r^H \cdot \mathbf{u}_r - i\boldsymbol{\varphi}_0^T \cdot \boldsymbol{\Gamma}^H \mathbf{A}_r^H \cdot \mathbf{A}_r\mathbf{u}_0 + \\ & + \boldsymbol{\varphi}_0^T \cdot \boldsymbol{\Gamma}^H \mathbf{A}_r^H \cdot \mathbf{A}_r\boldsymbol{\Gamma} \cdot \boldsymbol{\varphi}_0 - \\ & - \boldsymbol{\Lambda}_r^H \cdot i\mathbf{A}_r\boldsymbol{\Gamma} \cdot \boldsymbol{\varphi}_0 + i\boldsymbol{\varphi}_0^T \cdot \boldsymbol{\Gamma}^H \mathbf{A}_r^H \cdot \boldsymbol{\Lambda}_r. \end{aligned} \tag{A.23}$$

In order to find $\boldsymbol{\varphi}_0$ we compute $\frac{\partial}{\partial \boldsymbol{\varphi}_0} \sum_{r=1}^K \frac{1}{\gamma_r \sigma_r^2} \widetilde{\mathcal{S}}_r$ and set it equal to zero. Taking into account that [142]

$$\frac{\partial}{\partial \mathbf{x}} \mathbf{x}^T \mathbf{A} = \mathbf{A}^T, \;\; \frac{\partial}{\partial \mathbf{x}} \mathbf{x}^T \mathbf{A} \mathbf{x} = \mathbf{x}^T \mathbf{A}^T + \mathbf{x}^T \mathbf{A} \tag{A.24}$$

$$(\mathbf{u}_r^H \cdot \mathbf{A}_r) \cdot \boldsymbol{\Gamma} = (\mathbf{u}_r^H \cdot \mathbf{A}_r) \circ (a \cdot \exp(i\boldsymbol{\phi}_0^T)) = \mathbf{u}_r^H \mathbf{A}_r \circ \mathbf{u}_0^T, \tag{A.25}$$

we arrive at

$$\sum_{r=1}^K \frac{2}{\gamma_r \sigma_r^2} \mathrm{Re}\{\boldsymbol{\Gamma}^H \mathbf{A}_r^H \mathbf{A}_r \boldsymbol{\Gamma}\} \cdot \boldsymbol{\varphi}_0 + 2\,\mathrm{Im}\{\mathbf{u}_0^* \circ \sum_{r=1}^K \frac{1}{\gamma_r \sigma_r^2} \mathbf{A}_r^H (\mathbf{A}_r\mathbf{u}_0 - \mathbf{u}_r - \boldsymbol{\Lambda}_r)\} = 0. \tag{A.26}$$

Eq. (A.26) can be rearranged to obtain the following normal equation

$$-\frac{\partial}{\partial \boldsymbol{\phi}_0} \mathcal{J}_{AL} = \sum_{r=1}^K \frac{2}{\gamma_r \sigma_r^2} \mathrm{Re}\{\boldsymbol{\Gamma}^T \mathbf{A}_r^T \mathbf{A}_r^* \boldsymbol{\Gamma}^*\} \cdot \boldsymbol{\varphi}_0, \tag{A.27}$$

what results in

$$\begin{aligned} \boldsymbol{\varphi}_0 = & -\frac{1}{2} \left(\sum_{r=1}^K \frac{1}{\gamma_r \sigma_r^2} \mathrm{Re}\{\boldsymbol{\Gamma}^T \mathbf{A}_r^T \mathbf{A}_r^* \boldsymbol{\Gamma}^*\} \right)^{-1} \cdot \frac{\partial}{\partial \boldsymbol{\phi}_0} \mathcal{J}_{AL} = \\ = & -\left(\sum_{r=1}^K \frac{1}{\gamma_r \sigma_r^2} \mathrm{Re}\{\boldsymbol{\Gamma}^T \mathbf{A}_r^T \mathbf{A}_r^* \boldsymbol{\Gamma}^*\} \right)^{-1} \cdot \mathrm{Im}\{\mathbf{u}_0^* \circ \sum_{r=1}^K \frac{1}{\gamma_r \sigma_r^2} \mathbf{A}_r^H (\mathbf{A}_r\mathbf{u}_0 - \mathbf{u}_r - \boldsymbol{\Lambda}_r)\}. \end{aligned} \tag{A.28}$$

It determined the update of the object phase in the Gauss–Newton AL–Ph algorithm. If the phase is determined, the scalar object amplitude is defined by Eqs. (A.17)–(A.18).

Appendix B: 4f configuration for phase retrieval

B.1 4f optical system

Let us consider the wave field propagation model in the 4f configuration with a reflective phase modulating spatial light modulator (SLM) placed at the Fourier plane as it is presented in Fig. 5.1. The lenses L_1 and L_2 with the same focal distance f arranged in a 4f configuration provides mapping of the object wave field to the Fourier plane and then to the sensor plane. The wave field at the Fourier transform plane $u_F(\frac{v}{\lambda f})$ can be easily found as the result of convolution of the wave field $u'(\xi)$, $\xi = (\xi_1, \xi_2)$ falling to the lens L_1 with the Fresnel diffraction kernel $g_f(\xi - x)$ of the wave field propagation to the distance f

$$u'(\xi) = \{u_0 \circledast g_f\}(\xi) = \frac{e^{ikf}}{i\lambda f} \iint_{-\infty}^{\infty} u_0(x) e^{i\frac{k}{2f}||\xi - x||^2} dx, \tag{B.1}$$

Recall that the transverse wave field distributions $u_0(x)$, $u_F(\frac{v}{\lambda f})$ and $u_r(y)$ are given in the 2D spatial coordinates $x = (x_1, x_2)$, $v = (v_1, v_2)$, $y = (y_1, y_2) \in \mathbb{R}^2$. Since the lens transmittance [125, cf. Eq. (2.85)], [138, see Table VI.1]

$$T(\xi) = e^{-i\frac{k}{2f}||\xi||^2}, \tag{B.2}$$

then the link between the wave field at the object and Fourier planes is defined as follows

$$\begin{aligned} u_F\left(\frac{v}{\lambda f}\right) &= \frac{e^{ikf}}{i\lambda f} \iint_{-\infty}^{\infty} u'(\xi) \underbrace{e^{-i\frac{k}{2f}||\xi||^2}}_{T(\xi)} e^{i\frac{k}{2f}||v-\xi||^2} d\xi = \\ &= \frac{e^{i2kf}}{i\lambda f} \iint_{-\infty}^{\infty} u_0(x) \frac{e^{i\frac{k}{2f}||v||^2}}{i\lambda f} \iint_{-\infty}^{\infty} e^{i\frac{k}{2f}||\xi - x||^2} e^{-i\frac{k}{f}\langle v, \xi\rangle} d\xi dx, \end{aligned} \tag{B.3}$$

where $\langle v, x\rangle = v_1 x_1 + v_2 x_2$ denotes the inner product of two vectors.

Using the change of variables $q = (q_1, q_2) = \xi - x = (\xi_1 - x_1, \xi_2 - x_2)$ and

taking into account Eq. (1.66), we arrive at

$$\begin{aligned} u_F\left(\frac{v}{\lambda f}\right) &= \frac{e^{i2kf}}{i\lambda f}\iint_{-\infty}^{\infty} u_0(x)e^{-i\frac{k}{f}\langle v,x\rangle}dx \times \\ &\times \iint_{-\infty}^{\infty} e^{i\frac{k}{2f}||q||^2}e^{-i\frac{k}{f}\langle v,q\rangle}dq\frac{e^{i\frac{k}{2f}||v||^2}}{i\lambda f} \overset{\text{Eq.(1.66)}}{=} \\ &= \frac{e^{i2kf}}{i\lambda f}\iint_{-\infty}^{\infty} u_0(x)e^{-i\frac{k}{f}\langle v,x\rangle}dx = \frac{e^{i2kf}}{i\lambda f}\mathcal{F}\{u_0(x)\}\left(\frac{v}{\lambda f}\right). \end{aligned} \tag{B.4}$$

The wave field at the sensor plane $u_r(y)$ can be found similarly

$$u_r(y) = \frac{e^{i2kf}}{i\lambda f}\mathcal{F}\{u_F\left(\frac{v}{\lambda f}\right)\cdot\mathcal{M}\left(\frac{v}{\lambda f}\right)\}(-y), \tag{B.5}$$

provided that the wave field at the Fourier plane is modulated by an optical mask with the complex-valued transmittance $\mathcal{M}(\frac{v}{\lambda f})$. If the complex transmittance of the optical mask (SLM) $\mathcal{M}(\frac{v}{\lambda f}) = 1\ \forall v$, then the output of the optical system is

$$u_r(y) = -e^{i4kf}\iint_{-\infty}^{\infty} u_0(x)\underbrace{\iint_{-\infty}^{\infty} e^{-i2\pi\langle\frac{v}{\lambda f},x+y\rangle}d\frac{v}{\lambda f}}_{\delta(x_1-(-y_1))\delta(x_2-(-y_2))}dx = -e^{i4kf}\cdot u_0(-y), \tag{B.6}$$

where the negative sign of the argument of the function shows that $|u_r(y)|$ is the inverted copy of $|u_0(-y)|$.

B.2 Phase modulation by LC-SLM

In the 4f configuration used for imitating the wave field propagation we use an electronically addressed phase-only[1] LC-SLM. The structure of this SLM as a 2D array of square liquid crystal cells is illustrated in Fig. B.1 (see also [10, 11], [125, §3.5.1] for more details). Here the lateral pixel size (pixel pitch) and its active area are denoted by $\Delta_1 \times \Delta_2$ and $a_1 \times a_2$, respectively. For square pixels $\Delta_1 = \Delta_2 = \Delta$ the physical size of the LC-SLM is $N_1\Delta \times N_2\Delta$. The phase modulation of the (n_1,n_2)-th pixel is defined as $\exp(i\boldsymbol{\phi}_{n_1,n_2})$ for $n_1 = 1...N_1$, $n_2 = 1...N_2$. In general, the transmittance of the LC-SLM is defined as follows [10, 11, Eqs. (1)–(4)]

[1] There always exists an amplitude modulation for phase-only SLMs and vice versa: a phase modulation for an amplitude modulating DOE/SLM. The couple of the phase and amplitude modulations in case of application of SLMs, and the linearity of the input/output response for the phase-only SLM is out of scope of this thesis.

$$\mathcal{M}(v_1,v_2)=[\sum_{n_1=1}^{N_1}\sum_{n_2=1}^{N_2}\exp(i\boldsymbol{\phi}_{n_1,n_2})\times \tag{B.7}$$
$$\times\delta(v_1-(n_1-N_1/2-1)\Delta_1,v_2-(n_2-N_2/2-1)\Delta_2)\times$$
$$\times\underbrace{\text{rect}\left(\frac{v_1}{N_1\Delta_1}\right)\text{rect}\left(\frac{v_2}{N_2\Delta_2}\right)]}_{\text{aperture of the LC-SLM}}\circledast\underbrace{[\text{rect}\left(\frac{v_1}{a_1}\right)\text{rect}\left(\frac{v_2}{a_2}\right)]}_{\text{area of the LC-SLM cell}},$$

where rect$(\cdot)$ is the rectangular function (Eq. (9)).

Note that $\boldsymbol{\phi}$ in Eq. (B.7) is a finite size 2D matrix. It can also be considered as an infinite sparse 2D matrix with non-zeros components for $n_1=1...N_1$, $n_2=1...N_2$ or the corresponding discrete 2D function $\phi(n_1\Delta_1,n_2\Delta_2)$ [76]. Thus, $\mathcal{M}(v_1,v_2)$ in Eq. (B.7) can be rewritten as

$$\mathcal{M}(v_1,v_2)= \tag{B.8}$$
$$\{[\sum_{n_1=-\infty}^{\infty}\sum_{n_2=-\infty}^{\infty}\delta(v_1-(n_1-N_1/2-1)\Delta,v_2-(n_2-N_2/2-1)\Delta_2)\times$$
$$\times\exp(i\boldsymbol{\phi}((n_1-N_1/2-1)\Delta_1,(n_2-N_2/2-1)\Delta_2))]\circledast$$
$$\circledast[\text{rect}\left(\frac{v_1}{a_1}\right)\text{rect}\left(\frac{v_2}{a_2}\right)]\}\cdot\text{rect}\left(\frac{v_1}{N_1\Delta_1}\right)\text{rect}\left(\frac{v_2}{N_2\Delta_2}\right).$$

In a discrete model with the SLM as a $N_1\times N_2$ array of liquid crystal cells of the pixel size $\Delta_1\times\Delta_2$ the sampled representation of ASD, the discrete distributions of the optical masks (5.4) to be programmed into the SLM are

$$\mathbf{M}_r[n_1,n_2]=\int_{-\infty}^{\infty}\!\!\int\mathcal{M}_r\left(\frac{v_1}{\lambda f},\frac{v_2}{\lambda f}\right)\text{rect}\left(\frac{v_1}{\lambda f N_1\Delta_1}\right)\times \tag{B.9}$$
$$\times\,\text{rect}\left(\frac{v_2}{\lambda f N_2\Delta_2}\right)\delta(v_1-n_1\Delta_1,v_2-n_2\Delta_2)dv_1dv_2=$$
$$=\exp\left(\underbrace{ikz_r\sqrt{1-\frac{(|n_1\Delta_1|^2+|n_2\Delta_2|^2)}{f^2}}}_{\boldsymbol{\phi}_{n_1,n_2}\text{ in Eq.(B.7)}}\right),$$

where $r=1,...K$ and $n_1=-N_1/2...N_1/2-1$, $n_2=-N_2/2...N_2/2-1$ for the central symmetry. Here and in our publications we assume, for simplicity, 100% fill factor of the SLM cells, i.e. $a_1=\Delta_1$, $a_2=\Delta_2$. Note that the resulting signal at the sensor plane is significantly different from what we have by the free-space propagation model, namely: taking into account that $\mathcal{F}\{\text{rect}(\frac{v}{\lambda f\Delta})\}(x)=\int\text{rect}(\frac{v}{\lambda f\Delta})e^{-i\frac{2\pi v}{\lambda f}x}dv=\text{sinc}(x\Delta)\cdot\lambda f\Delta$, Eq. (5.2) can be rewritten as

$$u_r(x,y)=-e^{i4kf}\,\{u_0(-x,-y)\circledast[(\lambda f)^2\,\text{sinc}(-x\Delta_1)\,\text{sinc}(-y\Delta_2)\times \tag{B.10}$$
$$\times\,\Delta_1\Delta_2\cdot\mathcal{F}\Big\{\sum_{n_1=-N_1/2}^{N_1/2-1}\sum_{n_2=-N_2/2}^{N_2/2-1}\mathbf{M}_r[n_1,n_2]\cdot\text{rect}\left(\frac{v_1}{\lambda f N_1\Delta_1}\right)\times$$
$$\times\,\text{rect}\left(\frac{v_2}{\lambda f N_2\Delta_2}\right)\delta\left(\frac{v_1}{\lambda f}-n_1\Delta_1,\frac{v_2}{\lambda f}-n_2\Delta_2\right)\Big\}(-x,-y)]\},\ r=1,...K.$$

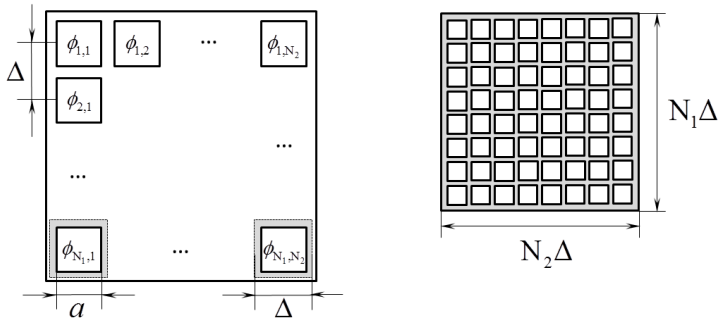

Figure B.1: Structure of the pixelated phase-only LC-SLM as a 2D array of square liquid crystal cells. Following [10, Fig. 1], Δ and a denote the lateral size of the pixel (pixel pitch) and its active area, respectively. Here these sizes are presented to be the same with respect to the x- and y-direction [125, cf. Fig. 3.41].

The flexibility of the optical model with an SLM is the ability to use (in principle) completely arbitrary values in $\mathbf{M}_r[n_1, n_2]$ provided the invertibility of the resulting transfer functions. Moreover, the reprogramming of the SLM (tens of milliseconds) is much faster then the change of the optical setup (replacement of a sensor).

In the wave field propagation models for phase retrieval we use ASD (Eq. (B.9)), F–DDT or M–DDT (**P3**–**P7**), and do not consider complex diffraction kernels describing the real transfer functions of LC-SLMs (Eq. (B.10)). Instead of this, all changes from the theoretically predicted results of the wave field propagation and nonidealities related to, e.g., the bandlimitedness of the transfer function or various distortions in the optical path of the used coherent imaging system (Fig. 5.1) are considered as a cumulative disturbance of the object wave field, a "background" to be estimated and compensated (see Section 5.3, **P7**).

References

[1] Matlab code with additional materials is available on the web page of our project http://www.cs.tut.fi/∼lasip/DDT .

[2] M. Afonso, J. Bioucas-Dias, and M. Figueiredo, "Fast image recovery using variable splitting and constrained optimization," *IEEE Trans. on Image Proc.* **19**, 2345–2356 (2010).

[3] M. Agour, "Determination of the complex amplitude of monochromatic light from a set of intensity observations," PhD thesis, Universität Bremen (2011).

[4] M. Agour, C. Falldorf, C. v. Kopylow, R. B. Bergmann, "Automated compensation of misalignment in phase retrieval based on a spatial light modulator," *Appl. Opt.* **50**, 4779–4787 (2011).

[5] I. Aizenberg and J. Astola, "Discrete generalized Fresnel functions and transforms in an arbitrary discrete basis," *IEEE Trans on Signal Processing* **54**, 4261–4270 (2006).

[6] L. Allen and M. P. Oxley, "Phase retrieval from series of images obtained by defocus variation," *Opt. Commun.* **199**, 65–75 (2001).

[7] P. Almoro, G. Pedrini, and W. Osten, "Complete wavefront reconstruction using sequential intensity measurements of a volume speckle field," *Appl. Opt.* **45**, 8596–8605 (2006).

[8] P. Almoro, A. M. Maallo, and S. Hanson, "Fast-convergent algorithm for speckle-based phase retrieval and a design for dynamic wavefront sensing," *Appl. Opt.* **48**, 1485–1493 (2009).

[9] L. A. D'Arcio, J. J. M. Braat, and H. J. Frankena, "Numerical evaluation of diffraction integrals for apertures of complicated shape," *J. Opt. Soc. Am. A* **11**, 2664–2674 (1994).

[10] V. M. Arrizón, E. Carreón and M. Testorf, "Implementation of Fourier array illuminators using pixelated SLM: efficiency limitations," *Optics Comm.* **160**, 207–213 (1999).

[11] V. M. Arrizón, D. Sánchez-de-la-Llave and L. A. González, "Holographic implementation of complex filters with phase-only pixelated spatial light modulators," *Proc. SPIE* **4435**, 96–106 (2001).

[12] V. M. Arrizón and D. Sánchez-de-la-Llave, "Double-phase holograms implemented with phase-only spatial light modulators: performance evaluation and improvement," *Appl. Opt.* **41**, 3436–3447 (2002).

[13] J. Astola and L. P. Yaroslavsky ed., *Advances in signal transforms: theory and applications*, (Hindawi, 2007).

[14] A. Asundi and K. H. Yung, "Phase-shifting and logical moiré," *J. Opt. Soc. Am. A* **8**, 1591–1600 (1991).

[15] K. A. Bauchert, S. A. Serati, G. D. Sharp and D. J. McKnight, "Complex phase/amplitude spatial light modulator advances and use in a multispectral optical correlator", *Proc. SPIE* **3073**, 170–177 (1997).

[16] T. Baumbach, W. Osten, C. von Kopylow, and W. Jüptner, "Remote metrology by comparative digital holography," *Appl. Opt.* **45**, 925–934 (2006).

[17] H. H. Bauschke, P. L. Combettes, and D. R. Luke, "Phase retrieval, error reduction algorithm, and Fienup variants: a view from convex optimization," *J. Opt. Soc. Am. A* **19**, 1334–1345 (2002).

[18] H. H. Bauschke, P. L. Combettes, and D. R. Luke, "Hybrid projectionreection method for phase retrieval," *J. Opt. Soc. Am. A* **20**, 1025–1034 (2003).

[19] D. P. Bertsekas and J. N. Tsitsiklis, *Parallel and distributed computation: numerical methods*, (Prentice-Hall, 1989).

[20] M. Born and E. Wolf, *Principles of optics: electromagnetic theory of propagation, interference and diffraction of light*, 7th ed. (Cambridge University Press, 2000).

[21] W. E. Boyce and R. C. DiPrima, *Elementary differential equations and boundary value problems*, 7th ed. (John Wiley, 2001).

[22] G. R. Brady and J. R. Fienup. "Nonlinear optimization algorithm for retrieving the full complex pupil function," *Opt. Express* **14**, 474–486 (2006).

[23] B. R. Brown, A. W. Lohmann, "Complex spatial filtering with binary masks," *Appl. Opt.* **5**, 967-969 (1966).

[24] B. R. Brown, A. Lohmann, "Computer generated binary holograms," *IMB J. Res. Dev.* **13**, 160-168 (1969).

[25] E. Buckley, A. Cable, N. Lawrence, and T. Wilkinson, "Viewing angle enhancement for two- and three-dimensional holographic displays with random superresolution phase masks," *Appl. Opt.* **45**, 7334–7341 (2006).

[26] J. Burke and D. R. Luke, "Variational analysis applied to the problem of optical phase retrieval," *SIAM J. on Control and Optim.* **42**, 576–595 (2003).

[27] W. S. C. Chang, *Principles of lasers and optics*, (Cambridge University Press, 2005).

[28] K. Choi and A. D. Lanterman, "Phase retrieval from noisy data based on minimization of penalized I-divergence," *J. Opt. Soc. Am. A* **24**, 34–49 (2007).

[29] J. N. Clark, C. T. Putkunz, M. A. Pfeifer, A. G. Peele, G. J. Williams, B. Chen, K. A. Nugent, C. Hall, W. Fullagar, S. Kim, and I. McNulty, "Use of a complex constraint in coherent diffractive imaging," *Opt. Express* **18**, 1981–1993 (2010).

[30] A. Criminisi, P. Perez, and K. Toyama, "Object removal by exemplar-based inpainting," CVPR'03, (2003).

[31] T. R. Crimmins and J. R. Fienup, "Uniqueness of phase retrieval for functions with sufficiently disconnected support," *J. Opt. Soc. Am.* **73**, 218–221 (1983).

[32] E. Cuche, F. Bevilacqua, and C. Depeursinge, "Digital holography for quantitative phase contrast imaging," *Opt. Lett.* **24**, 291–293 (1999).

[33] E. Cuche, P. Marquet, and C. Depeursinge, "Spatial filtering for zero-order and twin-image elimination in digital off-axis holography," *Appl. Opt.* **39**, 4070–4075 (2000).

[34] K. Dabov, A. Foi, V. Katkovnik, and K. Egiazarian, "Image denoising with block-matching and 3D filtering," *Proc. SPIE* **6064** (2006).

[35] K. Dabov, A. Foi, V. Katkovnik, and K. Egiazarian, "Image restoration by sparse 3D transform-domain collaborative filtering," *Proc. SPIE* **6812** (2008).

[36] J. C. Dainty and J. R. Fienup, "Phase retrieval and image reconstruction for astronomy," in H. Stark, ed., *Image recovery: theory and application*, (Academic Press, 1987), 231–275.

[37] A. Danielyan, V. Katkovnik, and K. Egiazarian, "Image deblurring by augmented Lagrangian with BM3D frame prior," in *Workshop on Information Theoretic Methods in Science and Engineering* (WITMSE), Tampere, Finland, (2010).

[38] A. Danielyan, V. Katkovnik, and K. Egiazarian, "BM3D frames and variational image deblurring," *IEEE Trans. on Image Proc.* **21**, 1715–1728 (2012).

[39] O. Darrigol, A history of optic*s from greek antiquity to the nineteenth century*, (Oxford University Press, 2012).

[40] R. W. Deming, "Phase retrieval from intensity-only data by relative entropy minimization," *J. Opt. Soc. Am. A* **24**, 3666–3679 (2007).

[41] Y. N. Denisyuk, "Photographic reconstruction of the optical properties of an object in its own scattered field," *Sov. Phys. Dokl.* **7**, 543–545 (1962).

[42] D. L. Donoho, "Compressed sensing," *IEEE Trans. Inf. Theory* **52**, 1289–1306 (2006).

[43] D. Dudley, W. Duncan, and J. Slaughter, "Emerging digital micromirror device (DMD) applications," *Proc. SPIE* **4985**, 14–29 (2003), available online.

[44] J. Bioucas-Dias and J. Leitão, "The ZpM algorithm for interferometric image reconstruction in SAR/SAS," *IEEE Trans. on Image Proc.* **11**, 408–422, (2002).

[45] J. Bioucas-Dias, V. Katkovnik, J. Astola, and K. Egiazarian, "Absolute phase estimation: adaptive local denoising and global unwrapping," *Appl. Opt.* **47**, 5358–5369 (2008).

[46] J. Eckstein and D. Bertsekas, "On the Douglas–Rachford splitting method and the proximal point algorithm for maximal monotone operators," *Math. Program.* **5**, 293–318 (1992).

[47] U. Efron, ed., *Spatial light modulator technology: materials, devices, and applications*, (Marcel Dekker, New York, 1995).

[48] M. Elad, *Sparse and redundant representations: from theory to applications in signal and image processing*, (Springer, 2010).

[49] V. Elser, "Phase retrieval by iterated projections," *J. Opt. Soc. Am. A* **20**, 40–55 (2003).

[50] F. Facchinei, and C. Kanzow, "Generalized Nash equilibrium problems," *4OR* **5**, 173–210 (2007).

[51] C. Falldorf, W. Osten, F. Elandaloussi, E. Kolenovic, and W. Jüptner. "Features of the subjective speckle eld and their use for noise-immune unwrapping," in W. Osten, W. Jüptner, and M. Kujawinska eds., *Optical Measurement Systems for Industrial Inspection II: Application in Industrial Design*, Proc. SPIE **4398**, 238–246 (2001).

[52] C. Falldorf, E. Kolenovic, and W. Osten, "Speckle shearography using a multiband light source," *Opt. Lasers Eng.* **40**, 543–552 (2003).

[53] C. Falldorf, M. Agour, C. v. Kopylow, and R. B. Bergmann, "Phase retrieval by means of a spatial light modulator in the Fourier domain of an imaging system," *Appl. Opt.* **49**, 1826–1830 (2010).

[54] C. Falldorf, "Measuring the complex amplitude of wave fields by means of shear interferometry," *J. Opt. Soc. Am. A* **28**, 1636–1647 (2011).

[55] R. P. Feynman, R. B. Leighton, and M. L. Sands, Mainly *The Feynman lectures on physics, Vol. I: Mainly Mechanics, Radiation, and Heat*, (Addison-Wesley, 1963).

[56] R. P. Feynman, R. B. Leighton, and M. L. Sands, Mainly *The Feynman lectures on physics, Vol. II: Mainly electromagnetism and matter*, (Addison-Wesley, 1963).

[57] J. R. Fienup, "Reconstruction of an object from the modulus of its Fourier transform," *Opt. Lett.* **3**, 27–29 (1978).

[58] J. R. Fienup, "Iterative method applied to image reconstruction and to computer generated holograms," *Opt. Eng.* **19**, 297–305 (1980).

[59] J. R. Fienup, "Phase retrieval algorithms: a comparison," *Appl. Opt.* **21**, 2758–2769 (1982).

[60] J. R. Fienup, "Phase retrieval using boundary conditions," *J. Opt. Soc. Am. A* **3**, 284–288 (1986).

[61] J. R. Fienup and C. C. Wackerman, "Phase-retrieval stagnation problems and solutions," *J. Opt. Soc. Am. A* **3**, 1897–1907 (1986).

[62] J. R. Fienup, "Phase retrieval for the Hubble Space Telescope using iterative propagation algorithms," in A. G. Tescher, ed., *Applications of digital image processing XIV*, *Proc. Soc. Photo-Opt. Instrum. Eng.* **1567** (1991), 327–332.

[63] J. R. Fienup, "Phase-retrieval algorithms for a complicated optical system," *Appl. Opt.* **32**, 1737–1746 (1993).

[64] J. R. Fienup, "Phase retrieval for imaging and wavefront sensing," General dynamics distinguished lecture at EECS department of the University of Michigan, (2006), available online.

[65] S. Finger, *Origins of neuroscience. a history of explorations into brain function*, (Oxford University Press, 1994).

[66] A. Foi, M. Trimeche, V. Katkovnik, and K. Egiazarian, "Practical Poissonian-Gaussian noise modeling and fitting for single image raw-data," *IEEE Trans. Image Process.* **17**, 1737–1754, (2008), available online.

[67] L. M. Frantz, A. A. Sawchuk, and W. von der Ohe, "Optical phase measurement in real time," *Appl. Opt.* **18**, 3301–3306 (1979).

[68] D. Gabor, "A new microscopic principle," *Nature* **161**, 777–778, (1948).

[69] O. El Gawhary and H. P. Urbach, "Spatial correlation for propagated fields and the phase problem," 8th EOS Topical meeting on Diffractive Optics 2012 (DO 2012), Delft, Netherlands, (2012).

[70] G. Gbur and T. D. Visser, "Phase singularities and coherence vortices in linear optical systems" *Optics Comm.* **259**, 428–435 (2006).

[71] R. W. Gerchberg and W. O. Saxton, "A practical algorithm for the determination of the phase from image and diffraction plane pictures," *Optik* **35**, 237-246 (1972).

[72] D. C. Ghiglia and M. D. Pritt, *Two-dimensional phase unwrapping: theory, algorithms, and software*, (Wiley, 1998).

[73] C. Giacovazzo, *Direct phasing in crystallography: fundamentals and applications*, (Oxford University Press, 1998).

[74] P. E. Gill, W. Murray, M. A. Saunders, and M. H. Wright, "Some theoretical properties of an augmented Lagrangian merit function," in P. M. Pardalos ed., *Advances in optimization and parallel computing*, (North-Holland, 1992), 101–128.

[75] G. H. Golub, M. Heath and G. Wahba, "Generalized cross-validation as a method for choosing a good ridge parameter," *Technometrics* **21**, 215–223 (1979).

[76] R. C. Gonzalez and R. E. Woods, *Digital image processing*, 2nd ed. (Prentice Hall, 2002).

[77] N. R. Goodman, "Statistical analysis based on a certain multivariate complex Gaussian distribution (an introduction)," *Ann. Math. Statist.* **34**, 152-177 (1963).

[78] J. W. Goodman and R. W. Lawrence, "Digital image formation from electronically detected holograms," *Appl. Phys. Letters* **11**, 77–79 (1967).

[79] J. W. Goodman, *Introduction to Fourier Optics*, 2nd ed. (McGraw-Hill, 1996).

[80] J. W. Goodman, *Introduction to Fourier Optics*, (ed. G. I. Kosourov, Russian translation: translated by V. U. Gelitsky and M. P. Golovey, Mir, 1970).

[81] J. W. Goodman, *Statistical optics*, (Wiley-Blackwell, 2000).

[82] G. Gould, "The LASER, Light amplification by stimulated emission of radiation," in P. A. Franken and R. H. Sands, eds., *The ann arbor conference on pptical pumping*, the University of Michigan, (1959).

[83] I. S. Gradstein, I. M. Ryzhik, *Tables of integrals, series, and products*, 5th ed., (Academic Press, 1994); I. S. Gradstein, I. M. Ryzhik, *Tables of integrals, series, and products*, (FizMatLit, 1963), in Russian.

[84] S. Grilli, P. Ferraro, S. D. Nicola, A. Finizio, G. Pierattini, and R. Meucci, "Whole optical wavefields reconstruction by digital holography, " *Opt. Express* **9**, 294–302 (2001).

[85] F. M. Grimaldi, "Physico-mathesis de lvmine, coloribvs, et iride, aliisque adnexis libri duo," 1–11 (Bologna, Vittorio Bonati, 1665).

[86] M. T. Gruneisen, M. B. Garvin, R. C. Dymale, and J. R. Rotgé, "Mosaic imaging with spatial light modulator technology," *Appl. Opt.* **45**, 7211–7223 (2006).

[87] I. P. Gurov, "Computer photonics: principles, problems and prospects," *Scientific and Technical Journal ITMO* **21**, 5–20 (2005), in Russian.

[88] J. Hadamard, *Lectures on Cauchy's problem in linear partial differential equ*ations, (Yale University Press, 1923).

[89] D. Han, K. Kornelson, D. Larson, and E. Weber, *Frames for Undergraduates*, (Student Mathematical Library, AMS, 2007).

[90] M. Handschy, M. J. O'callaghan, C. M. Walker, "Phase mask for use in holographic data storge," European Patent EP1751746.

[91] P. C. Hansen, *Rank-deficient and discrete ill-posed problems: numerical aspects of linear inversion*, (SIAM, 1987).

[92] P.C. Hansen, "Analysis of discrete ill-posed problems by means of the L-curve," *SIAM Rev.* **34**, 561–580 (1992).

[93] P.C. Hansen and D. P. O'Leary, "The use of the L-curve in the regularization of discrete ill- posed problems," *SIAM J. Sci. Comput.* **14**, 487–1503 (1993).

[94] P. C. Hansen, M. Kilmer and R. H. Kjeldsen, "Exploiting residual information in the parameter choice for discrete ill-posed problems," *BIT* **46**, 41–59, (2006).

[95] P. C. Hansen, "Regularization Tools Version 4.0 for Matlab 7.3," Numer. Algo. 46, 189–194 (2007); P. C. Hansen, *Regularization Tools Version 4.1 for Matlab 7.3*, (2008), available online ; Matlab code is available here.

[96] R. W. Harrison, "Phase problem in crystallography," *J. Opt. Soc. Am. A* **10**, 1046–1055 (1993).

[97] J. F. Hartmann, "Bemerkungen über den Bau und die Justirung von Spektrographen," *Zt. Instrumentenkd.* **20**, 47–58 (1900).

[98] M. R. Hestenes, "Multiplier and gradient methods," *JOTA* **4**, 303–320 (1969).

[99] R. A. Horn, C. R. Johnson, Topics in Matrix Analysis, (Cambridge University Press, 1991).

[100] M. Huebschman, B. Munjuluri, and H. Garner, "Dynamic holographic 3-D image projection," *Opt. Express* **11**, 437–445 (2003).

[101] J. P. Huignard, "Spatial light modulators and their applications," *J. Optics* **18**, 181–186 (1987).

[102] Y. Y. Hung and J.Q. Wang, "Dual-beam phase shift shearography for measurement of in-plane strains," *Opt. Lasers Eng.* **24**, 403–413 (1996).

[103] Y. Y. Hung and H.P. Ho, "Shearography: an optical measurement technology and applications," *Mater. Sci. Eng. R* **49**, 61–87 (2005).

[104] N. E. Hurt, *Phase retrieval and zero crossings: mathematical methods in image reconstruction*, (Kluwer Academic Publishers, 1989).

[105] M.-D. Iordache, J. Bioucas-Dias, and A. Plaza, "Total variation spatial regularization for sparse hyperspectral unmixing," *IEEE Trans Geosci Rem Sens.* **PP**, 1–19 (2012).

[106] V. Yu. Ivanov, V. P. Sivokon, and M. A. Vorontsov, "Phase retrieval from a set of intensity measurements: theory and experiment," *J. Opt. Soc. Am. A* **9**, 1515–1524 (1992).

[107] P. Jaming, "Uniqueness results for the phase retrieval problem of fractional Fourier transforms of variable order," arXiv/1009.3418 (2010), available online .

[108] B. Jin and J. Zou "Augmented Tikhonov regularization," *Inverse Problems* **25**, 025001 (2009).

[109] J. Kaipio and E. Somersalo, Statistical and computational inverse problems, (Springer, 2005), available online .

[110] C. Kanzow, "Einführung in die Spieltheorie. Theorie und Numerik von Nash Gleichgewichtsproblemen," Universität Würzburg (2007), in German, available online.

[111] V. Katkovnik, J. Astola, and K. Egiazarian, "Wavefield reconstruction and design as discrete inverse problems," 3DTV08, 265–268 (2008).

[112] V. Katkovnik, J. Astola, and K. Egiazarian, "Discrete diffraction transform for propagation, reconstruction, and design of wavefield distributions," *Appl. Opt.* **47**, 3481–3493 (2008).

[113] V. Katkovnik, **A. Migukin**, and J. Astola, "Backward discrete wave field propagation modeling as an inverse problem: toward perfect reconstruction of wave field distributions," *Appl. Opt.* **48**, 3407–3423 (2009).

[114] V. Katkovnik, **A.Migukin**, and J. Astola, "Digital 2D wavefield reconstruction based on novel two-matrix forward/backward propagation modeling", ISMTII'2009, St. Petersburg, Russia, (2009).

[115] V. Katkovnik, **A. Migukin**, and J. Astola, "Computational inverse holographic imaging: toward perfect reconstruction of wavefield distributions," in W. Osten, M. Kujawinska eds., *Fringe 2009, 6th International workshop on advanced optical metrology*, (Springer, 2009), 542–549.

[116] V. Katkovnik, **A. Migukin**, and J. Astola, "Computational inverse coherent wave field imaging, " ICIP (2009), 3773–3776.

[117] V. Katkovnik, A. Danielyan, and K. Egiazarian, "Decoupled inverse and denoising for image deblurring: variational BM3D-frame technique," ICIP (2011), 3514 – 3517.

[118] V. Katkovnik and J. Astola, "Phase retrieval via spatial light modulator phase modulation in 4f optical setup: numerical inverse imaging with sparse regularization for phase and amplitude," *J. Opt. Soc. Am. A* **29**, 105–116 (2012).

[119] M. V. Klibanov, P. E. Sacks, and A. V. Tikhonravov, "The phase retrieval problem," *Inverse problems* **11**, 1–28 (1995).

[120] E. Kolenovic. "Correlation between intensity and phase in monochromatic light," *J. Opt. Soc. Am. A* **22**, 899–906 (2005).

[121] V. V. Kotlyar, P.G. Serafimovich and O.K. Zalyalov, "Noise-insensitive iterative method for interferogram processing," *Opt. and Laser Technology* **27**, 251–254 (1995).

[122] V. V. Kotlyar and O. K. Zalyalov, "Iterative reconstruction algorithm three-dimensional shape of the object," *Computer Optics* **16**, 71–73 (1996), in Russian, available online .

[123] D. Krawczyk-Stańdo and M. Rudnicki, "Regularization parameterselection in discrete ill-posed problems - the use of the U-curve," *Int. J. Appl. Math. Comput. Sci.* **17**, 157–164 (2007).

[124] T. Kreis, P. Aswendt, R. Höfling, "Hologram reconstruction using a digital micromirror device," *Opt. Commun.* **40**, 926–933 (2001).

[125] T. Kreis, *Handbook of Holographic Interferometry: Optical and Digital Methods*, (Wiley-VCH, 2005).

[126] T. Kreis, "Digital holography methods in 3D-TV," Proc. of 3DTV-Con 01, Kos (2007).

[127] M. A. Kronrod, N. S. Merzlyakov, and L. P. Yaroslavskii, "Reconstruction of a hologram with a computer," *Sov. Phys. Tech. Phys.* **17**, 333–334 (1972) in Russian.

[128] M. A. Kronrod, N. S. Merzlyakov and L. P. Yaroslavsky, "Computer synthesis of transparency holograms," *Sov. Phys. Tech. Phys.* **13**, 414–418 (1972) in Russian.

[129] A. A. Kulkarni and U. V. Shanbhag, "New insights on generalized Nash games with shared constraints: constrained and variational equilibria," *IEEE Conf. on Decision and Control* (CDC/CCC 2009), 151–156 (2009).

[130] E. Lalor, "Conditions for the validity of the angular spectrum of plane waves," *J. Opt. Soc. Am. A* **58**, 1235–1237 (1968).

[131] M. J. Langa and S. M. Block, "Resource Letter: LBOT-1: Laser-based optical tweezers," *Am. J. Phys.* **71**, 201–215 (2003).

[132] E. N. Leith and J. Upatnieks, "Reconstructed wavefronts and communication theory," *J. Opt. Soc. Am.* **52**, 1123–1128 (1962).

[133] E. N. Leith and J. Upatnieks, "Wavefront Reconstruction with Continuous-Tone Objects," *J. Opt. Soc. Am.* **53**, 1377–1381 (1963).

[134] L. B. Lesem, P. M. Hirsch and J. A. Jordan, "Computer synthesis of holograms for 3-D display," *Commun. of associat. for comp. machinery* **11**, 661–674, (1968).

[135] L. B. Lesem, P. M. Hirsch and J. A. Jordan, "Kinoform," *IBM Journ. Res. Dev.* **13**, 150–155 (1969).

[136] A. Levi and H. Stark, "Image restoration by the method of generalized projections with application to restoration from magnitude," *J. Opt. Soc. Am. A* **1**, 932–943 (1984).

[137] G. N. Lewis, "The conservation of photons," Nature **118**, 874-875 (1926).

[138] O. N. Litvinenko, *Basics of radiooptics*, (Technica, 1974) in Russian.

[139] A. W. Lohmann and D. P. Paris, "Binary Fraunhofer holograms, generated by computer," *Appl. Opt.* **6**, 1739–1748 (1967).

[140] D. R. Luke, J. V. Burke, and R. Lyon, "Optical wavefront reconstruction: theory and numerical methods," *SIAM Rev.* **44**, 169–224 (2002).

[141] T. H. Maiman, "Stimulated optical radiation in ruby," *Nature* **187**, 493–494 (1960).

[142] J. R. Magnus, H. Neudecker, *Matrix Differential Calculus with Applications in Statistics and Econometrics*, (Wiley, 1999).

[143] D. Malacara, M. Servín, M. and Z. Malacara, *Interferogram analysis for optical testing*, 2nd ed., (Taylor & Francis, 2005).

[144] S. Marchesini, "Phase retrieval and saddle-point optimization," *J. Opt. Soc. Am. A* **24**, 3289–3296 (2007).

[145] **A. Migukin**, V. Katkovnik, and J. Astola, "Multiple plane phase retrieval based on inverse regularized imaging and discrete diffraction transform," *AIP Conf. Proc.* **1236**, 81–86 (2010).

[146] **A. Migukin**, V. Katkovnik, and J. Astola, "3D Wave field phase retrieval from multi-plane observations, " IEEE Conf. 3DTV-CON, Tampere, Finland, 2010.

[147] **A. Migukin**, V. Katkovnik, and J. Astola, "Phase retrieval from multiple plane observations: constrained variational formalization and augmented Lagrangian recursive algorithm, "in Workshop on Information Theoretic Methods in Science and Engineering, WITMSE'2010, Tampere, Finland, 2010.

[148] **A. Migukin**, V. Katkovnik, and J. Astola, "Wave field reconstruction from multiple plane intensity-only data: augmented Lagrangian algorithm, " *J. Opt. Soc. Am. A* **28**, 993–1002 (2011).

[149] **A. Migukin**, V. Katkovnik, and J. Astola, "Advanced phase retrieval: maximum likelihood technique with sparse regularization of phase and amplitude," arXiv:1108.3251v1.

[150] **A. Migukin**, V. Katkovnik, and J. Astola, "Optimal phase retrieval from multiple observations with Gaussian noise: augmented Lagrangian algorithm for phase objects,"in P. H. Lehmann, W. Osten, and K. Gastinger eds., *Optical measurement systems for instrumental inspection VII*, *Proc. SPIE* **8082**, 80820L, 2011.

[151] **A. Migukin**, V. Katkovnik, and J. Astola, "Advanced multi-plane phase retrieval using Graphic Processing Unit: augmented Lagrangian technique with sparse regularization,"in F. Wyrowski, J. T. Sheridan, J. Tervo, and Y. Meuret eds., *Optical Modelling and Design II*, *Proc. SPIE* **8429**, 84291N, 2012.

[152] **A. Migukin**, M. Agour, and V. Katkovnik, "Phase retrieval with background compensation in 4f optical system: decoupled augmented Lagrangian technique for binary amplitude object, " *Appl. Opt.* **52**, A269–A280 (2013).

[153] R. P. Millane, "Phase retrieval in crystallography and optics," *J. Opt. Soc. Am. A* **7**, 394–411 (1990).

[154] R. P. Millane, "Multidimensional phase problems," *J. Opt. Soc. Am. A* **13**, 725-734 (1996).

[155] D. L. Misell, "A method for the solution of the phase problem in electron microscopy," *J. Phys. D* **6**, L6–L9 (1973).

[156] V. A. Morozov, *Methods for solving incorrectly posed problems*, (Springer, 1984).

[157] M. Mosarraf, G. Sheoran, D. Singh, and C. Shakher, "Contouring of diffused objects by using digital holography," *Opt Lasers Eng.* **45**, 684–689 (2007).

[158] V. Nascov and P. Cătălin Logofătu, "Fast computation algorithm for the Rayleigh-Sommerfeld diffraction formula using a type of scaled convolution," *Appl. Opt.* **48**, 4310–4319 (2009)

[159] J. A. Neff, R. A. Athale, and S. H. Lee, "Two-dimensional spatial light modulators: a tutorial," *IEEE Proc.* **78**, 826–855 (1990).

[160] H. Neudecker, "Some theorems on matrix differentiation with special reference to Kronecker matrix products," *J. Amer. Statist. Assoc.* **64**, 953—963 (1969).

[161] K. C. Neuman and S. M. Blocka, "Optical trapping, Review of scientific instruments," *Am. Institute of Phys.* **75**, 2787-2809 (2004).

[162] J. Nocedal and S. J. Wright, *Numerical optimization*, 2nd. ed., (Springer, 2006).

[163] J. F. Nye and M. V. Berry, "Dislocations in wave trains," *Proc. R. Soc. Lond. A* **336**, 165–190 (1974).

[164] F. S. Oktem and R. E. Blahut, "Schulz-Snyder phase retrieval algorithm as an alternating minimization algorithm," in *Computational Optical Sensing and Imaging*, OSA Technical Digest (2011), paper CMC3.

[165] L. Onural, "Some mathematical properties of the uniformly sampled quadratic phase function and associated issues in digital Fresnel diffraction simulations," *Opt. Eng.* **43**, 2557–2563 (2004).

[166] L. Onural, "Exact analysis of the effects of sampling of the scalar diffraction field," *J. Opt. Soc. Am. A* **24**, 359–367 (2007).

[167] A. V. Oppenheim and R. W. Schafer, *Digital signal processing*, (Prentice-Hall, 1975).

[168] A. V. Oppenheim and R. W. Schafer, *Discrete-time signal processing*, (Prentice-Hall, 1989).

[169] W. Osten, T. Baumbach, and W. Jüptner, "Comparative digital holography," *Optics Lett.* **27**, 1764–1766 (2002).

[170] N. Otsu. "A threshold selection method from gray-level histograms," IEEE Transactions of Systems, Man and Cybernetics **9**, 62–66 (1979).

[171] D. Paganin, A. Barty, P. J. McMahon, and K. Nugent, "Quantitative phase-amplitude microscopy. III. The effects of noise," *J. Microsc.* **214**, 51–61 (2004).

[172] D. G. Papazoglou, M. Loulakis, G. Siganakis and N. A. Vainos, "Holographic read - write projector of video images," *Opt. Express* **10**, 280–285 (2002).

[173] D. A. Park, *The fire within the eye: a historical essay on the nature and meaning of light*, (Princeton University Press, 1997).

[174] R. G. Paxman, T. J. Schulz, and J. R. Fienup, "Joint estimation of object and aberrations by using phase diversity," *J. Opt. Soc. Am. A* **9**, 1072–1085 (1992).

[175] G. Pedrini, S. Schedin, and H. J. Tiziani, "Aberration compensation in digital holographic reconstruction of microscopic objects," *J. Mod. Opt.* **48**, 1035–1041 (2001).

[176] G. Pedrini and H. J. Tiziani, "Short-coherence digital microscopy by use of a lensless holographic imaging system," *Appl Opt.* **41**, 4489–4496 (2002).

[177] G. Pedrini, S. Schedin, and H. J. Tiziani, "Pulsed digital holography combined with laser vibrometry for 3D measurements of vibrating objects," *Opt. Lasers Eng.* **38**, 117–129 (2002).

[178] G. Pedrini, W. Osten, and Y. Zhang, "Wave-front reconstruction from a sequence of interferograms recorded at different planes," *Opt. Lett.* **30**, 833–835 (2005).

[179] S. Perkowitz, *Empire of light: a history of discovery in science and art*, (Joseph Henry Press, 1996).

[180] R. Piche, "Regularization operators for multidimentional inverse problems with Kronecker product structure," ECCOMAS2004, (2004), available online .

[181] B. C. Platt and R. V. Shack, "History and principles of Shack-Hartmann wavefront sensing," *J. Refract Surg.* **17**, S573–S577 (2001), available online .

[182] Pliny the Elder, *The Natural History* (eds. J. Bostock, M.D., F.R.S., H. T. Riley, Esq., B.A., London. Taylor and Francis, Red Lion Court, Fleet Street, 1855), Book XXXVII, Chap. 16.

[183] B. T. Polyak, *Introduction to optimization*, (Nauka, 1983), in Russian; B. T. Polyak, *Introduction to optimization*, (Optimization Software, 1987).

[184] N. Ponomarenko, V. Lukin, M. Zriakhov, and A. Kaarna, "Improved grouping and noise cancellation for automatic lossy compression of AVIRIS images," in J. Blanc-Talon, D. Bone, W. Philips, D. Popescu, and P. Scheunders, ed., *Advanced concepts for intelligent vision systems*, (Springer, 2010), 261–271.

[185] M. J. D. Powell, "A method for nonlinear constraints in minimization problems," in R. Fletcher, ed., *Optimization*, (Academic Press, 1969), 283–298.

[186] G. V. Rocha and B. Yu, "Greedy and relaxed approximations to model selection: a simulation study," in P. Grunwald, P. Myllymaki, I. Tabus, M. Weinberger and B. Yu eds., *Festschrift in honor of Jorma Rissannen on the occasion of his 75th birthday*, (TICSP Report # 38, 2008), 63–80.

[187] P. Rodrigo, R. Eriksen, V. Daria, and J. Glückstad, "Shack-Hartmann multiple-beam optical tweezers," *Opt. Express* **11**, 208–214 (2003).

[188] V. Ronchi, *The nature of light: an historical study*, (Heinemann, 1970).

[189] W. Rudin, *Principles of mathematical analysis*, 3rd. ed., (McGraw-Hill, 1976).

[190] B. E. A. Saleh and M. C. Teich, *Fundamentals of photonics* (2nd ed., John Wiley and Sons, Inc., 2007).

[191] O. Scherzer, "The use of Morozov's discrepancy principle for Tikhonov regularization for solving nonlinear ill-posed problems," *Computing* **51**, 45–60 (1993).

[192] U. Schnars and W. Jüptner, "Direct recording of holograms by a CCD target and numerical reconstruction," *Appl. Opt.* **33**, 179–181 (1994).

[193] U. Schnars and W. Jüptner, "Digital recording and numerical reconstruction of holograms," *Meas. Sci. Technol.* **13**, R85–R101 (2002).

[194] U. Schnars and W. Jüptner, *Digital holography: digital hologram recording, numerical reconstruction, and related techniques*, (Springer, 2005).

[195] R. V. Shack and B. C. Platt, "Production and use of a lenticular Hartmann screen," *J. Opt. Soc. Am.* **61**, 656–660 (1971).

[196] F. Shen and A. Wang, "Fast-Fourier-transform based numerical integration method for the Rayleigh-Sommerfeld diffraction formula," *Appl. Opt.* **45**, 1102–1110 (2006).

[197] G. S. Sherman, "Integral-transform formulation of diffraction theory," *J. Opt. Soc. Am.* **57**, 1490-1498 (1967).

[198] T. J. J. See, "New Theory of the Aether," *Astronomische Nachrichten* **212**, 385–454 (1921).

[199] S. Seebacher, W. Osten, T. Baumbach, and W. Juptner, "The determination of material parameters of microcomponents using digital holography," *Opt. Lasers Eng.* **36**, 103-126 (2001).

[200] L. Seifert, J. Liesener, H.J. Tiziani, "The adaptive Shack–Hartmann sensor," *Opt. Commun.* **216**, 313–319 (2003).

[201] J. H. Seldin and J. R. Fienup, "Numerical investigation of the uniqueness of phase retrieval," *J. Opt. Soc. Am. A* **7**, 412–427 (1990).

[202] A. Semichaevsky and M. Testorf, "Phase-space interpretation of deterministic phase retrieval," *J. Opt. Soc. Am. A* **21**, 2173–2179 (2004).

[203] G. Sinclair, J. Leach, P. Jordan, G. Gibson, E. Yao, Z. Laczik, M. Padgett, and J. Courtial, "Interactive application in holographic optical tweezers of a multi-plane Gerchberg-Saxton algorithm for three-dimensional light shaping," *Opt. Express* **12**, 1665–1670 (2004).

[204] D. V. Sivuhin, *General physics course*, vol. 4, Optics, (Phyzmatlit, 2005), in Russian.

[205] G. Sluder, and D. E. Wolf , *Digital microscopy*, (Elsevier Academic Press, 2007).

[206] M. Soto and E. Acosta, "Improved phase imaging from intensity measurements in multiple planes," *Appl. Opt.* **46**, 7978–7981 (2007).

[207] V. A. Soyfer, ed., *Methods of computer optics*, 2nd ed., (FisMatLit, 2003), in Russian.

[208] V. A. Soyfer, ed., *Computer image processing, Part I: Basic concepts and theory*, (VDM Verlag Dr. Müller, 2010); V. A. Soyfer, ed., *Computer image processing, Part II: Methods and algorithms*, (VDM Verlag Dr. Müller, 2010).

[209] V. Srinivasan, H. C. Liu, and M. Halioua, "Automated phase-measuring profilometry of 3-D diffuse objects," *Appl. Opt.* **23**, 3105–3108 (1984).

[210] E. Stapparets, "Combined spatial light modulator and phase mask for holographic storge system," U.S. Pat. No. 5914802.

[211] H. Stark, ed., *Image recovery: theory and application*, (Academic Press, 1987).

[212] H. Takajo, T. Takahashi, R. Ueda, and M. Taninaka, "Study on the convergence property of the hybrid input–output algorithm used for phase retrieval," *J. Opt. Soc. Am. A* **15**, 2849–2861 (1998).

[213] H. Takasaki, "Moiré topography," *Appl. Opt.* **9**, 1467–1472 (1970).

[214] M. Takeda, H. Ina, and S. Kobayashi, "Fourier-transform method of fringe-pattern analysis for computer-based topography and interferometry," *J. Opt. Soc. Am.* **72**, 156–160 (1982).

[215] M. Takeda and K. Mutoh, "Fourier transform profilometry for the automatic measurement of 3-D object shapes," *Appl. Opt.* **22**, 3977–3982 (1983).

[216] M. R. Teague, "Irradiance moments: their propagation and use for unique retrieval of phase," *J. Opt. Soc. Am.* **72**, 1199–1209 (1982).

[217] M. R. Teague, "Deterministic phase retrieval: a Green's function solution," *J. Opt. Soc. Am.* **73**, 1434–1441 (1983).

[218] M. R. Teague, "Image formation in terms of the transport equation," *J. Opt. Soc. Am. A* **2**, 2019–2026 (1985).

[219] A. N. Tikhonov and V.Y. Arsenin. *Solution of ill-posed problems* (Wiley, 1977).

[220] S. Tolansky, *Revolution in optics*, (Penguin, 1968).

[221] V. Uzunov, "Light field reconstruction and synthesis from irregularly distributed data points," PhD thesis, Tampere University of Technology, (2011).

[222] G. Valadão and J. Bioucas-Dias, "PUMA: Phase unwrapping via max flows," *IEEE Trans. Image Process.* **16**, 698–709 (2007).

[223] L. Waller, Y. Luo, S. Y. Yang, and G. Barbastathis, "Transport of intensity phase imaging in a volume holographic microscope," *Opt. Lett.* **35**, 2961–2963 (2010).

[224] L. Waller, M. Tsang, S. Ponda, S. Y. Yang, and G. Barbastathis, "Phase and amplitude imaging from noisy images by Kalman filtering," *Opt. Express* **19**, 2805–2814 (2011).

[225] Z. Wang, A. C. Bovik, H. R. Sheikh and E. P. Simoncelli, "Image quality assessment: From error visibility to structural similarity," *IEEE Trans. Image Process.* **13**, 600–612 (2004), available online.

[226] K. B. Wolf and G. Krötzsch, "Geometry and dynamics in refracting systems," *Eur. J. of Phys.* **16**, 14–20 (1995).

[227] Q. Xue, Z. Wang, J. Huang, and J. Gao, "The elimination of the errors in the calibration image of 3D measurement with Structured Light," *Proc. SPIE* **8430**, 84300N, (2012).

[228] I. Yamaguchi, J. Kato, S. Ohta, and J. Mizuno, "Image formation in phase-shifting digital holography and applications to microscopy," *Appl. Opt.* **40**, 6177–6186 (2001).

[229] I. Yamaguchi, J. Kato, and S. Ohta, "Surface shape measurement by phase shifting digital holography," *Opt. Rev.* **8**, 85–89 (2001).

[230] I. Yamaguchi, T. Matsumura, and J. Kato, "Phase-shifting color digital holography," *Opt. Lett.* **27**, 1108–1110 (2002).

[231] G. Yang, , B. Dong, B. Gu, J. Zhuang, and O. Ersoy, "Gerchberg–Saxton and Yang–Gu algorithms for phase retrieval in a nonunitary transform system: a comparison," *Appl. Opt.* **33**, 209–218 (1994).

[232] L. Yaroslavsky, *Digital signal processing in optics and holography: introduction to digital optics*, (Radio i Svyaz, 1987) in Russian.

[233] L. Yaroslavsky and M. Eden, *Fundamentals of digital optics*, (Birkhuser, 1996).

[234] L. Yaroslavsky, *Digital holography and digital image processing: principles, methods, algorithms*, (Kluwer Academic, 2004).

[235] L. P. Yaroslavsky, "Discrete transforms, fast algorithms, and point spread functions of numerical reconstruction of digitally recorded holograms," in J. Astola and L. P. Yaroslavsky ed., *Advances in signal transforms: theory and applications*, (Hindawi, 2007), 93–141.

[236] L. Yaroslavsky and J. Astola, *Introduction to digital holography*, (Bentham e-books, 2009), lectures are available online.

[237] T. Yatagai, S. Nakadata, M. Idesawa and H. Saito, "Automatic fringe analysis using digital image processing techniques" *Opt. Eng.* **21**, 432–435 (1982).

[238] Z. Zalevsky, D. Mendlovic, and R. G. Dorsch, "Gerchberg-Saxton algorithm applied in the fractional Fourier or the Fresnel domain," *Opt. Lett.* **21**, 842–844 (1996).

[239] F. Zernike, "Phase contrast, a new method for the microscopic observation of transparent objects," *Physica* **9**, 686–693 (1942).

[240] Y. Zhang, G. Pedrini, W. Osten, and H. Tiziani, "Whole optical wave field reconstruction from double or multi in-line holograms by phase retrieval algorithm," *Opt. Express* **11**, 3234–3241 (2003).

[241] F. Zhang, G. Pedrini, and W. Osten, "Phase retrieval of arbitrary complex-valued fields through aperture-plane modulation," *Phys. Rev. A*, **75** 043805 (2007).

[242] S. M. Zhao, J. Leach, L. Y. Gong, J. Ding, and B. Y. Zheng, "Aberration corrections for free-space optical communications in atmosphere turbulence using orbital angular momentum states," *Opt. Express* **20**, 452–461 (2012).